ASDEX CONTRIBUTIONS TO THE 15th EUROPEAN CONFERENCE ON CONTROLLED FUSION AND PLASMA PHYSICS

(Dubrovnik (Cavtat), May 16 - 20, 1988)

IPP III/136 Mai 1988

MAX-PLANCK-INSTITUT FÜR PLASMAPHYSIK

8046 GARCHING BEI MÜNCHEN

ASDEX CONTRIBUTIONS TO THE 15th EUROPEAN CONFERENCE ON CONTROLLED FUSION AND PLASMA PHYSICS

(Dubrovnik (Cavtat), May 16 - 20, 1988)

IPP III/136 Mai 1988

ASDEX CONTRIBUTIONS TO THE 15th EUROPEAN CONFERENCE ON CONTROLLED FUSION AND PLASMA PHYSICS

(Dubrovnik (Cavtat), May 16 - 20, 1988)

Long-Pulse Heating of ASDEX Plasmas

H.Niedermeyer, G.Becker, B.Bomba, H.Bruhns, K.Büchl, A.Carlson, G.Dodel[1], A.Eberhagen, H.-U.Fahrbach, G.Fussmann, O.Gehre, K.Gentle[2], J.Gernhardt, L.Giannone, G.v.Gierke, E.Glock, S.v.Goeler[3], O.Gruber, G.Haas, H.Herrmann, J.Hofmann, E.Holzhauer[1], K.Hübner[4], G.Janeschitz, S.Kaesdorf, F.Karger, M.Kaufmann, M.Keilhacker[5], O.Klüber, M.Kornherr, K.Krieger, K.Lackner, R.Lang, P.Lee[6], G.Lisitano, M.Lörcher, T.C.Luce[6], F.Mast, H.M.Mayer, K.McCormick, D.Meisel, V.Mertens, Y.Miura[7], E.R.Müller, H.Murmann, J.Neuhauser, R.Nolte, J.M.Noterdaeme, M.P.Petrov[8], W.Poschenrieder, R.Preis, H.Rapp, D.E.Roberts[9], H.Röhr, A.Rudyj, W.Sandmann, F.Schneider, U.Schneider, G.Siller, E.Simmet, E.Speth, F.Söldner, A.Stäbler, K.Steinmetz, K.H.Steuer, U.Stroth, N.Tsois[10], O.Vollmer, F.Wagner, J.B.Whitley[11], H.Würz[12], D.Zasche

Max-Planck-Institut für Plasmaphysik
EURATOM Association, D-8046 Garching

1 University of Stuttgart, Germany
2 University of Texas at Austin, USA
3 Princeton University, USA
4 University of Heidelberg, Germany
5 Present address: JET Joint Undertaking, England
6 GA Technologies Inc., San Diego, USA
7 JAERI Tokai Research, Ibaraki -Ken, Japan
8 Ioffe Institute, Leningrad, USSR
9 Atomic Energy Corp. of South Africa, Pretoria
10 NRS Demokritos, Attiki, Greece
11 Sandia National Lab., Albuquerque, USA
12 Kernforschungszentrum Karlsruhe

ABSTRACT

The Divertor Tokamak ASDEX, its neutral injection system and its ICRH system have been modified to permit additional heating with a power of 6 MW for pulse lengths up to 10 s. The paper summarizes the arguments for long-pulse heating, describes the technical modifications of the divertor performed, their effect on the operational behaviour of the tokamak and presents a few typical results of recent experiments exploiting the long-pulse heating facilities.

KEYWORDS

Tokamak, divertor, heating, long pulses, neutral injection, ICRH, pellets, density limit, confinement, impurities.

INTRODUCTION

ASDEX started in 1980 with ohmic discharges and soon reached a pulse length of 3 s limited only by the flux swing of the primary (Keilhacker and co-workers 1981). Slide-away discharges with very low loop voltage up to 11 s could also be obtained (Fussmann and co-workers 1981). Neutral beam heating was available in 1981 with pulses of only 200 ms duration. This short pulse length was considered inadequate and long-pulse neutral particle injection and ICRH systems were prepared. The aim were pulses of up to 10 s at a power of 3 MW from each of the systems.

In the years between planning and realization of the long-pulse heating systems progress has been made with minor upgrades of NI which lead to a pulse length of 400 ms (Vollmer and co-workers 1986), with ICRH (2.5 MW, 1 s, Steinmetz and co-workers 1986) and with lower hybrid heating (0.6 MW, 1 s, Söldner and co-workers 1985). After a shut-down phase between April 1986 and April 1987 ASDEX was technically suited for long-pulse heating.

This paper deals only with the long pulse heating facilities available now. In the first section the arguments leading to the long-pulse heating project will be reviewed. The technical realization will then be presented. The properties of ASDEX after the modification will be summarized. Finally a few examples of investigations performed with long-pulse heating will show its usefulness.

WHY LONG-PULSE HEATING?

Long Time Constants Require Long Pulses

The pulse length of early NI systems was technically limited to a few 100 ms. Compared with the energy confinement times of the machines this was sufficient. A tokamak involves however many time constants which can be much longer than the energy confinement time (see Table 1). Limiting the pulse length limits the range of validity of an experimental result. Many of the most important investigations can suffer from a too short pulse duration.

More than one of the time constants quoted in Table 1 influence the following plasma properties or effects.

- Energy confinement
- Density profiles
- Current drive
- Beta-limit
- Impurity concentration
- Recycling

Two examples may demonstrate this.

H-Mode at the beta limit. Fig. 1 shows characteristic signals of a discharge which comes close to the beta limit.

The discharge parameters are

– Plasma current	280 kA
– Toroidal field	1.74 T
Corresponding q_c	3.0
– Density	$3.0 \cdot 10^{19}$ m^{-3} (D^+)
– NI power	4 MW (D^0 beams)

TABLE 1 Time Constants of a Tokamak
(typical ASDEX values in parentheses)

Energy confinement time	(25 … 150 ms)
Particle diffusion time	(25 ms … > 1 s)
Impurity accumulation time	(100 ms… > 1 s)
Magnetic field diffusion time	(100 ms … 1s)
Sawtooth period	(10 ms … > 1 s)
Surface relaxation times	(500 ms … > 10 s)
Surface heating times	(100 ms … > 10 s)

The discharge reaches the H-phase shortly after the beginning of injection. In the middle of a 100 ms H-phase beta reaches its maximum near the expected beta limit. During the succeeding L-phase beta keeps decaying until the end of the NI pulse. This short duration of the H-phase is caused by the operation close to the beta-limit and not typical for the H-mode.

The loop voltage undershoots after the beginning of injection to zero and rises until the end of the heating pulse.

Energy confinement time, poloidal field diffusion time and the time constants of the feedback systems for the radial position and for the plasma current govern the transient behaviour of the discharge.

A heating pulse of 300 ms duration is clearly too short to determine whether or not the discharge reaches its equilibrium.

Co- and counter-NI. A comparison of two shots heated with a 200 ms neutral beam pulse in co and counter direction respectively is shown in Fig.2. From the traces shown one might guess that the poloidal beta of the counter discharge would rise if the heating pulse were longer. It also seems that the impurity level saturates in both cases at a different level. The statistical excursions of the curves indicate however that the extrapolation of the signals is not permitted.

The duration of the heating pulse, which is a multiple of the confinement time, is insufficient to distinguish the character of both discharges.

We will see later that time constants for hydrogen and impurity transport influence counter injection heated discharges.

Conclusion. While it is certainly most important to investigate additional heating methods on a time scale of the energy confinement time it is absolutely necessary to extend the discharges to much longer durations.

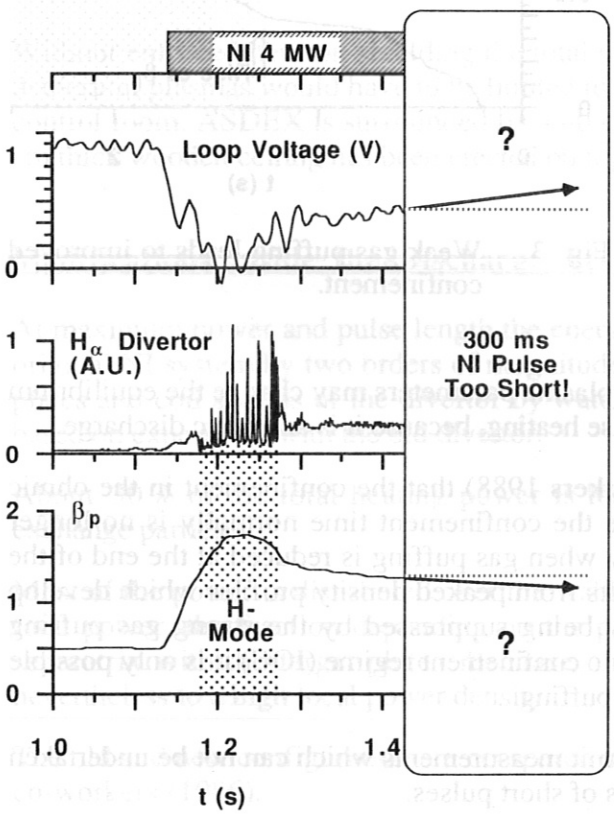

Fig. 1. H-mode discharge at the beta limit.

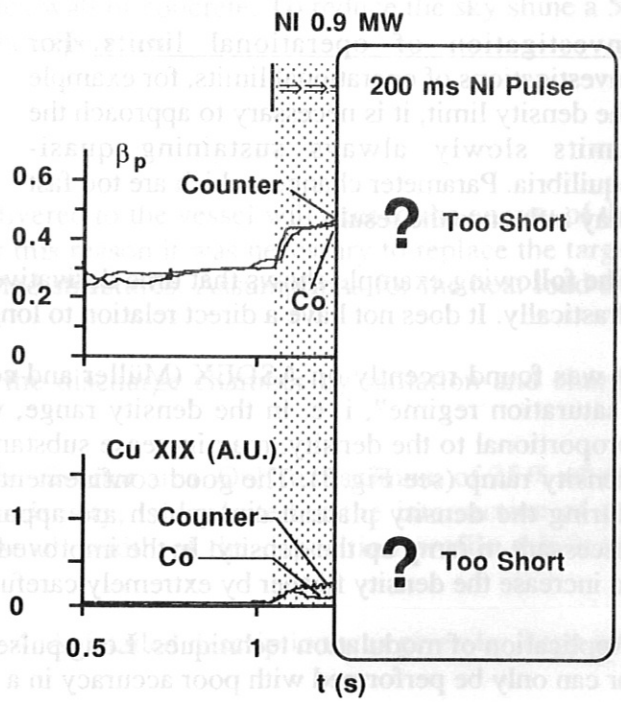

Fig.2. Comparison of co- and counter-injection.

The actual duration of a "long pulse" depends on the size of the machine and the parameters of the discharge, because the time constants depend on these factors. Reduction of the time constants by deterioration of the discharges may be applicable in rare cases.

For ASDEX a maximum pulse length of 10 s at a maximum total power of 6 MW with slightly reduced plasma current and toroidal field has been technically feasible and sufficient for most investigations. It will be reached if the heating applied is efficient enough to reduce the loop voltage substantially. In many cases 1 - 2 s are adequate.

Long Pulses Facilitate Experimental Work

As well as the physical arguments for long-pulse heating, there are also some important practical reasons.

Efficient use of discharge time. Time can be saved and accuracy can be increased if parameter scans, for example of plasma density, plasma current or heating power, are performed during one discharge.

Multi-channel diagnostics are desirable but expensive and not always available. In a long steady state discharge it is possible to perform instrumental scans, for example wavelength scans with spectrometers, frequency sweeps with frequency analyzers and similar techniques.

In a long pulse several programmes may be performed. This is useful for the commissioning of new heating systems or for special experiments like laser blow-off techniques.

Investigation of operational limits. For investigations of operational limits, for example the density limit, it is necessary to approach the limits slowly always sustaining quasi-equilibria. Parameter changes which are too fast may influence the result.

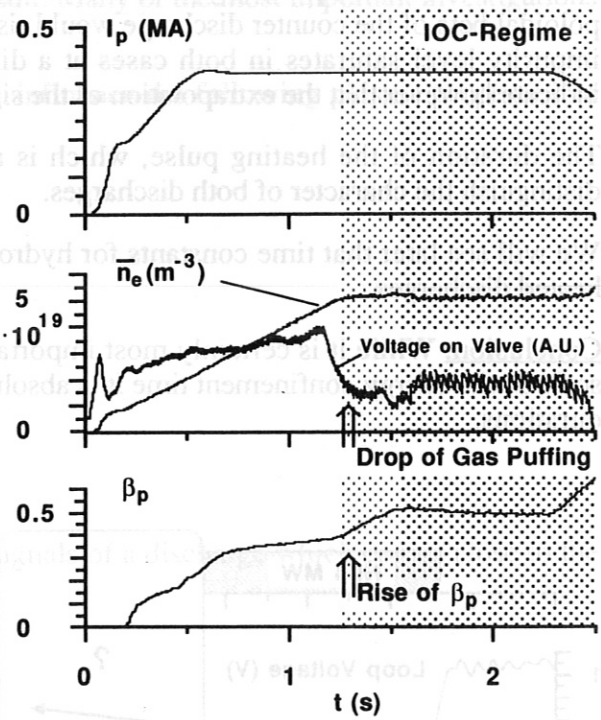

Fig. 3. Weak gas puffing leads to improved confinement.

The following example shows that time derivatives of plasma parameters may change the equilibrium drastically. It does not have a direct relation to long-pulse heating, because it is an ohmic discharge.

It was found recently on ASDEX (Müller and co-workers 1988) that the confinement in the ohmic "saturation regime", i. e. in the density range, where the confinement time normally is no longer proportional to the density, may increase substantially when gas puffing is reduced at the end of the density ramp (see Fig. 3). The good confinement results from peaked density profiles which develop during the density plateau and which are apparently being suppressed by the strong gas puffing necessary to ramp up the density. In the improved ohmic confinement regime (IOC) it is only possible to increase the density further by extremely careful gas puffing.

Application of modulation techniques. Long pulses permit measurements which can not be undertaken or can only be performed with poor accuracy in a series of short pulses.

- By modulation of the heating power the local power absorption can be determined.
- The local coefficients of particle diffusion and inward drift can be measured by modulation of the electron density.

Periods in the order of the heat or particle diffusion time are required and the analysis needs a large number of periods.

TECHNICAL MODIFICATIONS OF ASDEX

Long Pulse NI Sources

To permit long NI pulses, new beamlines had to be constructed (Feist and co-workers 1984). For economic reasons a major part of the components of the old beamlines had to be re-used.

The most important and technically difficult change was the replacement of the inertial cooled grids of the sources and beam dumps by water cooled ones. The basic components of the sources are still the same but new grids had to be developed. The copper construction is directly water cooled on the whole active surface.

Long Pulse ICRH Systems

Generators and transmission lines were designed for 10 s pulses from the beginning. A minor upgrade of the generators permits now to generate 2 MW with each of both systems under ideal matching conditions so that at least 3 MW can be fed to the antennae in practice.

The old antennae were inertially cooled. The Faraday screens and side limiters had to be replaced by water cooled ones.

Neutron Shielding

Without enforced neutron shielding the total number of long NI pulses with deuterium injection into deuterium plasmas would have to be limited to a very small number to avoid excessive radiation in the control room. ASDEX is surrounded by a 80 cm thick wall of concrete. To reduce the sky shine a 50 cm thick wooden ceiling has been erected on top of the experiment.

Modifications inside the Discharge Vessel

At maximum power and pulse length the energy delivered to the vessel will exceed the energy of the original NI system by two orders of magnitude. For this reason it was necessary to replace the target plates and coil shields of the divertor by water cooled structures. Assumptions for the heat load are based on experience with the old divertor.

About 30 % of the total heating power is lost in the discharge chamber by radiation and charge exchange particles.

Most of the power is distributed over the walls in the divertor area. Only a maximum of 25 % of the total power, the fraction depending on the plasma density, is deposited at the intersection of the separatrix with the target plates. Because of the small width of the deposition profile this leads nevertheless to a high local power density.

The old and new configuration are compared in Fig. 4. A detailed description was given by Rapp and co-workers (1986).

The design of the new divertor fulfills the following demands:

- The existing divertor coils had to stay in place.
- Sensitive components in the divertor chamber had to be shielded against the diffuse radiation and CX emission.
- The power deposited locally at the separatrix had to be removed during pulses of many seconds duration.

The first demand imposed space restrictions.

The second demand led to a narrow and almost closed divertor chamber. The divertor shields are made from water cooled tubes or bars. There is no direct line of sight from the plasma to the coils, but the structure is not gas tight.

The third demand led to copper as material for the target plates. The outer shields are made from stainless steel.

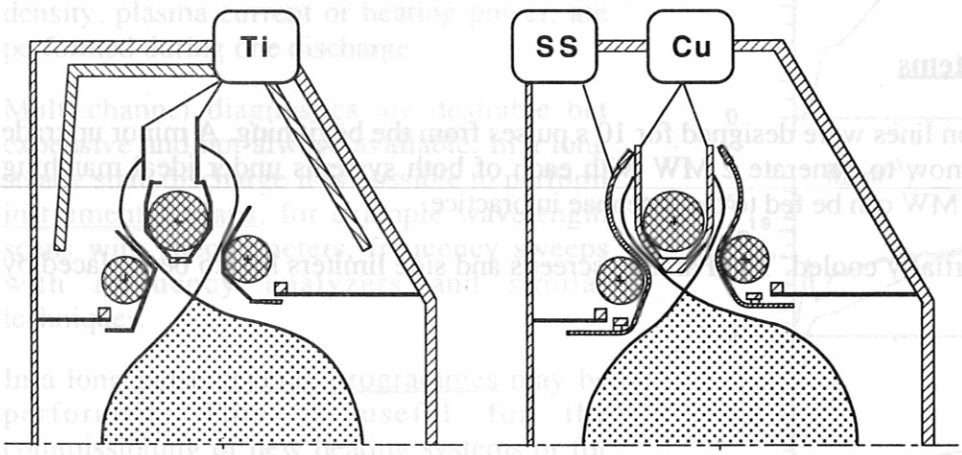

Fig. 4. Old ASDEX divertor DV I (left) and new divertor DV II.

The following changes are relevant for the discharge

- Different target material (higher sputtering, different atomic physics in hot plasma, no gettering with copper).
- Smaller surface results in smaller time constant.
- Gettering behind the shields (no atoms impinging on getters) is less efficient.
- Larger vacuum conductance between divertor and discharge leads to higher back-flow of neutral gas..

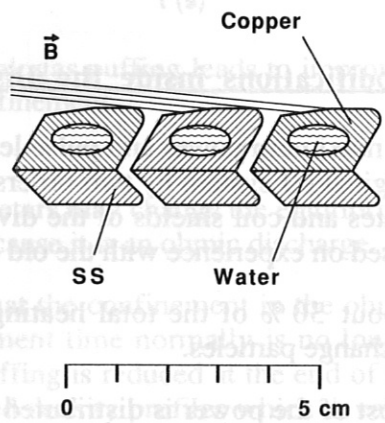

Fig. 5. Cross-section of the new target plates seen from top).

A cross section of the target plates is shown in Fig. 5.

Heat is deposited on copper bars and removed by water flowing through the cooling ducts. Copper had been chosen because of its good heat conductivity.

The target plates had to be made from narrow bars to reduce eddy currents and resulting forces during disruptions. Nevertheless reinforcement of the copper with SS was necessary to withstand the forces because of the poor mechanical properties of copper.

The structure was tested with an electron beam to withstand a heat load of more than 1 kW/cm^2 which is about a factor of 3 higher than the maximum calculated load assuming toroidal symmetry and deposition of 25 % of the total power at the intersection of the separatrix.

Copper has a higher sputtering coefficient than iron, nickel or titanium. Results from earlier experiments indicated that this was tolerable and no attempt was made to coat the surface because of technical risks.

PROPERTIES OF ASDEX AFTER THE MODIFICATION

Engineering

Though the complicated design of the new divertor requires hundreds of O-rings and thousands of brazings in the cooling circuit inside the vacuum vessel there were no technical problems at all with the new divertor after commissioning. The new injection sources do not yet work at their design parameters. There are no serious problems, but the optimization will need some time. At the moment pulse lengths of about 2 s are reached at a power of about 2.5 MW.

Operational Range and General Properties.

The design of the new divertor has imposed a few restrictions on the operational range of plasma parameters.

- It is not permitted to work at very low densities with high heating power because the required heat loss of the divertor plasma is only sufficiently high at high plasma densities. Until more experience is available operation with a power exceeding 1.5 MW has been restricted to densities above $3 \cdot 10^{19}$ m^{-3} .
- Fast electrons may not penetrate into the divertor. Runaway electrons are no problem. Slideaway electrons generated during lower hybrid current drive experiments at very low densities can carry a rather high power and deposit their energy in a zone only a few millimeters wide. They damaged the old divertor plates (Rapp and co-workers 1986). Careful monitoring of the slideaway electrons impinging on the target plates will be necessary during the experiments with lower hybrid current drive planned for autumn 1988.

The inability to apply high power at very low plasma densities imposes no serious restriction on the scientific programme.

With a few minor exceptions, the operational characteristics of the machine are unchanged after the modification. The operational limits imposed by the plasma did not change significantly.

Copper Concentration in the Discharge

Spectroscopic measurements showed that the concentration of copper in the discharge is a steep function of the electron density (Janeschitz 1988). Sputtering, the most important erosion mechanism in the divertor, is a steep function of the plasma temperature in front of the plates. The temperature drops with increasing density and is sufficiently low at interesting densities above about $4 \cdot 10^{19}$ m^{-3}. It was also found that the capacity of the divertor to retain impurities grows with increasing density.

Excessive copper contamination of the discharge is only a problem at low densities and high heating power. This parameter range is excluded anyway for technical reasons.

Gas Consumption

The gas consumption of a discharge is now much lower than with the old divertor. The reasons are

- Non-gettering target plates
- Smaller surface of the divertor volume.

In the old divertor neutral gas pumping could be further increased by gettering in the divertor chambers. Atoms could impinge directly on the active surfaces increasing, the pumping speed by an order of magnitude. Gettering is still possible, but the getters are hidden behind the coil shields. These are permeable to gas, but atoms can not penetrate directly. For this reason efficient divertor pumping is no longer possible.

After switching off the gas puffing in the old divertor the density dropped with a time constant of a few 100 ms without gettering and with a time constant below 100 ms with gettering. Now the density decays very slowly without or with gettering with a time constant of more than 0.5 s depending on discharge and wall conditions

The changed recycling conditions have a few consequences:

- In density modulation experiments the modulation depth is restricted.
- Density excursions of the plasma can no longer be counteracted.
- It is not possible to vary n_0 in the divertor at a given n_e. For divertor studies it was useful to have control of the neutral density in the divertor at a given density of the discharge. Investigations of this kind have been performed before the modification by gettering or gas puffing in the divertor. This is no longer possible.

Back-streaming of Neutral Gas into the Discharge

The components separating the divertor from the discharge chamber are permeable to some degree. This has been also the case in the old divertor and in the past attempts have been made to reduce this conductance. Now the conductance is higher than ever before. The consequences are serious:

- Smaller neutral density in the divertor (Haas and co-workers 1988)
- Difficulties in achieving a good H-mode.

Before the modification to ASDEX it was known that gettering required an increase of gas puffing into the discharge and this had a detrimental effect on the H-mode. The effect of the back-streaming neutral gas is similar: lower neutral density in the divertor and higher gas flow into the discharge.

It has been possible with the new ASDEX divertor to produce H-mode discharges. The power threshold is higher than before and the improvement of the confinement time is smaller. Recently discharges with short, good H-phases were obtained at unusual parameter settings. It is expected that the closing of all unnecessary gaps between the divertor and discharge chamber will solve the problems with the H-mode.

Changes of Unknown Reason

There are a few minor changes requiring slightly different start-up programs. The most important change which is barely understood is the appearance of the IOC-regime mentioned above.

The IOC-regime was never observed in ASDEX before the modification. Different recycling conditions or different impurities might be responsible.

EXPERIMENTS WITH LONG-PULSE HEATING

ASDEX is now working with heating pulse lengths up to two seconds at power levels of about 2.5 MW for NI and ICRH. Most of the time constants influencing the behaviour of the discharge become apparent in pulses of this duration. Many of the investigations performed on ASDEX after the modification exploited the long-pulse capabilities. Examples of these reported elsewhere in detail are

- Particle diffusion coefficients (density modulation technique, Gehre and co-workers 1988)
- Momentum confinement (measured spectroscopically, Roberts and co-workers 1988)
- Z_{eff} (from bremsstrahlung, Steuer and co-workers 1988)

The examples shown in the following are a selection which should demonstrate the spectrum of investigations which may benefit from additional heating with pulse lengths in the order of 1 to 2 s corresponding to a multiple of the poloidal field diffusion time (skin time).

NI Heated L-Mode Discharge

A typical example of a beam heated L-mode discharge is shown in Fig. 6.

The discharge with a total length of 3.5 s was run in deuterium at a toroidal field of 2.17 T and a plasma current plateau of 380 kA corresponding to $q_{cyl} = 2.8$. The density of $5.7 \cdot 10^{19}$ m^{-3} was kept nearly constant (feedback controlled) from 1.0 to 2.9 s. Neutral beam injection (hydrogen) was run from 1.0 to 3.0 s with a power of 2.5 MW decaying by 6 % during the pulse.

After the beginning of NI the gas consumption increases within a few 10 ms (change from OH-confinement to L-mode). After the first step signals characteristic for the recycling properties (n_0 in divertor, gas consumption, several H_α signals) change first with a time constant of a few 100 ms, then they change slowly until the end of the NI pulse. This behaviour indicates a first rapid, then slow change of recycling influenced by saturating surfaces and perhaps thermal effects.

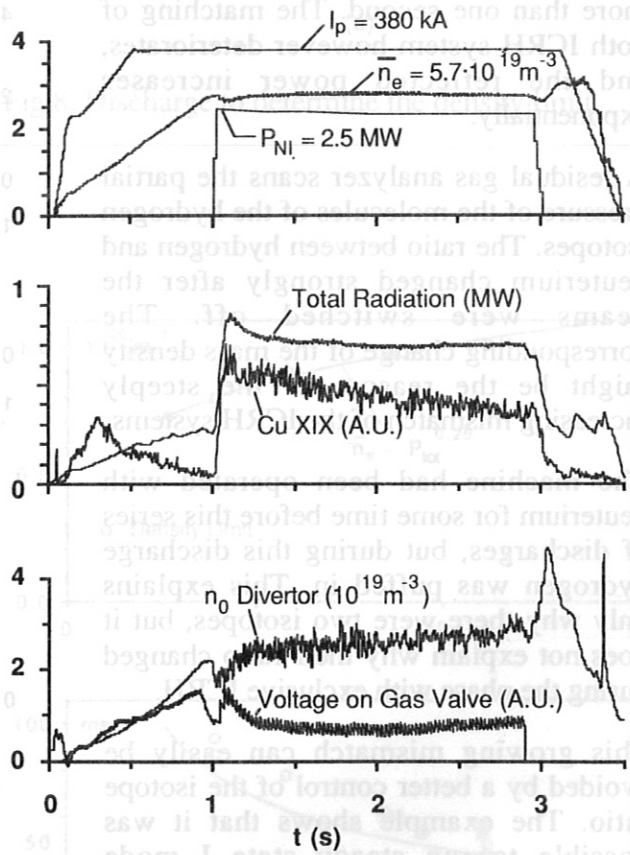

Fig. 6. Typical 2 sec L-mode discharge.

T_e is constant during the NI pulse after a short time, U_{loop} needs a few 100 ms to stabilize.

Carbon and oxygen lines are constant. The bolometer signal, which responds to UV-light and neutral particle emission, overshoots and then stays nearly constant.

Copper, the target plate material, decays until the end of NI. The concentration of the target plate material depends on erosion and retention of the divertor. Erosion decreases and retention increases steeply with the neutral density in the divertor. The slight increase of n_0 during the NI-pulse might explain the strong decay of the target plate material in the discharge.

There is no doubt that this kind of discharge could be continued indefinitely with a slow change of recycling and impurity conditions.

ICRH Discharge

It is extremely difficult if not impossible in ASDEX to switch on ICRH at the second harmonic frequency with high power in an ohmic discharge. For this reason one normally works in combination with NI. An example is shown in Fig. 7.

During a 1 s NI phase at a moderate power level of 0.5 MW the power of the ICRH generators is ramped up to 2.1 MW. After the end of the NI pulse the discharge tolerates ICRH and nearly all measured parameters stay constant for a duration of more than one second. The matching of both ICRH system however deteriorates, and the reflected power increases exponentially.

A residual gas analyzer scans the partial pressure of the molecules of the hydrogen isotopes. The ratio between hydrogen and deuterium changed strongly after the beams were switched off. The corresponding change of the mass density might be the reason for the steeply increasing mismatch of the ICRH systems.

The machine had been operated with deuterium for some time before this series of discharges, but during this discharge hydrogen was puffed in. This explains only why there were two isotopes, but it does not explain why their ratio changed during the phase with exclusive ICRH.

This growing mismatch can easily be avoided by a better control of the isotope ratio. The example shows that it was possible to run steady state L-mode discharges with ICRH as well as with co-injection.

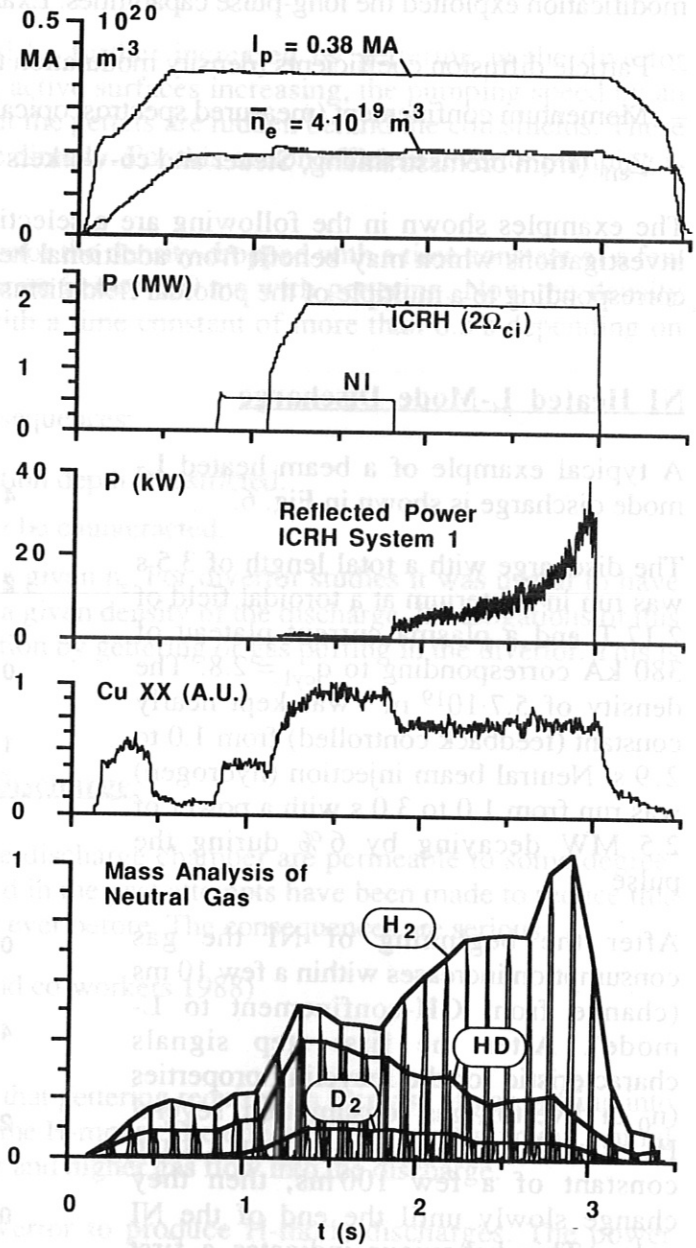

Fig. 7. ICRH discharge.

Density Limit at Low q

Determination of the Density Limit. During a stable state of the discharge with a density level sufficiently below the ohmic density limit the beams are turned on. By means of gas puffing with a predefined voltage programme the density is raised, first quickly, then slowly. The level reached immediately before the disruption is considered as the density limit. It is believed that this method determines a density value which cannot be exceeded on other paths in the parameter space if the slope of the density ramp is low enough.

Power Scan at q = 1.96. Fig. 9 shows the result of a power scan performed according to the method described before at the extremely low q_c value of 1.96.

The density limit is a weak function of the heating power. At high q-values one observes a steeper function. Within the error bars the confinement time corresponds to the Kaye-Goldston fit. This shows that discharges at these extreme conditions are still normal L-mode discharges.

The density profiles are extremely flat in these discharges. If one assumes that the density limit is an edge density limit one can hope to reach higher densities if one succeeds to produce peaked density profiles. This happens in the next example.

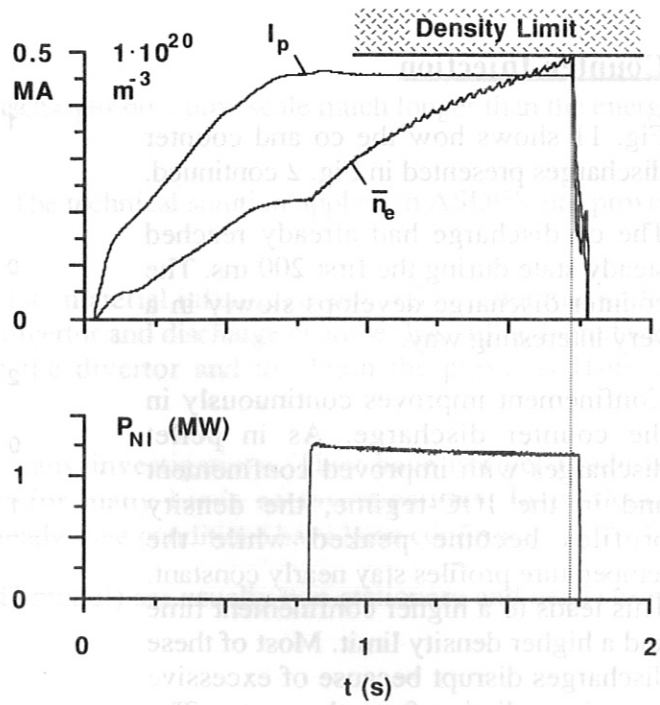

Fig.8. Discharge to determine the density limit.

Pellet Injection with NI

Pellet experiments are described in more detail by Mertens and co-workers (1988). Fig. 10 shows an example of a density limit discharge with pellet injection and NI.

During a beam heated L-mode discharge the density is being ramped up by means of gas puffing and simultaneous repetitive pellet injection. 23 deuterium pellets with a size of $1.8 \cdot 10^{20}$ particles were injected at a speed of 570 m/s at a time interval of 33 ms. The pellets penetrate to about half the minor radius and produce more strongly peaked density profiles.

This leads to an increase of the density limit and a 30 % improvement of the confinement time. This is not comparable to the improvement obtained in ohmic discharges (Niedermeyer and co-workers 1986). Pellet injection with NI is however by far not fully optimized.

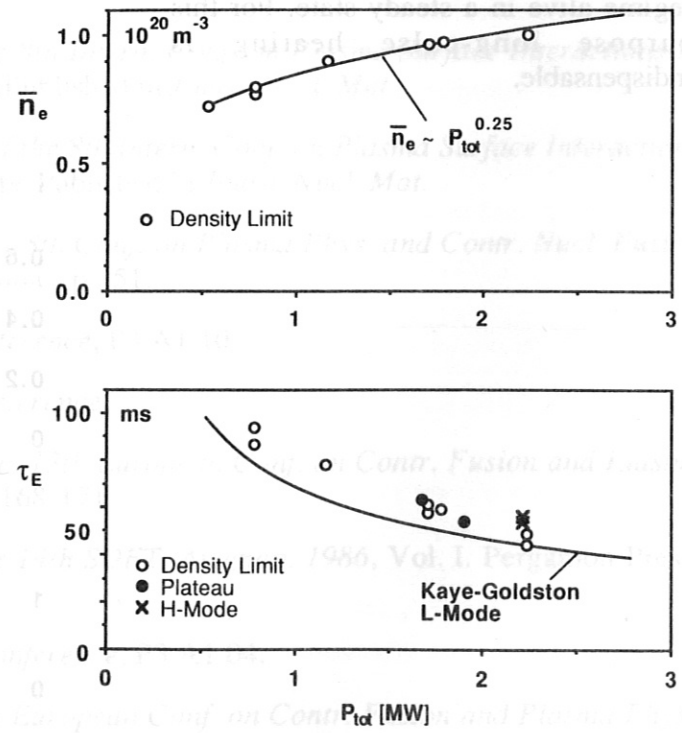

Fig.9. Density limit and confinement time at $q_c = 1.96$ as a function of the total heating power.

Counter-Injection

Fig. 11 shows how the co and counter discharges presented in Fig. 2 continued.

The co discharge had already reached steady state during the first 200 ms. The counter discharge develops slowly in a very interesting way.

Confinement improves continuously in the counter discharge. As in pellet discharges with improved confinement and in the IOC-regime, the density profiles become peaked while the temperature profiles stay nearly constant. This leads to a higher confinement time and a higher density limit. Most of these discharges disrupt because of excessive impurity radiation from the centre. The IOC-discharge shown in Fig. 3 was one of the rare exceptions which prove that a solution of this problem is possible in principle.

It will be one of the tasks for the near future to keep the improved confinement regime alive in a steady state. For this purpose long-pulse heating is indispensable.

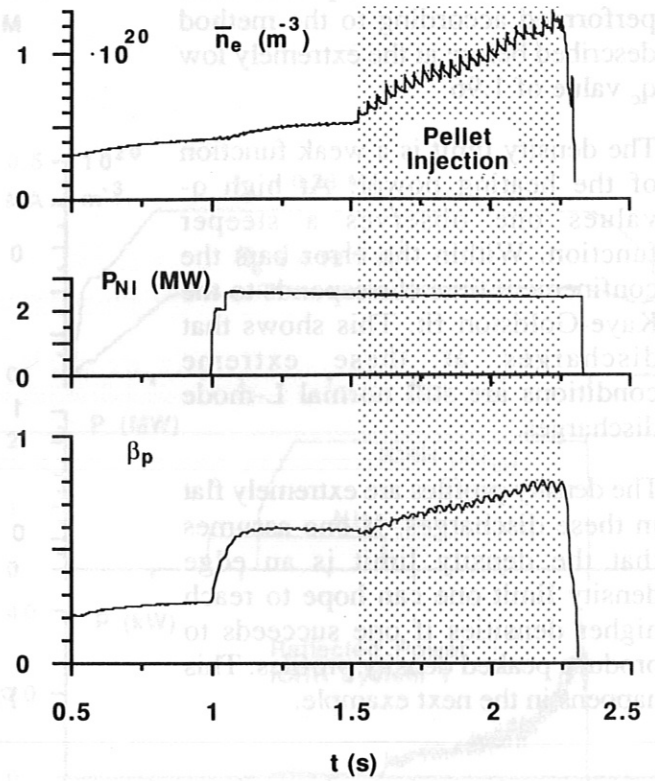

Fig. 10. Density limit discharge with NI and pellet injection.

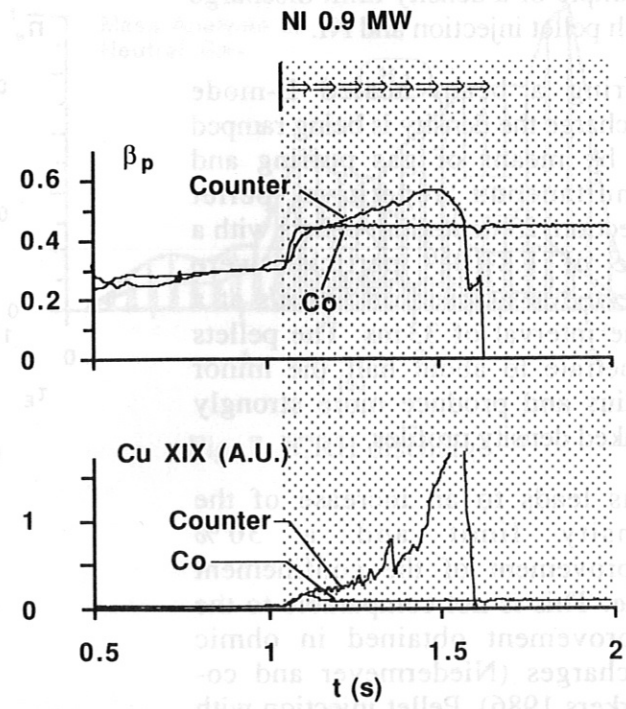

Fig. 11. Continuation of the co- and counter-NI heated discharges shown in Fig. 2.

SUMMARY

It is necessary to investigate additionally heated discharges on a time scale much longer than the energy confinement time.

Long pulse heating needs a major technical effort. The technical solution applied to ASDEX has proved to be reliable.

The change of the divertor geometry and target plate material influenced only a few properties of the machine. The high vacuum conductance between divertor and discharge chamber has still to be reduced in order to increase the neutral gas density in the divertor and to obtain the previous H-mode conditions.

Pulses up to 2 seconds are used routinely for many investigations. They have not yet produced surprising results but have been a useful tool for many kinds of investigations. In particular expectations concerned with the achievement of steady state conditions have been confirmed.

Discharges with improved confinement (not the H-mode!) are usually non-stationary and need strong attempts to stabilize them.

REFERENCES

Feist, J.-H., and co-workers (1984). *Proc. of the 4th Intern. Symp. on Heating in Tor. Plasmas, Rome 1984*. Vol I, p 1051-1056.

Fussmann, G., and co-workers (1981). *Phys. Rev. Letters*, 47, 1004-1007.

Gehre, O., and co-workers (1988). *This Conference*, P3 A1 02.

Haas, G., and co-workers (1988). *Proc. of the 8th Intern. Conf. on Plasma Surface Interactions in Controlled Fusion Devices, Jülich 1988*. To be Published in *Journ. Nucl. Mat.*

Janeschitz, G., and co-workers (1988). *Proc. of the 8th Intern. Conf. on Plasma Surface Interactions in Controlled Fusion Devices, Jülich 1988*. To be Published in *Journ. Nucl. Mat.*

Keilhacker, M., and co-workers (1981). *Proc. 8th Conf. on Plasma Phys. and Contr. Nucl. Fusion Research, Brussels, 1980*, Vol. II. IAEA, Vienna. p 351.

Mertens, V., and co-workers (1988). *This Conference*, P3 A1 10.

Müller, E.R., and co-workers (1988). *This Conference*,

Niedermeyer, H., and co-workers (1986). *Proc. 13th European Conf. on Contr. Fusion and Plasma Heating, Schliersee 1986*, Vol 10C, Part I. p 168-171.

Rapp, H., and co-workers (1986). *Proc. of the 14th SOFT, Avignon, 1986*, Vol. I. Pergamon Press, Oxford. p 595.

Roberts, D.E., and co-workers (1988). *This Conference*, P3 A1 04.

Söldner, F. and co-workers (1985). *Proc. 12th European Conf. on Contr. Fusion and Plasma Phys., Budapest 1985*, Vol 9F, Part II. p 244-247.

Steinmetz, K., and co-workers (1986). *Plasma Physics and Controlled Fusion*, 28, No. 1A 235-238.

Steuer, K.-H., and co-workers (1988). *This Conference*, P3 A1 08.

Vollmer, O., and co-workers (1986). *Proc. of the 14th SOFT, Avignon, 1986*, Vol. II. Pergamon Press, Oxford. p 1115.

AUXILIARY HEATED MULTIPELLET-FUELLED DISCHARGES IN ASDEX AND INFLUENCE OF DENSITY PROFILE SHAPE ON CONFINEMENT

O. Gruber, H.U. Fahrbach, O. Gehre, W. Herrmann, M. Kaufmann, K. Lackner, V. Mertens, E.R. Müller, F. Söldner, F. Wagner, R. Wunderlich, G. Becker, B. Bomba, H. Bruhns, K. Büchl, A. Carlson, G. Dodel[1], A. Eberhagen, G. Fussmann, K. Gentle[2], L. Giannone, G.v. Gierke, E. Glock, S.v. Goeler[3], G. Haas, J. Hofmann, E. Holzhauer[1], K. Hübner[4], G. Janeschitz, S. Kaesdorf, F. Karger, O. Klüber, M. Kornherr, K. Krieger, R. Lang, P. Lee[5], G. Lisitano, M. Lörcher, T.C. Luce[5], F. Mast, H.M. Mayer, K. McCormick, D. Meisel, Y. Miura[6], H. Murmann, J. Neuhauser, H. Niedermeyer, R. Nolte, J. M. Notredaeme, M.P. Petrov[7], W. Poschenrieder, H. Rapp, H. Röhr, D.E. Roberts[8], A. Rudji, W. Sandmann, F. Schneider, U. Schneider, G. Siller, E. Simmet, E. Speth, A. Stäbler, K. Steinmetz, K.H. Steuer , U. Stroth, N. Tsois[9], O. Vollmer, J.B. Whitley[10], H. Würz[11], D. Zasche

Max-Planck-Institut für Plasmaphysik, EURATOM Association, D-8046 Garching

Abstract

Strongly peaked electron density profiles have been obtained in ASDEX by different refuelling methods: pellet fuelling (ohmic and co-injection heating), NBI counter-injection and recently by reduced gas puff fuelling scenarios. These discharges show in common increased density limits, a canonical electron temperature profile independent of the density profile and an improvement of the particle and energy confinement. Whereas the changes in particle transport are not fully understood, transport analyses point out that the improved energy transport can be explained by reduced ion conduction losses coming close to the neoclassical ones. The different result for the ion transport with flat and peaked density profiles is quantitatively consistent with that expected from η_i-driven modes. The analyses cannot yet explain the anomalous electron energy transport, apart from identified continuous trends such as inverse scaling with the isotope mass and enhancement with heating power.

Keywords

Tokamak, confinement, density profile shape, pellets, ohmic heating, additional heating, eta-modes

1. Introduction

Standard gas puff-fuelled (GP) discharges in ASDEX with ohmic (OH) and co-beam heating show very uniform behaviour of the density profile shape, which is found to depend significantly on only the value of the security factor $q_a = 5B_t a^2/(RI_p)$ [T,MA,m] and the hydrogen species, and to a less extent on the line averaged electron density and the additional heating power (Gehre et al., 1986). In the last few years, however, a number of discharge conditions have been identified which lead to unusual peaking of the $n_e(r)$ profile. The transition can be induced by pellet fuelling (Kaufmann et al., 1988; Gruber et al., 1988a; Mertens et al., 1988) or counter-injection (Gehre et al., 1988a). More recently, we have discovered that the transition to peaked density profiles can also be provoked by a sudden reduction in the gas puff rate during density ramp-up experiments leading to a regime of improved ohmic confinement, called IOC in the folowing (Müller et al., 1988; Söldner et al., 1988). Even earlier, spontaneous transitions had sometimes been observed when the sawtooth activity in OH deuterium discharges was lost, which could not be associated with any intentional changes in external control parameters

[1] University of Stuttgart, Germany; [2] University of Texas at Austin, USA; [3] Princeton University, USA; [4] University of Heidelberg, W-Germany; [5] GA Technologies Inc., San Diego, USA; [6] JAERI Tokai Research, Ibaraki- Ken, Japan; [7] Ioffe Institute, Leningrad, USSR; [8] Atomic Energy Corp. of South Africa, Pretoria; [9] NRS Demokritos, Attiki, Greece; [10] Sandia National Lab., Albuquerque, USA; [11] Kernforschungszentrum Karlsruhe, W- Germany

(Wagner et al., 1986a). In no case could the changes be explained solely by changes in the charged particle deposition profiles. They imply rather a change in the particle transport. In contrast to the case of the density, the electron temperature (T_e) profiles are very little affected by any parameter other than q_a and remain self- similar within the experimental error bars (Wagner et al., 1986b).

Common to all cases with peaked density profiles is that they show an improvement in global energy, particle and - with ctr-injection - momentum confinement times with respect to the values in standard ohmically heated or L-regime discharges at the same line averaged density $\overline{n_e}$ and heating power. In OH discharges without sawteeth the energy transport is reduced too, but the effect of improved confinement is offset by enhanced core radiation. Similar results have been reported from pellet refuelled OH discharges in Alcator-C (Greenwald et al., 1984; Wolfe et al., 1986) and there may be connections with the Super-mode in TFTR (Goldston et al., 1986). Good particle confinement and high axis values $n_e(0)$ inevitably lead to high-Z impurity accumulation and peaking of the radiated power density p_{rad} on axis (Fussmann et al., 1988). In the core, p_{rad} thereby often reaches power densities comparable to the total net input power going into the electrons, whereas the total radiation losses are still below the net input power. In a final phase the central radiation can give rise to hollow T_e profiles and frequently to disruptions. Z_{eff} increases in the plasma centre too mainly owing to light impurities ($\Delta Z_{eff}(0)<0.5$; Steuer et al., 1988). The tendency toward reduced or even absent sawtooth activity frequently observed with peaked density profiles may be a result.

According to drift wave theory peaked density profiles may lead to reduced anomalous heat transport if the threshold conditions of the 'trapped electron' or 'ion temperature gradient' modes are not violated (Horton et al., 1981; Dominguez and Waltz, 1986; Romanelli et al., 1986; Lee and Diamond, 1986). These thresholds are determined by the temperature and density gradients according to $\eta_{i,e} = (d\ln T_{i,e}/dr)/(d\ln n_{i,e}/dr) = (L_n)_{i,e}/(L_T)_{i,e} > 1$. The measured η_e and - as $T_i \approx T_e$ at high densities - η_i values of the high confinement discharges indeed decrease to values below 1 over a large part of the plasma radius.

In the following, we describe first the particle transport aspects of these discharges with special emphasis on the pellet injection cases. We then discuss the consequences for energy transport. Comprehensive local transport analyses covering the whole plasma cross-section and including a comparison with first-principle theoretical transport models were carried out with the TRANSP code.

2. Build-up and profile shape of plasma density

A simple and useful quantitative measure of the density profile peaking is the ratio $n_e(0)/\langle n_e\rangle$ of the central to the volume averaged electron density, which is reported in Fig. 1 for ASDEX discharges. The electron density is measured with a 4-channel HCN-laser interferometer and a 16-channel Thomson scattering system, providing data every 17 ms. In GP-fuelled discharges with OH and co-beam heating we observe flat density profiles with a peaking factor increasing with q_a and the mass of the hydrogen species. Thereby the peaking of profiles with q_a is more pronounced in a scan at constant B_t (like in Fig.1, at B_t=2.2 T) then in one at constant I_p. Increasing the plasma density results in a slight reduction of the density peaking factor, which may be caused by a shorter penetration depth of the neutrals and is, with beam heating, owing to a broadening of the beam deposition profile. For non-standard refuelling scenarios (pellets, ctr-NBI, IOC) we carried out extensive scans for $q_a \approx 2.7$. The profile peaking is strongest in purely ohmically heated pellet fuelled discharges ($n_e(0)/\langle n_e\rangle \leq 2.6$), and tends to decrease on application of additional heating power P_{add} provided with H^0 NBI (up to 2.2 MW) as well as with second harmonic hydrogen ICRH (up to 1.6 MW), although steep density gradients persist in the central part (see Fig. 1 and 2 for P_{NBI}=1.35 MW). Also the "improved ohmic confinement" , the ctr-NBI and the sawtooth-less discharges display a peaking ratio of $n_e(0)/\langle n_e\rangle \approx 1.7 \div 2.0$ well above that of the 'flat' profiles.

(Wagner et al., 1986a). In no case could the changes be explained solely by changes in the charged particle deposition profiles. They imply rather a change in the particle transport. In contrast to the case of the density, the electron temperature (T_e) profiles are very little affected by any parameter other than q_a and remain self- similar within the experimental error bars (Wagner et al., 1986b).

Common to all cases with peaked density profiles is that they show an improvement in global energy, particle and - with ctr-injection - momentum confinement times with respect to the values in standard ohmically heated or L-regime discharges at the same line averaged density $\overline{n_e}$ and heating power. In OH discharges without sawteeth the energy transport is reduced too, but the effect of improved confinement is offset by enhanced core radiation. Similar results have been reported from pellet refuelled OH discharges in Alcator-C (Greenwald et al., 1984; Wolfe et al., 1986) and there may be connections with the Super-mode in TFTR (Goldston et al., 1986). Good particle confinement and high axis values $n_e(0)$ inevitably lead to high-Z impurity accumulation and peaking of the radiated power density p_{rad} on axis (Fussmann et al., 1988). In the core, p_{rad} thereby often reaches power densities comparable to the total net input power going into the electrons, whereas the total radiation losses are still below the net input power. In a final phase the central radiation can give rise to hollow T_e profiles and frequently to disruptions. Z_{eff} increases in the plasma centre too mainly owing to light impurities ($\Delta Z_{eff}(0)<0.5$; Steuer et al., 1988). The tendency toward reduced or even absent sawtooth activity frequently observed with peaked density profiles may be a result.

According to drift wave theory peaked density profiles may lead to reduced anomalous heat transport if the threshold conditions of the 'trapped electron' or 'ion temperature gradient' modes are not violated (Horton et al., 1981; Dominguez and Waltz, 1986; Romanelli et al., 1986; Lee and Diamond, 1986). These thresholds are determined by the temperature and density gradients according to $\eta_{i,e} = (d\ln T_{i,e}/dr)/(d\ln n_{i,e}/dr) = (L_n)_{i,e}/(L_T)_{i,e} > 1$. The measured η_e and - as $T_i \approx T_e$ at high densities - η_i values of the high confinement discharges indeed decrease to values below 1 over a large part of the plasma radius.

In the following, we describe first the particle transport aspects of these discharges with special emphasis on the pellet injection cases. We then discuss the consequences for energy transport. Comprehensive local transport analyses covering the whole plasma cross-section and including a comparison with first-principle theoretical transport models were carried out with the TRANSP code.

2. Build-up and profile shape of plasma density

A simple and useful quantitative measure of the density profile peaking is the ratio $n_e(0)/\langle n_e\rangle$ of the central to the volume averaged electron density, which is reported in Fig. 1 for ASDEX discharges. The electron density is measured with a 4-channel HCN-laser interferometer and a 16-channel Thomson scattering system, providing data every 17 ms. In GP-fuelled discharges with OH and co-beam heating we observe flat density profiles with a peaking factor increasing with q_a and the mass of the hydrogen species. Thereby the peaking of profiles with q_a is more pronounced in a scan at constant B_t (like in Fig.1, at B_t=2.2 T) then in one at constant I_p. Increasing the plasma density results in a slight reduction of the density peaking factor, which may be caused by a shorter penetration depth of the neutrals and is, with beam heating, owing to a broadening of the beam deposition profile. For non-standard refuelling scenarios (pellets, ctr-NBI, IOC) we carried out extensive scans for $q_a \approx 2.7$. The profile peaking is strongest in purely ohmically heated pellet fuelled discharges ($n_e(0)/\langle n_e\rangle \leq 2.6$), and tends to decrease on application of additional heating power P_{add} provided with H^0 NBI (up to 2.2 MW) as well as with second harmonic hydrogen ICRH (up to 1.6 MW), although steep density gradients persist in the central part (see Fig. 1 and 2 for P_{NBI}=1.35 MW). Also the "improved ohmic confinement" , the ctr-NBI and the sawtooth-less discharges display a peaking ratio of $n_e(0)/\langle n_e\rangle \approx 1.7 \div 2.0$ well above that of the 'flat' profiles.

In contrast to the case of the density, the normalized electron temperature profiles are very little affected by any parameter other than q_a remaining very similar for both hydrogen isotopes, in both purely ohmically and L-regime NBI-heated discharges. The $T_e(0)/<T_e>$ ratio is also invariant with respect to density peaking as long as the central radiation power loss stays sufficiently below the net-energy input to the electrons (see Fig.1, T_e is measured via Thomson scattering). In particular, the T_e profiles recover their canonical shape after each pellet within a time of less than 2 ms - this is the time difference between a pellet injection and the instant of the next measured T_e profile in Fig. 3 - being much shorter than the usual diffusive time scale (see Fig. **3**). This indicates fast energy transport into the ablation region, as first reported by the Equipe TFR (1985) and interpreted as a cooling wave travelling in front of the pellet.

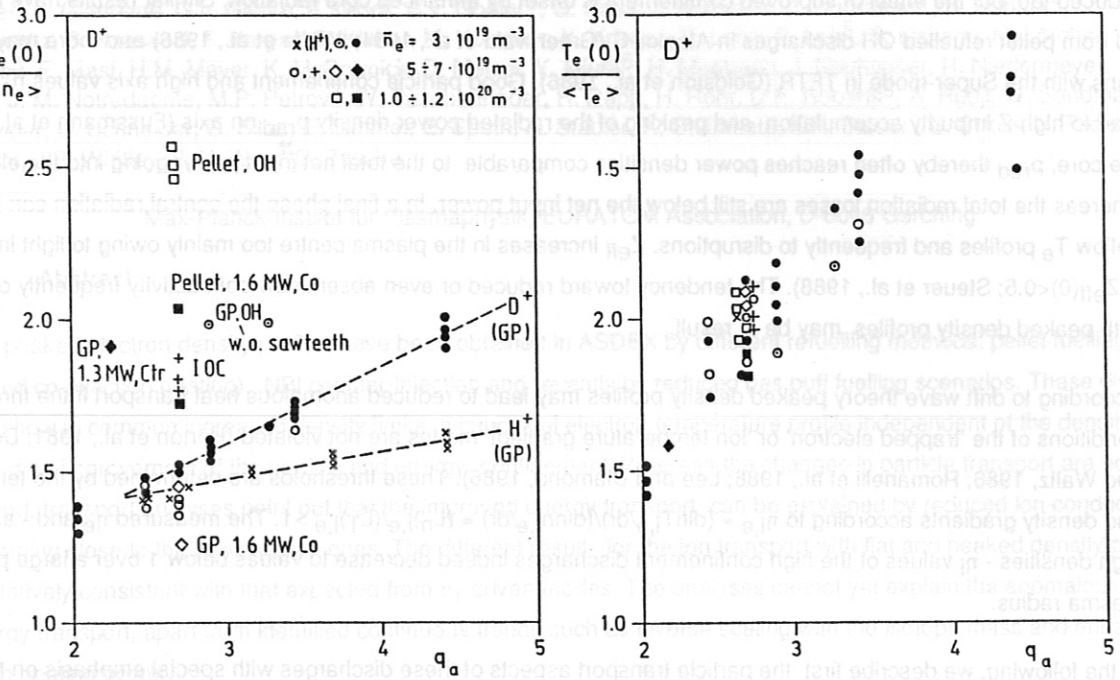

Fig.1: Density and temperature profile peaking factor vs. safety factor q_a for discharge conditions in ASDEX with purely ohmic and L-regime NBI heating (D^+ gas, except the x points). GP ... gas puff-fuelled, IOC ... Improved Ohmic Confinement regime. Detailed parameter scans reported were made at $q_a \approx 2.7$ (I_p=380 kA, B_t=2.2 T). Numbers given are the total heating powers, which amount to 0.5 ÷0.6 MW with ohmic heating alone (I_p=380 kA).

Between 2 and 40 deuterium or hydrogen pellets were injected into a single discharge at time intervals of between 30 to 100 ms at a velocity of approximately 600 m s^{-1}. Two different sizes were used, contributing 1 and $3 \cdot 10^{19}$ m^{-3}, respectively, to $<n_e>$. The penetration depths increased with pellet size from 0.2 to 0.3 m with OH and were reduced with additional heating (ASDEX minor radius a = 0.4 m). In the latter case a large fraction of the injected pellet mass was missing (Carlson et al., 1988), so that it was only with the larger pellets that a significant increase of $\bar{n}_e$ and of the density peaking factor was achieved. The parameter scans covered a range between $\bar{n}_e = 3 \cdot 10^{19}$ and $1.2 \cdot 10^{20}$ m^{-3} (OH) and $1.4 \cdot 10^{20}$ m^{-3} (2.6 MW NBI). The latter two values constitute increases by approx. $0.6 \cdot 10^{20}$ m^{-3} over the respective density limits in gas-puff discharges and correspond to Murakami parameters of $\bar{n}_e R/B_t$ = 8. and $10.5 \cdot 10^{19}$ [$m^{-2}T^{-1}$]. These performances could only be obtained under conditions providing for substantial gas flow onto the plasma boundary (produced by outgassing of the carbonized walls, additional gas puffing and outflow from the divertor chamber owing to high gas pressure). The new ASDEX divertor configuration for long pulse heating (Niedermeyer et al., 1988) having a reduced gas-pumping surface and - owing to large by-passes from the divertor chamber to the main discharge - a high neutral gas backflow rate enhances these favourable conditions, thus allowing the IOC regime even in GP discharges with reduced external gasfeed.

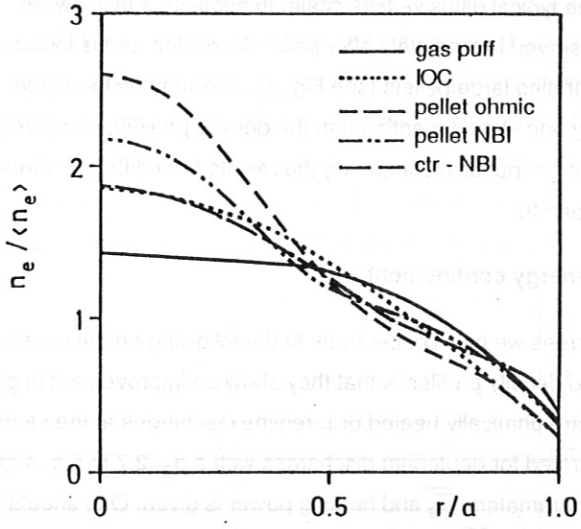

Fig.2: Normalized density profiles for different discharge conditions at the time instants used for the TRANSP analyses reported here (D^+ gas).

Gas puff	$\langle n_e\rangle$=	$5.0\cdot10^{19}$ m^{-3}
IOC		$4.0\cdot10^{19}$ m^{-3}
Pellet ohmic		$7.6\cdot10^{19}$ m^{-3}
Pellet NBI (P_{NBI}=1.35MW)		$7.8\cdot10^{19}$ m^{-3}
Ctr-NBI (P_{NBI}=0.8MW)		$7.6\cdot10^{19}$ m^{-3}

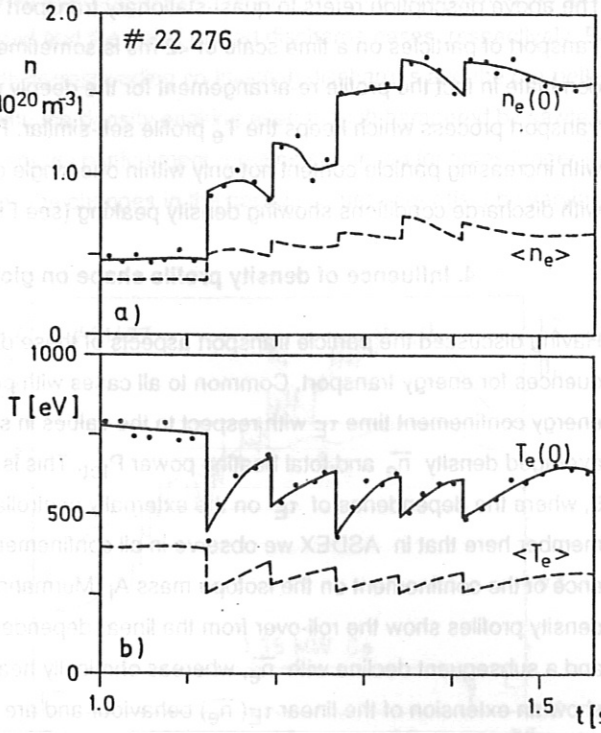

Fig. 3. Peak (r=0) and volume averaged (<>) electron density and temperature vs. time for a ohmic hydrogen pellet discharge. The data points measured by Thomson scattering are smoothed between adjacent pellet pop times and extrapolated to them.

3. Bulk particle transport

Pellet injection and IOC discharges give rise to density peaking inside the deposition radius of the pellet particles and the neutrals, respectively, which cannot be explained by changes in the charged particle deposition profile. Besides a particular plasma boundary behaviour, which is obviously influenced by the refuelling method used, distinct changes in the bulk particle transport are necessary and can be explained by an increase in the ratio $-v_D/D$ of the inwards drift velocity and the diffusion coefficient used to describe formally the particle transport. One way to interprete this is in terms of a non-diagonal model of particle and energy transport satisfying the Onsager relation (Mercier and Capes, 1982; O'Rourke,1987)

$$\Gamma_p = nD(-\nabla n/n) + \alpha(-\nabla T/T)$$

$$\Gamma_q = \alpha(-\nabla n/n) + n\chi(-\nabla T/T),$$

where Γ_p is the usual particle flux and Γ_q is the conductive heat flux q_e normalized by kT, yielding $nv_D = \alpha(-\nabla T/T)$.

From the nearly stationary and source-free density profiles ($\Gamma_p \approx 0$) before and after density peaking (see Fig. 2) it is possible to deduce a ratio $-v_D/D = -\nabla n/n$ which strongly increases towards the plasma edge and is roughly given by $1\cdot r/a^2$ (time averaged over sawteeth) and $5\cdot r/a^2$, respectively, for the highest density peaking factors inside r< 2a/3. Sawteeth play an important role by providing for a further diffusive mixing process which can prevent the density peaking to a large extent, particularly with additional heating in pellet-fuelled (Mertens et al., 1988) and ctr-injection (see Fig. 6) discharges. During the peaking of the density and the associated increase of the central radiation the sawtooth activity is decreasing, and maximum peaking is realized if they are completely supressed. The latter happens especially in D^+ discharges (with pellets as well as with ctr-NBI). In sawtooth- free OH discharges a ratio of $-v_D/D = 3.5\cdot r/a^2$ is already reached with a peaking factor of $n_e(0)/\langle n_e\rangle \approx 2$.

The above description refers to quasi-stationary transport on the typical diffusive time scale. In addition, a fast inward transport of particles on a time scale of <2 ms is sometimes observed immediately after pellet deposition and is found to dominate in fact the profile re-arrangement for the deeply penetrating large pellets (see Fig. 3). This may be the same transport process which keeps the T_e profile self-similar. Finally one should mention that the density peaking increases with increasing particle content not only within one single discharge but also comparing the results from different shots with discharge conditions showing density peaking (see Fig. 1 and 2).

4. Influence of density profile shape on global energy confinement

Having discussed the particle transport aspects of these discharges we now concentrate in the following on the consequences for energy transport. Common to all cases with peaked density profiles is that they show an improvement in global energy confinement time τ_E with respect to the values in standard ohmically heated or L-regime discharges at the same line averaged density $\overline{n}_e$ and total heating power P_{tot}. This is illustrated for deuterium discharges with a $q_a \approx 2.7$ in Fig. 4 and 5, where the dependence of τ_E on the externally controllable parameters $\overline{n}_e$ and heating power is given. One should remember here that in ASDEX we observe in all confinement regimes and under all heating conditions a positive dependence of the confinement on the isotope mass A_i (Murmann et al., 1988). Standard gas puff-fuelled OH discharges with flat density profiles show the roll-over from the linear dependence $\tau_E \sim \overline{n}_e$ to a saturated τ_E regime with 85 ms (60 ms for H^+) and a subsequent decline with $\overline{n}_e$, whereas ohmically heated discharges transiting into the peaked density (IOC) regime show an extension of the linear $\tau_E(\overline{n}_e)$ behaviour and are up to 60% above the comparison cases. An even higher gain is shown by the pellet-fuelled OH-cases, with values of τ_E = 160 ms (110 ms for H^+; Gruber et al., 1988a) being reached and sustained for times much longer than τ_E in the post-pellet phases. Also with additional heating in case of co-beam heated pellet-fuelled (Fig. 5) and of ctr-beam heated GP discharges (Fig.4) τ_E remains above the corresponding standard L-regime values, although the gain diminishes with increasing power from a factor of 2 at ohmic power levels (≈ 0.5 MW) to 1.3 at $P_{tot} \approx 2.6$ MW (not shown in Fig. 5) for $H^0 \rightarrow D^+$ injection. As the density peaking is reduced at the same time, a further dependence of $\tau_E = \tau_E(\overline{n}_e, P_{tot}, A_i)$ on the density peaking factor $n_e(0)/\langle n_e \rangle$ can be inferred from these results.

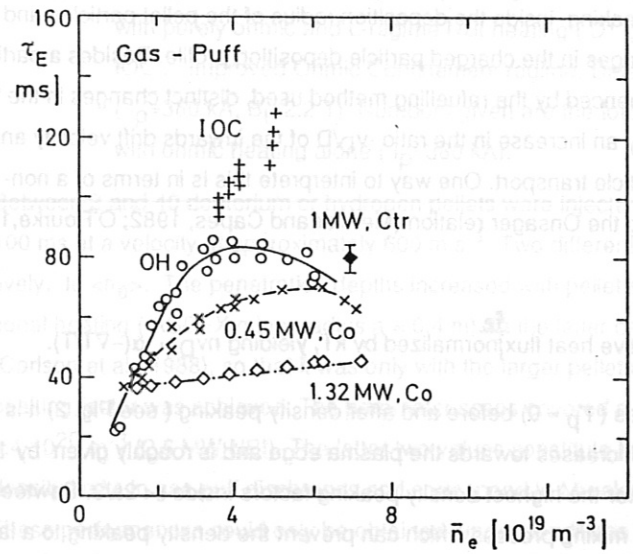

Fig. 4. Global energy confinement time τ_E vs. $\overline{n}_e$ for gas puff-fuelled discharges with ohmic and L-regime NBI- heating (H^0) in deuterium (q_a=2.7, except the ctr-injection case with q_a=2.1). Heating powers given are the beam powers.

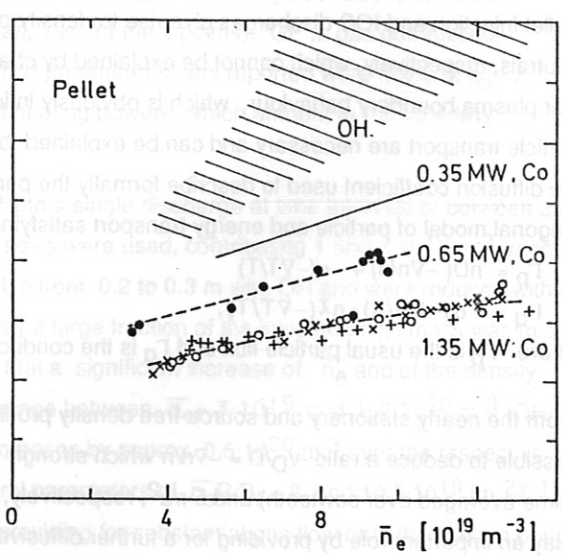

Fig. 5. Global energy confinement time τ_E vs. $\overline{n}_e$ for pellet-fuelled discharges with ohmic and L-regime NBI heating (H^0) in deuterium (q_a=2.7). Heating powers given are the beam powers.

The improvement of energy confinement in NBI-heated discharges accompanying density peaking is illustrated in Figs. 6 and 7 by means of the β_p traces for the counter-injection heated and the pellet fuelled discharge cases, respectively. Both lead to doubling of $\Delta\beta_p$ due to beam heating as compared with corresponding co-injection discharges and the pre-pellet phase, respectively. Confinement gradually improves along with the density peaking even though hampered by sawteeth. After the last sawtooth (ctr-injection) and pellet, respectively, energy confinement remains enhanced for times longer than τ_E - for instance about 200 ms in the pellet discharge. Thereby the changes in the particle content are offset by varying temperatures, whereas the profile shapes are preserved.

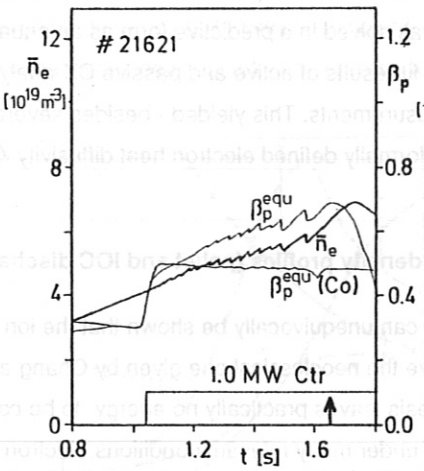

Fig. 6. Time behaviour of line averaged density and β_p determined from equilibrium analysis of a ctr-injection heated discharge ($H^0 \rightarrow D^+$, I_p=420 kA, B_t=2.0 T, a=0.38 m, q_a=2.1). For comparison β_p vs. t of a co-NBI discharge is shown too (P_{NBI}=1 MW, I_p=380 kA, B_t=2.2 T, a=0.4 m, q_a=2.7). The ctr-injection discharge reaches $\tau_E \approx$80 ms as compared with 50 ms in the co-injection case. The arrow indicates time instant of the TRANSP analysis reported in Fig. 14a.

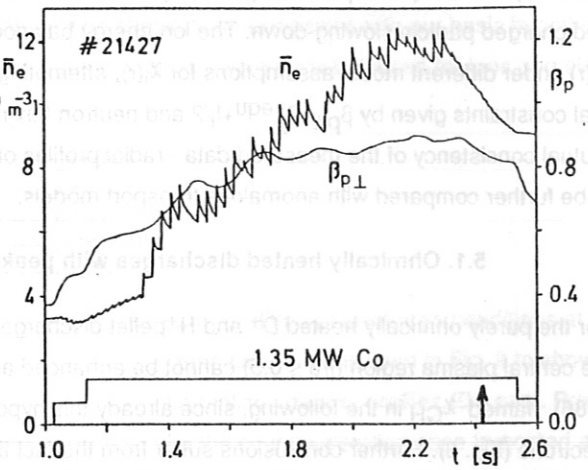

Fig. 7. Time traces of line averaged density and diamagnetic $\beta_{p\perp}$ during co-NBI heated discharge with multiple deuterium pellet injection ($H^0 \rightarrow D^+$, I_p=380 kA, B_t=2.2 T, q_a=2.7). During pellet-fuelling the confinement time rises to 65 ms as compared with 45ms in the pre-pellet NBI phase. The arrow indicates the time instant of the TRANSP analysis reported inFig.14b.

During the experimental periods having both sufficient NBI heating power and proper discharge conditions available to reach the H-mode it was only possible to inject small pellets. With the small pellets the H-mode was obtained, but showed n_e profiles without peaking and typical of H-mode plasmas with GP fuelling. Similar to these discharges, the line averaged density increased also without additional gas puffing and in between the pellets. The energy confinement times were typical as well, being 70 ms at $\bar{n}_e = 5 \cdot 10^{19}$ m^{-3} and reduced to 40 ms at $\bar{n}_e = 1.2 \cdot 10^{20}$ m^{-3} owing to enhanced ELM activity (P_{NI}=3 MW). With ctr-injection transient H-mode phases lasting about 20-30 ms occurred even at an additional heating power of only 1-1.3 MW which is below the threshold power with co- injection (≈1.6 MW). In these phases the density rises faster than in the L-mode phase of the ctr-injection discharge described above.

The global confinement results suggest that the peaking of the density profile removes the cause for the τ_E saturation observed in ohmic discharges and improves also the behaviour of additionally heated plasmas. One possible explanation involves the profile consistency concept - assuming $T_e(r)/T_e(0)$ to depend only on q_a - and a strong correlation of the global confinement with transport processes in the plasma boundary zone. The roll-over of τ_E vs. $\bar{n}_e$ in GP-fuelled discharges results then from a decrease of $T_e(0)$ and the concomitant increase in ohmic heating, whereas the pellet discharges gain in τ_E owing to a more favourable weighting of the fixed T_e profile with the peaked density profile. There may also be a close connection between particle and energy transport according to the above-mentioned non-diagonal model,

resulting in the observed $\tau_E(n_e(0)/<n_e>)$ dependence. In the following, we use local transport analyses to identify the dominating energy loss channels, and describe the heat fluxes by effective local diffusivities.

5. Results of local transport analyses

To improve our understanding of transport processes, we performed for a number of discharges detailed analyses with the TRANSP code, which is a 1 1/2-D time-dependent transport analysis code with Monte-Carlo beam simulation, developed at PPPL (Goldston et al., 1981). For these investigations we took the measured radial profiles of n_e, T_e, p_{rad}, Z_{eff} (Steuer et al., 1988) and computed power deposition profiles from the solutions of the equations for current diffusion, NBI deposition and charged particle slowing-down. The ion energy balance was solved in a predictive form as an equation determining $T_i(r)$ under different model assumptions for $\chi_i(r)$, attempting to fit results of active and passive CX-analyzers and the integral constraints given by $\beta_{p\perp}$, $\beta_p^{equ}+l_i/2$ and neutron flux measurements. This yielded - besides several checks on the mutual consistency of the measured data - radial profiles of a formally defined electron heat diffusivity $\chi_e = -q_e/(kn_e\nabla T_e)$, to be further compared with anomalous transport models.

5.1. Ohmically heated discharges with peaked density profiles (pellet and IOC discharges)

For the purely ohmically heated D^+ and H^+pellet discharges it can unequivocally be shown that the ion energy transport in the central plasma region ($r/a \leq 0.5$) cannot be enhanced above the neoclassical one given by Chang and Hinton (1982; 1986), named χ_{CH} in the following, since already this hypothesis leaves practically no energy to be conducted by the electrons (Fig. 8). Further conclusions suffer from the fact that under many relevant conditions electron and ion energy transport cannot be sufficiently well separated owing to the error bars in the plasma parameter measurements. The following analysis can therefore only establish that a single, uniform hypothesis explains qualitatively and quantitatively all ion energy balance features considered. The electron energy transport following under this assumption shows a uniform trend with isotope mass and heating power, but an extensive comparison with theoretical models has still to be carried out. The hypothesis tested is that conductive ion energy transport is only due to χ_{CH} and an additional contribution from η_i- modes.

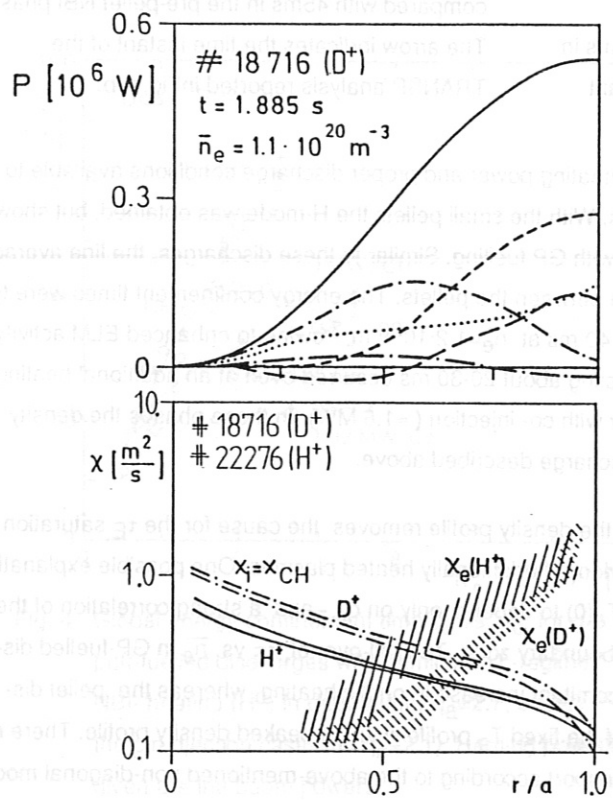

Fig. 8. Radial dependence of heating power and loss power fluxes resulting from TRANSP analysis of a post-pellet phase in a Ohmically heated D^+ discharge (q_a=2.7).

Fig. 9. Profiles of χ_e and χ_i as resulting from TRANSP analysis of pellet-fuelled, ohmically heated discharges in deuterium (compare Fig. 8) and hydrogen (compare Fig. 3). Pellets injected were of the same isotope as the recipient plasma. For more than 0.15 s the T_e and n_e profiles develop very similarly except of a 20% higher density in the D^+ discharge.

In the ohmically heated pellet-fuelled discharges , as those of Fig. 8 and 9, η_e and η_i (since $T_i \approx T_e$ at $\bar{n}_e$ above $1 \cdot 10^{20}$ m^{-3}) are below 1 over a large part of the plasma cross-section during the phase with peaked density profile, whereas they are well above 1 in the pre-pellet phase with flat density profiles (see also Fig. 10 and12a; Gruber et al., 1988a). As remarked in the introduction, in these discharge phases with $\eta_i<1$ η_i-modes should be either quenched or make only a small contribution to χ_i over the whole plasma cross-section, so that our model would also predict $\chi_i = \chi_{CH}$ in the outer discharge region. Anomalous electron energy transport has thus to be dominant there and to be of sufficiently large magnitude even to determine the scaling of global τ_E. This conclusion also allows one to reconcile the predicted increase of $\chi_i = \chi_{CH}$ with the square root of isotope mass A_i and the observation that τ_E values in D^+ are larger than in H^+ pellet discharges. A resulting decrease of χ_e with A_i, which here can only be shown to be consistent with our basic hypothesis (see Fig. 9), could be clearly established in lower-density discharges with separable energy balances for ions and electrons.

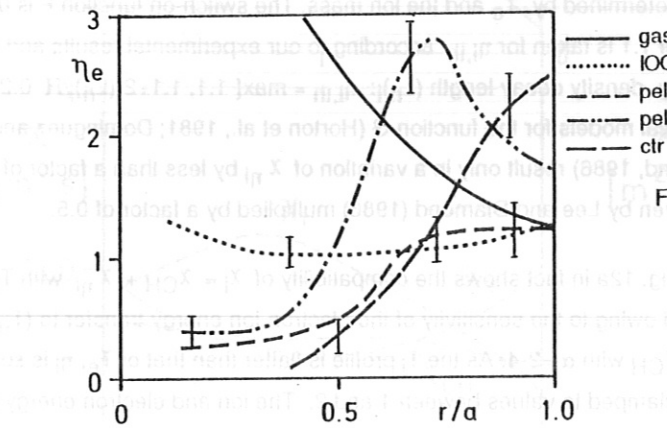

Fig. 10. $\eta_e(r)$ for different discharge conditions at the same time instants used in Fig. 2 to show the normalized density profiles (D^+ gas). Profile for the counter-injection case truncated at small r/a as T_e-profile becomes hollow.

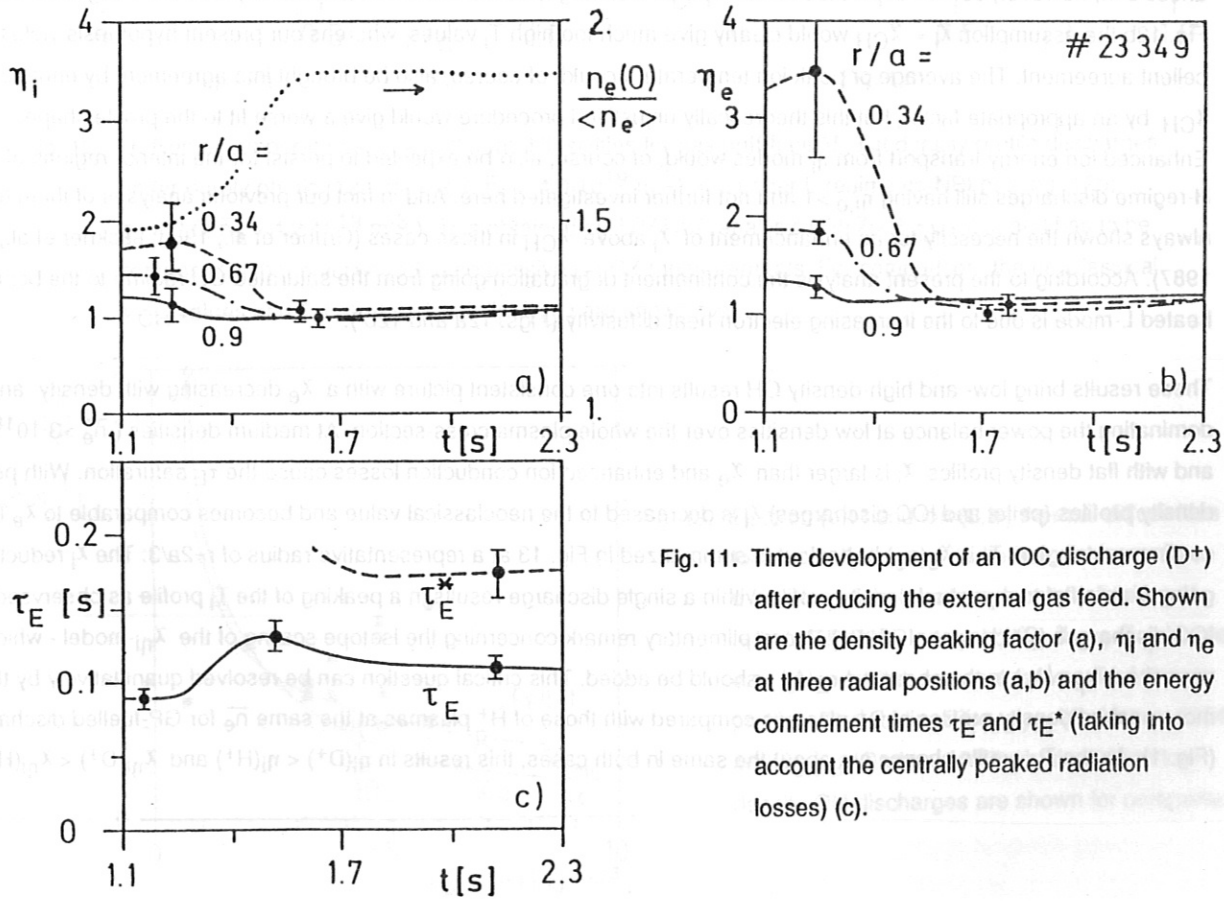

Fig. 11. Time development of an IOC discharge (D^+) after reducing the external gas feed. Shown are the density peaking factor (a), η_i and η_e at three radial positions (a,b) and the energy confinement times τ_E and τ_E^* (taking into account the centrally peaked radiation losses) (c).

Ohmically heated pellet-fuelled discharges allow only a test of the threshold conditions of η_i - modes. A similar conclusion can be drawn from the IOC discharges which again show a reduction of η_e and η_i to a value close to 1 in parallel to confinement improvement (Fig. 10 and 11). Here we reach stationary discharge conditions with regard to n, T and radiated power profiles owing to a reduced, but surviving sawtooth activity. A quantitative comparison of η_i-modes with their predicted contribution to χ_i can however be made for the flat density profile discharges.

5.2. Gas puff-refuelled discharges with flat density profiles

To describe the influence of the ion temperature gradient mode on the ion energy transport in flat density profile discharges we use the formula

$$\chi_{\eta i} = F(\eta_i, \eta_{i,th})\, G\, \rho_s^2\, c_s / ((L_n)_i \cdot 0.3)\,,$$

with the Larmor radius ρ_s and the sound speed c_s determined by T_e and the ion mass. The switch-on function F is 0 for $\eta_i < \eta_{i,th}$ and equal to 1 for $\eta_i > \eta_{i,th} + 0.8$. A value of 1.1 is taken for $\eta_{i,th}$ according to our experimental results and includes an enhanced threshold for regions with a long density decay length $(L_n)_i$: $\eta_{i,th} = \max\{1.1, 1.1 + 2((L_n)_i/R - 0.2)\}$. As, for measured ASDEX profiles, different theoretical models for the function G (Horton et al., 1981; Dominguez and Waltz, 1987; Romanelli et al., 1986; Lee and Diamond, 1986) result only in a variation of $\chi_{\eta i}$ by less than a factor of 2, we have choosen in a first step the G expression given by Lee and Diamond (1986) multiplied by a factor of 0.5.

An analysis of the purely ohmically heated case of Fig. 12a in fact shows the compatibility of $\chi_i = \chi_{CH} + \chi_{\eta i}$ with T_i measurements but cannot - within the error bars and owing to the sensitivity of the electron-ion energy transfer to $(T_e - T_i)$ - uniquely discriminate against the assumption $\chi_i = \alpha\, \chi_{CH}$ with $\alpha = 2$-4. As the T_i profile is flatter than that of T_e, η_i is somewhat smaller than η_e (compare with Fig.10) and is clamped to values beween 1 and 2. The ion and electron energy balances can, however, be well separated in NBI-heated discharges at the same electron density. For the L-regime case of Fig. 12b the assumption $\chi_i = \chi_{CH}$ would clearly give much too high T_i values, whereas our present hypothesis yields excellent agreement. The average or peak ion temperature could, of course, also be brought into agreement by enhancing χ_{CH} by an appropriate factor, but this theoretically unjustified procedure would give a worse fit to the profile shape. Enhanced ion energy transport from η_i-modes would, of course, also be expected to persist for the interior regions of H-regime discharges still having $\eta_{i,e} > 1$ and not further investigated here. And in fact our previous analyses of them have always shown the necessity for an enhancement of χ_i above χ_{CH} in those cases (Gruber et al., 1986; Lackner et al., 1987). According to the present analysis the confinement degradation going from the saturated OH regime to the beam heated L-mode is due to the increasing electron heat diffusivity (Figs. 12a and 12b).

These results bring low- and high-density OH results into one consistent picture with a χ_e decreasing with density and dominating the power balance at low densities over the whole plasma cross-section. At medium densities ($\overline{n_e} > 3 \cdot 10^{19}$ m^{-3}) and with flat density profiles χ_i is larger than χ_e and enhanced ion conduction losses cause the τ_E saturation. With peaked density profiles (pellet and IOC discharges) χ_i is decreased to the neoclassical value and becomes comparable to χ_e in the confinement region. This $\chi_e(n_e)$ behaviour is summarized in Fig. 13 at a representative radius of r=2a/3. The χ_i reduction going from a flat to a peaked density profile within a single discharge results in a peaking of the T_i profile as observsed in IOC discharges (Söldner et al., 1988). A complimentary remark concerning the isotope scaling of the $\chi_{\eta i}$-model - which is opposite ($\chi_{\eta i} \sim \sqrt{A_i}$) to the observed $\tau_E(A_i)$ - should be added. This critical question can be resolved quantitatively by the more peaked density profiles of D^+ plasmas compared with those of H^+ plasmas at the same $\overline{n_e}$ for GP-fuelled discharges (Fig. 1). As the T_e profile shapes are about the same in both cases, this results in $\eta_i(D^+) < \eta_i(H^+)$ and $\chi_{\eta i}(D^+) < \chi_{\eta i}(H^+)$.

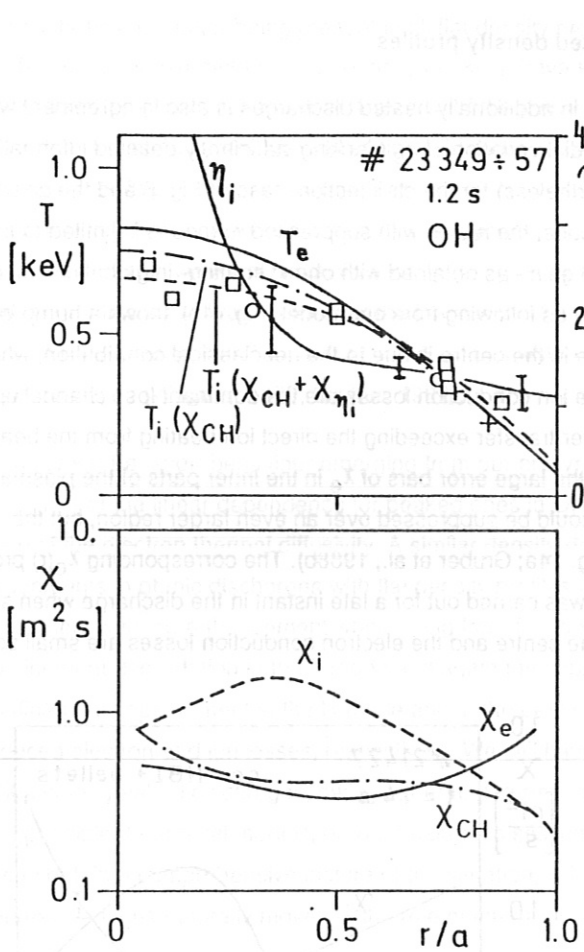

Fig. 12a

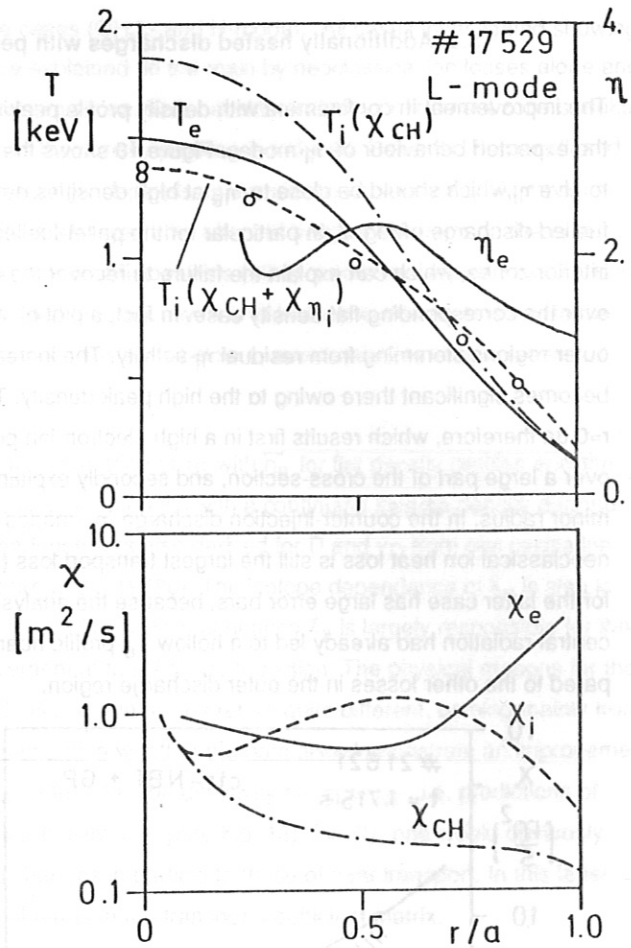

Fig. 12b

Fig. 12. Profiles of temperatures, $\eta_{i,e}$ and heat diffusivities for gas puff-fuelled , flat density profile discharges under purely ohmic (12a; $q_a = 2.7$; $\overline{n_e} = 4.9 \cdot 10^{19}$ m^{-3}) and under L-regime co-NBI heating (12b; $q_a = 2.5$; $\overline{n_e} = 4.2 \cdot 10^{19}$ m^{-3}). T_i is obtained by TRANSP analysis with $\chi_i = \chi_{CH} + \chi_{\eta i}$ and has to be compared with the active (o,□)and passive (+) CX measurements. For comparison the neoclassical χ_{CH} values and T_i calculated with $\chi_i = \chi_{CH}$ are shown too.

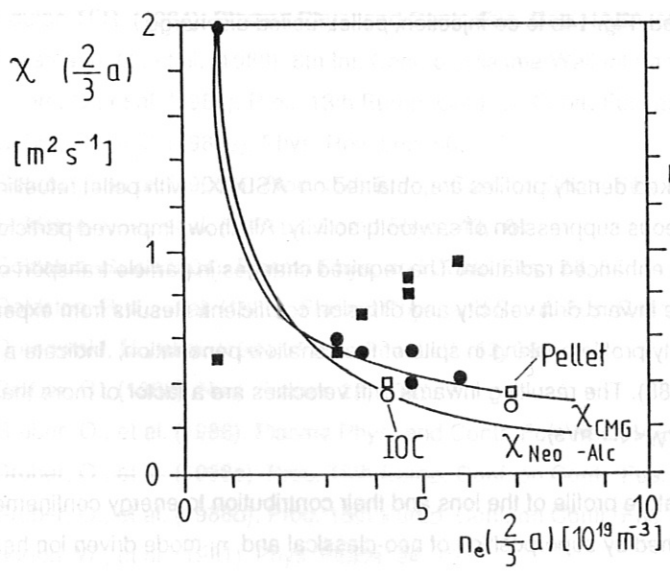

Fig. 13. Electron (o,●) and ion (□,■) thermal diffusivities for ohmically heated deuterium discharges as a function of the electron density (all taken at r=2a/3; TRANSP analysis). $\chi_i = \chi_{CH} + \chi_{\eta i}$ is used. ●,■ represent flat, o,□represent peaked density profiles. The scalings $\chi_{Neo-Alc}$ (Goldston, 1984) and χ_{CMG} (Gruber, 1982) obtained from low-density OH discharges are shown for comparison.

5.3. Additionally heated discharges with peaked density profiles

The improvement in confinement with density profile peaking in additionally heated discharges is also in agreement with the expected behaviour of η_i-modes. Figure 10 shows the radial variation of η_e (lacking sufficiently detailed information to give η_i,which should be close to η_e at high densities nevertheless) for the ctr-injection case of Fig. 6 and the pellet-fuelled discharge of Fig. 7. In particular for the pellet-fuelled case, the region with suppressed η_i-modes is limited to the interior zones, which can explain the failure to recover the full gain - as obtained with ohmic heating- in global confinement over the corresponding flat density case. In fact, a plot of $\chi_i(r)$ as following from our model (Fig.14b) shows a hump in the outer regions stemming from residual η_i-activity. The increase in the centre is due to the neoclassical contribution, which becomes significant there owing to the high peak density. The ion conduction losses are the dominant loss channel up to r≈0.8a therefore, which results first in a high electron-ion power transfer exceeding the direct ion heating from the beams over a large part of the cross-section, and secondly explains the large error bars of χ_e in the inner parts of the plasma minor radius. In the counter-injection discharge η_i -modes should be suppressed over an even larger region, but the neoclassical ion heat loss is still the largest transport loss (Fig. 14a; Gruber et al., 1988b). The corresponding $\chi_e(r)$ profile for the latter case has large error bars, because the analysis was carried out for a late instant in the discharge when strong central radiation had already led to a hollow T_e-profile near the centre and the electron conduction losses are small compared to the other losses in the outer discharge region.

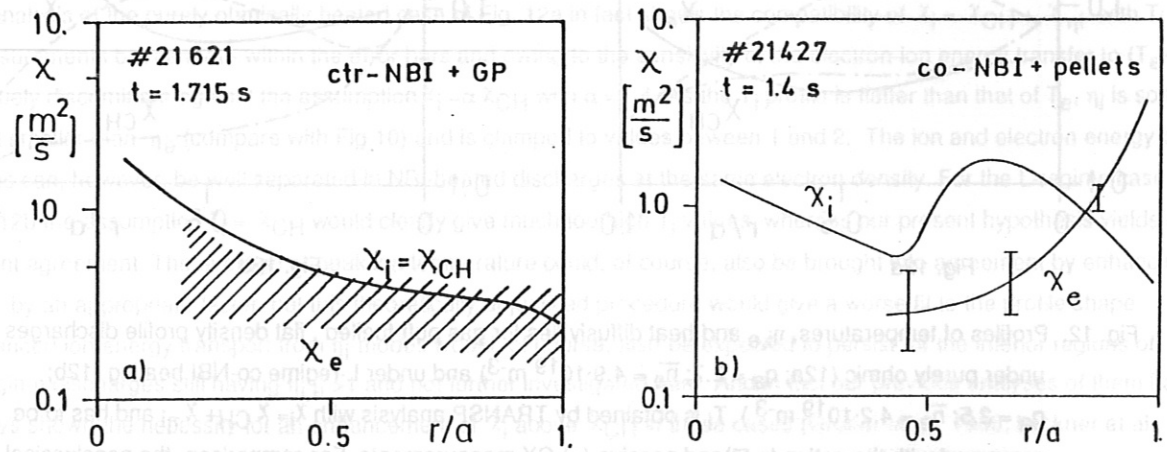

Fig. 14. Profiles of χ_e and χ_i resulting from TRANSP analysis of peaked density profile, NBI-heated L-regime discharges ($H^0 \rightarrow D^+$) reported in Figs 6 and 7. Fig. 14a refers to ctr-injection heated, gas puff-fuelled, Fig. 14b to co-injection, pellet-fuelled discharge.

6. Conclusions and discussion

There exist four discharge conditions under which peaked density profiles are obtained on ASDEX: with pellet refuelling, with ctr-NBI, with reduced GP (IOC) and with spontaneous suppression of sawtooth activity. All show improved particle and energy confinement, with the latter partly offset by enhanced radiation. The required changes in particle transport can be formally described by an increase of the ratio of the inward drift velocity and diffusion coefficient. Results from experiments with slow pellets (V≈200 m/s), leading to density profile peaking in spite of their shallow penetration, indicate a stronger change of D than of v_D (Kaufmann et al., 1988). The resulting inwards drift velocities are a factor of more than 10 as high as the neoclassical Ware pinch velocities (v_W<0.1 m/s).

Local energy transport analyses show that the temperature profile of the ions and their contribution to energy confinement depend on the density profile shape and can be explained by superposition of neo-classical and η_i-mode driven ion heat

conductivities, the latter being present in all flat density profile cases (OH,L- and H-mode). All cases investigated showing confinement improvement through density peaking have to be explained in the main by neoclassical ion losses alone and correspond to η_i (and η_e)<1 over a large part of the plasma cross-section. This neoclassical ion confinement zone shrinks towards the plasma centre with increasing additional heating as the density peaking is reduced. Recently, Romanelli and Briguglio (1988) pointed out that the threshold of the η_i-mode strongly depends on the electron collisionality. At medium collisionalities (≈1) as in the case of all ASDEX peaked density discharges, the effect of trapped electrons on the η_i induced transport is weak and negligible for $\eta_i < \eta_{i,th}$. However, at low collisionalities (<0.1) and in low aspect ratio devices like JET, only a small improvement of the ion transport is expected theoretically. It is of interest in this context that in the PULSATOR device (R=0.7 m; a=0.11 m; $\nu^*>>1$), in which η_i was consistently below 1, neoclassical ion transport was always observed (Wagner, 1979; Gruber, 1982).

With the ion transport behaviour emerging from our analysis, the saturation of τ_E with $\overline{n}_e$ for flat density profiles and the extension of the linear dependence for peaked ones in OH discharges then fits with a continuing inverse density dependence of the electron thermal diffusivity. A similar density dependence was also derived for D and v_D from gas oscillation experiments in ohmic discharges with flat density profiles (Gehre et al., 1988b). The isotope dependence of χ_e is also in agreement with τ_E enhancement when going from D^+ to H^+ ions. With additional heating χ_e is largely responsible for the confinement degradation in the L-mode and again the improvement at the H-mode transition. The physical reasons for the confinement improvement in the H-mode and in the peaked density mode are therefore quite different, coming mainly from reduced electron and ion losses, respectively. We still have to examine whether the data also demonstrate an improvement of χ_e in the peaked discharges, owing either to a dependence of the electron diffusivity on η_i or η_e, i.e. predictions of first-principle theoretical models, or to a favourable scaling with density (compare Fig. 13). Finally, one would obviously like to obtain a comprehensive picture of the situation, linking changes in particle to those of heat transport. In this latter context the focus naturally moves to the role of the off-diagonal terms in the transport coefficient matrix.

References

Chang, C. S., and Hinton, F. L. (1982). Phys.Fluids, **25**, 1493.

Chang, C. S., and Hinton, F. L. (1986). Phys.Fluids, **29**, 3314.

Carlson, A., et al. (1988). Proc. 15th Europ. Conf. on Contr. Fus. and Plasma Heating, **12B**, Part III, 1069.

Dominguez, R., and Waltz, R. E. (1986). Report GA-A18184.

Equipe TFR. (1984). Plasma Phys. and Contr. Fus. Res., IAEA, Vienna, **I**, 103.

Fussmann, G., et al. (1988). 8th Int. Conf. on Plasma Wall Interaction (PSI), Jülich, to be publisched in J. of Nucl. Mater.

Gehre, O., et al. (1986). Proc. 13th Europ. Conf. on Contr. Fus. and Plasma Heating, **10C**, Part I, 220.

Gehre, O., et al. (1988a). Phys. Rev. Lett. **60**, 1502.

Gehre, O., et al. (1988b). Proc. 15th Europ. Conf. on Contr. Fus. and Plasma Heating, **12B**, Part I, 7.

Goldston, R. J., et al. (1981). J.Comp.Phys., **43**, 61.

Goldston, R. J. (1984). Plasma Phys. and Contr. Fus., **26**, 87.

Goldston, R. J., et al. (1986). Plasma Phys. and Contr. Fus. Res., IAEA, Vienna, **I**,75

Greenwald, M., et al. (1984). Phys. Rev. Lett., **53**, 352

Gruber, O., (1982). Nucl. Fusion, **22**, 1349.

Gruber, O., et al. (1986). Plasma Phys. and Contr. Fus. Res., IAEA, Vienna, **I**, 357.

Gruber, O., et al. (1988a). Proc. 15th Europ. Conf. on Contr. Fus. and Plasma Heating, **12B**, Part I, 27.

Gruber, O., et al. (1988b). Proc. 15th Europ. Conf. on Contr. Fus. and Plasma Heating, **12B**, Part I, 23.

Horton, W., et al. (1981). Phys. Fluids, **24**, 1077

Kaufmann, M., et al. (1988). to appear in Nucl. Fusion

Lackner, K., Gruber, O., and Grassie, K. (1987). Workshop on Theory of Fusion Plasmas, Varenna, EUR 1136 EN, 377.

Lee, C. S., and Diamond, P. H. (1986). Phys. Fluids, **29**, 3291.

Mercier, C., and Capes, R. (1982). Plasma Phys. and Contr. Fus. Res., IAEA, Vienna, **I**, 337.

Mertens, V., et al. (1988). Proc. 15th Europ. Conf. on Contr. Fus. and Plasma Heating, **12B**, Part I, 39.

Müller, E. R., et al. (1988). Proc. 15th Europ. Conf. on Contr. Fus. and Plasma Heating, **12B**, Part I, 19.

Murmann, H., et al. (1988). Proc. 15th Europ. Conf. on Contr. Fus. and Plasma Heating, **12B**, Part I, 3.

Niedermeyer, H., et al. (1988). this conference, to be published in Plasma Phys. and Contr. Fus.

Romanelli, F., et al. (1986). Nuc. Fus., **26**, 1515.

Romanelli, F., and Briguglio, S. (1988). to be published in Plasma Phys. and Contr. Fus.

O'Rourke, J. (1987). Nucl. Fus., **27**, 2075.

Söldner, F. X., et al., to be published

Steuer, K. H., et al. (1988). Proc. 15th Europ. Conf. on Contr. Fus. and Plasma Heating, **12B**, Part I, 31.

Wagner, F. (1979). internal IPP-report **III/52**.

Wagner, F., et al. (1986a). Plasma Phys. and Contr. Fus., **28**, 1225.

Wagner, F., et al. (1986b). Phys. Rev. Lett., **56**, 2187.

Wolfe, S. M., et al. (1986). Nucl. Fus., **26**, 329

INFLUENCE OF DENSITY PROFILE SHAPE ON PLASMA TRANSPORT IN ASDEX

O. Gruber, F. Wagner, M. Kaufmann, K. Lackner, H. Murmann, D.E. Roberts, O. Vollmer

IPP Garching, EURATOM Association, Fed. Rep. of Germany

1. Introduction

In ASDEX divertor discharges we observe - besides the H-mode - four regimes of long lasting improved energy and particle confinement compared with gas-fuelled (GP) ohmic (OH) and co-beam heated plasmas, namely OH and beam heated pellet refuelled discharges [1, 2], OH discharges without sawteeth, discharges with neutral injection in the counter direction (ctr-NI) [3] and ohmic discharges near the density limit with reduced gas-puff (GP) [4]. All these discharges have strongly peaked density profiles with ratios of the axial ($n_e(0)$) to the volume averaged ($< n_e >$) electron density of up to 2.5 compared with $1.4 \div 1.6$ of the other discharge types. During the density increase to line-averaged values ($\bar{n}_e$) of up to $1.2 \cdot 10^{20} m^{-3}$ the electron temperature (T_e) profile shape stays nearly self-similar depending only on q_a. Good particle confinement and high $n_e(0)$ lead to high-Z impurity accumulation and high central radiation losses, which can dominate the central power balance and can give rise to hollow T_e-profiles and internal disruptions in a final phase. The tendency toward the observed reduced sawtooth activity may be a further result. Z_{eff} increases owing to light impurities.

According to theory peaked density profiles may lead to reduced anomalous heat transport if the threshold condition of the trapped electron or ion temperature gradient modes, namely $\eta_{e,i} = d\ell nT_{e,i}/d\ell nn_e = L_{n_e}/L_{T_{e,i}} \geq \eta_c \approx 1.5$, is not violated [5]. The measured η_e and - as $T_i \approx T_e$ at the high $\bar{n}_e$'s $-\eta_i$ values of the high confinement discharges indeed decrease to values below 1 over a large part of the plasma radius (see Fig. 3a, [1]). An alternative explanation follows the profile consistency model. According to it, $T_e(r)/T_e(0)$ in the bulk of the plasma is fixed by stability restrictions, whereas the normalization constant is determined by local transport processes in a near-boundary zone. The roll-over of $\tau_E(\bar{n}_e)$ in GP OH discharges follows then from a decrease of $T_e(0)$ with density and the concomitant increase in ohmic dissipation, whereas the high confinement discharges gain in τ_E from a more favourable weighting of $T_e(r)/T_e(0)$ with the peaked density profiles.

In this paper we try to identify the dominating energy loss channels using the TRANSP analysis code and measured plasma parameters: n_e, T_e, T_i and radiation profiles and global parameters (loop voltage, Z_{eff}, β_{pol}).

2. Gas-fuelled OH and co-beam heated discharges

In ASDEX we observe "broad" density profiles with $n_e(o)/ < n_e > 1.4 \div 1.6$ and $\eta_{e,i} > 1$ at all radii in gas-fuelled ohmic and co-beam heated plasmas at q-values around 3. OH discharges show the roll-over from the linear dependence $\tau_E \sim \bar{n}_e$ to a saturated τ_E regime beyond $\bar{n}_e \approx 3 \cdot 10^{19} m^{-3}$. Confinement is degraded in the additionally heated L-mode plasmas and improves again in the H-mode even at high

heating powers. In all three regimes a reduction of τ_E of hydrogen (H^+) discharges in comparison with deuterium (D^+) discharges holds. To describe the observed confinement we have to add to an anomalous electron heat conduction channel and to the neo-classical ion energy losses as given by Chang-Hinton, χ_{CH}, an additional heat conductiviy contribution causing for instance the saturation of ohmic confinement at high densities. CX measurements of T_i, measured β_p and neutron productions can be described consistently when we assume enhanced ion losses with an enhancement factor of $\chi_i = (3 \div 4)\chi_{CH}$ over the neoclassical value.

This brings low and high density OH results into line with a $\chi_e(OH) \sim 1/(nT_eq)$ [1], dominating at low densities the power balance. We have started to simulate the ion losses by a $\chi_i = \chi_{CH} + \chi_{\eta_i}$ [5] with $\chi_{\eta_i} = o$ for $\eta_i \leq 1$ and fully developed for $\eta_i \geq 1.8$ including an enhanced threshold for the long density decay length (L_{n_e}) region. Figure 1 shows for a GP ohmic discharge that χ_{η_i} yields obviously the necessary χ_i enhancement, and η_i, which is smaller than η_e, is clamped to values between 1 and 2. Electron and ion heat conduction losses (P_{ce}, P_{ci}) are about the same at this medium density. The η-modes have, however, in their present theoretical form the wrong dependence on the ion mass A_i (χ_η is increasing with A_i) to explain the observed isotope dependence of τ_E. This discrepancy may be explained by the more peaked density and broader T_i profiles of the D^+ plasmas compared with those of the H^+ plasmas at nearly the same T_e shape yielding $\eta_i(D^+) < \eta_i(H^+)$ and $\chi_{\eta_i}(D^+) < \chi_{\eta_i}(H^+)$.

In L-mode discharges P_{ce} exceeds P_{ci} and $\chi_e(L) > \chi_e(OH)$ holds at the same $\bar{n}_e$ and increased temperatures. This can be seen by comparing Fig. 1 and Fig. 2, which shows the analysis results for a H° beam heated D^+ discharge. Only an $\chi_i > \chi_{CH}$ can explain the T_i measurements, whereas a $\chi_i = \chi_{CH}$ would yield too high T_i values.

3. Pellet fuelled discharges

Ohmic and co-beam heated pellet-fuelled discharges with strong density profile peaking exhibit a confinement improvement compared with GP fuelled discharges (doubling of τ_E) [1, 2]. In the OH pellet discharges with a density peaking of $n_e(o)/ < n_e >$ up to 2.5 the reason for the roll-over of τ_E is removed and the effect causing the ion transport enhancement has to be quenched: $\chi_i > \chi_{CH}$ would require an electron heat transport against ∇T_e in order to satisfy the power balance. With $\chi_i = \chi_{CH}$ during these pellet phases, however, a $\chi_e \sim 1/(nT_e)$ at fixed q results again. Global confinement is then governed by the electron heat transport. The confinement times for D^+ ($\leq$ 160 ms) exceed those for H^+ ($\leq$ 110 ms) considerably and a $\chi_e \sim A_i^{-\alpha}$ with $\alpha = 0.3 \div 0.7$ can be deduced [1].

4. Ctr-beam heated discharges

Ctr-injection in ASDEX leads to a doubling of $\Delta\beta_p$ due to NI compared with a comparable co-injection discharge and an improvement of τ_E up to 80 ms [3]. Confinement is gradually improving along with a continuously peaking of n_e yielding $n_e(o)$ above $1 \cdot 10^{20} m^{-3}$ and a peaking factor $n_e(o)/ < n_e >$ up to 1.9. The T_e profile shape changes mainly in the central part, where it becomes hollow due to increasing radiation losses. η_e and the calculated η_i values are below 1 over 2/3 of the plasma radius (see Fig. 3a).

Again as in the pellet discharges $\chi_i = \chi_{CH}$ has to be assumed: with $\chi_i > \chi_{CH}$ the energy content of the plasma is underestimated even in the extreme of no additional electron transport. In this situation the neoclassical ion losses dominate over the electron heat losses ($T_i \approx T_e$). χ_e (see Fig. 3b) is strongly decreased compared with that of the co-NI case shown in Fig. 2, having nearly the same plasma current, but a somewhat higher heating power. Along with the improvement of the energy and particle confinement also the one of momentum is observed to increase with ctr-NI. The plasma rotation velocity is measured outside a/2; it increases throughout the ctr-beam phase up to $v_\phi(\frac{a}{2}) \simeq 1.5 \cdot 10^5 m/s$. Assuming a $v_\phi \sim (1 - r^2/a^2)^{1.3}$ the momentum confinement time at the end of the ctr-phase is $\tau_\phi = 90ms$ and the momentum diffusivity is comparable to the electron heat diffusivity.

5. Summary

There are 4 regimes with peaked density profiles at ASDEX: pellet refuelled and ctr-NI discharges, OH discharges without sawteeth and those with reduced GP. The reason for the development of the peaked density profiles may be quite different and is not yet understood in all cases. But all regions have improved confinement which is partly offset by core radiation. Transport analysis - only performed for the first two regimes up to now - reveals that the ion transport has to be reduced in comparison to the broad density profile cases (OH-saturation and co-NI L and H-mode). η_i-modes may explain this result. Interestingly, in the small tokamak Pulsator the η_i-values are below 1 and the ion transport was consistently observed to be neoclassical.

References

[1]O. Gruber, M. Kaufmann, et al., this conference.
[2]V. Mertens, W. Sandmann, et al., this conference.
[3]O. Gehre, O. Gruber, et al., to be publ. in Phys. Rev. Lett.
[4]E. Müller, F. Söldner, et al., this conference.
[5]G.S. Lee, P.H. Diamond, Phys. Fluids **29**, 3291 (1986).

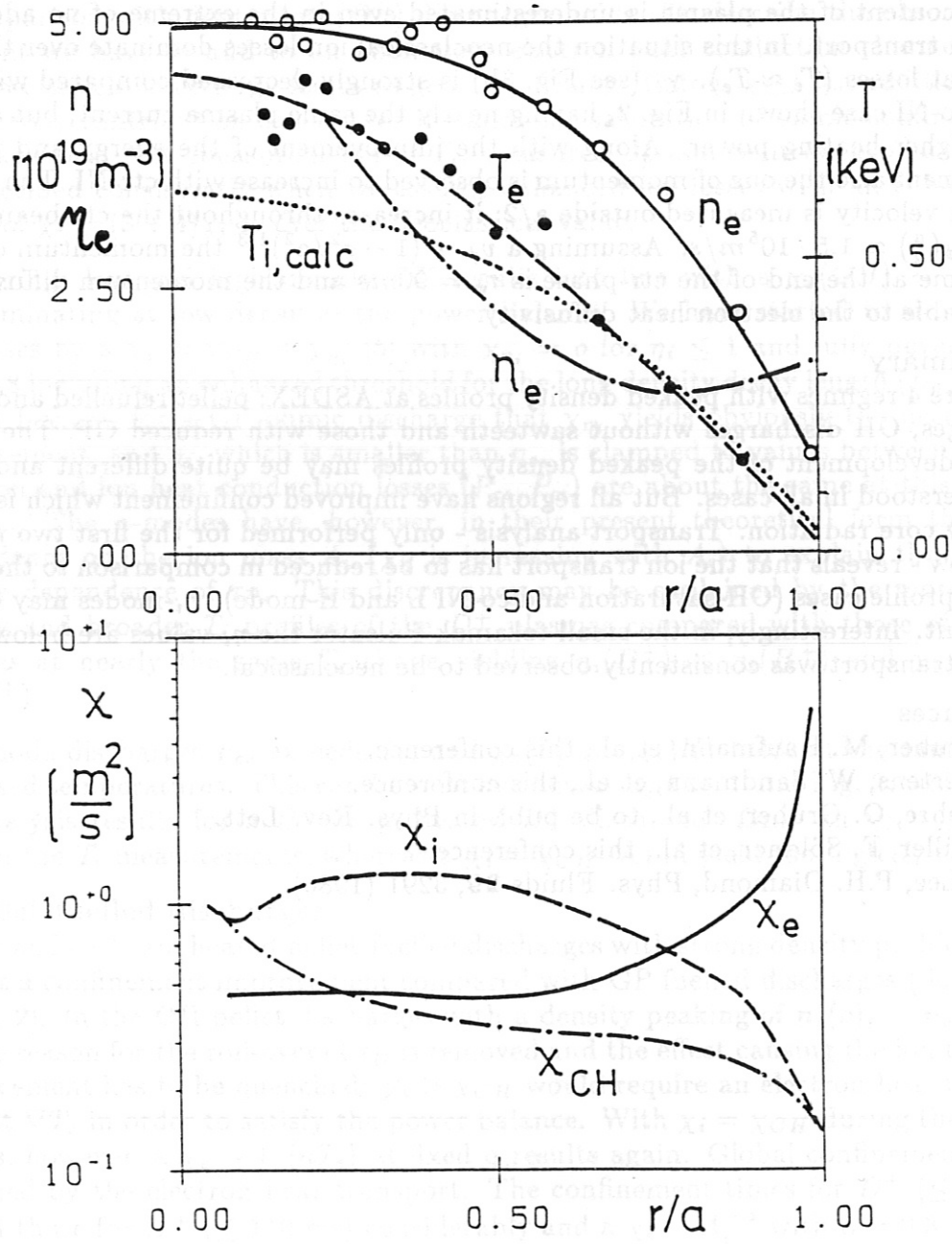

Fig. 1:Radial profiles for a OH discharge ($I_p = 380kA$, $B_t = 2.2T$; $\bar{n}_e = 4 \cdot 10^{19} m^{-3}$); a) $T_e(\bullet)$ and $n_e(o)$ from Thomson scattering, η_e and T_i (calc. using $\chi_i = \chi_{NC} + \chi_{\eta_i}$); b) transport coefficients from TRANSP analysis.

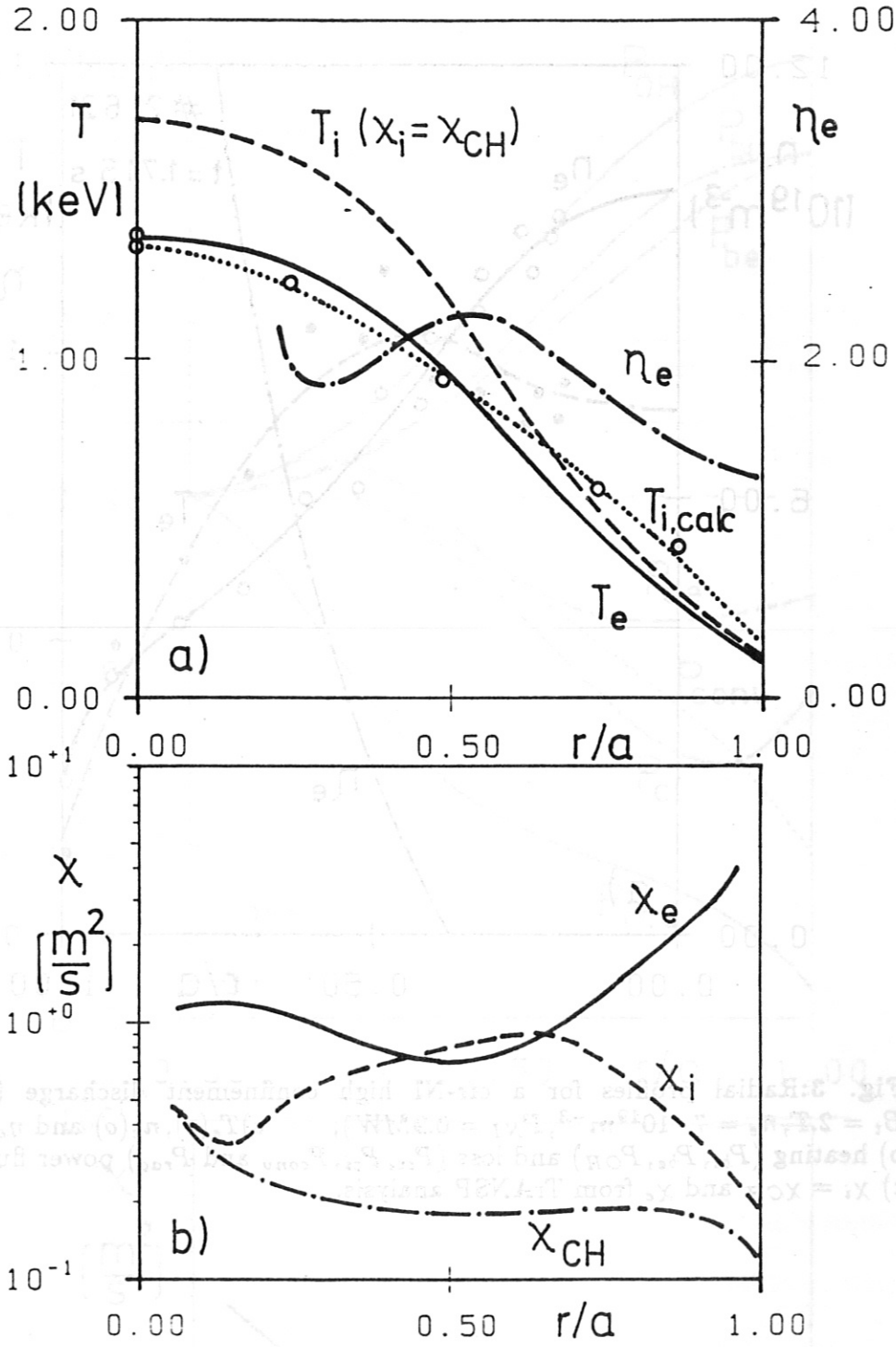

Fig. 2:Radial profiles for a co-NI L-mode discharge ($I_p = 440kA; B_t = 2.3T$; $\bar{n}_e = 4.5 \cdot 10^{19} m^{-3}, P_{NI} = 1.35MW$);
a) $T_e, T_i(o)$ from pass. CX-meas., η_e, T_i (using $\chi_i = \chi_{NC} + \chi_{\eta_i}$) and T_i ($\chi_i = \chi_{NC}$);
b) transport coefficients from TRANSP analysis.

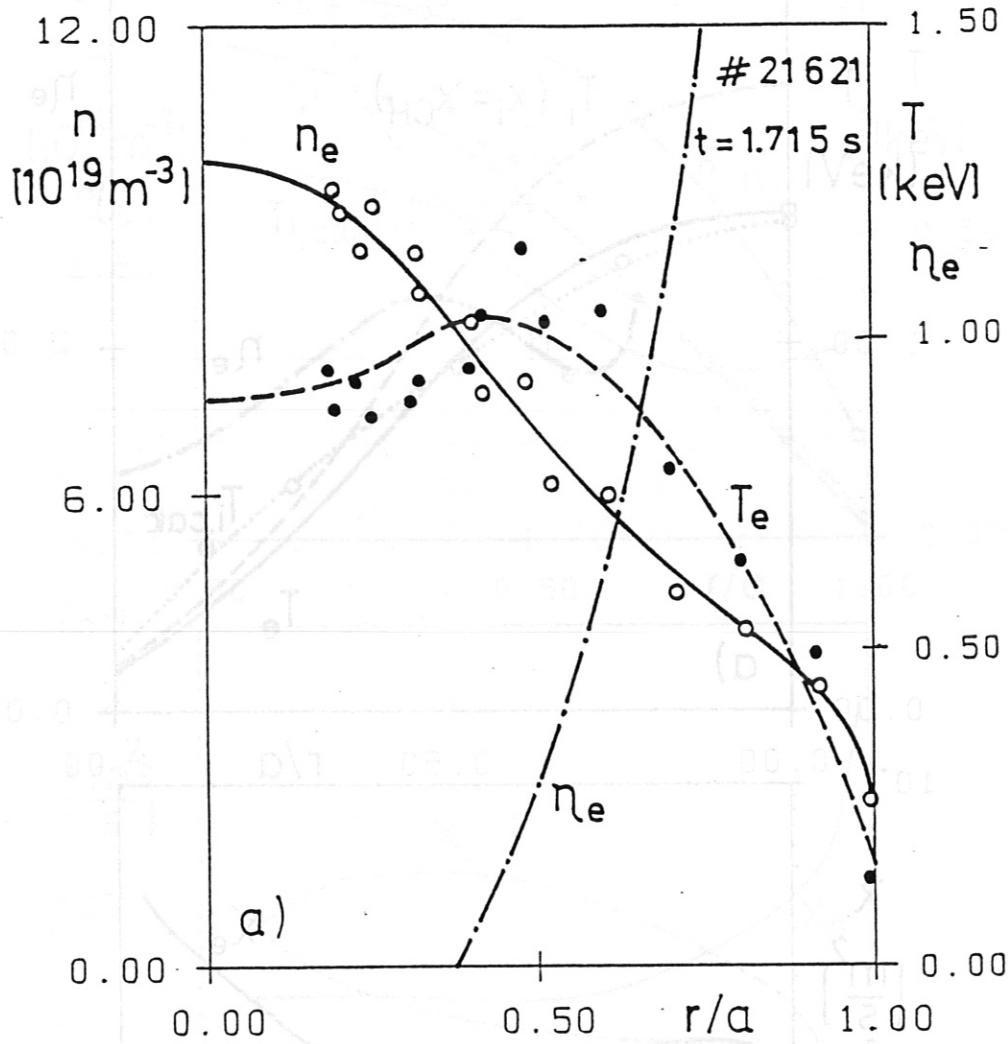

Fig. 3: Radial profiles for a ctr-NI high confinement discharge ($I_p = 420kA$, $B_t = 2.T, \bar{n}_e = 7 \cdot 10^{19} m^{-3}, P_{NI} = 0.9MW$); a)$T_e(\bullet), n_e(o)$ and η_e; b) heating (P_{bi}, P_{be}, P_{OH}) and loss (P_{ce}, P_{ci}, P_{conv} and P_{rad}) power fluxes. c) $\chi_i = \chi_{CH}$ and χ_e from TrANSP analysis.

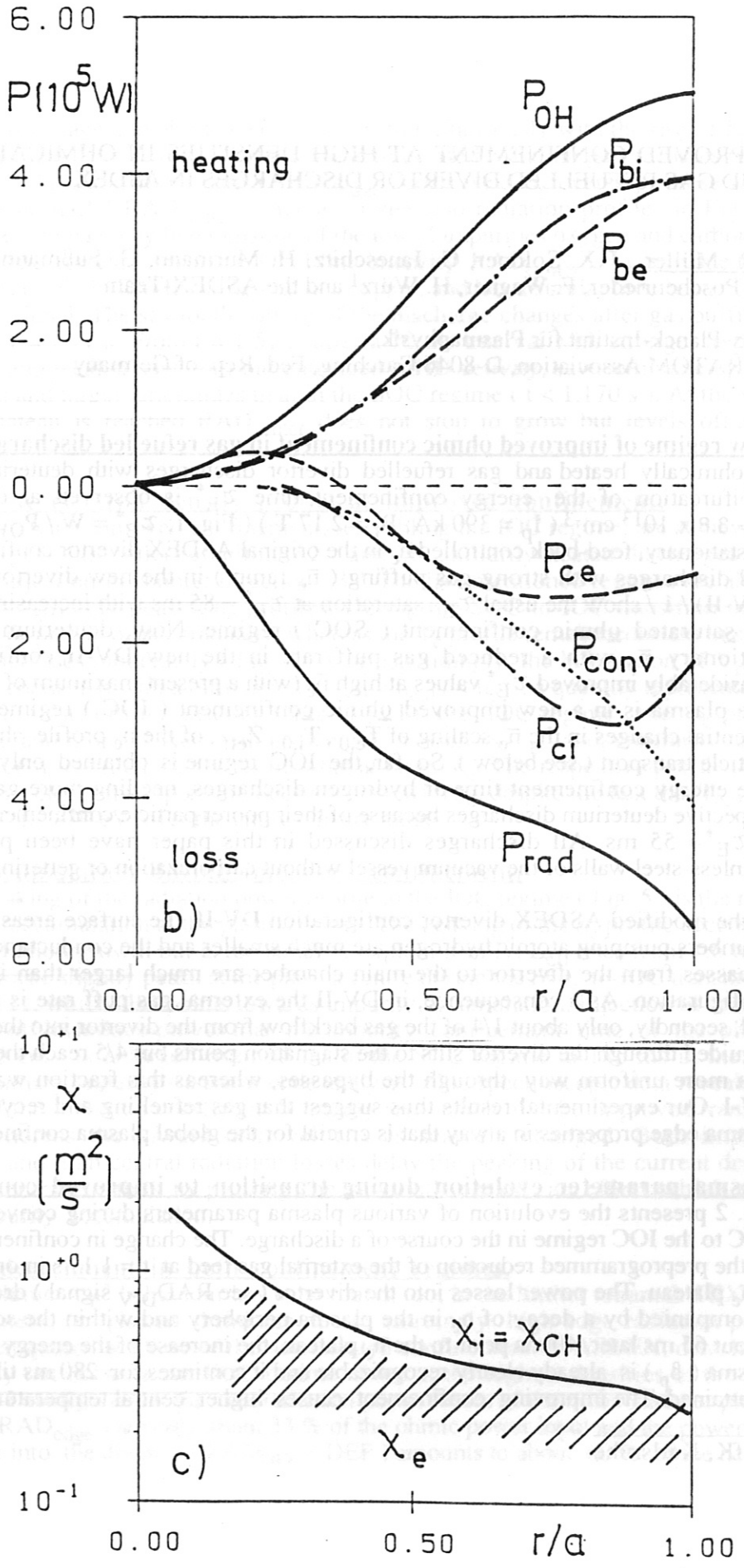
6.00
P(10^5 W)
4.00
2.00
0.00
2.00
4.00
6.00
heating
loss
b)
P_OH
P_bi
P_be
P_ce
P_conv
P_ci
P_rad
0.00
0.50
r/a
1.00
10^+1
χ
(m^2/s)
10^+0
10^-1
χ_i = χ_CH
χ_e
c)
0.00
0.50
r/a
1.00

Fig. 3

IMPROVED CONFINEMENT AT HIGH DENSITIES IN OHMICALLY HEATED AND GAS REFUELLED DIVERTOR DISCHARGES IN ASDEX

E.R. Müller , F.X. Söldner, G. Janeschitz, H. Murmann, G. Fußmann, M. Kornherr, W. Poschenrieder, F. Wagner, H. Würz[1] and the ASDEX-Team

Max-Planck-Institut für Plasmaphysik
EURATOM Association, D-8046 Garching, Fed. Rep. of Germany

New regime of improved ohmic confinement in gas refuelled discharges.

In ohmically heated and gas refuelled divertor discharges with deuterium in ASDEX, a bifurcation of the energy confinement time τ_E^* is observed at densities above $\bar{n}_e \approx 3.8 \times 10^{13}$ cm^{-3} ($I_p = 390$ kA; $B_t = 2.17$ T) (Fig. 1; $\tau_E^* = W / P_{OH}$). Discharges at stationary, feed-back controlled $\bar{n}_e$ in the original ASDEX divertor configuration (DV-I) and discharges with strong gas puffing ($\bar{n}_e$ ramp) in the new divertor configuration (DV-II) / 1 / show the usual τ_E^* saturation at $\tau_E^* \approx 85$ ms with increasing $\bar{n}_e$ and are in the saturated ohmic confinement (SOC) regime. Now, deuterium discharges at stationary $\bar{n}_e$ with a reduced gas puff rate in the new DV-II configuration yield considerably improved τ_E^* values at high $\bar{n}_e$ (with a present maximum of $\tau_E^* \approx 110$ ms). The plasma is in a new improved ohmic confinement (IOC) regime, indicated by essential changes in the $\bar{n}_e$ scaling of $T_{e,0}$, $T_{i,0}$, Z_{eff} , of the n_e profile shape and of the particle transport (see below). So far, the IOC regime is obtained only in deuterium. The energy confinement time of hydrogen discharges, needing more gas puffing than respective deuterium discharges because of their poorer particle confinement, still saturates at $\tau_E^* \approx 55$ ms. All discharges discussed in this paper have been performed with stainless-steel walls of the vacuum vessel without carbonization or gettering.

In the modified ASDEX divertor configuration DV-II, the surface areas in the divertor chambers pumping atomic hydrogen are much smaller and the conductance values of the bypasses from the divertor to the main chamber are much larger than in the old DV-I configuration. As a consequence, in DV-II the external gas puff rate is roughly halved and, secondly, only about 1/4 of the gas backflow from the divertor into the main chamber is guided through the divertor slits to the stagnation points but 4/5 reach the main chamber in a more uniform way through the bypasses, whereas this fraction was negligible in DV-I. Our experimental results thus suggest that gas refuelling and recycling affect the plasma edge properties in a way that is crucial for the global plasma confinement.

Plasma parameter evolution during transition to improved confinement.

Fig. 2 presents the evolution of various plasma parameters during conversion from the SOC to the IOC regime in the course of a discharge. The change in confinement is initiated by the preprogrammed reduction of the external gas feed at $t = 1.17$ s in order to establish a $\bar{n}_e$ plateau. The power losses into the divertor (see RAD_{DIV} signal) drop immediately accompanied by a decay of n_e in the plasma periphery and within the scrape-off layer. About 65 ms later, 40 ms prior to the $\bar{n}_e$ plateau, the increase of the energy content of the plasma (β_p) is already clearly recognizable and it continues for 280 ms till the β_p plateau is attained. The improving confinement causes higher central temperatures $T_{e,0}$ and $T_{i,0}$

[1] KfK, Karlsruhe

at reduced loop voltage and ohmic heating power.Simultaneously with the rise of β_p and the peaking of the n_e profile (Fig. 3), the volume integrated radiation power losses within the outer half of plasma minor radius (RAD_{edge}) decrease and, reversely, those within the inner plasma half (RAD_{center}) increase (see also radiation profiles in Fig. 5). RAD_{edge} is predominated by line radiation of the low-Z impurities oxygen and carbon and is, therefore, time-correlated with the O VI line intensity. RAD_{center} is mainly due to the metals iron and (only in DV-II configuration) copper, and has a similar time behaviour as the soft X-ray signal. The sawtooth pattern of the discharge changes after gas puffing is diminished at t = 1.17 s. From t = 1.51 s, after a 70 ms interval with stronger impurity accumulation and weaker sawtooth but enhanced MHD activity, sawteeth develop with longer periods and larger amplitudes than in the SOC regime (t < 1.170 s). At the same time, the β_p plateau is reached. RAD_{center} does not stop to grow but levels off about 120 ms later.

Peaking of the electron density profile at improved confinement.

Plasma regimes with improved confinement, resembling the IOC regime, are achieved in ohmic discharges with pellet refuelling / 2 / and in auxiliarily heated discharges with neutral-beam injection in counter direction / 3 /. The last-mentioned regimes are always associated with strongly peaked n_e profiles. During the SOC-to-IOC transition in one discharge, the n_e profile peaks gradually, whereas the T_e profile remains constant in shape though $T_{e,0}$ increases moderately (Fig. 3). Correspondingly, the bifurcation of τ_E^* on the $\bar{n}_e$ scale is connected with a bifurcation of $Q_n = n_{e,0} / < n_e >$, a quantity representative of the degree of n_e profile peaking (Fig. 4) : In the IOC regime , the n_e profile becomes more and more peaked with growing $\bar{n}_e$ as well as τ_E^* and, contrarily, in the SOC regime the n_e profile broadens somewhat at larger $\bar{n}_e$. The respective profile shape factor Q_T for the electron temperature does not vary with $\bar{n}_e$, despite the fact that $T_{e,0}$ falls from 1920 eV to 880 eV over the entire density range.

Impurity accumulation during improved confinement.

The central peaking of the radiation power profile in the IOC regime (Fig. 5) is the result of an impurity accumulation at the plasma centre. The peaking of the n_e profile accelerates the central radiation growth but is too small to explain it fully. Z_{eff} rises from 1.6 to 2.7 and the Z_{eff} profile slightly peaks at the plasma centre during the SOC-to-IOC transition in shot #22990 / 4 /, which also points towards impurity accumulation. Injection of titanium by laser blow-off technique proves that the impurity confinement time of the plasma core (0-to-30 cm) is enlarged from 55 ms in the SOC regime to 185 ms in the IOC regime. Preliminary impurity transport code analysis using spectroscopic data reveals that a reduction of the diffusion coefficient is mainly responsible for the improved transport properties, whereas the inward drift velocity is scarcely changed. Both impurity accumulation and high central radiation losses delay the peaking of the current density profile and contribute thus to prolong the sawtooth period, an effect which again facilitates impurity accumulation.

No plasma detachment in both confinement regimes.

Bifurcating ohmic τ_E^* behaviour has been found, too, in the limiter tokamak TEXTOR / 5 /. Detachment, i.e. plasma shrinkage due to extremely high edge radiation power losses has been quoted as cause of the deteriorated confinement. In ASDEX, detachment does definitely not occur in the SOC regime. Even at the highest densities of the SOC regime in DV-I configuration, the total radiation power losses of the main chamber plasma ($RAD_{center} + RAD_{edge}$) are only about 33 % of the ohmic power input and the power flow accounted for into the divertor (RAD_{DIV} + DEP) amounts to about 60 % of the heating

power (Fig. 6 (a)). In the SOC regime, both the electron density and temperature profile do not show any shrinking at the edge. Just the reverse is observed, at improved confinement in the IOC regime the n_e profile is more centrally peaked and the edge density is reduced. In the IOC regime, also both RAD_{center} and RAD_{edge} are larger and the energy losses into the divertor (RAD_{DIV}) are smaller (compare Figs. 6 (a) and (b)), a fact which is in contrast with TEXTOR results. It should be stressed, however, that there is also no detachment in the IOC regime. The SOC regime in DV-II demonstrates that n_e profiles broader than in the IOC regime well exist at RAD_{edge} values higher than in the IOC regime (compare Figs. 6 (b) and (c)).

References

/ 1 / H. Niedermeyer, et al., this conference.
/ 2 / M. Kaufmann, et al., acc. for publ. in Nucl. Fus.; O. Gruber, et al., this conference.
/ 3 / O. Gehre, et al., accepted for publication in Phys. Rev. Lett.
/ 4 / K.H. Steuer, et al., this conference.
/ 5 / R.R. Weynants, Report No. 85, LPP-ERM/KMS, Brussels (1987).

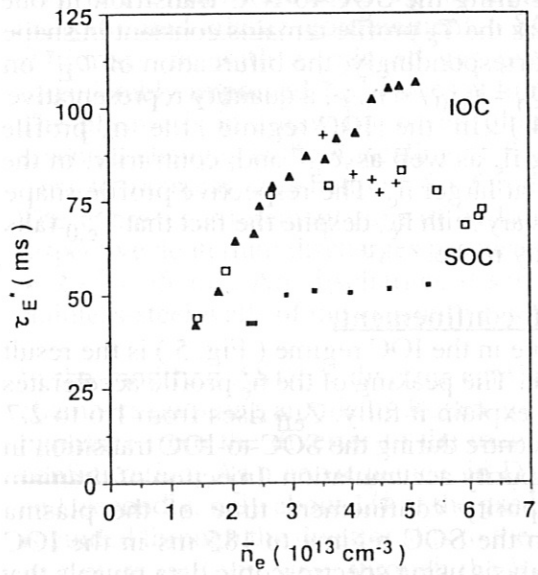

Fig. 1 (above) : Energy confinement time τ_E^* versus line averaged density $\bar{n}_e$ in ohmic divertor discharges ($I_p \approx 390$ kA; $B_t = 2.17$ T)

(A) ▲ D_2-gas; DV-II; $\bar{n}_e$-plateau
(B) + D_2-gas; DV-II; $\bar{n}_e$-ramp
(C) ▫ D_2-gas; DV-I ; $\bar{n}_e$-plateau
(D) ▪ H_2-gas; DV-II; $\bar{n}_e$-plateau

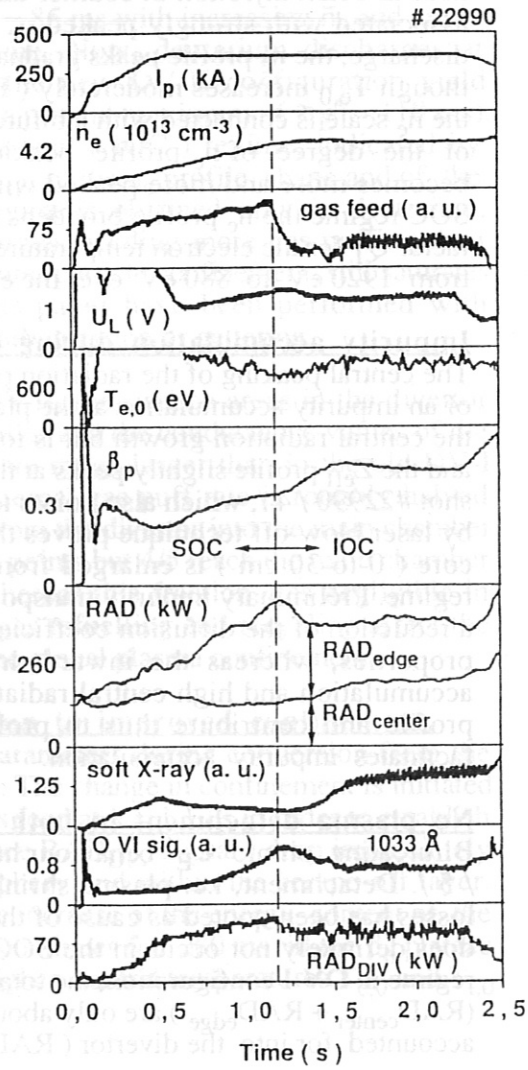

Fig. 2 (right) : Time evolution of various plasma parameters during transition from τ_E^* saturation (SOC) to improved τ_E^* regime (IOC) - note the increase in β_p.

Radiation power losses of the torus plasma are divided into central (RADcenter) and edge part (RADedge). The volume power losses of the divertor plasma (RAD_{DIV}) are mainly due to neutral particle losses.
(D_2-gas; DV-II; $I_p = 390$ kA; $B_t = 2.17$ T)

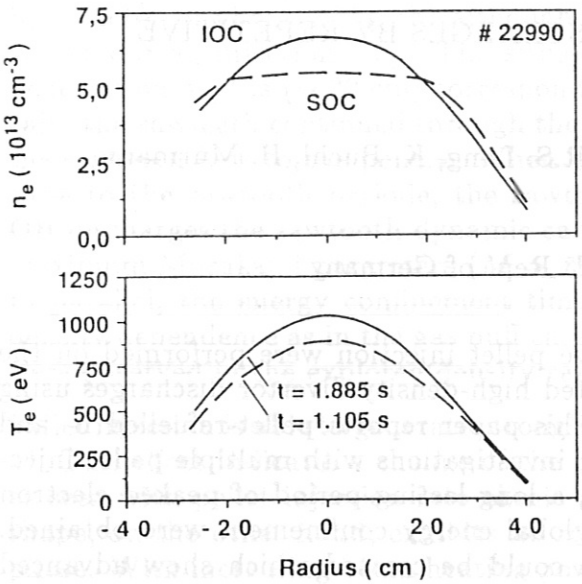

Fig. 3 : Radial profiles of electron density n_e and temperature T_e at two discrete times representative of the two kinds of ohmic confinement regime during one discharge (for plasma parameters, see Fig. 2).

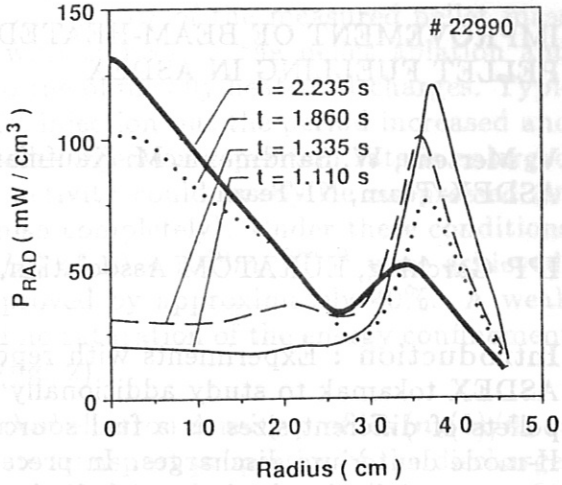

Fig. 5 : Evolution of radiation power density profile during transition from SOC to IOC regime (same discharge as in Fig. 2).

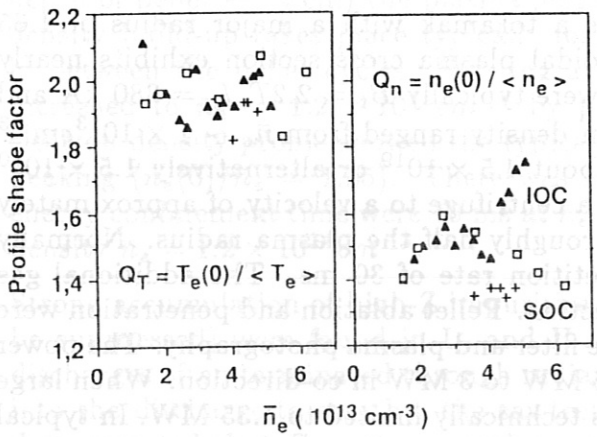

Fig. 4 : Plasma density ($\bar{n}_e$) dependence of profile shape factors of electron temperature (Q_T) and density (Q_n) for both cases of ohmic confinement regime (same discharges and symbols as in Fig.1).

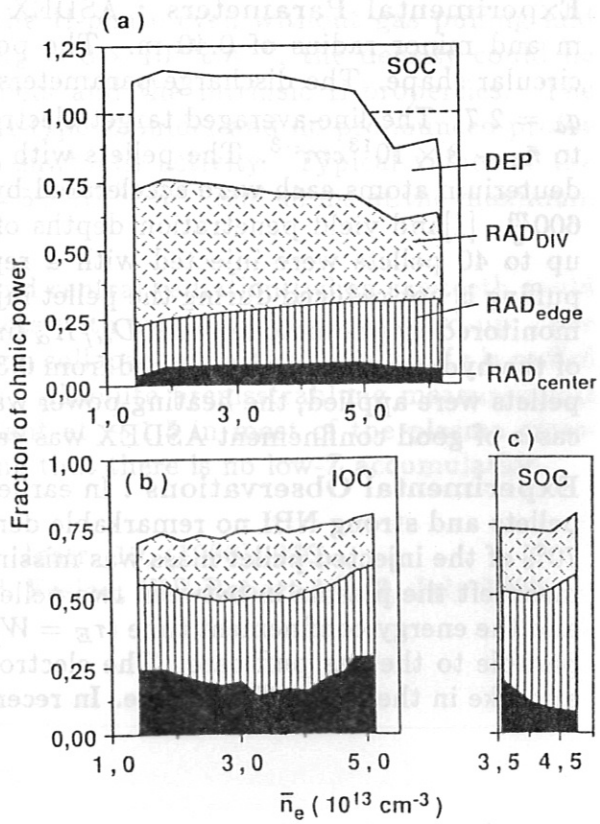

Fig. 6 (right) :
Global power balance versus $\bar{n}_e$ for
(a) SOC regime in $\bar{n}_e$-plateau of DV-I (discharge parameter set C of Fig. 1)
(b) IOC regime in $\bar{n}_e$-plateau of DV-II (discharge parameter set A of Fig. 1)
(c) SOC regime in DV-II during strong gas puffing (parameter set B of Fig. 1)
DEP denotes the power deposition on the divertor neutralizer plates.

IMPROVEMENT OF BEAM-HEATED DISCHARGES BY REPETITIVE PELLET FUELLING IN ASDEX

V. Mertens, W. Sandmann, M. Kaufmann, R.S. Lang, K. Buchl, H. Murmann, ASDEX-Team, NI-Team

IPP Garching, EURATOM Association, Fed. Rep. of Germany

Introduction : Experiments with repetitive pellet injection were performed on the ASDEX tokamak to study additionally heated high-density divertor discharges using pellets of different sizes as a fuel source. This paper reports pellet-refuelled L- and H-mode deuterium discharges. In preceding investigations with multiple pellet injection, especially in ohmic heated discharges, a long-lasting period of peaked electron density profile and considerably improved global energy confinement were obtained. In recent experimentation L-mode plasmas could be created which show advanced plasma performance in relation to the common gas fuelled and neutral-beam-heated (NBI) discharges. These large pellet refuelled plasmas were characterized by moderately centrally peaked electron density profiles, high edge recycling, reduced sawtooth activity, central impurity radiation and significantly improved energy confinement. At a heating power of 2.5 MW the H-regime could be attained together with injection of small pellets.

Experimental Parameters : ASDEX is a tokamak with a major radius of 1.65 m and minor radius of 0.40 m. The poloidal plasma cross section exhibits nearly circular shape. The discharge parameters were typically $B_t = 2.2T, I_p = 380$ kA and $q_a = 2.7$. The line-averaged target electron density ranged from $\bar{n}_e \sim 1 \times 10^{13} cm^{-3}$ to $\bar{n}_e \sim 8 \times 10^{13} cm^{-3}$. The pellets with about 4.5×10^{19} or alternatively 1.5×10^{20} deuterium atoms each were accelerated by a centrifuge to a velocity of approximately $600 \frac{m}{s}$ [1]and yield penetration depths of roughly half the plasma radius. Normally up to 40 pellets were injected with a repetition rate of 30 ms. The additional gas puffing is not reduced during the pellet injection. Pellet ablation and penetration were monitored by photodiodes with D_α / H_α line filter and plasma photography. The power of the hydrogen beams is scanned from 0.35 MW to 3 MW in co-direction. When large pellets were applied, the heating power was technically limited to 1.35 MW. In typical cases of good confinement ASDEX was carbonized.

Experimental Observations : In earlier investigations combining injection of small pellets and strong NBI no remarkable density build-up could be produced [2]. Up to 70% of the injected pellet mass was missing in the discharge and nearly all the ablated mass left the plasma in between two pellets (fig. 1a). The sawtooth activity increased and the energy confinement time ($\tau_E = W_p / (P_{heat} - dW_p/dt)$) degraded to values comparable to the gas puff case. The electron density and temperature profiles behaved also like in the gas puff L-regime. In recent experimentation with increased pellet size

and limited NBI power it was possible to improve significantly the plasma performance of the L-mode. The operational density range is extended to $\bar{n}_e = 1.3 \times 10^{14} cm^{-3}$. During the heating phase the plasma stored energy from beta measurements increased by a factor of about 2 (fig.1b) although still up to 50% of the measured pellet mass is lost during injection [3]. The situation with respect to the pellet ablation and penetration depths ($\sim$ 22 cm) corresponded to the ohmically heated discharges. Typically the sawteeth continued through the pellet injection but the period increased and the sawteeth lock to the pellets. When the pellet injection repetition rate is enlarged close to the sawtooth periode, the sawtooth activity could nearly be suppressed (in OH discharges the sawtooth dynamic can vanish completely). Under these conditions maximum Murakami paramters ($M = \bar{n}_e R/B_t$) of $10 \times 10^{19} m^{-2} T^{-1}$ were achieved. In parallel, the energy confinement time improved by approximately 40%. A weak density dependence as in the gas puff case and no saturation of the energy confinement were observed in the explored density range (fig. 2).

Pellet injection is able to generate strongly peaked electron density profiles ($n_e(0)/\bar{n}_e \approx 2$). This effect indicates a change of the particle transport properties of the discharge, as seen with pellet injection into ohmic discharges. The electron temperature profile shape, on the other hand, exhibits no remarkable change compared to the pre-pellet phase. With increasing beam heating power,the electron density profile peaking in the L-mode becomes less prominent (fig. 3), and the energy confinement degrades (fig. 4) [4]. The confinement degrades much faster than the density profile peaking. At 1.35 MW neutral beam power the profile peaking is close to the standard gas refuelled L-mode discharge.

In the first H-regime experiments together with injection of small pellets (penetration depth of pellet $\sim$ 12 cm) the plasma performance is very similar to the gas puff case: density build-up takes place typically for the H-phase even without gas puffing and in between the pellet cycles. Starting at $\bar{n}_e = 8 \times 10^{13} cm^{-3}$, the density could be increased to $\bar{n}_e = 1.2 \times 10^{14} cm^{-3}$ by pellets and the intrinsic H-properties. The electron density profile showed the typical H-type shoulder and no pronounced profile peaking ($n_e(0)/\bar{n}_e = 1.25$). There was no sawtooth activity. Typical values of the energy confinement time were 70 ms at $\bar{n}_e = 5 \times 10^{13} cm^{-3}$ and 40 ms at the maximum density $\bar{n}_e = 1.2 \times 10^{14} cm^{-3}$.

Strong accumulation of high-Z impurities and central radiation (when sawteeth could be suppressed) were found in L- and H-shots with successful density build-up. The discharges often terminated through radiation collapse, in particular when Kr is puffed into the discharge to smother the sawteeth. Absolute bremsstrahlung measurements demonstrated that Z_{eff} stays nearly constant at $\sim$ 1.5 in most of the plasma cross-section during pellet injection [5], indicating that there is no low-Z accumulation.

References :

[1] W. Amenda, R.S. Lang, J. Phys. E: Sci. Instr. 19, (1986), 970
[2] M. Kaufmann et al., to be publ. in Nucl. Fusion, IPP Report 1/242, July 1987
[3] A. Carlson et al., this conference
[4] O. Gruber et al., this conference
[5] K.-H. Steuer et al., this conference

Figure Captions :

1 : The density build-up of two pellet-refuelled and NBI-heated discharges is shown. In conjunction with the successful density build-up of discharge #21427 the global energy confinement time increases during pellet injection to ~ 65 ms. The increase of the diamagnetic beta (dashed-dotted curve) is also shown. When small pellets are injected (#18913), neither a high density nor improved confinement is attained.

2 : Global energy confinement time as a function of the line-averaged electron density of pellet-refuelled (a) and gas-puff-refuelled (b) deuterium discharges at different NBI heating powers. The confinement time and electron density of pellet-refuelled discharges reach values which are considerably higher than those of the standard gas-puff case.

3 : Peaking factor (ratio of the peak electron density to the volume-averaged electron density) as a function of the total plasma heating power P_{tot} of pellet-refuelled discharges. This power is the sum of the ohmic input power P_{OH} and the absorbed neutral-beam power: $P_{tot} = P_{OH} + 0.9 \times P_{NBI}$. The peaking factor at $P_{tot} = 0.5$ MW corresponds to pure ohmically heated discharges with injection of small pellets. When NBI power is applied, only discharges refuelled via large pellets are considered. The peaking factors at $P_{tot} = 0.5$ MW and 1.0 MW are determined during stationary density phases. The other values are ascertained close to stationary density conditions.

4 : Global energy confinement time as a function of the total heating power P_{tot} of pellet-refuelled discharges (see also caption of figure 3). All energy confinement times are determined at a line-averaged electron density of $\bar{n}_e = 1 \times 10^{14} cm^{-3}$.

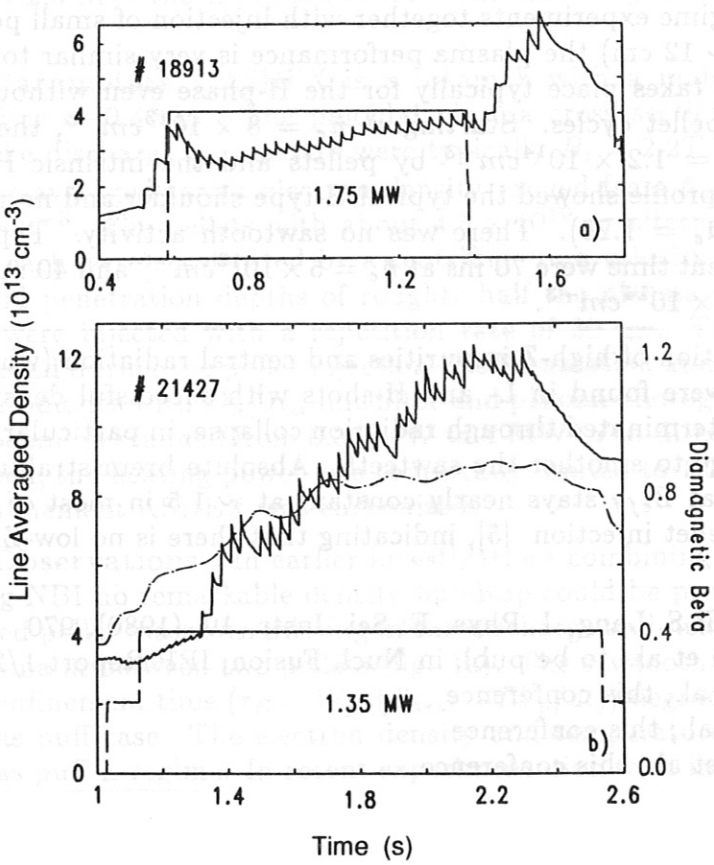

Fig. 1

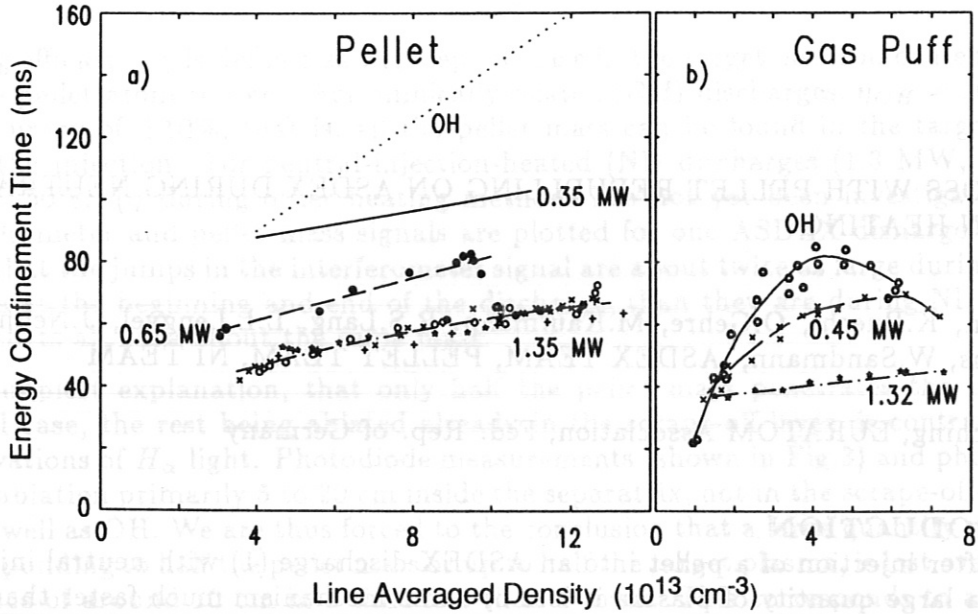

Fig. 2

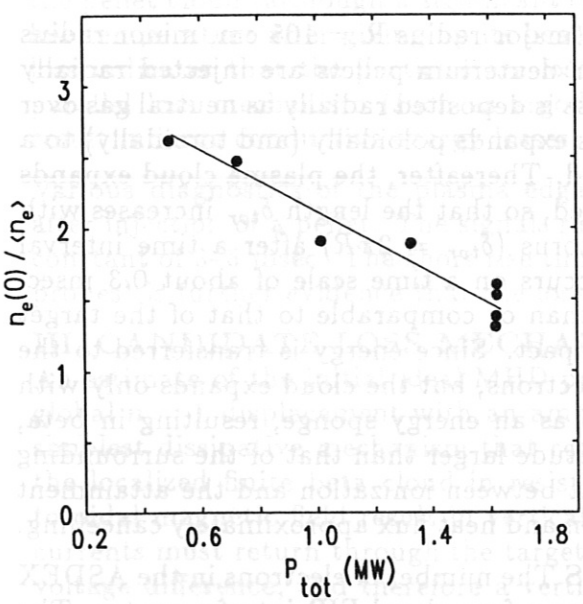

Fig. 3

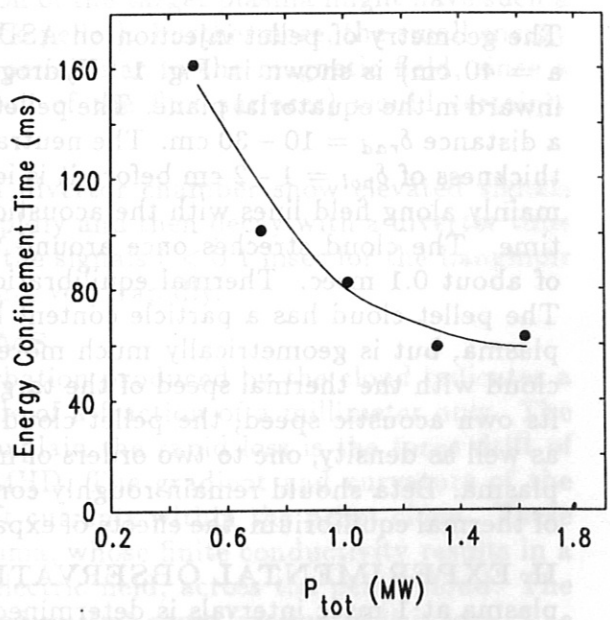

Fig. 4

MASS LOSS WITH PELLET REFUELLING ON ASDEX DURING NEUTRAL INJECTION HEATING

A.Carlson, K.Buechl, O.Gehre, M.Kaufmann, R.S.Lang, L.L.Lengyel, J.Neuhauser, V.Mertens, W.Sandmann, ASDEX TEAM, PELLET TEAM, NI TEAM

IPP Garching, EURATOM Association, Fed. Rep. of Germany

I. INTRODUCTION

Shortly after injection of a pellet into an ASDEX discharge (1) with neutral injection heating, a large quantity of plasma is lost by some mechanism much faster than that normally active. The measured increase of particles in the target plasma (with about 1 msec time resolution) corresponds to only about half the measured number of particles in the pellet. Other measurements verify that the pellet particles do indeed penetrate deep into the target. The nature of the plasma cloud produced by the pellet is understood in general, but the further interaction of the cloud with the target plasma can be very complex. Two mechanisms to account for the observed loss are proposed: an outward drift due to toroidal geometry and finite resistance, or transport from instabilities driven by the large pressure and density gradients or the corresponding large current perturbation.

The geometry of pellet injection on ASDEX (major radius R = 165 cm, minor radius a = 40 cm) is shown in Fig. 1. Hydrogen or deuterium pellets are injected radially inward in the equatorial plane. The pellet mass is deposited radially as neutral gas over a distance δ_{rad} = 10 – 30 cm. The neutral gas expands poloidally (and toroidally) to a thickness of δ_{pol} = 1 - 2 cm before it is ionized. Thereafter, the plasma cloud expands mainly along field lines with the acoustic speed, so that the length δ_{tor} increases with time. The cloud streches once around the torus ($\delta_{tor} = 2\pi R$) after a time interval of about 0.1 msec. Thermal equilibration occurs on a time scale of about 0.3 msec. The pellet cloud has a particle content less than or comparable to that of the target plasma, but is geometrically much more compact. Since energy is transferred to the cloud with the thermal speed of the target electrons, but the cloud expands only with its own acoustic speed, the pellet cloud acts as an energy sponge, resulting in beta, as well as density, one to two orders of magnitude larger than that of the surrounding plasma. Beta should remain roughly constant between ionization and the attainment of thermal equilibrium, the effects of expansion and heat flux approximately cancelling.

II. EXPERIMENTAL OBSERVATIONS

The number of electrons in the ASDEX plasma at 1 msec intervals is determined using a four-chord FIR interferometer. The accuracy of these measurements is verified and improved by comparison with Thomson scattering profiles and lithium beam measurements of the edge density. The number of atoms in each pellet is measured in flight using a resonant microwave cavity. The

fueling efficiency η is defined as the step increase in the target electron content divided by the pellet atom content. For ohmically-heated (OH) discharges, $\eta_{OH} = 100\%$ with an accuracy of $\pm 10\%$, that is, all the pellet mass can be found in the target plasma after the injection. For neutral-injection-heated (NI) discharges (1.3 MW, L-mode), $\eta_{NI} = 50\%$. (η during other heating methods has not yet been investigated.) The interferometer and pellet mass signals are plotted for one ASDEX disharge in Fig. 2. Note that the jumps in the interferometer signal are about twice as large during the OH phases at the beginning and end of the discharge, than they are during NI, although the pellets all have about the same mass.

The simplest explanation, that only half the pellet mass penetrates the plasma in the NI case, the rest being ablated already in the scrape-off layer, is contradicted by observations of H_α light. Photodiode measurements (shown in Fig.3) and photographs show ablation primarily 5 to 20 cm inside the separatrix, not in the scrape-off-layer, for NI as well as OH. We are thus forced to the conclusion that a large quantity of plasma, corresponding to half the pellet mass or up to half the target plasma, is lost over a radial distance of around 10 cm in a time less than 1 msec. This corresponds to a diffusion constant greater than $10^5 \mathrm{cm}^2/\mathrm{sec}$, which is one to two orders of magnitude larger than that found in ASDEX under normal conditions (e.g. between pellets), so that a different and much more effective particle transport mechanism must be involved.

Measurements of the plasma energy show a step-like decrease at the time of each pellet injection during NI. Assuming that it is distributed evenly among the electrons and ions lost, this energy difference corresponds to a temperature of around 140 eV. This relatively low temperature, roughly twice the temperature at the separatrix, indicates that the energy loss is mostly convective and that the particles lost probably come from the pellet cloud (although a significant fraction of the target plasma might have such a low temperature after giving up its heat to the pellet). Furthermore, the small energy loss indicates that the particles are lost perpendicular to the magnetic field, since a parallel loss mechanism (such as ergodization of the flux surfaces) would certainly result in large conductive energy losses.

Various diagnostics of the plasma edge and divertor chamber show elevated signals after injection of a pellet. The signals rise rapidly and then decay with a divertor time constant of 3–5 msec. The short rise time of the signals (< 0.1 msec for the Langmuir probes) is further evidence that the loss occurs very rapidly.

III. CANDIDATE LOSS MECHANISMS

An estimate of the initial ideal MHD perturbation produced by the cloud indicates a global $n = 1$ displacement with an amplitude of a fraction of a millimeter only. The simplest dissipative mechanism that could explain the rapid loss is the torus drift of the localized finite beta cloud in resistive MHD. The gradient and curvature of the toroidal magnetic field result in vertical drift currents within the pellet cloud. These currents must return through the target plasma, whose finite conductivity results in a voltage difference, and therefore a vertical electric field, across the pellet cloud. The electric field causes the cloud to drift outward so that some fraction of it is lost. The loss continues until the pellet cloud has distributed itself poloidally, at which time the net outward drift stops. The total currents involved are of the order of several tens of kiloamperes. Order of magnitude estimates of the E×B drift velocity easily yield

values above the 10^5 cm/sec required to produce substantial losses within the 0.2 msec available. This shows that non-turbulent resistive loss could be significant, so that this mechanism deserves more careful consideration. However, it is not clear that this model will be able to satisfactorily explain the observed difference between NI and OH discharges.

A second candidate mechanism is loss due to resistive instabilities of various kinds. Tearing, driven by the large currents related to the pellet perturbation, and ballooning, driven by the pressure gradients at the edge of the cloud, are commonly discussed, but a quantitative assessment of the expected anomalous transport is not available. We note, however, that the fact that the pressure profiles before pellet injection are much closer to the ideal ballooning limit during NI than during OH could possibly provide an explanation for the difference in mass loss for the two cases.

The clarification of the mechanism responsible for the rapid loss of plasma during pellet refuelling will aid the design of pellet systems for future experiments, but more important, it may help our general understanding of particle transport processes in tokamaks.

References

(1) Kaufmann, et al.,"Pellet Injection with Improved Confinement in ASDEX", to be published in Nucl. Fusion. See also contributions from V. Mertens and from L.L. Lengyel, this conference.

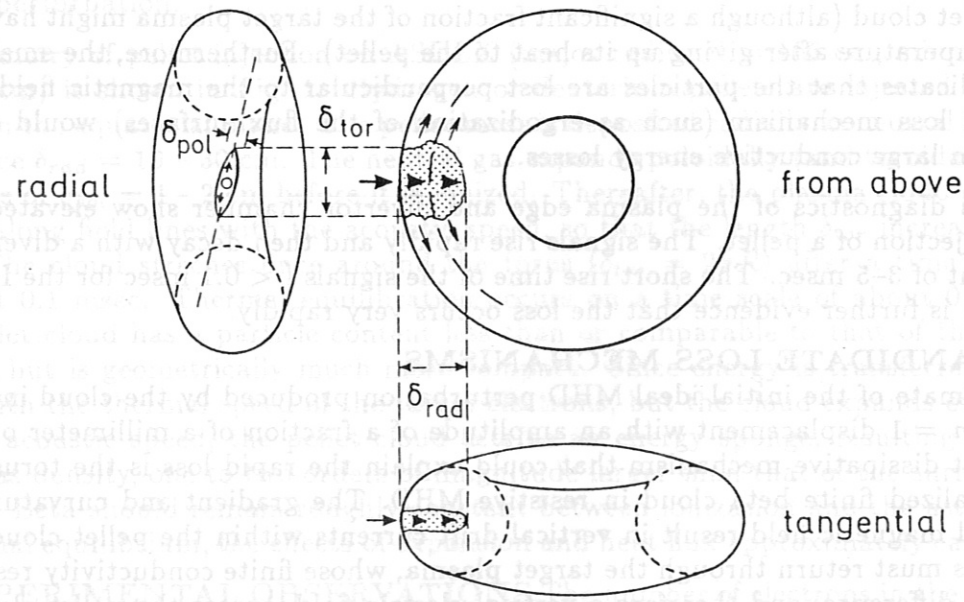

Fig. 1: Geometry of pellet injection. Three views of ASDEX, showing the path of the injected pellet (large arrows) and the expansion of the pellet cloud (small arrows) along field lines (broken line).

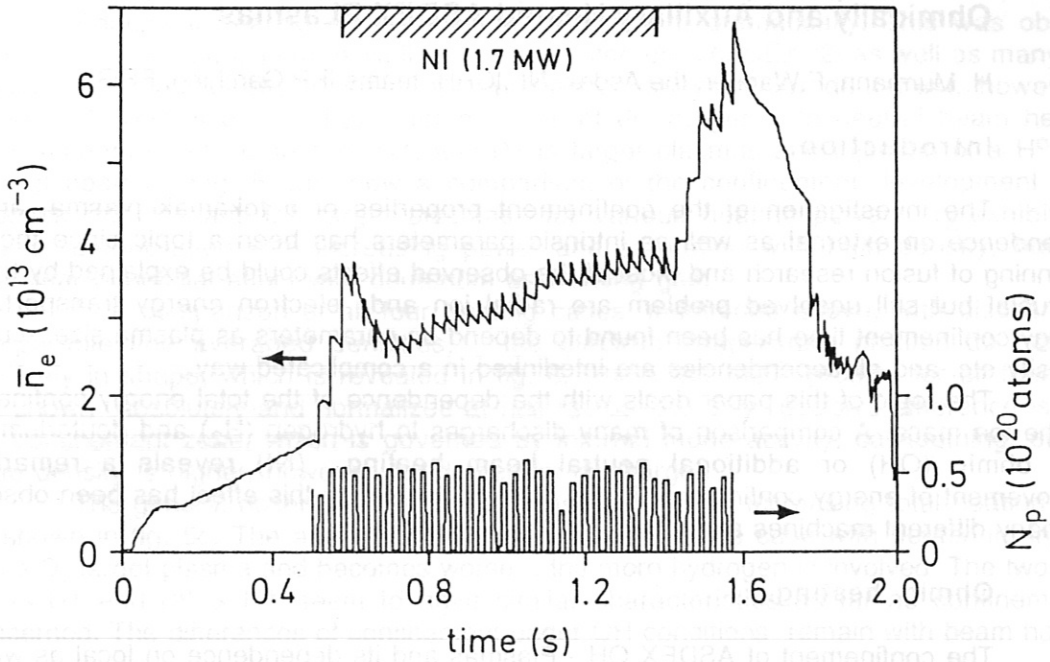

Fig. 2: Interferometer and pellet mass signals for ASDEX discharge 18913. The jump in density during ohmic heating (the first three and the last five pellets) is about twice as large as during neutral injection heating, although the pellet mass is constant.

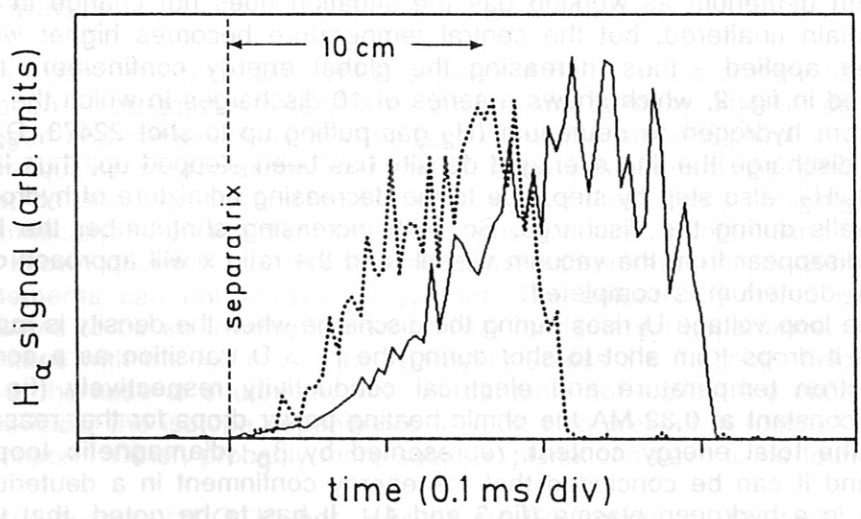

Fig. 3: Photodiode measurements of H_α light for the second and ninth pellets of ASDEX discharge 18913. The second pellet, injected in the OH phase, penetrated 18 cm (distance = (620 m/sec) $\times$ time); the ninth pellet, injected during NI, penetrated 13 cm.

The Isotope Dependence of Global Confinement in Ohmically and Auxiliary Heated ASDEX PLasmas

H. Murmann, F.Wagner, the Asdex-,NI-,ICRH- teams IPP Garching, FRG

Introduction.

The investigation of the confinement properties of a tokamak plasma, and its dependence on external as well as intrinsic parameters has been a topic since the very beginning of fusion research and most of the observed effects could be explained by theory. A crucial but still unsolved problem are radial ion and electron energy transport. The energy confinement time has been found to depend on parameters as plasma size, -current, -density etc. and all dependencies are interlinked in a complicated way.

The topic of this paper deals with the dependence of the total energy confinement on the ion mass. A comparison of many discharges in hydrogen (H_2) and deuterium (D_2) with ohmic (OH) or additional neutral beam heating (NI) reveals a remarkable improvement of energy confinement in the case of deuterium; this effect has been observed on many different machines so far.

Ohmic heating.

The confinement of ASDEX OH - Plasmas and its dependence on local as well as global parameters has been studied extensively /1/ for hydrogen discharges, and various scaling laws have been given. The general behavior since then has not changed although the divertor chamber has been rebuilt completely to enable long pulse additional heating and the recycling properties have changed significantly. In fig.1 the energy confinement time τ_E is plotted versus line averaged density and shows the familiar linear rise for small densities and saturation at about 50 ms as stated before; evidently there is also a dependence on the safety factor q_a , indicating the influence of T_e and n_e profile shapes on energy transport, which will have to be studied in a separate work.

With deuterium as working gas the situation does not change in principle; the profiles remain unaltered, but the central temperature becomes higher with the same input power applied - thus increasing the global energy confinement time. This is demonstrated in fig. 2, which shows a series of 10 discharges in which the machine was switched from hydrogen to deuterium (H_2 gas puffing up to shot 22473, D_2 thereafter). During the discharge the line averaged density has been stepped up, thus increasing the ratio $x = D_2/H_2$ also step by step, due to the decreasing admixture of hydrogen recycling from the walls during the discharge. So, with increasing shotnumber the hydrogen will eventually disappear from the vacuum vessel and the ratio x will approach one when the transition to deuterium is completed.

The loop voltage U_l rises during the discharge when the density is ramped up , but on average it drops from shot to shot during the H -> D transition as a consequence of higher electron temperature and electrical conductivity respectively (fig. 3); with I_p being kept constant at 0,32 MA the ohmic heating power drops for that reason during the transition; the total energy content, represented by β_p (diamagnetic loop) increases, however, and it can be concluded that the energy confinment in a deuterium plasma is better than in a hydrogen plasma (fig.3 and 4). It has to be noted, that this improved confinement does obviously exist already at low densities in the linear range where the confinement is exclusively dominated by electron transport. In the saturation region deuterium plasmas exhibit the same qualitative levelling off behavior as in the H_2-case, but the saturation level is much higher than in the H_2 case. (s.fig. 2)

The transition from ohmic to neutral beam heating .

Additional heating affects plasma confinement dramatically. This was observed for hydrogen and deuterium as well and documented on ASDEX /2/ as well as many other machines . The beneficial effect of improved confinement for deuterium, however, is conserved. This is demonstrated for a series of discharges with neutral beam heating;. Four scanarios are compared: H^+, and D^+as target plasmas and injection of a H^o or D^o neutral beams . Fig. 5 a,b show a comparison of the confinement development for H^o injection into H^+ and D^+ target plasmas for various heating powers. τ_E exhibits the familiar deterioration with increasing power and saturation with high density, but there is a clear beneficial effect with deuterium as working gas.

In a comparison of all four heating cases, mentioned above, with discharges of comparable line averaged densities, the electron temperature profiles do not differ relatively in shape, which is revealed in fig. 6, where the radial profiles for all four cases are shown absolutely and normalized at half radius; the only decisive difference is within the confinement zone, which is governed by internal mode activity, sawtoothing, etc. The edge density is higher, however, for deuterium discharges. .

The general observation is the decrease of τ_E with increasing total heating power as shown in fig. 5c. The average confinement is best in the case with deuterium injection into a D_2 target plasma and becomes worse , the more hydrogen is involved. The two cases H^o -> D^+ and D^o -> H^+ seem to have similar characteristics as far as confinement is concerned. The differences of confinement under OH conditions remain with beam heating.

In the high confinement regime (H-regime) during additional heating above the threshold power, the energy confinement time rises again and τ_E values corresponding to those during ohmic heating alone are recovered on ASDEX. This behavior is observable for hydrogen and deuterium as well. In fig. 5c a few examples are shown, representing additional heated plasmas after its transition to the H regime for three cases: H^o -> H^+, H^o -> D^+ and D^o ->D^+ injection. An extensive study of the parameter dependence of τ_E in steady state H-regime discharges, however, is a still matter of forthcoming experimental work.

Summary.

The global energy confinement is dependent on the mass of the plasma ions. This effect has been investigated on ASDEX by comparison of many different discharge types using hydrogen and deuterium as working gas. All of the relevant physical quantities that describe the quality of a plasma in terms of good confinement, as electron- and ion temperature, density, particle and energy confinement times, heat conductivities etc. do change dramatically, when the discharge conditions are altered. Interlinking dependencies, as the well known ohmically constraint obstruct the interpretation of measured data , and unique statements can not always be derived. The emperically found isotope effect, however, seems to be an invariant effect of very fundamental importance. As the gyro radius increases with the ion mass, the transport across the magnetic field is exspected to inhance in the case of deuterium; this can certainly not explain the observed isotope effect. In particular the isotope dependence of τ_E is also present in regimes dominated by electron transport. Other, probably more subtle explanations have to be found.

References : /1/ O. Klüber, H.Murmann IPP report III/72 -198
/2/ A.Stäbler, F.Wagner 4th Int. Sympos. of Heating, Rome 1984

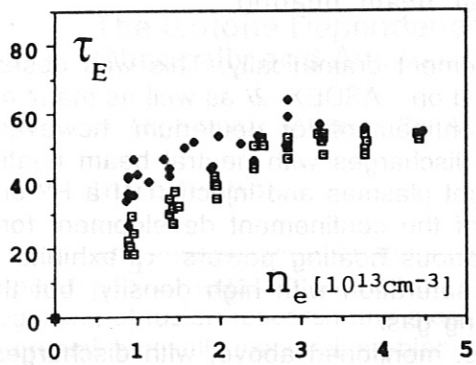

Fig 1. Energy confinement time τ_E vs. line averaged density n_e.
Hydrogen, ohmic heating, divertor plasma.
▫ $2 < q_a < 3$; ◆ $4 < q_a < 5$;

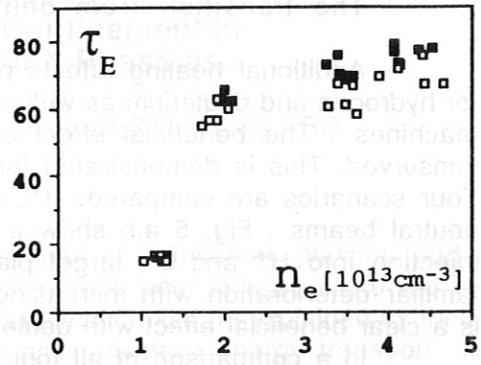

Fig. 2. Energy confinement time τ_E vs. n_e for the transition of H^+ to D^+ for a ohmically heated plasma within 10 shots.
open symb: last hydrogen discharge and beginning of transition
solid symbols: 5th to 10th shot in D_2

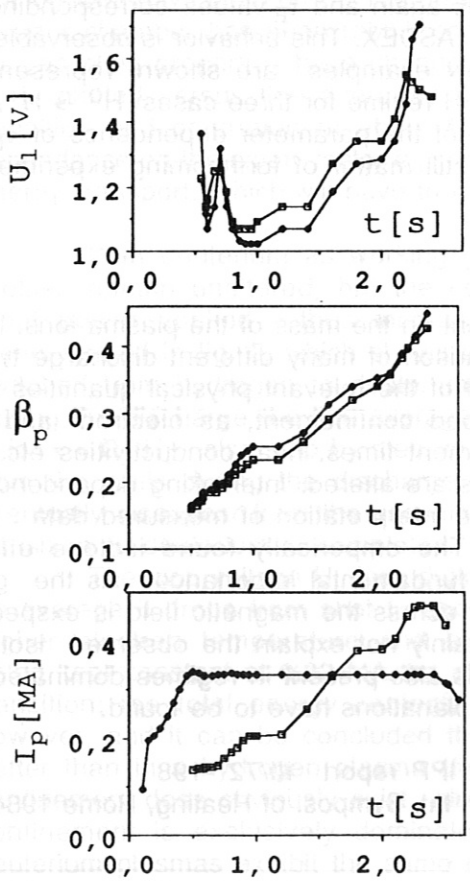

Fig. 3a. Loop voltage U_l vs. time for two ohmically heated discharges, while the line averaged density is being stepped up. Transition from H_2 to D_2 within 10 discharges :
-⊡- Hydrogen (shot 22474)
-◆- deuterium (shot 22483)
Ip = 320 kA ; Bt = 2,2 T for all discharges.

Fig. 3b. Beta poloidal β_p vs. time for the same shots as in fig. 3a. During the transition to deuterium the thermal energy rises although the input power is reduced.

Fig 4.: (shot 22475-22483): line averaged density and plasma current vs time.

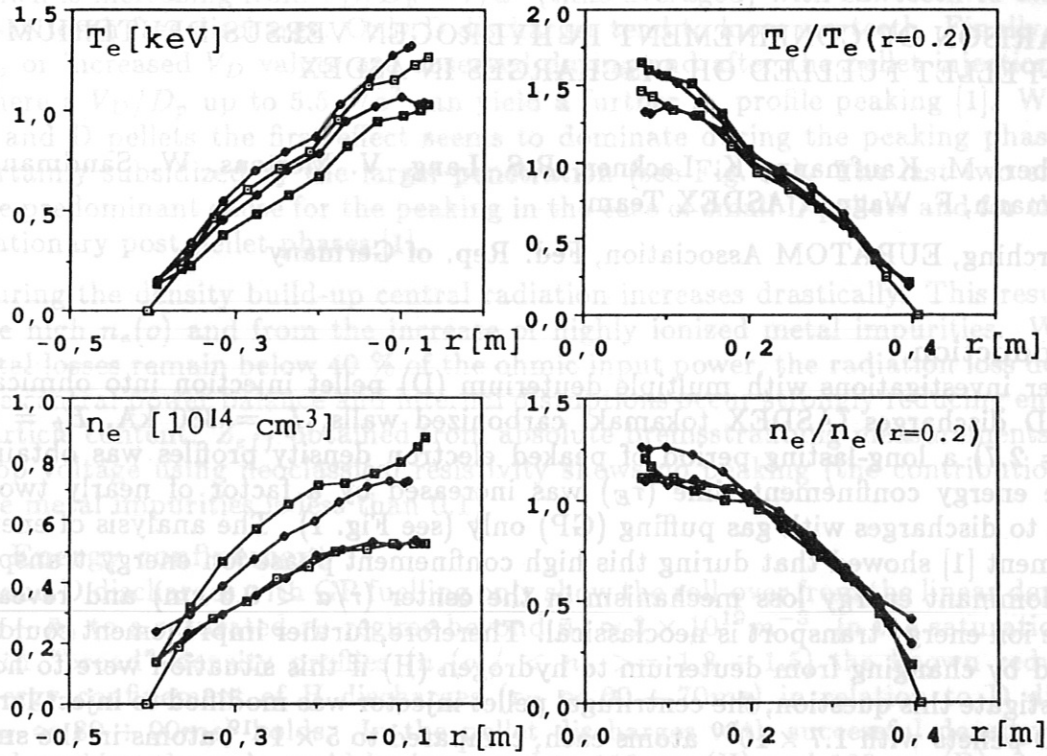

Fig. 6: Thomson scattering measurement of electron temperature Te- and density ne for four neutral injection heating scenarios:

- injection of H^0 into a H^+ plasma,
- injection of D^0 into a H^+ plasma,
- injection of H^0 into a D^+ plasma,
- injection of D^0 into a D^+ plasma;

(6a) T_e of a flux tube versus it's radius , (6b) T_e normalized at half radius,

(6c) n_e vs. flux tube radius , (6d) n_e normalized at half radius.

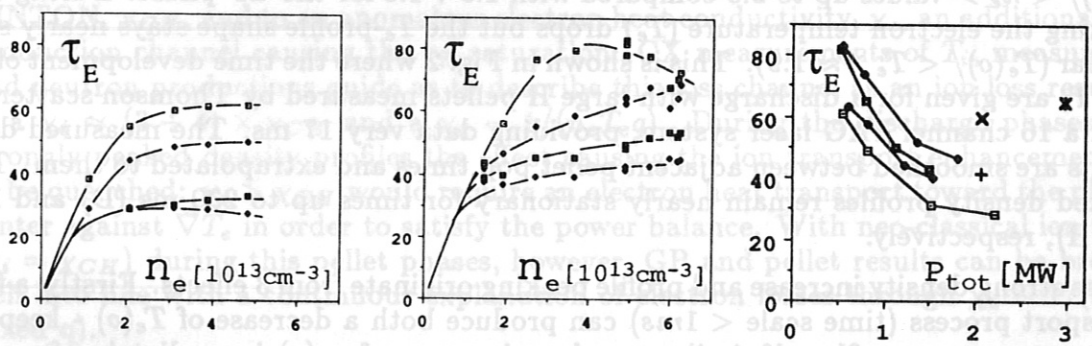

Fig. 5 : Energy confinement time τ_E vs. line averaged density n_e for ohmic heating and various neutral injection powers :

(a) hydrogen injection into a hydrogen target plasma ; ▫ = OH ; ▪ =2 sources

(b) Hyrdogen injection into a dueterium target plasma; ● = 1 source ; ◆ =4 sources

(c) τ_E versus the total heating power (OH and NI) ; symbols as in fig. 6;

transition to the H-regime: + H^0->H^+; × H^0->D^+; ⧓ D^0->D^+;

COMPARISON OF CONFINEMENT IN HYDROGEN VERSUS DEUTERIUM IN MULTI-PELLET FUELLED OH DISCHARGES IN ASDEX

O. Gruber, M. Kaufmann, K. Lackner, R.S. Lang, V. Mertens, W. Sandmann, H. Murmann, F. Wagner, ASDEX Team

IPP Garching, EURATOM Association, Fed. Rep. of Germany

1. Introduction

In earlier investigations with multiple deuterium (D) pellet injection into ohmically heated D discharges (ASDEX tokamak, carbonized walls, $I_p = 380$ kA, $B_t = 2.2$ T, $q^* = 2.7$) a long-lasting period of peaked electron density profiles was obtained and the energy confinement time (τ_E) was increased by a factor of nearly two in relation to discharges with gas puffing (GP) only (see Fig. 1). The analysis of energy confinement [1] showed that during this high confinement phase ion energy transport is the dominant energy loss mechanism in the center ($r/a < 0.6$ cm) and revealed that the ion energy transport is neoclassical. Therefore, further improvement could be expected by changing from deuterium to hydrogen (H) if this situation were to hold. To investigate this question, the centrifugal pellet injector was modified to inject larger H and D pellets with 1.7×10^{20} atoms each, compared to 5×10^{19} atoms in the small D pellets. At the same velocity of 600 m/s the typical penetration depths increased from $20 \div 25$ cm (small pellets) to $30 \div 35$ cm (large pellets). We describe first the density build-up and particle transport and then we compare the bulk plasma energy transport of both H and D pellet refuelled discharges.

2. Density build-up and bulk plasma particle transport

With both D and H pellet injection a strong increase of the line-averaged ($\bar{n}_e$ up to $1.2 \times 10^{20} m^{-3}$) and volume-averaged ($< n_e >$ up to $8.5 \times 10^{20} m^{-3}$) densities could be obtained. This is accompanied by a strong peaking of the density profiles with $n_e(o)/ < n_e >$-values up to 2.5 compared with $1.3 \div 1.5$ for the GP phase. During this peaking the electron temperature (T_e) drops but the T_e-profile shape stays nearly self-similar ($T_e(o)/ < T_e > \approx 1.9$). This is shown in Fig. 2 where the time development of n_e and T_e are given for a discharge with large H pellets measured by Thomson scattering with a 16 channel YAG laser system, providing data very 17 ms. The measured data points are smoothed between adjacent pellet pop times and extrapolated to them. The peaked density profiles remain nearly stationary for times up to 230 ms (D) and 150 ms (H), respectively.

These strong density increase and profile peaking originate from 3 effects. Firstly, a fast transport process (time scale $< 1ms$) can produce both a decrease of $T_e(o)$ - keeping the temperature profile self-similar - and an increase of $n_e(o)$ immediately after the pellet injection despite of the penetration depth being smaller than the plasma radius a. Secondly, reduced sawtooth activity leads to a n_e-profile peaking due to the omission of an instantaneous particle outward flow during a sawtooth disruption. From the nearly

stationary and source-free density profiles of GP D plasmas one can deduce the ratio of an inward velocity V_D and the particle diffusion coefficient D_p by $V_D/D_p = -dn/dr/n$ which is increasing from $V_D/D_p = r/a^2$ (time averaged) with sawteeth to 3.5 r/a^2 in a sawtooth free discharge. Only D discharges tend to loose sawteeth. Finally, reduced D_p or increased V_D values are observed during and after the pellet injection phases, where a V_D/D_p up to 5.5 r/a^2 can yield a further n_e profile peaking [1]. With large H and D pellets the first effect seems to dominate during the peaking phase, but is certainly subsidized by the larger penetration (see Fig. 2a). The last two effects are the predominant cause for the peaking in the case of small D pellets and for the nearly stationary post pellet phases [1].

During the density build-up central radiation increases drastically. This results from the high $n_e(o)$ and from the increase of highly ionized metal impurities. While the total losses remain below 40 % of the ohmic input power, the radiation loss dominates the central power balance and internal disruptions occur strongly reducing energy and particle content. Z_{eff} obtained from absolute bremsstrahlung measurements and the loop voltage using neoclassical resistivity shows no peaking (the contribution due to the metal impurities is less than 0.1).

3. Energy confinement

H and D discharges with GP fuelling only show the roll-over from the linear dependence $\tau_E \sim \bar{n}_e$ to a saturated τ_E regime beyond $\bar{n}_e \approx 3 \times 10^{19} m^{-3}$. In the saturation region with "broad" density profiles ($n_e(o)/ < n_e >= 1.3 \div 1.5$) the known reduction of energy confinement of H discharges ($\tau_E \approx 60 \div 70ms$) in relation to D discharges ($\tau_E \approx 80 \div 90ms$) holds. In the pellet discharges with successful density build-up and peaking the τ_E's could be improved to 110 ms (H) and 160 ms (D) at the same discharge conditions (see Fig. 1).

This suggests that the pellets remove the reason for the roll-over which can be explained by two alternatives. A profile consistency picture with fixed $T_e(r)/T_e(o)$ depending only on q yields a τ_E saturation in GP discharges from a decrease of $T_e(o)$ and an increase of ohmic dissipation, whereas the pellet discharges gain in τ_E due to a more favourable weighting of $T_e(r)/T_e(o)$ with the high $n_e(o)$ values [1]. A "local" model for conductive energy transport was investigated with the TRANSP code. To describe the τ_E saturation we have to add to the neo-classical ion energy losses as given by CHANG-HINTON, χ_{CH}, and to an anomalous electron heat conductivity, χ_e, an additional heat conduction channel causing the τ_E saturation. CX measurements of T_i, measured β_p and neutron productions guide as to describe this loss channel as an ion loss resulting in a $\chi_i \approx (3 \div 4) \times \chi_{CH}$ and a $\chi_e \sim 1/(n_e T_e q)$. During the discharge phases with strongly peaked density profiles the effect causing the ion transport enhancement has to be quenched: $\chi_i > \chi_{CH}$ would require an electron heat transport toward the plasma center against ∇T_e in order to satisfy the power balance. With neo-classical ion losses ($\chi_i = \chi_{CH}$) during this pellet phases, however, GP and pellet results can be brought well into line with a continuous explanation of electron losses through $\chi_e \sim 1/(n_e T_e)$ (fixed q).

The Alcator team has suggested first to attribute this additional ion loss to the ion temperature gradient mode triggered when the criterion $\eta_i = dlnT_i/dlnn_i = L_{n_i}/L_{T_i} > 1.5$ is fulfilled [2]. Figure 3a shows that due to the n_e peaking $\eta_i \approx \eta_e$ ($T_i \approx T_e$ at high $\bar{n}_e$)

decreases from above 1.8 at all radii in the GP phase to values below 1 over a large part of the plasma cross-section. Using a $\chi_i = \chi_{CH} + \chi_{\eta i}$ with $\chi_{\eta i} = 0$ for $\eta_i < 1$ and fully developed for $\eta_i \geq 1.8$ [3] the time development given in Fig. 3c for the i and e heat diffusivities at r/a = 2/3 of a H pellet discharge are obtained. While χ_e is only slightly decreasing with time, χ_i drops immediately after the first pellet from $(3 \div 4)\chi_{NC}$ to χ_{NC}. This model assumption is further supported by two facts. τ_E is at once improved when already the first pellet reduces η_i to 1 (as is the case given in Fig. 3), but is only gradually rising when the n_e-peaking and η_i reduction occur more slowly which happens especially with small pellets. Secondly the confinement improvement is only marginal when the $\eta_i < 1$ region is small.

The neoclassical ion loss in the high confinement pellet regime accounts still for the major part of the total non-radiated power flow within half the plasma radius. But the global energy confinement is governed by the anomalous electron heat transport in the outer plasma region with $\chi_e >> \chi_i$. As χ_{NC} is the upper bound for χ_i one can calculate the radial dependence of χ_e. Figure 4 compares χ_{CH} and χ_e both for a H and D post pellet phase at the same $q^* = 2.7$, having about equal T_e profiles and the same n_e profile shape. The χ_i's differ by the $\chi_{NC} \sim \sqrt{A_i}$ dependence (ion mass A_i), whereas $\chi_e(H)$ clearly exceeds $\chi_e(D)$. Taking into account the higher density of the D discharge a $\chi_e \sim A_i^{-\alpha}$ with $\alpha = 0.3 \div 0.7$ can be extracted; explaining also the inferior energy confinement times of H pellet discharges.

4. Summary

H and D ohmic heated pellet discharges show a density build-up (beyond the GP density limit) with strongly peaked n_e profiles $(n_e(o)/ < n_e > \leq 2.5)$. They show in parallel a remarkable improvement of energy confinement by nearly a factor of two. With these peaked density profiles χ_i is restricted to χ_{CH}. This allows a determination of $\chi_e \sim A_i^{-\alpha} (\alpha \approx 0.5)$ dominating the global energy confinement and reducing $\tau_E(D) \approx$ 160 ms to $\tau_E(H) \approx 110$ ms.

References

[1] M. Kaufmann, et al., IPP-Report 1/242, to be published in Nucl. Fusion.

[2] G.S. Lee, P.H. Diamond, Phys. Fluids **29**, 3291 (1986).

[3] O. Gruber, et al., this conference.

Figure Captions

Fig. 1: Energy confinement time τ_E vs. $\bar{n}_e$ for GP (points) and pellet fuelled hydrogen (H) and deuterium (D) single ohmic discharges.

Fig. 2: Axial (r=o) and volume averaged (<>) n_e and T_e vs. time for a hydrogen pellet discharge (points are measured by Thomson scattering).

Fig. 3: a) $\eta_e = dlnT_e/dlnn_e$ at three radial positions,
b) τ_E, electron (τ_{Ee}) and ion (τ_{Ei}) confinement times and
c) χ_e, χ_i and χ_{CH} at r/a = 2/3 as a function of time for the discharge of Fig. 2.

Fig. 4: Radial dependence of χ_e and χ_i during post-pellet phase of a H and D ohmic discharge.

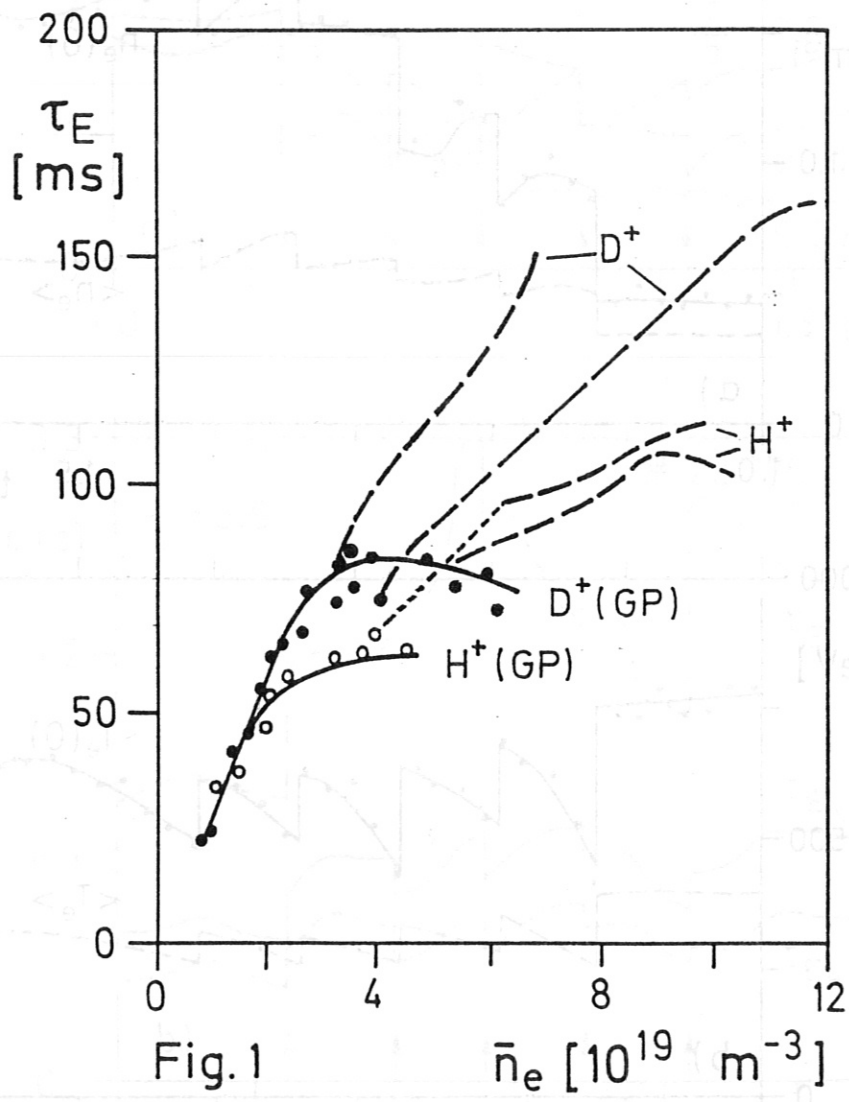

Fig. 1

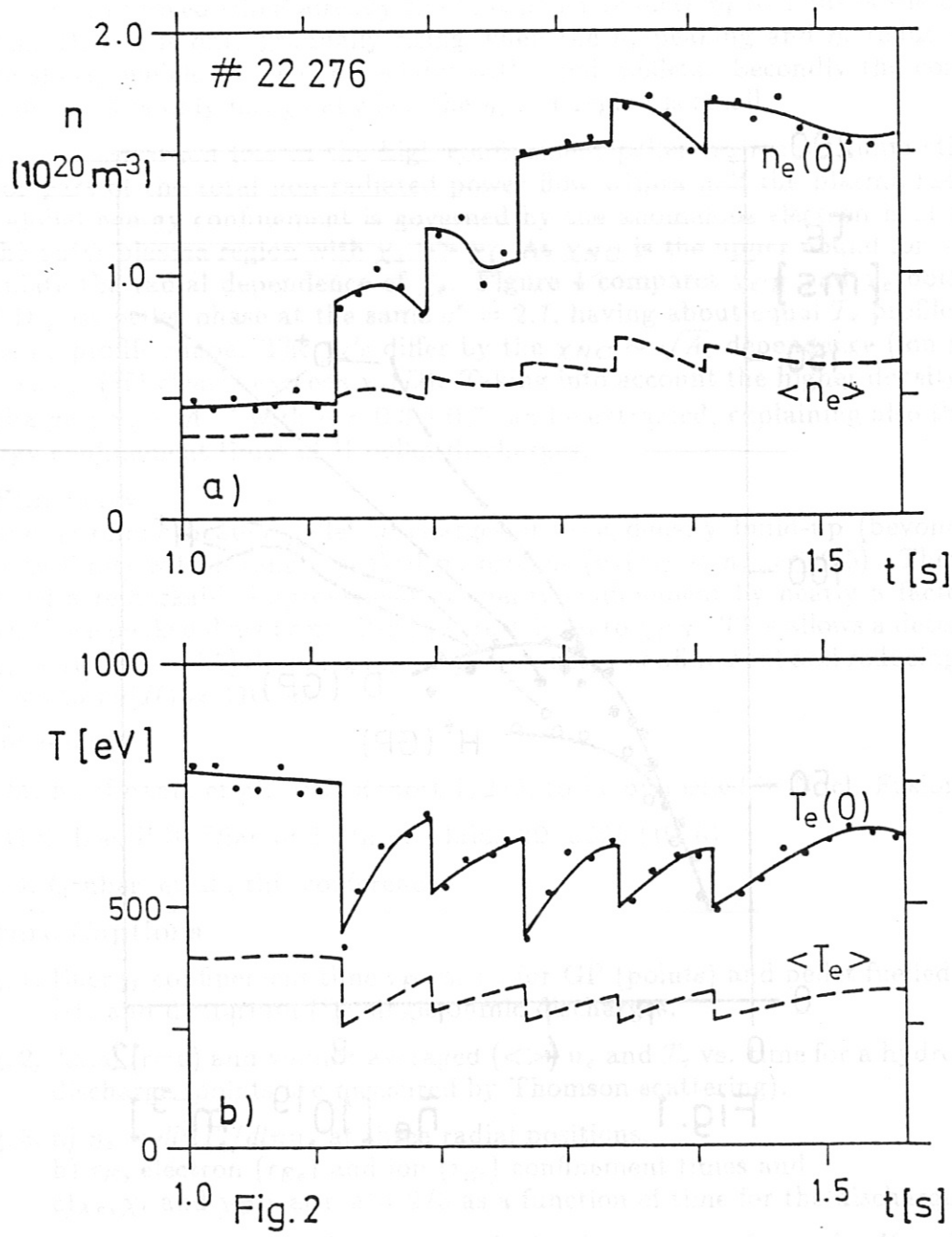
2.0
22 276
n
[10^20 m^-3]
1.0
0
n_e(0)
<n_e>
a)
1.0
1.5
t [s]
1000
T [eV]
500
0
T_e(0)
<T_e>
b)
1.0
1.5
t [s]

Fig. 2

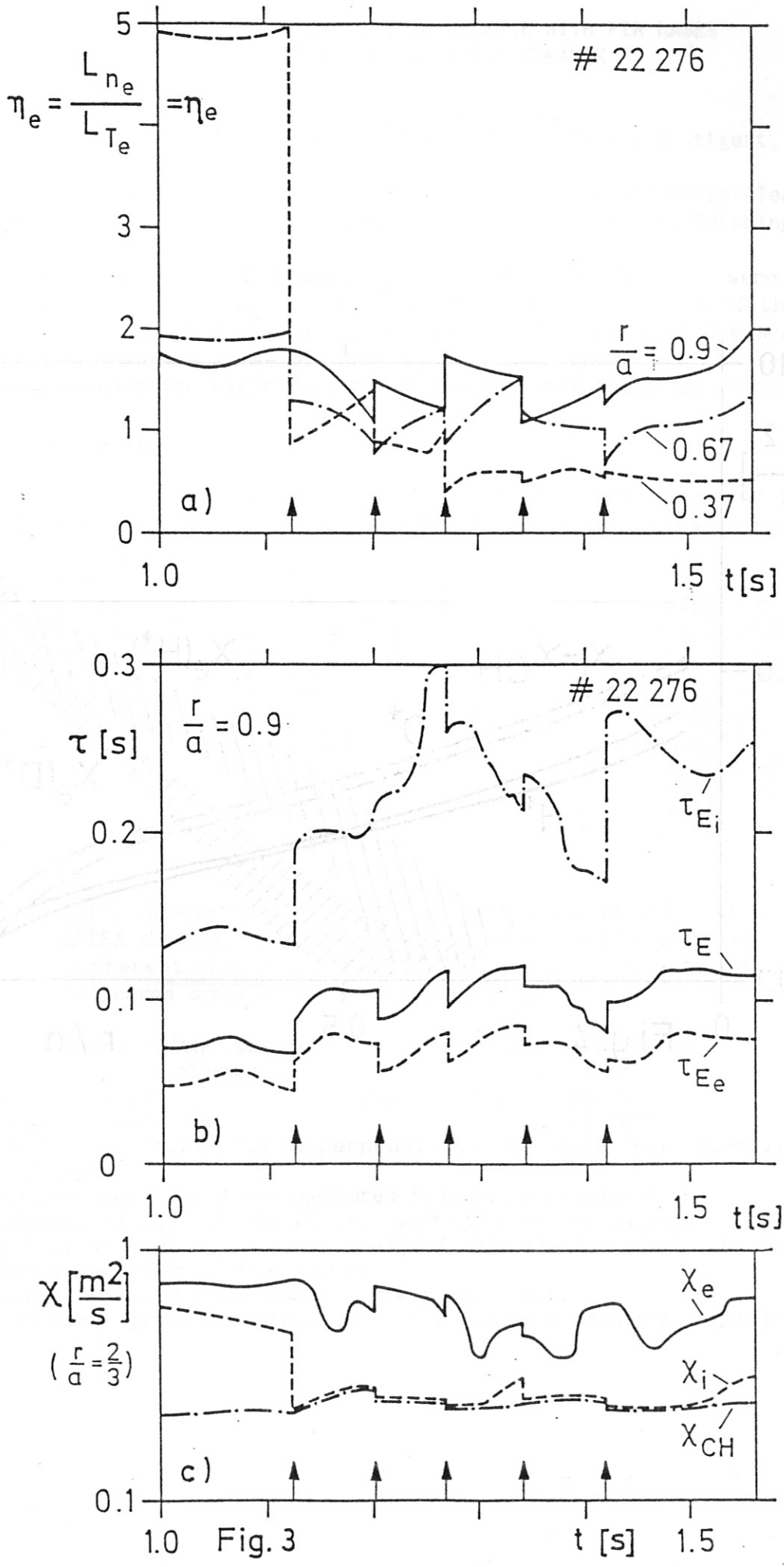
$\eta_e = \frac{L_{n_e}}{L_{T_e}} = \eta_e$
22 276
$\frac{r}{a} = 0.9$
0.67
0.37
a)
t [s]
τ [s]
$\frac{r}{a} = 0.9$
τ_{E_i}
τ_E
τ_{E_e}
b)
$\chi \left[\frac{m^2}{s}\right]$
$(\frac{r}{a} = \frac{2}{3})$
χ_e
χ_i
χ_{CH}
c)

Fig. 3

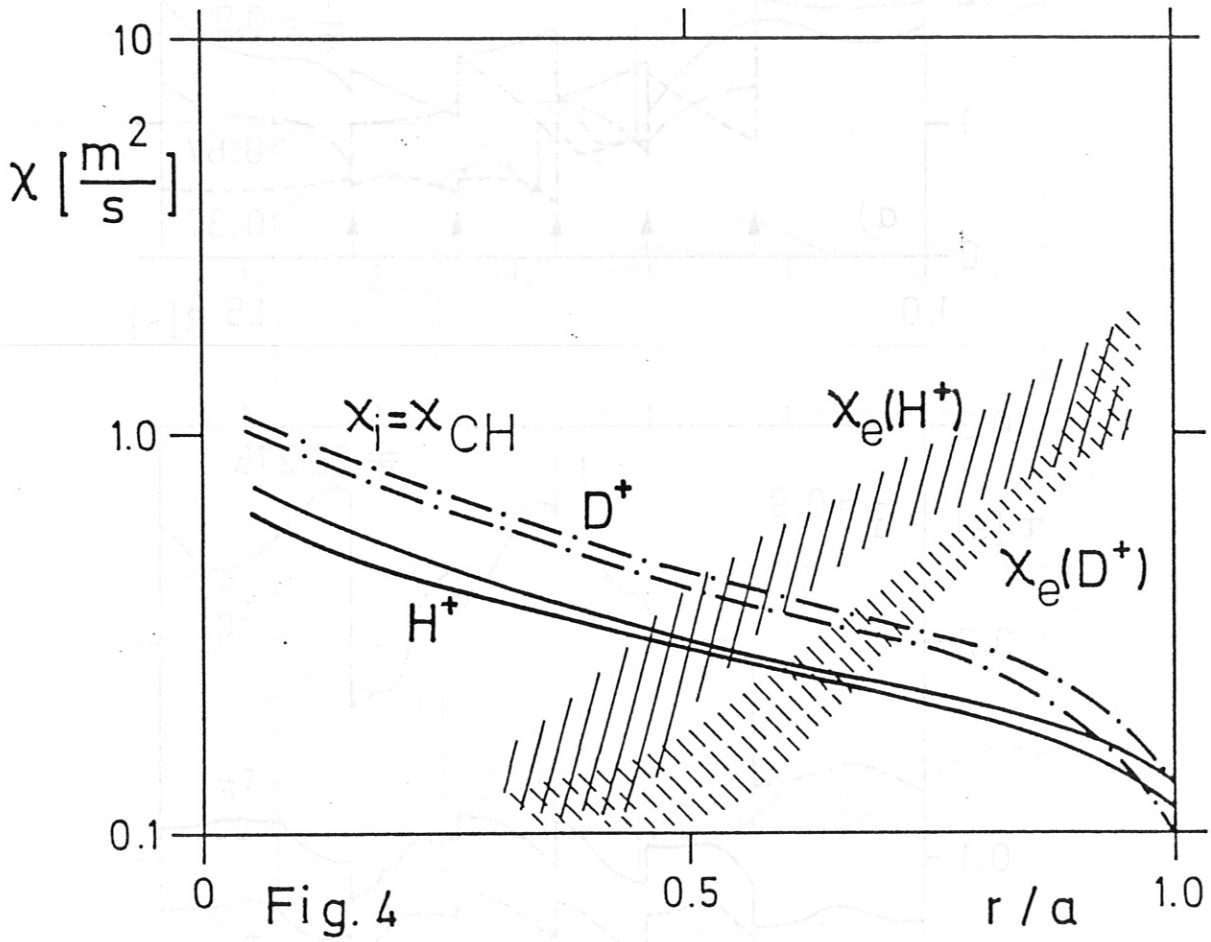

Fig. 4

MEASUREMENTS OF DENSITY TURBULENCE WITH FIR LASER SCATTERING IN THE ASDEX TOKAMAK

G. Dodel and E. Holzhauer
Institut für Plasmaforschung, Universität Stuttgart, Stuttgart, FRG

H. Niedermeyer, K. McCormick, ASDEX-, ICRH-, NI- and Pellet-Teams
Max-Planck-Institut für Plasmaphysik, EURATOM Association, Garching, FRG

Previous measurements of density turbulence in ASDEX [1], [2] were limited to a wavenumber range $k_\perp > 5\ cm^{-1}$ and to distances ≤ 21 cm of the measuring chords from the plasma centre. After modification of the scattering system the important range of lower $k_\perp$ and the region near the separatrix are now accessible. First results of the investigations are presented.

Scattering system:

The scattering system using a 100 mW, 119 µm CW CH_3OH laser and homodyne detection with a Schottky diode is shown in a schematic view in Fig.1.

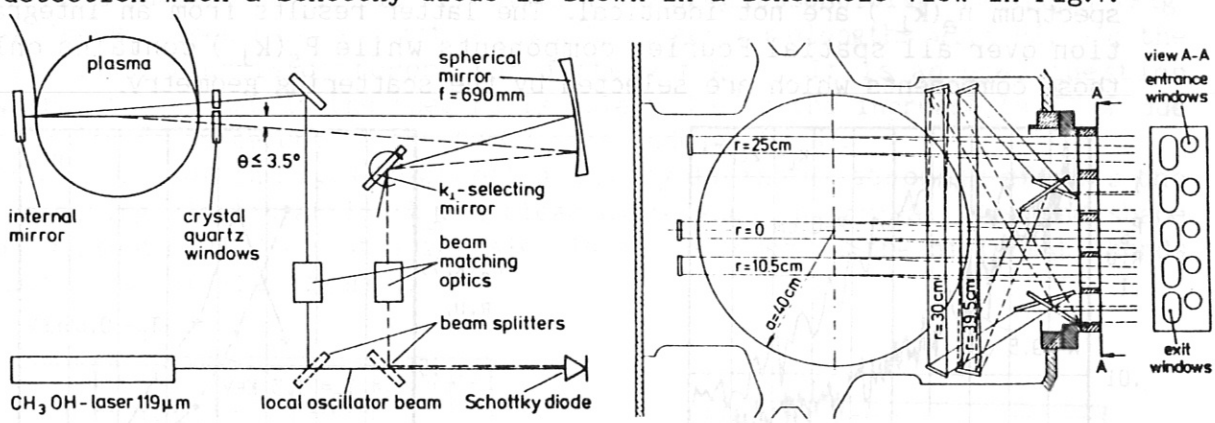

Fig. 1 Left: Schematic of the optical setup. Right: Poloidal section of ASDEX showing the beam paths inside the plasma vessel for the different chords and the window array. The scattered beams are indicated schematically by dashed lines.

The parameters of the scattering experiment are as follows:
beam waist in the plasma: $w_o = 1.6$ cm
wavenumber range: $2.5\ cm^{-1} \lesssim k_\perp < 25\ cm^{-1}$
wavenumber resolution: $\pm 1.25\ cm^{-1}$
spatial resolution: ± 1.6 cm perpendicular to beam, chord averaged along line of sight
Accessible chords (distance measured from plasma center):
horizontal: 0 cm, 10.5 cm, 25 cm; vertical: 33 cm, 39.5 cm
frequency analysis: spectrum analyser with fixed channels and continuous frequency sweeps in plateau phases
wavenumber scan: possible within one plasma shot.
spatial scan: different measuring chords can be chosen from shot to shot.

Ohmic discharges: Evidence for driftwave nature of the turbulence.

The following findings on ASDEX are consistent with the assumption of density gradient driven driftwave turbulence:

a) The rms value of the frequency integrated scattered power scales linearly with the mean electron density if the relative density profiles remain fairly similar. This was established for $n_e < 5 \times 10^{13}$ cm^{-3} (where $\tau_E \propto n_e$ in ASDEX) in the important $k_\perp$ range and in different chords.

b) In the central chord which sees primarily poloidally propagating fluctuations a maximum of the scattered power is observed around ~100 kHz in the dominant $k_\perp$ range. This is on the order of the diamagnetic drift frequency evaluated in the gradient region of the discharge. In the outer vertical chord which sees predominantly radially propagating fluctuations the frequency spectra are significantly narrower (Fig. 2).

c) The maximum of the frequency integrated $k_\perp$ spectrum shifts towards lower $k_\perp$ with increasing T_e (Fig. 3). A value $k_\perp^{max} \cdot \varrho_s \approx 0.3$ is inferred from the "cold" shots in Fig. 3. It should be kept in mind, however, that the shape of $P_s(k_\perp)$ and the shape of the fluctuation spectrum $n_e(k_\perp)$ are not identical. The latter results from an integration over all spatial Fourier components while $P_s(k_\perp)$ contains only those components which are selected by the scattering geometry.

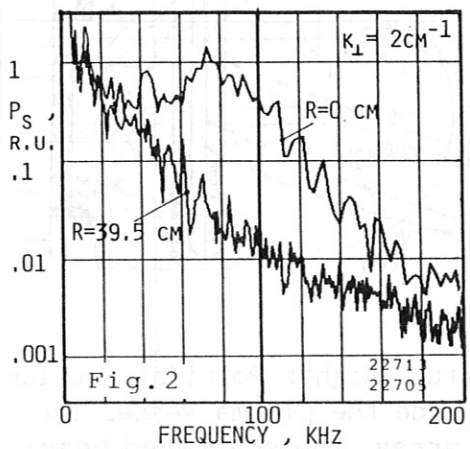

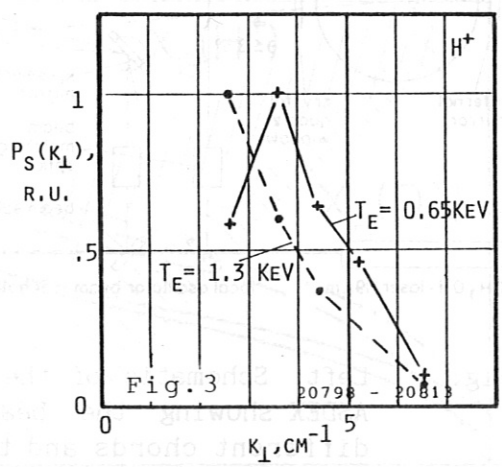

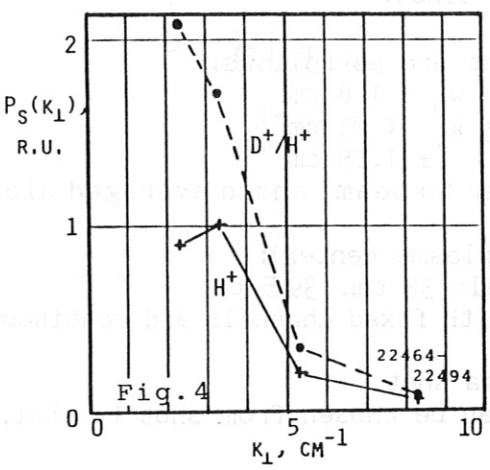

Fig.2: Frequency spectra of scattered power in the central horizontal chord and outer vertical chord (D^+ plasma)

Fig.3: Wavenumber spectra in "hot" and "cold" ohmic hydrogen plasmas. The densities in the center are 1.75×10^{13} cm^{-3} and 4.8×10^{13} cm^{-3}, respectively. Signals are normalized to maximum value. Chord 10.5 cm.

Fig.4: Change of wavenumber spectra with gas filling. Note: Same vertical scale for both curves.

d) The maximum of the frequency integrated $k_\perp$ spectrum shifts towards lower $k_\perp$ and its value increases when the gas filling is changed from pure hydrogen to a ≈1:1 mixture of hydrogen and deuterium at constant electron density (Fig. 4).
e) The frequency and wavenumber integrated scattered power decreases with increasing toroidal magnetic field at constant plasma current.

A detailed analysis is beyond the scope of this summary. It should be noted that unambiguous experimental tests of theoretical models for drift wave turbulence would require pure one-parameter scans which in general are difficult to realize.

L-phase with neutral beam injection (NI):

NI heating produces complex changes of the density turbulence. A dramatic broadening of the frequency spectra with respect to the ohmic phase occurs as is illustrated in Fig. 5. The temporal development of the frequency integrated scattering signal was recorded at the transition from an ohmic to an L-phase, the density profiles remaining essentially unchanged (Fig. 6). The $k_\perp$ spectrum is shifted towards longer wavelengths with NI, and the time behaviour is different for different $k_\perp$. It is an open question wether the change in the spectra is solely due to the increase in T_e or due to a change in nature of the turbulence induced by NI.
As can be seen in Fig. 6 sawtooth activity during NI strongly affects the scattering signals at low $k_\perp$. A clear difference in arrival time and shape of sawteeth on the scattering signals is observed in the different chords (not shown in the figure).

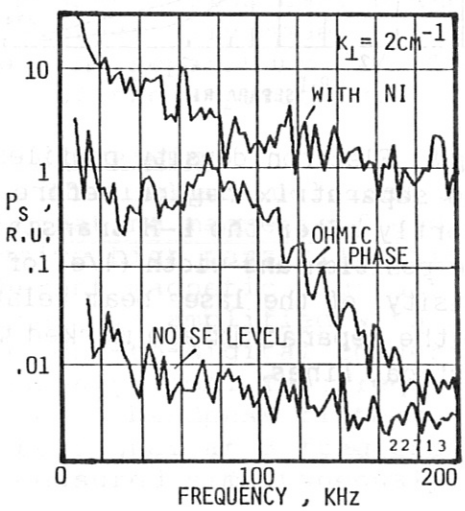

Fig.5: Change of frequency spectra with NI-heating (L-shot; chord 0 cm)

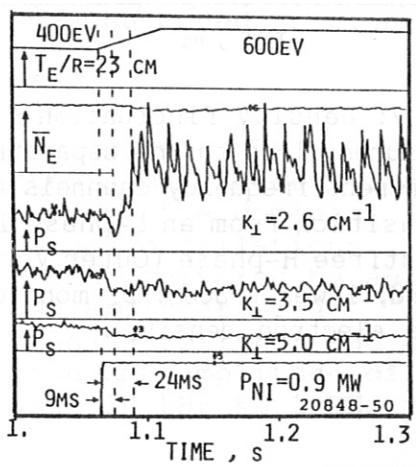

Fig.6: Change of frequency integrated scattering signals for different $k_\perp$ in a series of identical L-shots.

Transition from the L into the burst-free H-phase.

By shifting the horizontal plasma position by a few cm the region inside and outside the separatrix can be scanned with the outer vertical chord. In a series of L-H transitions the behaviour of the fluctuations was investigated at distances of~0.5 cm outside and ~1 cm inside the separatrix. In both cases the scattering signals decrease sharply at the time of the transition (Fig. 7). This behaviour cannot be explained by a drop in density and/or decrease in the density gradient length, as can be seen from Fig. 8. It shows the density profiles obtained from the Li beam probe before and after the transition as well as the position and radial extent of the FIR laser beam with respect to the separatrix radius r_s.

Further investigations are necessary in order to obtain a conclusive picture of the fluctuation behaviour at the L-H transition.

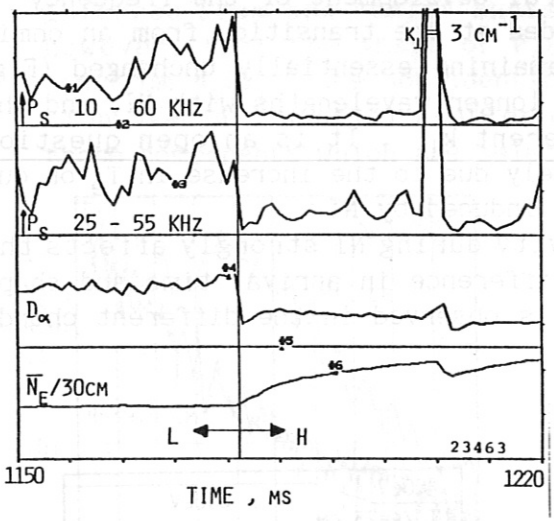

Fig.7: Density fluctuation signals measured close to the separatrix in different frequency channels at the transition from an L-phase into a burstfree H-phase (Outer vertical chord; lower traces: D_α monitor and line electron density).

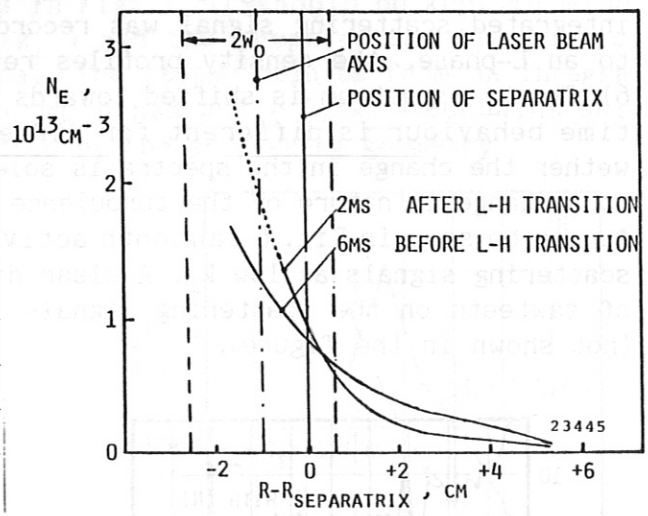

Fig.8: Electron density profiles in the separatrix region before and shortly after the L-H transition. The position and width ($1/e^2$ of intensity) of the laser beam relative to the separatrix are marked with vertical lines.

References

[1] G. Dodel, E. Holzhauer, J. Massig, J. Gernhardt, ASDEX-, ICRH-, LH-, NI- and Pellet Teams, 14th European Conference on Controlled Fusion and Plasma Physics, Madrid, June 1987, Europhys. Conf. Abstr. 11D, I, p. 249

[2] G. Dodel, E. Holzhauer, ASDEX- and NI-Teams, 3rd Int. Symp. on Laser-Aided Plasma Diagnostics, Los Angeles, Oct. 1987, Proceedings p. 146.

RADIAL DECAY OF BROADBAND MAGNETIC FLUCTUATIONS IN ASDEX

L. Giannone, E. Holzhauer* and J. Gernhardt

Max Planck Institut für Plamsaphysik,
Garching, F. R. G.

* Institut für Plasmaforschung,
Universität Stuttgart, F.R.G

1. INTRODUCTION

A new magnetic probe system, consisting of coils mounted on a pneumatically driven manipulator, has been installed on ASDEX. The manipulator may be scanned through a distance of 8 cm in the radial direction within 150 ms. This system then possesses the capability of obtaining measurements of the radial decay of broadband magnetic fluctuations at a single poloidal location /1/. Other experiments have used coils positioned at different poloidal locations and measured the radial decay by plotting the fluctuation amplitude as a function of the radial position of each coil /2,3/.Measurements of magnetic fluctuation amplitude during L and H transitions were previously made by coils located at a distance of 14 cm from the separatrix /4/. The new coils may be moved to within 4 cm of the separatrix.

2. EXPERIMENT

The radial, poloidal and toroidal components of the fluctuating magnetic field may be detected simultaneously. A passive high pass filter is used to attenuate the dominant coherent magnetic fluctuations due to Mirnov oscillations. The signal is amplified with a gain of 200 and monitored by an analogue-to-digital converter, a spectrum analyser or a frequency comb. The frequency comb contains a splitter and a set of 8 bandpass filters. This allows the RMS amplitude of the probe signal at 8 frequencies in the range 30 kHz to 1 MHz to be measured simultaneously.

The signal-to-noise ratio at distance of 4 cm from the separatrix is greater than 20 dB up to a frequency of 1 MHz for the radial and poloidal components in Ohmic discharges. At low frequencies the toroidal component is smaller than the poloidal and radial components, while at higher frequencies they are of comparable magnitude. In ASDEX, the measured poloidal field contains a component generated by switching noise on the

multipole and vertical field coils. Radial profiles of the fluctuation amplitude of the radial component were therefore studied.

The radial decay of broadband magnetic fluctuations was measured by scanning the coils through a distance of 8 cm. The probe starts 12 cm away from the separatrix, moves to within 4 cm of the separatrix and returns (see Fig. 1). The closest distance to the separatrix was determined by observed increases in the hard x-ray flux, which resulted from runaway electron collisions with the probe. Ohmically heated and neutral beam heated plasmas with various values of magnetic field and plasma current have been studied.

The poloidal mode number, m, has been inferred from the radial decay of the magnetic fluctuation amplitude, since in a current free region the amplitude decreases as $r^{-(m+1)}$ in cylindrical geometry /2,3/. This implicitly assumes that the conducting wall is positioned at an infinite distance from the plasma and that the toroidal wavelength is infinite ($k_z = 0$). A plot of the logarithm of the amplitude versus the logarithm of the minor radial positon was used to find m. The decay of magnetic fluctuation amplitude in the presence of a conducting wall at a finite distance from the plasma with $k_z \neq 0$ has been considered /5/. The expected radial decay for a single mode may be expressed in terms of modified Bessel functions. With the conducting wall on ASDEX at r = 61 cm and the separatrix at r = 40 cm, it was found that the m number was overestimated, when the effect of the conducting wall and finite k_z were ignored.

Modes with the lowest m predominate when a number of modes with different m are unstable, because of the strong dependence of the radial decay on m. From these measurements of the radial decay of broadband magnetic fluctuations, it is found that $m \leq 8$ on ASDEX. This value is consistent with those observed in other experiments /1-3/.

3. THEORY

The identification of the plasma instability responsible for the generation of broadband magnetic fluctuations and the extent to which magnetic fluctuations cause anomalous electon transport are important topics in fusion research. It has been suggested that broadband magnetic fluctuations are due to microtearing modes /2,6/. These modes are high m temperature gradient driven tearing modes.

Calculations concerning the linear instability of microtearing modes in ASDEX, show that modes with $m \leq 10$ may be unstable for typical discharge conditions /7/. In Ohmic discharges the unstable modes are located at radial positions

inside of half the plasma minor radius, while in neutral beam heated plasmas the most unstable modes are located closer to the plasma boundary (see Fig. 3). This result suggests that the enhanced magnetic fluctuation level measured in neutral beam heated plasmas /4/ may be partly due to a change in the position of the unstable modes, and this should be taken into account in those experiments considering the scaling of the inverse of confinement time, τ_E^{-1}, with broadband magnetic fluctuation amplitude /8/.

4. CONCLUSION

For ASDEX plasma parameters, experimental observations and theoretical calculations suggest that the microtearing mode remains as a candidate for the plasma instability which is responsible for the generation of the broadband magnetic fluctuations.

Further work is required to apply a more sophisticated theory which describes the non-linear and toroidal coupling of different modes and the saturation of each mode to the experiment. In the linear theory each mode generates fluctuations at a frequency determined by the plasma parameters. A broadband spectrum is produced as a result of the non-linear and toroidal coupling of modes that are located at different radial positions within the plasma.

/1/ F. Ryter, A. Pochelon and F. Hoffmann,
14th European Conference on Controlled Fusion and Plasma Physics, Madrid, Vol. I, 265, 1987.

/2/ N. Ohyabu et al.,
Phys. Rev. Lett., 58, 120, 1987

/3/ M. Malacarne et al.,
JET Report, JET-P(87) 22.

/4/ G. Dodel, E.Holzhauer and J.Massig,
14th European Conference on Controlled Fusion and Plasma Physics, Madrid, Vol. I, 249, 1987.

/5/ G.Bateman,
"MHD Instabilities", p.111,
MIT Press, 1978.

/6/ J.F. Drake and Y.C. Lee,
Phys. Fluids, 20, 1347, 1977.

/7/ L.Giannone,
"Linear stability of microtearing modes in ASDEX",
IPP Report, IPP III-125, 1987.

/8/ M. Malacarne and P.A. Duperrex,
JET Report, JET-P(87) 26.

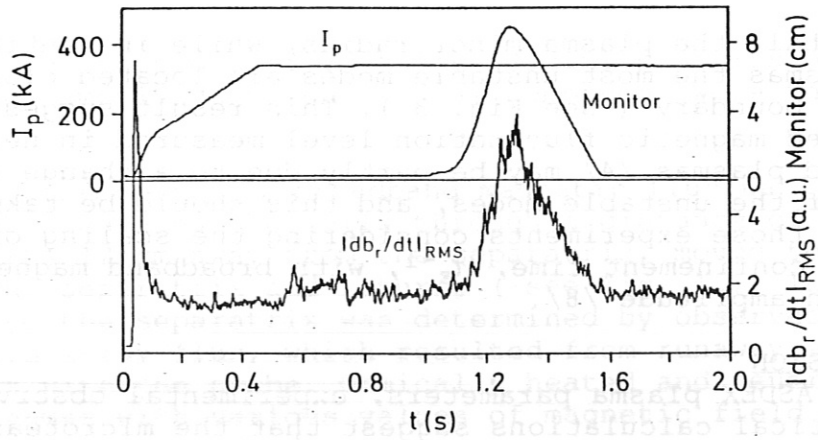

Fig. 1

Fig. 1 The movement of the manipulator is monitored and the radial profile of the RMS amplitude of $\delta b_r/dt$ is measured at f = 82 kHz in an Ohmic discharge with B = 1.85 T and I_p = 320 kA. The bandpass filter has $\Delta f/f$ = 0.1.

Fig. 2 Radial decay of broadband magnetic fluctuation amplitude as a function of frequency for an Ohmic discharge. A plot of the logarithm of the amplitude versus the logarithm of the minor radial position yields the poloidal mode number, m. The presence of the conducting wall needs to be taken into account.

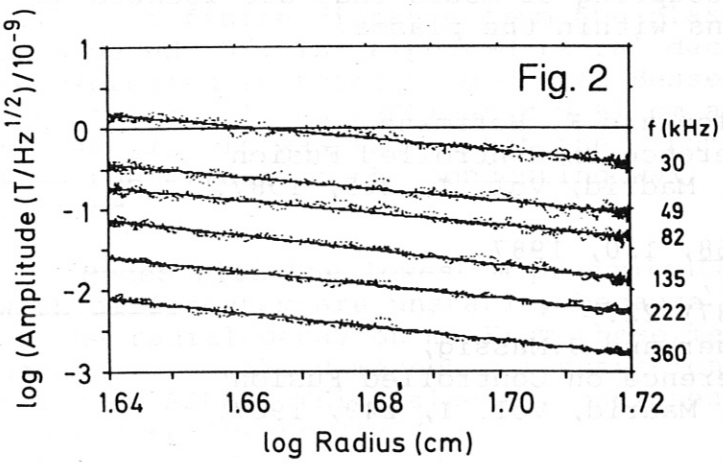

Fig. 3 Microtearing mode stability in a plasma with B = 1.85 T and I_p = 320 kA. The imaginary part of the eigenvalue, γ, versus normalised radius for an Ohmic discharge is plotted in Fig. 3(a) and for a discharge with neutral beam injection in Fig. 3(b). The mode is unstable when $\gamma > 0$.

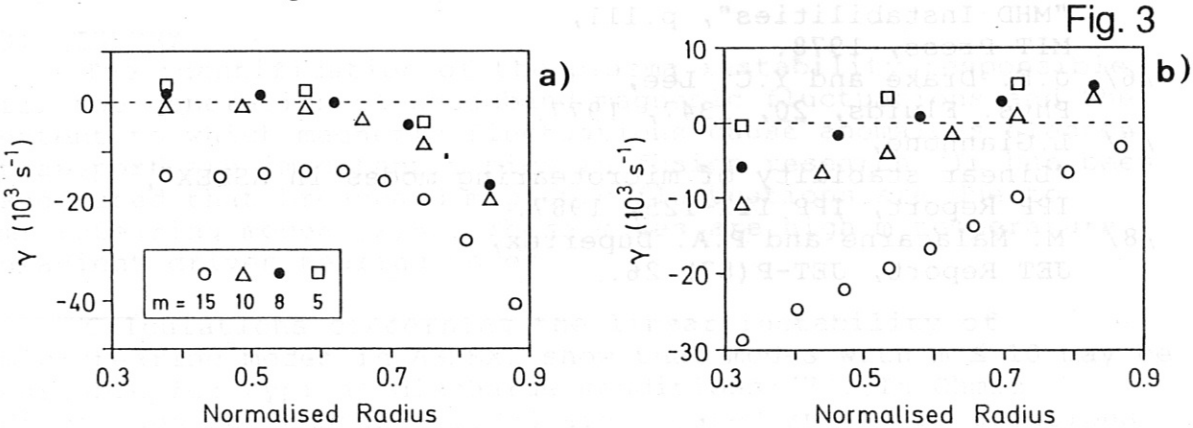

EVALUATION OF PARTICLE TRANSPORT FROM GASOSCILLATION EXPERIMENTS IN OHMIC AND NEUTRAL BEAM HEATED ASDEX PLASMAS

O. Gehre, K.W. Gentle*, B. Richards* (*University of Texas),
A. Eberhagen, J. Gernhardt, O. Vollmer

Max-Planck-Institut für Plasmaphysik
EURATOM Association, Garching, FRG

INTRODUCTION:

Gasoscillation experiments were performed at the divertor tokamak ASDEX to evaluate particle transport under different discharge conditions. These experiments followed a method described in /1/. In order to induce density perturbations in the plasma, the external gas feed was modulated with a sinusoidal wave form of chosen frequency (5, 10 or 20 Hz) and the density modulation at the four horizontal chords (r = 0, 10, 21, and 30 cm) of the ASDEX HCN-laser interferometer was observed. A typical result of this measurement is shown in Fig. 1.
The precision of the technique arises from the extraction of the complex Fourier amplitudes from the full wave form over several periods. The amplitude and phase have an accuracy typical of a signal averaged over several hundred milliseconds.

DETAILS OF THE ANALYSIS

The transport parameters are determined by picking functional forms for the diffusion coefficient D(r) and the inward convection velocity V(r), which is a major improvement to /1/, where only constant D and V were considered. The particle transport equation is solved and the chord integrals are performed, adjusting the free parameters to give the best least-squares fit to the experimental points. Conceptually, the system can be idealized as a boundary-value problem in which the outermost channel gives the edge density and the inner channels are computed from it, although the actual analysis is more complete with a model for the source layer and plasma beyond the separatrix radius. Furthermore, the experimental data are normalized to the centre channel for comparison with the calculations because the centre channel is most accurate, thus propagating the minimum error.

Mathematically, there are three complex numbers (amplitude and phase of the density perturbation) to be fitted and generally three free parameters (two in the density and one in V) to be adjusted for each fit type.

The allowed functional forms for D and V are tabulated below; they may be combined in various ways.

D	V
D	V(r/a)
D(1+b(r/a))	V((r/a)^2)
D(1+b(r/a)^2)	V((r/a)^3)
D(r<b), D(r>b)	V((r/a)(1-r/a))

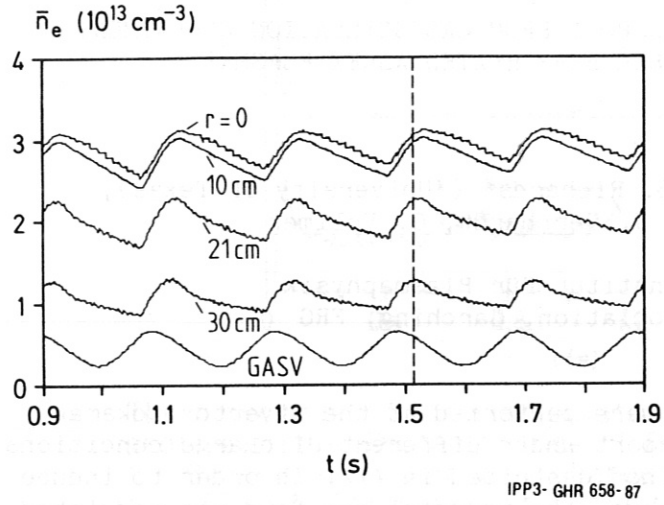

Fig. 1: Density modulation on four chords of the HCN-laser interferometer, induced by sinusoidal modulation of the gas valve (GASV) during a plateau phase of an ohmic discharge. The broken line marks the phase lag between the outer and central channels.

For each set of experimental data and each choice of functional forms, a fitting program will find the two or three free constants. For the two-step D, there is also the radius b at which the step occurs. All solutions are strongly constrained by the transport equation and chord integration.

No choice of free parameters will be able to fit random numbers for the experimental data, similarly, even infinite freedom of D(r) could not provide acceptable fits if V = 0 is imposed.

Questions of accuracy, uniqueness, and robustness must be answered semi-empirically. A measurement of the accuracy of the inferences may be obtained by measuring values of the amplitude and phase in different but apparently identical shots, or by repeating the measurements at different times in a long plateau or at different modulation frequencies. Comparison of the transport coefficients evaluated from several data sets of that kind provides one estimate of the accuracy of the coefficients, which can only be regarded as being determined to within the observed variation.

The quantitative evaluation of the error is based on the "SSQ", the sum of the squares of the differences between observed and computed complex amplitudes at the different radial positions. It determines the choices of functional form and values of the constants and the uniqueness of these choices. When this parameter is used, the coefficients for each data set and fit type are well determined: Convective velocities differing by 20% and diffusion coefficients differing by 10% produce distinctly poorer fits. However, values obtained for different modulation frequencies or shots at the same nominal plasma parameters often differ by more than that. A total error of perhaps 30% in V and 20% in D should be used in assigning transport coefficients to discharge conditions.

TRANSPORT RESULTS

The following discharge conditions were analyzed and the results are summarized in the table below. The functional dependences of the transport coefficients are those which fit the experimental data best. For the diffusion coefficient the most common one is a two-step D, having one D ($r<16$ cm) and another D ($r>16$ cm); the two values are listed in order, D always being larger towards the periphery.

Discharge type	I_p kA	$\bar{n}_e$ 10^{13} cm^{-3}	D m^2 s^{-1}	V m s^{-1}	n
ohmic, H^+	320	1 (carbon-ized)	2.00/4.60	61.0	3
ohmic, H^+	320	1.5 "	1.00/1.10	13.0	3
ohmic, H^+	320	2 "	0.70/9.6	54.0	3
ohmic, H^+	320	4 "	0.40/0.69	3.6	3
ohmic, H^+ →near dens.	320	5.2 "	0.34/0.50	6.6	3
ohmic, H^+ →limit	320	3.1	0.25/1.1	8.5	3
ohmic, H^+	320	1.4	2.00/2.42	48.0	3
ohmic, D^+	380	3.0	0.26/0.50	6.0	1
ohmic, D^+	380	4.2	0.10/0.30	3.0	1
Co-NI, $H^o \rightarrow D^+$ 0.65 MW	380	3.0	0.88/2.20	6.0	1
Ctr-NI, $H^o \rightarrow D^+$ 0.65 MW, with sawteeth	380	3.0	0.80/1.40	8.0	1
Co-NI, $H^o \rightarrow D^+$ 0.35 MW	380	4.2	0.30	3.7	1
Co-NI, $H^o \rightarrow D^+$ 0.67 MW	380	4.2	0.40	2.7	1
Co-NI, $H^o \rightarrow D^+$ 1.35 MW	380	4.2	0.40/0.70	3.0	1

Convective velocities of the form $V(r/a)^n$ are considered. The coefficient V and the exponent n are tabulated. The ohmic hydrogen discharges are best fit with a $(r/a)^3$ convective velocity, the results are less clear for deuterium. In cases where no clear distinction could be made, the simple (r/a) form is listed. With the application of injection power the (r/a) form is better than the other radial dependences for V.

CONCLUSIONS

The analysis of a density scan in hydrogen indicates a decrease in central D of almost an order of magnitude, when $\bar{n}_e$ is increased from 1 x 10^{13}cm^{-3} to ~2.3 x 10^{13}cm^{-3}. In parallel the energy confinement time τ_e linearly increases in this range from ~20 msec to a saturation value of 53 msec (Fig. 2).

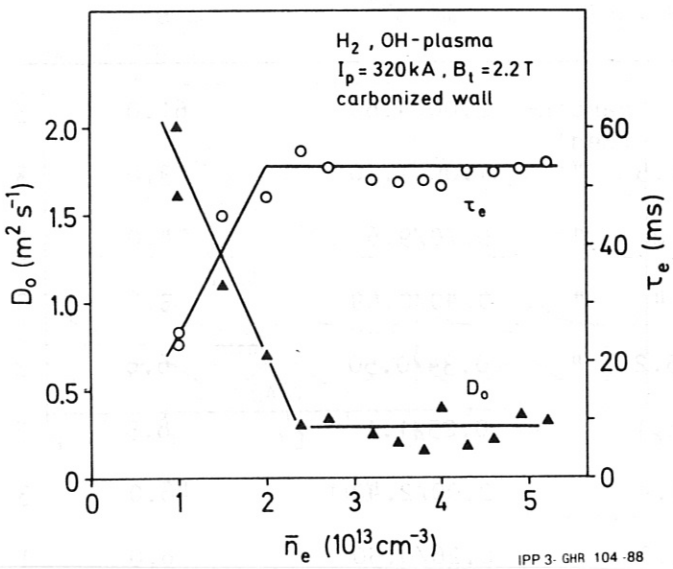

Fig. 2: Density scan in an ohmic hydrogen plasma, showing a pronounced decrease of the central diffusion coefficient D_o in the density range 1 to 2.3 x $10^{13}cm^{-3}$. During the same phase the energy confinement time τ_e linearly increases to its saturation value at higher densites.

The density profile peaks during this phase and the electron temperature monotonically drops, with a slight broadening of the profile. The linear increase in τ_e, found at low densities, seems to be closely connected to an improvement in central particle confinement.

The changes in transport near the density limit and with neutral injection are significant and characteristic of the phenomena.

The behaviour near the density limit can best be described as a decrease in D near the centre, which has the effect of improving the central particle confinement. The decrease is quite marked and the results may well be consistent with neo-classical D on axis. Comparable results have been found for TEXT and a similar behaviour is also known for impurities from ISX-B /2/. With carbonized wall the central D rather shows a flat response over a wide density range up to the density limit.

The effect of neutral injection is to increase the rate of diffusion in relation to the ohmic case for the same isotope. No significant effect on convection is to be seen but the effect on D is pronounced even at low powers and becomes stronger (up to a factor of three) with increasing NI-power. Only L-type cases with sawteeth during injection could be measured and for these no difference of co- versus counter-injection is found. Quantitatively, the increase in particle diffusivity seems to be even greater than the increase in thermal diffusivity associated with the L-mode.

/1/ K.W. Gentle, B. Richards and F. Waelbroeck,
Plasma Physics, Vol. 29, No. 9, 1077 (1987)
/2/ R.C. Isler, et al., Phys. Rev. Lett. 55, 2413 (1985)

TRANSPORT ANALYSIS OF THE L-TO-H TRANSITION IN ASDEX BY COMPUTER SIMULATION

G. Becker

Max-Planck-Institut für Plasmaphysik
EURATOM Association, D-8046 Garching

ABSTRACT: The transport properties and ideal ballooning stability during the L-phase and a burst-free period at the beginning of the H-phase are explored by computer modelling. It is found that the diffusivities χ_e and D are reduced in the steep gradient zone by a typical factor of six a few ms after the H-transition. Local transport in the inner plasma improves at an early stage by a factor of about two. Prior to and after the H-transition both electrons and ions are in the banana regime. Ideal ballooning modes are shown to be stable everywhere, including the edge zone.

INTRODUCTION:The first H-regime studies /1, 2, 3/ already revealed that the L-to-H transition starts at the plasma edge and that processes near the separatrix are of crucial importance. At present, the roles of the divertor chamber, scrape-off layer and steep gradient zone in the H-mode transition are still poorly understood. In order to get more insight, simulations of ASDEX discharges are carried out by modified versions of the BALDUR predictive transport code /4, 5/. The code is appropriate for analysing edge processes since it includes a scrape-off layer model and runs with a non-equidistant radial grid capable of resolving the very steep density and temperature gradients close to the separatrix (r_s = 40 cm). Anomalous energy and particle fluxes are modelled by local (flux-surface-averaged), empirical electron heat diffusivities χ_e, diffusion coefficients D and inward drift velocities v_{in}. The conditions and processes prior to and at the H-transition are studied, with special attention being paid to the plasma periphery. Computed time developments of electron density and temperature profiles and beta poloidal are compared with measured results. The search for critical parameters which might trigger the H-mode /6/ is being continued. Self-consistent modelling of the processes in the divertor and scrape-off plasmas /7/ is not attempted, since sufficient reliable information is lacking.

TRANSPORT BEHAVIOUR OF THE INTERIOR AND EDGE PLASMA: An H-discharge with line-averaged density $\bar{n}_e = 3.3 \times 10^{13}$ cm^{-3}, plasma current I_p = 320 kA, toroidal magnetic field B_t = 1.85 T and neutral injection power P_{NI} = 3.45 MW ($H^0 \rightarrow D^+$) is analysed (see Fig. 1). The discharge shows a relatively late L-to-H transition at t^* = 1.229 s succeeded by a burst-free period of 35 ms. Both $\bar{n}_e$ and β_p^{dia} almost reach a saturated L-state and quickly rise during the quiescent H-phase. The time developments of electron temperature and density profiles measured by periodic multichannel Thomson scattering (circles) are presented in Figs. 2 and 3. The solid curves are modelled with the $\chi_e(r)$ given in Fig. 4, $D(r) = 0.5\ \chi_e(r)$ and $v_{in} = 233\ r/r_W$ cm s^{-1}

with wall radius r_W = 49 cm. The density and temperature gradients near the separatrix were determined on ASDEX on a shot-to-shot basis by an edge Thomson scattering device /8/. The steep gradient zone Δ extends over about 2.5 cm and persists throughout the H-phase. A few ms after t^* the electron temperature measured by the ECE diagnostics begins to rise, indicating reduced diffusivities in the edge zone at this very early stage. In the simulations reduced values of χ_e and D in the zone Δ are thus applied for $t \geq t^*$. It is found that the electron heat diffusivity has to be diminished by a factor of about six (see Fig. 4) in order to obtain the measured temperature pedestal.

The scrape-off region is modelled by classical $\chi_{e_{\parallel}}$, subsonic flow Mach number $M = v_{\parallel}/v_s = 0.11$ with $v_s = [2(T_e + T_i)/m_i]^{1/2}$ and cross-field diffusivities $\chi_{eSOL} = 1.2 \times 10^4$ cm^{2}s^{-1} and $D_{SOL} = 2 \times 10^3$ cm^{2}s^{-1}, yielding the measured decay lengths $\lambda_{Te} \simeq 1$ cm and $\lambda_n \simeq 1.5$ cm.

Figure 4 shows that χ_e^H in the inner plasma is reduced by a typical factor of two in relation to χ_e^L, which agrees with earlier transport analyses /9, 10/. The results of Fig. 2 are obtained with $\chi_e = \chi_e^H$ for $t \geq t^*$. Obviously, the modelling fits the measured T_e profiles. In addition, good fits to the measured β_p^{dia} and ion temperature profiles are obtained with ion heat diffusivities three times the neoclassical values /11/. The conclusion that both χ_e and D in the zone Δ drop immediately after the H-transition agrees with results on DIII-D, where the density and temperature gradients inside the separatrix were found to rise steeply within a few ms after t^*.

It is obvious from Fig. 3, however, that the transport model fails to simulate the measured high edge density and the density shoulder in the initial burst-free H-phase. Extensive studies have shown that a further reduction of D in the zone Δ raises the density gradient. A higher edge density is only obtained by strongly reducing the particle flow across the separatrix. This process seems to be crucial for the L-to-H transition.

The electron collisionality factor ν^*_e (see Fig. 4) and the ion collisionality factor ($\nu^*_i < 0.6$) do not change a lot in the L- and H-phases. The plasma at the periphery does not proceed to a different collisionality regime. At the edge, both electrons and ions are in the banana regime ($\nu^*_{e,i}<1$) already in the L-phase. It is concluded that a different collisionality regime is not reached, which contradicts the assumption in Ref. /12/ concerning the ion energy transport mechanism across the separatrix.

Ideal ballooning stability is studied by the transport code, which evaluates the local criterion for large aspect ratio

$$-\frac{2R_0 q^2}{B_t^2}\left(\frac{\partial p}{\partial r}\right)_c = f(s) \qquad (1)$$

where $(\partial p/\partial r)_c$ is the critical pressure gradient and f(s) is a known function of the dimensionless shear $s = (r/q)\partial q/\partial r$. At finite aspect ratio (A = 4.2) critical pressure gradients are obtained which are typically 25% higher. The profiles of j_t, q and s result from solving the diffusion equation for B_p. Both the thermal pressure and the anisotropic beam pressure are included.

The results presented in Fig. 4 were obtained with the Spitzer resistivity, which yields better agreement with the measured loop voltage and the expected q value on axis than the neoclassical resistivity. In the L-phase and the quiescent H-phase, the plasma is everywhere stable to ideal ballooning modes even in the steep gradient zone. At 1.261 s, i.e. a few ms prior to the first burst, the stability limit is not reached at the edge if the 25% higher $(\partial p/\partial r)_c$ due to small aspect ratio is taken into account.

Earlier analyses /13, 14/ are confirmed by the present result that the pressure gradient in the pre-transition L-phase is everywhere smaller than the critical value for ideal ballooning modes. This finding is incompatible with the model assumption made for the L-phase in Ref. /15/.

The profile parameter $\eta_e = d \ln T_e / d \ln n_e$, which is important for drift instabilities, does not change much in the L- and H-phases (see Fig. 4).The modest variation even at the edge results from raising both the density and temperature gradients in the zone Δ. In the initial phase of the H-transition particle flow blocking at the separatrix should yield transiently flat density profiles. The corresponding higher η_e or η_i values possibly trigger the reduction of the diffusivities in the steep gradient zone.

REFERENCES

/1/ Wagner, F., Becker, G., Behringer, K., Campbell, D., Eberhagen, A., et al., Phys. Rev. Lett. 49 (1982) 1408.

/2/ Wagner, F., Becker, G., Behringer, K., Campbell, D., Eberhagen, A., et al., in Plasma Physics and Controlled Nuclear Fusion Research 1982 (Proc. 9th Int. Conf. Baltimore, 1982), Vol. 1, IAEA, Vienna 1983, 43.

/3/ Wagner, F., Fussmann, G., Grave, T., Keilhacker, M., Kornherr, M., et al., Phys. Rev. Lett. 53 (1984) 1453.

/4/ Becker, G., ASDEX Team, Neutral Injection Team, Analysis of Local Transport in Neutral-beam-heated L and H Plasmas of ASDEX, Rep. IPP III/98, Max-Planck-Institut für Plasmaphysik, Garching (1984).

/5/ Post, D.E., Singer, C.E., McKenney, A.M., BALDUR: A One-dimensional Plasma Transport Code, Rep. 33, Princeton Plasma Physics Laboratory, Princeton (1981).

/6/ Becker, G., Nucl. Fusion 26 (1986) 415.

/7/ Singer, C.E., Redi, M.H., Boyd, D.A., Cavallo, A.J., Grek, B., et al., Nucl. Fusion 25 (1985) 1555.

/8/ Keilhacker, M., Becker, G., Bernhardi, K., Eberhagen, A., ElShaer, M., et al., Plasma Phys. Contr. Fusion 26 (1984) 49.

/9/ Becker, G., Campbell, D., Eberhagen, A., Gehre, O., Gernhardt, J., et al., Nucl. Fusion 23 (1983) 1293.

/10/ Kaye, S.M., Bell, M., Bol, K., Boyd, D., Brau, K., et al., in Controlled Fusion and Plasma Physics (Proc. 11th Europ. Conf. Aachen, 1983), Part I (1983) 19.

/11/ Chang, C.S., Hinton, F.L., Phys. Fluids 25 (1982) 1493.

/12/ Hinton, F.L., Nucl. Fusion 25 (1985) 1457.

/13/ Becker, G., ASDEX Team, Neutral Injection Team, Nucl. Fusion 27 (1987) 1785.

/14/ Becker, G., Gierke, G. v., Keilhacker, M., et al.,Nucl. Fusion 25 (1985) 705.

/15/ Bishop, C.M., Nucl. Fusion 26 (1986) 1063.

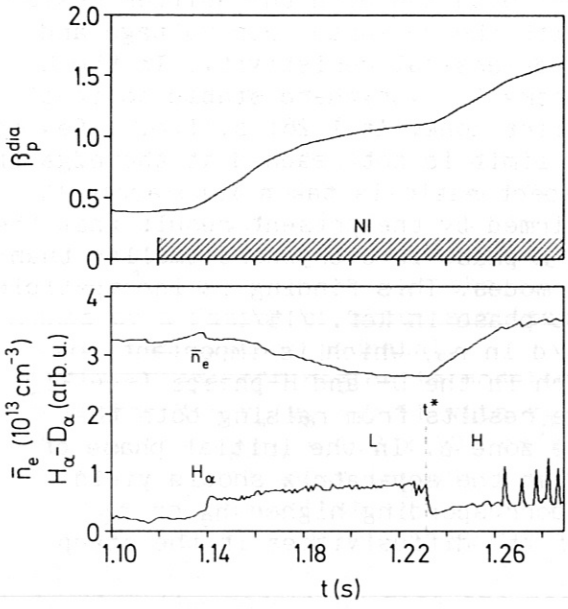

Fig. 1:

Time evolution of $\bar{n}_e$, H_α intensity and β_p^{dia} in an H-discharge.

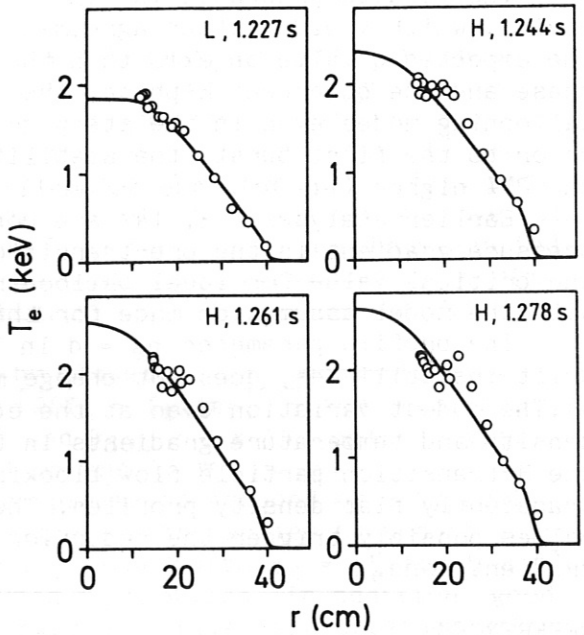

Fig. 2:

Comparison of measured (circles) and computed (solid curves) electron temperature profiles.

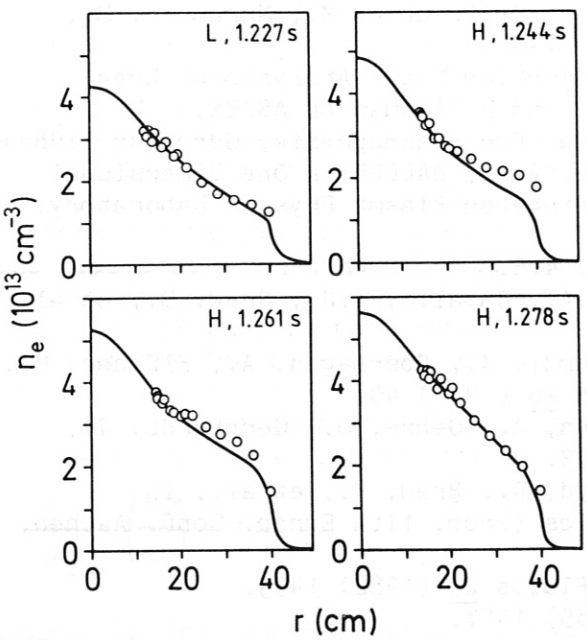

Fig. 3:

As in Fig. 2, but electron density profiles.

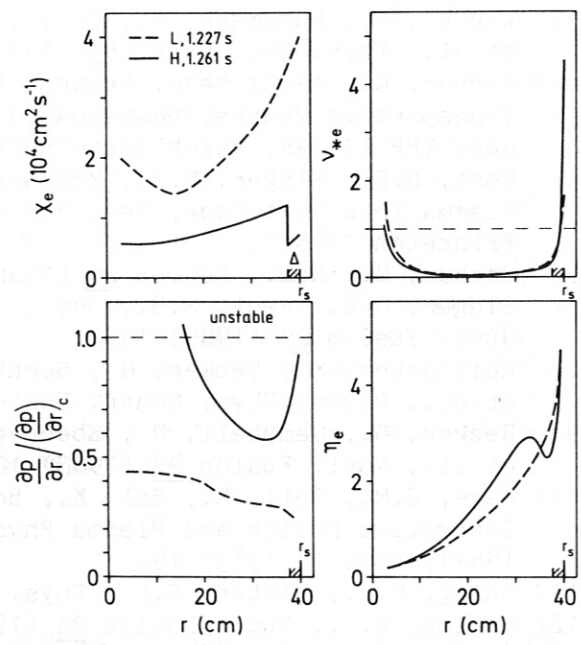

Fig. 4:

Profiles of χ_e, electron collisionality factor ν_{*e}, ideal ballooning stability parameter $\partial p/\partial r/(\partial p/\partial r)_c$ and $\eta_e = d \ln T_e / d \ln n_e$ in L- and H-phases.

THE POWER DEPENDENCE OF τ_E IN THE H-MODE OF ASDEX

F. Wagner, O. Gruber, O.Gehre, K. Lackner, E.R. Müller, and A. Stäbler

Max-Planck-Institut für Plasmaphysik
EURATOM Association, D-8046 Garching, Fed. Rep. of Germany

INTRODUCTION: The global energy confinement time τ_E of H-mode plasmas is found in ASDEX to be power independent for hydrogen injection into deuterium plasmas / 1 /. DIII-D reports the same behaviour for deuterium injection into deuterium plasmas / 2 /. These findings are contrary to those from JET / 3 / and JFT-2M / 4 /, where degradation of τ_E in the H-mode is observed as in the L-mode. This causes great uncertainty in predicting H-mode confinement of next - generation tokamak experiments. In this paper we try to analyze the power dependence of τ_E in the quiescent H-mode, H*, in comparison with regular H-mode results. The H*-mode may display the intrinsic H-mode confinement properties because ELMs do not additionally contribute to the energy losses. The power scaling studies of JET were done without ELMs, but the published results of ASDEX and DIII-D were obtained with ELMs.

POWER SCALING OF τ_E IN THE H*-MODE: Under the conditions I_p=0.32MA, B_t=2.2T power scans in the quiescent H-mode were possible in ASDEX both for H^o- and D^o- injection into deuterium plasmas in the restricted power range of $1.75 \le P_{NI} \le 3.5$ MW. Without ELMs an additional difficulty in the τ_E analysis arises because the H*-phase does not reach the steady state. During the beam pulse the H*-phase is terminated by a thermal quench caused by large impurity radiation which finally matches the power input (globally as well as locally in the plasma centre) and which initiates an intermediate L-phase / 5 /. The duration of the H*-phase depends on the heating power and increases from 95ms at 1.75MW to 125ms at 3.5MW. During the H*-phase the particle content increases linearly at a rate corresponding to 2-3 times the beam fuelling. The impurity radiation increases nearly exponentially. After the H*-transition, β_p increases once more owing to the improved confinement; when the impurity radiation starts to affect the energy balance, β_p rolls over and decreases already during the H*-phase.
Because of the non-steady-state conditions and the central radiation issue, the τ_E analysis was done in three steps: τ_E is evaluated according to $\tau_E^{(1)} = E / (P_{tot} - dE/dt)$ to correct for the lack of stationarity. These values allow the comparison with those from other experiments. In a second step the following relation is used:

$$\tau_E^{(2)} = \tau_E^{(1)} \cdot \left[1 - \frac{\int r \int p^{rad}(\rho)\, \rho d\rho dr}{\int r \int p^{heat}(\rho)\, \rho d\rho dr} \right]^{-1} \qquad (1)$$

Equ. (1) corrects for the radiation power emitted in the radial zone where the radiation - and heating power densities overlap. Mere edge radiation does not lead to a correction. The $\tau_E^{(2)}$ values should represent the actual transport properties of the quiescent H*-mode. There is a certain arbitrariness in the choice of $\tau_E^{(2)}$ as it is strongly varying with time. In a final step, full transport analysis (using TRANSP) is done for two H*-discharges, the one with the lowest and the one with the highest heating power, to have a further check on the data and the analysis.
Figure 1 shows the power dependence of the global confinement times $\tau_E^{(1)}$ and $\tau_E^{(2)}$ in the H*-mode, evaluated as described above in comparison with τ_E values of the regular H-mode with ELMs. As H-phases with ELMs reach steady state, τ_E is calculated in this case simply from $\tau_E = E / P_{tot}$. While the H-mode does not show any distinct power dependence (τ_E (ms) = 52.2•P (MW)$^{-0.05}$) with H^o into D^+, the quiescent H-mode does. The following power dependence is obtained for the H*- phase (based, however, on 4 data points only !): $\tau_E^{(1)}$=86•P$^{-0.45}$ for H^o into D^+ and $\tau_E^{(1)}$= 132 •P$^{-0.75}$ for D^o into D^+. The curve in Fig. 1 is the power fit to the D^o into D^+ cases; the horizontal line guides the eye to the results obtained with ELMs.
Figure 2 shows the time dependence of τ_E as obtained from the full transport analysis and of $\tau_E^{(1)}$. The confinement times are plotted from the OH-phase into the L- and finally into the H*-phase. The results are shown for the extreme power cases. The τ_E values in Fig. 2 are obtained taking into account the radiation losses and correspond to $\tau_E^{(2)}$ as obtained from equ.(1) / 5 /.
In summary we also find in ASDEX a power dependence of τ_E in the quiescent H*-mode as in JET. As such a dependence is not observed in the regular H-mode, it can be speculated that τ_E in this case is predominantly determined by the energy losses caused by ELMs superimposed on the heat transport losses so that the overall confinement time is power-independent. We shall try to analyze this possibility in the following.

THE EFFECT OF ELMs ON THE GLOBAL CONFINEMENT: As ELMs are an external mode, the global confinement is affected. Figure 3 shows a discharge where quiescent phases follow those with ELMs. As soon as ELMs set in, the particle and energy contents decrease. It is difficult to assess the energy losses per ELM. From the changes in slope of the β_p trace in Fig. 3 we conclude that τ_E^{ELM} (representing the ELM losses) is about 110 ms.
The energy lost at an ELM can be determined in three ways: $\Delta\beta_p$ can be measured direct by using the equilibrium coils, which are placed within the vacuum vessel and which have sufficient time response. Typically 5 % of the energy content is lost by an ELM. Another possibility is to determine the energy loss via the effect of an ELM on the plasma profiles. For n_e and T_e continuous measurement is possible. An ELM affects both n_e and T_e from the plasma edge to about r = 15 cm. The relative amplitude increases with radius for n_e and T_e in about the same way with $\Delta n_e / n_e \approx \Delta T_e / T_e \approx 10\%$ at r=30cm. On the assumption that the T_i profile is affected in the same way by an ELM, we can integrate the energy loss and conclude that about 8 % of the energy is lost. A final possibility to evaluate the energy loss of an ELM is by measuring the power flux into the divertor chamber onto the target plate. This measurement is rather inaccurate and can only serve as a consistency check. Typically an ELM leads to power deposition at the target plate with a peak power density of about 1 kW/cm^2 and a width of about 4 cm. The duration of increased energy loss during an ELM is approximately 0.4 ms; the energy loss is assessed to

about 10 kJ in rough agreement with the other estimates. The particle loss per ELM is typically $1 \bullet 10^{19}$ corresponding to $\Delta N_e / N_e \approx 5\%$.
The repetition time of ELMs depends somewhat on the heating power. At low power ELMs appear erratically and the ELM period fluctuates. At high power, ELMs appear in a more regular form and the repetition time becomes constant at about 6 ms. It was not possible to determine the amplitude distribution of the ELMs. The low-power, high-frequency ELMs are clearly smaller in amplitude. Assuming a constant ELM amplitude of $\Delta E / E$ of 6% and a repetition time $t_{ELM} = 6$ ms and superimposing these losses onto the transport losses (see Fig.1) we can calculate the power dependence of the global confinement time: $\tau_E^{-1} = \tau_E^{(2)-1} + \Delta E / E \bullet t_{ELM}^{-1}$. The results calculated in this way are also plotted in Fig. 1. They roughly agree with the measured τ_E data obtained with ELMs.

SUMMARY: First the global energy confinement time is shown to decrease with power when the H-mode is operated in the quiescent H-phase as in JET . This conclusion is drawn, however, from a rather weak experimental basis because of our limitations in operating the H-mode without ELMs . It is shown that the lack of power dependence in the regular H-mode with ELMs could be due to the power-dependent microscopic transport losses being superimposed on those caused by ELMs.
The ratio between τ_E in the quiescent H-mode of ASDEX and JET (both with D^o -> D^+) is about 20, which is a factor of 2 more than the ratio of the currents, indicating an additional size scaling given approximately by the major radius.

REFERENCES:

/ 1 / A. Stäbler, F. Wagner, et al.,4th Intern. Symp. on Heating in Tor. Plasmas, Rome (1984), Vol. I, p. 3.
/ 2 / K.H. Burrell, S. Ejima, et al., Phys. Rev. Lett. 59 (1987) 432.
/ 3 / M. Keilhacker, M. Bishop, et al., Proc. 14th Europ. Conf. on Contr. Fusion and Plasma Phys., Madrid, part III, p. 1339 (1987).
/ 4 / K. Odajima, A. Funahashi, et al., 11. Intern. Conf. on Plasma Phys. and Contr. Nucl. Fusion Research, IAEA, Vienna, Vol. I (1987) p. 151.
/ 5 / O. Gruber, W. Jilge, et al., Proc. 12th Europ. Conf. on Contr. Fusion and Plasma Phys., Budapest, part I, p. 18 (1985).

FIGURE CAPTIONS:

FIG.1 Global energy confinement time in the quiescent (H*) and the regular (H) H-mode with ELMs versus heating power. The curve is a power fit to the D^o -> D^+ case, the horizontal line guides the eye to the H-cases with H^o -> D^+. The circles are calculated from the H^o -> D^+ τ_E values with the radiation correction.

FIG.2 Energy confinement time (τ_E) and replacement time ($\tau_E^{(2)}$) of two H* discharges with different heating powers, as obtained from TRANSP.

FIG.3 Line - density n_e, divertor H_α radiation and β_{pol} for a discharge with intermittent quiescent and ELM - active phases.

Fig. 1

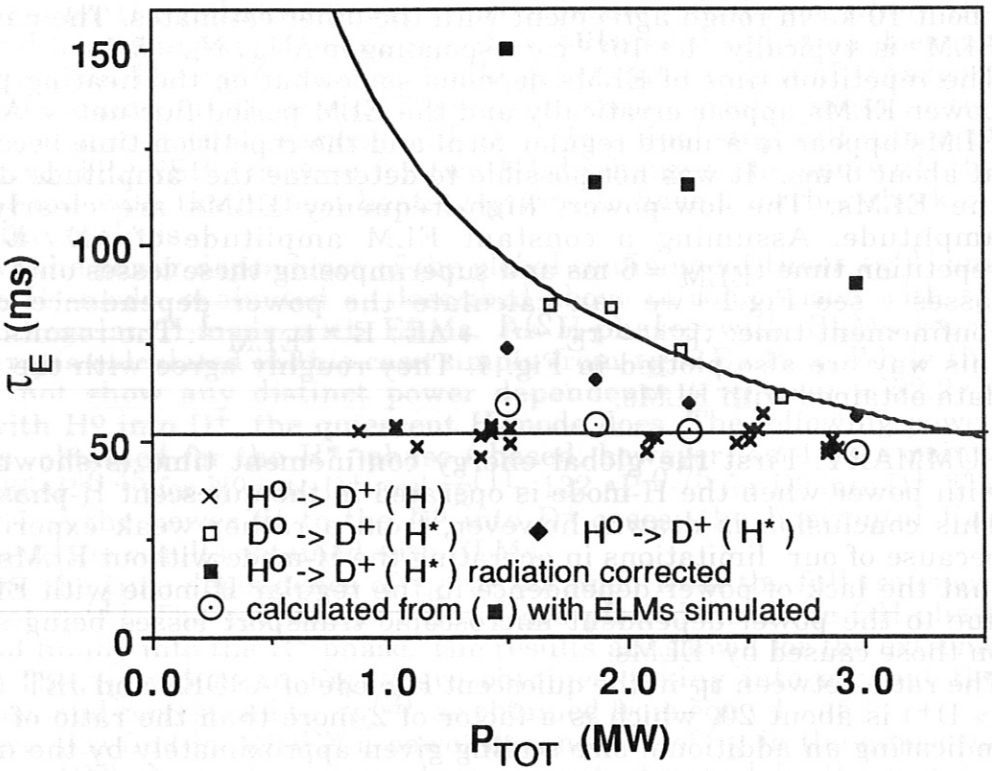

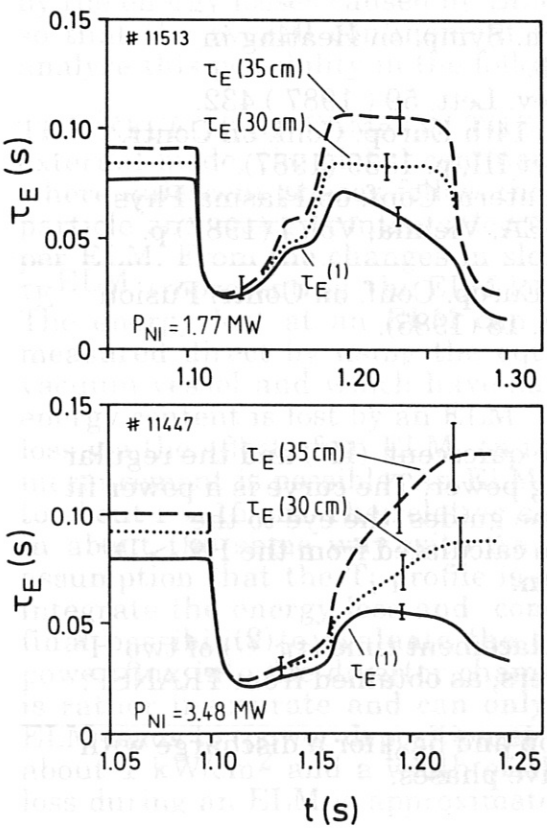

Fig. 2

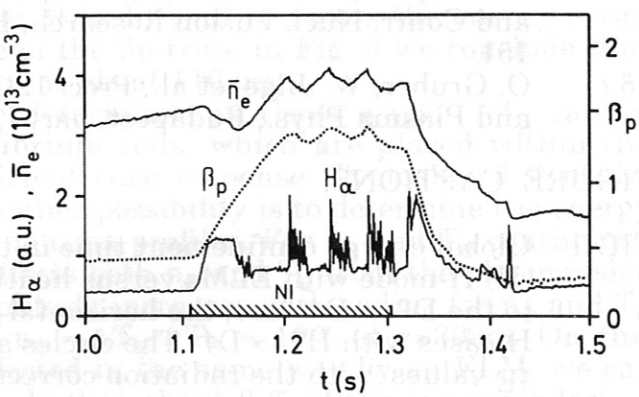

Fig. 3

MOMENTUM CONFINEMENT OF ASDEX PLASMAS DURING CO AND COUNTER NEUTRAL BEAM INJECTION

D.E. Roberts*, H.M. Mayer, G. Fussmann, B. Bomba, O. Gehre, O. Gruber, G. Janeschitz, M. Kornherr, A. Korotkov**, K.-H. Steuer, and ASDEX-, Pellet- and NI-Teams

IPP Garching, EURATOM Association, Fed. Rep. of Germany

* Atomic Energy Corporation, Pretoria, R.S.A.
** Ioffe Institute, Leningrad, USSR

I. Introduction

Toroidal rotation velocities of ASDEX plasmas of up to $2 \times 10^7 cms^{-1}$ have been measured under a variety of conditions and for both co- and counter neutral beam injection. The velocities were obtained from the Doppler shifts of OVIII 2976 $\AA$ and/or C VI 3434 $\AA$ excited by charge exchange recombination (CXR). Up to five lines of sight have been used (table I), each of which intersects the axis corresponding to a source in the north-west neutral injection beam line. The main objective has been to compare the global momentum confinement with the energy confinement of ASDEX plasmas for different plasma parameters and heating scenarios.

II. Estimates of Momentum Confinement Time

The experimental global momentum confinement time was estimated from $\tau_\phi = L/\Gamma$ where L is the total toroidal angular momentum of the plasma and Γ the momentum input from the beams. $L \simeq 2\pi R^2 m_p f \int_o^a V_\Phi(r) n_e(r) 2\pi r dr$ where f is the ratio of the average atomic mass to that of a pure hydrogen plasma at the same n_e. With the assumption that only carbon and oxygen impurities, present in roughly equal densities, contribute to Z_{eff}, $f \simeq \frac{1+2g}{1+g} + 0.16\frac{(Z_{eff}-1)}{(1+g)}$.
The ratio $g = n_D/n_H$ was typically rather small ($\simeq 1$) in the $H_o \rightarrow D_+$ plasmas and was estimated to about $\pm$ 50 % from neutron measurements. Z_{eff} was obtained from infra-red continuum measurements. Errors in g and Z_{eff} do not affect τ_ϕ too critically and these two quantities were assumed to be independent of radius. The main uncertainty in τ_ϕ arises from that in $V_\phi(r)$.
One problem with measuring V_ϕ with the observed CXR lines is that they are also excited in the plasma edge region even without NI. It has been possible to investigate the importance of edge excited lines, with plasmas heated by the SE beam which is not seen directly by any of the lines of sight in table I. Interference from the edge excited transition together with low signal to noise for the inner channels, due to beam penetration limitations (E_o= 41 keV), give rise to problems in measuring V_ϕ at small radii, particularly for CVI 3434$\AA$. However, at least for $r \geq 14cm$, V_ϕ is believed to be accurate to within a systematic uncertainty $\simeq \pm 10^6 cms^{-1}$ with statistical errors of a similar size. The estimated errors in τ_ϕ are $\approx \pm$ 15 % statistical with a further $\simeq \pm$ 20 % systematic.
Apart from neoclassical theory, which gives estimates of $\tau_\phi \simeq 10^3\times$ higher than experiment, the only theory which allows a quantitative estimate of τ_ϕ is the gyroviscous theory of Stacey et al. [1]. Here $\tau_{\phi G} \simeq 2R_o^2 B_o \langle Z_{eff}\rangle / \langle T_i \rangle$, where the brackets imply

volume averages. T_i can also be estimated from the CXR diagnostic and the uncertainty in $\tau_{\phi G}$ from experimental sources amounts to $\simeq \pm$ 25 %.
An estimate of τ_ϕ can, however, also be obtained from the diffusive transport of particles. In the source free case, with D = const, the particle confinement time is given by $\tau_p^*(r) = \frac{a^2}{4D}(1 - \frac{r^2}{a^2})$ [2]. Global dynamical confinement times τ_E^*, τ_ϕ^* and τ_p^* can then be estimated from $\tau_\psi^* = \int_o^a \psi\, \tau_p^*(r) r dr / \int_o^a \psi r dr$ with $\psi = n_e T, n_e V_\phi$ and n_e respectively. Assuming parabolic profiles of T, V_ϕ and n_e this yields $\tau_E^* = \tau_\phi^* = \frac{3}{16}a^2/D$ and $\tau_p^* = \frac{1}{6}a^2/D$. For peaked energy and momentum sources these decay times should become close to the stationary confinement times τ_E and τ_ϕ considered in this paper.

III. Results

Momentum confinement results have been obtained for H_o injection into mainly D_+ but also some H_+ plasmas with co- (L-mode) and counter injection. A study of H-mode discharges has also started.
Rotation measurements for a co-injection (L-mode) run at fixed power and different $\bar{n}_e$ are shown in Fig. 1. The rotation velocity falls with increasing $\bar{n}_e$ (as $\simeq \bar{n}_e^{-1/2}$) while the velocity profile is relatively broad ($V_\phi(r)/V_\phi(o) \simeq (1 - r^2/a^2)^{0.9}$) and shows no measurable change over the $\bar{n}_e$ range studied (Fig. 2). T_i also shows a slow decrease with $\bar{n}_e$ so that the ratio of toroidal velocity to deuteron thermal velocity decreases with $\bar{n}_e$ from $\simeq$ 0.44 to 0.30 (r = 34 cm). The average ratio of toroidal to oxygen ion thermal velocities is therefore $\simeq$ 1.0.
Unlike V_ϕ, τ_ϕ shows no clear $\bar{n}_e$ dependence (Fig. 3), due particularly to n_e profile effects and a strong decrease in Z_{eff} with increasing $\bar{n}_e$ (from $\simeq$ 4 to 1.5). The global energy confinement time τ_E likewise shows no marked $\bar{n}_e$ dependence and is larger than τ_ϕ though within the combined error limits. $\tau_{\phi G}$ tends to show a decrease with $\bar{n}_e$, a result of Z_{eff} falling off with $\bar{n}_e$ faster than T_i, but generally the agreement with experiment is better than a factor of 2. The diffusive transport model, with $D = 0.5 m^2 s^{-1}$, gives $\tau_E^* = \tau_\phi^* = 60 ms$, in surprisingly good agreement with experiment.
An extension of the gyroviscous theory was used by Stacey to attempt to explain the decrease in τ_E with input power for TFTR plasmas in terms of increasing viscous dissipation at higher rotation velocities [3]. In this case $\tau_{EG} \sim \tau_{Eo} / (1 + \frac{\tau_{Eo} V_\phi^2 f_p}{R^2 \omega})$, where ω is the ion gyrofrequency and f_p a profile factor.
The observed density dependence of V_ϕ for ASDEX plasma in principle provides a way of testing this theory at constant input power because in the ohmic ("reference") phase $V_\phi << V_\phi(NI)$ and $\tau_{EG} \simeq \tau_{Eo}$, which is essentially independent of $\bar{n}_e$ (Fig. 4). However, using experimental values for Z_{eff}, τ_{Eo} and V_ϕ, τ_{EG} is also essentially independent of $\bar{n}_e$, though with a reduction from the ohmic heating case about 2× lower than observed (Fig. 4). This is again due to the strong $\bar{n}_e$ dependence of Z_{eff}, which influences the effective ω.
Significantly different from the co-injection results are those obtained with counter injection. Here the velocities rise to values more than 2× those obtained at the same density with co-injection (Fig. 1) leading to values of τ_ϕ of up to 90 ms, similar in magntiude to τ_E (Fig. 3). In these discharges, the increased energy and momentum confinement is accompanied by improved particle confinement which leads to a steep rise in $\bar{n}_e$ with time. The corresponding impurity accumulation, which occurs for light

as well as heavy impurities, leads to large axial radiation losses and termination of the discharges by major disruption. Gyroviscous theory gives too small a τ_ϕ because Z_{eff} in the counter-NI case is not much larger than in the co-NI case while T_i is approximately the same. The diffusive model gives $\tau_\phi \simeq \tau_E$, as observed.
Co-injection discharges where the density is ramped up with time, as well as pellet injected discharges, (both of which can reach similar densities to the counter-injection cases) attain similar velocities to those in steady state co-discharges, well below the corresponding counter-injection velocities (Fig. 1).
H-mode discharges (single-null) with a high ELM frequency ($\approx 400 H_z$) show no significant differences in velocity to corresponding L-mode (double-null) discharges except at the relatively large radius of 35 cm. Here a distinctive increase of $\simeq 2\times$ in V_ϕ is seen which disappears when the discharge goes back into the L-mode. Such an increase in V_ϕ could be interpreted as a decrease in edge momentum diffusivity which accompanies a decrease in edge electron thermal diffusivity and particle diffusion. The lack of significant increase in global τ_ϕ for such discharges is also to be compared with a lack of increase in τ_E compared with the L-mode.

IV. Summary

In the results studied to-date τ_ϕ is always about the same size as τ_E. In two scenarios where improved energy confinement is seen relative to the L-mode, improved momentum confinement is also found (and indeed improved particle confinement). There is a global improvement with counter injection but only an edge improvement for the H-mode with high ELM frequency. Gyroviscous theory gives agreement with experiment within about a factor of 2 though systematic differences are apparent. A simple diffusion model also gives satisfactory agreement.

References

[1] W.M. Stacey Jr., C.M. Ryn and M.A. Malik, Nucl. Fusion **26**, (1986), 293.

[2] G. Fussmann, Nucl. Fusion **26**, (1986), 983.

[3] W.M. Stacey, to be published.

Channel	radial position (outer minor radius) (cm)	spatial resolution (cm)	angle with toroidal direction
CXR1	42.0	±2.0	4°
CXR2	34.5	±2.0	1°
CXR3	24.0	±2.0	4°
CXR4	14.0	±3.2	10°
CXR5	4.0	±4.0	24°

Table I: Details of lines of sight used for CXR spectroscopy
(The separatrix is at $r = 40$ cms and the limiter typically at $r = 46.0$ cms.)

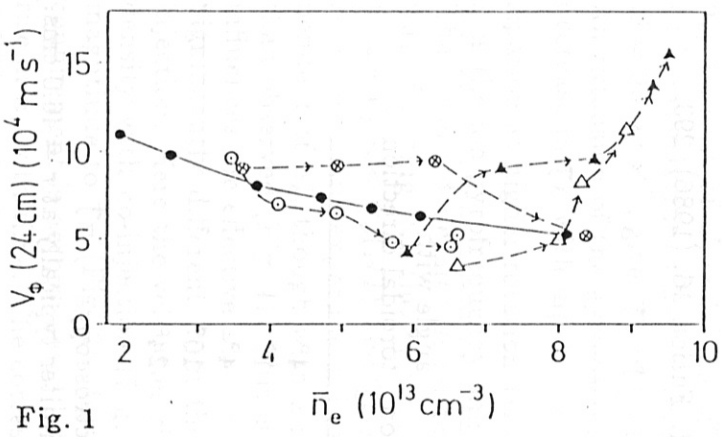

Fig. 1

V_ϕ (24cm) versus $\bar{n}_e$ for counter injection (triangles) and co-injection (circles) with $P_{NI} = 1.3MW, I_p = 380$ kA. The symbols ▲, △ (counter-NI) and ⊙, ⊗ (co-NI) each refer to one discharge, with the arrows indicating the time sequence. The symbols ● each correspond to an average of several measurements taken during the density plateau of a discharge.

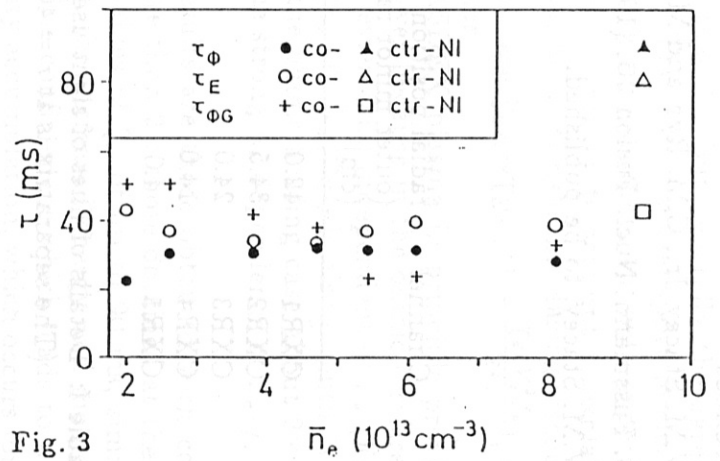

Fig. 3

Comparison of τ_ϕ with τ_E and $\tau_{\phi G}$ as a function of $\bar{n}_E$ for co- and counter injection.

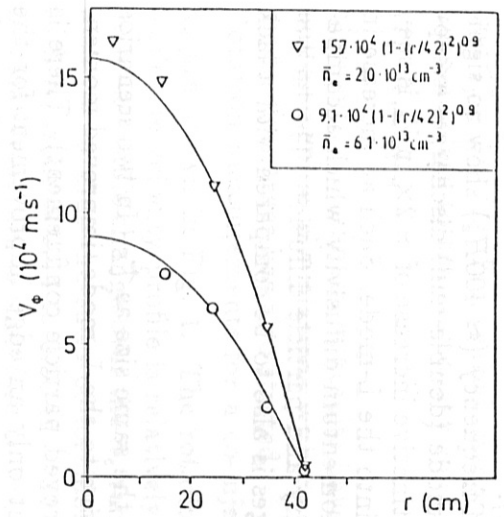

Fig. 2

Radial profile of V_ϕ for two values $\bar{n}_e$ for the density plateau co-injection series shown in Fig. 1.

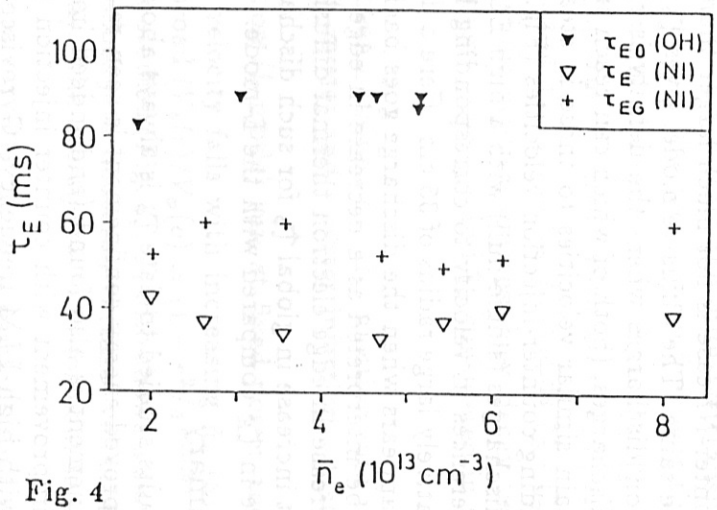

Fig. 4

Test of the velocity dependence of τ_E from gyroviscous theory. τ_{E0}, τ_E are the experimental confinement times for ohmic and beam heated plasmas respectively and τ_{EG} the values given by gyroviscous theory with experimental V_ϕ, Γ_{E0} and Z_{eff}.

PARAMETRIC DECAY IN THE EDGE PLASMA OF ASDEX DURING FAST WAVE HEATING IN THE ION CYCLOTRON FREQUENCY RANGE

J.-M. Noterdaeme, M. Brambilla, J. Gernhardt

Max-Planck Institut für Plasmaphysik, Euratom Association
D-8046 Garching, Federal Republic of Germany

R. Van Nieuwenhove, G. Van Oost

Laboratoire de Physique des Plasmas-Laboratorium voor Plasmafysica
Association"Euratom-Etat Belge"-Associatie"Euratom-Belgische Staat"
Ecole Royale Militaire-B 1040 Brussels-Koninklijke Militaire School

M. Porkolab

Department of Physics and Plasma Fusion Center
Massachusetts Institute of Technology
Cambrigde, Massachusetts 02139, U.S.A.

Abstract: For the first time, in an ICRF heated tokamak, parametric decay instabilities were observed in the plasma edge. Two types of decay processes were found. Those instabilities provide a mechanism for the direct energy deposition, seen in many tokamaks, on the ions and electrons of the scrape off layer.

Introduction: During hydrogen second harmonic heating at 67 MHz /1/, frequency spectra were measured with an electrical probe. The measuring probe is 10° toroidally away from one ICRH antenna, and 170° from the other. The target plasma can be pure hydrogen or a hydrogen-deuterium mixture (n_H/n_e=25 to 100 %), ohmically heated (P_{OH}=450 kW) or preheated by neutral injection (P_{NI}=0.8-3.5 MW). Analysis of the frequency spectra, revealed the presence of parametric decay effects /2/. Parametric decay is a process by which a wave, called the pump wave (index 0), decays nonlinearly into two modes (index 1 and 2). These modes have to fulfill the selection rules : $\omega_0 = \omega_1 + \omega_2$ and $\overline{k_0} = \overline{k_1} + \overline{k_2}$. Theoretical studies /2,3/ indicate that several types of parametric decay processes can occur, two of which have been observed on ASDEX.

Parametric decay processes: In a first type, the pump decays into an ion Bernstein wave with frequency close to the pump wave (2e in Fig. 1) and a low frequency electron quasimode (obscured in the spectrum by the zero frequency peak of the spectrum analyser). Growth rate estimates /2/, predict that the convective threshold is easily exceeded.
In the second process, the pump decays into an ion cyclotron quasimode (with frequency near the ion cyclotron harmonic of an ion species in the edge, $\omega_1 = \omega_{ci}$) and an ion Bernstein wave (with, according to the selection rule $\omega_2 = \omega_0 - \omega_1$). The study of this process can benefit from

thorough analysis previously performed in a small research machine /4/. Because of the dependence of the frequency of the quasimode on the magnetic field, it is possible to identify this mode unequivocally. In Fig. 1 three spectra, at different toroidal magnetic field, and for a fixed pump frequency (67 MHz) show clearly how the frequency of the quasimode 1H depends linearly on B_T, and how the frequency of the corresponding ion Bernstein wave 2H then obeys the selection rule. In a multispecies plasma (i = H, D), we find that this proces can occur for both species. In a machine with carbonized walls, there are even indications that C at different ionisation stages can be the ion species supporting the quasimode. On first turn on of the RF in a shot, a more complicated spectrum (Fig. 2) can appear, with splitting of the peaks. This is thought to be due to the initial outgassing of the antenna, which can change the boundary temperature directly in front of the antenna, and the isotope concentration.

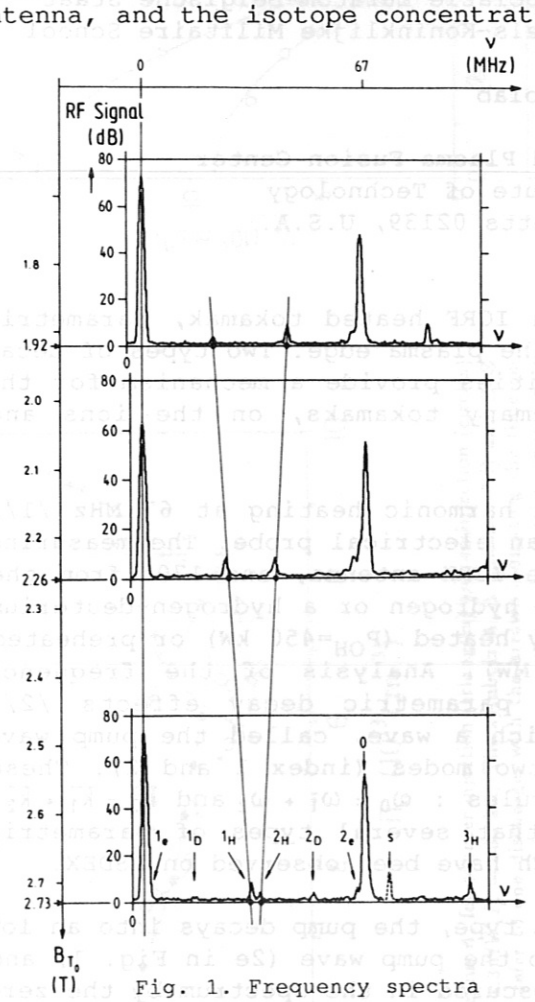

Fig. 1. Frequency spectra for three magnetic fields, showing the B dependence of the modes

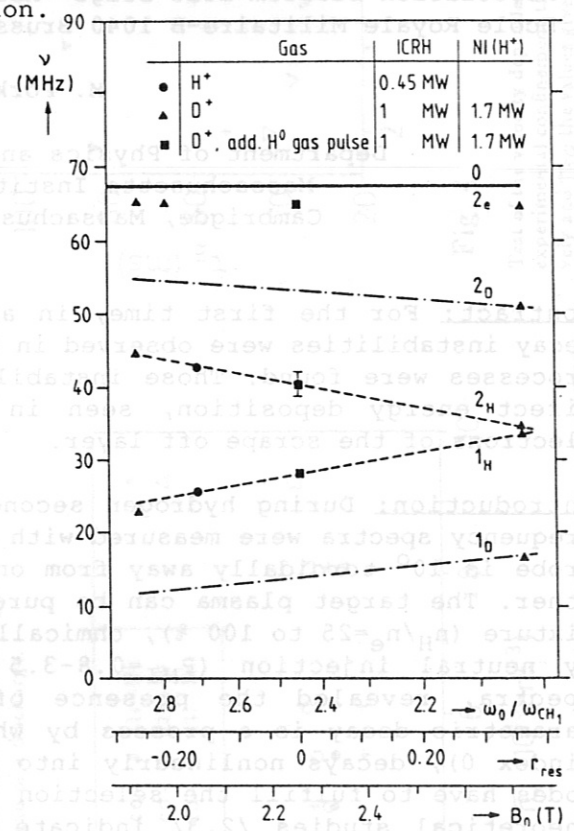

Fig. 3. Parameter region for the appearance of the decay instabilities

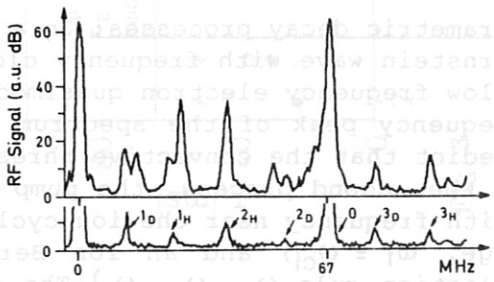

Fig. 2. Spectrum at the first turn on of the ICRH (top) compared to a spectrum (bottom), 800 ms later in the same pulse

Dependences: Whether or not the H and D decay processes were observed, depends strongly on the plasma composition and heating conditions. By varying the toroidal magnetic field, at constant pump frequency, the position of the second harmonic resonance layer was varied between r=-0.22m and r=+0.38m, with respect to the plasma centre at R=1.67m (with a=0.40m and the antenna protection limiters at r=0.45m). This also changes the ratio ω_0/ω_{ci}, in the edge between 2.87 and 2.03. Fig. 3 show some of those conditions.
In a H plasma, with 0.45 MW of ICRH, on the antenna closest to the probe, the decay processes were observed only for positions of the resonance layer r<-0.13m ($\omega_0/\omega_{ci}>2.7$), with data available only up to r=+0.16m ($\omega_0/\omega_{ci}=2.3$). In a D and H mixture (30% H) with 1MW ICRH, on the antenna furthest from the probe, and 1.7 MW NI, they were observed only for r<-0.22m or r>0.38m (corresponding to $\omega_0/\omega_{ci}>2.9$ or <2.0).

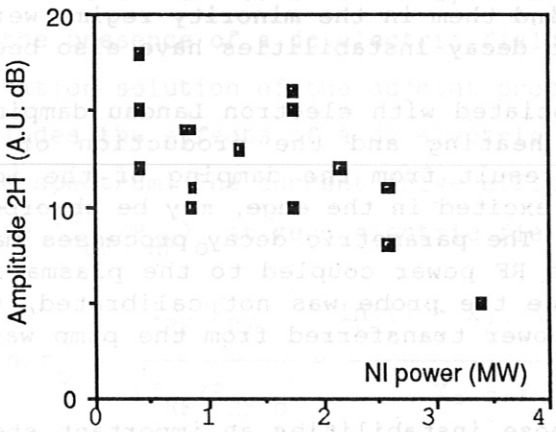

Fig. 4. Dependence of the 2H peak on NI power, for 1.2 MW of ICRH

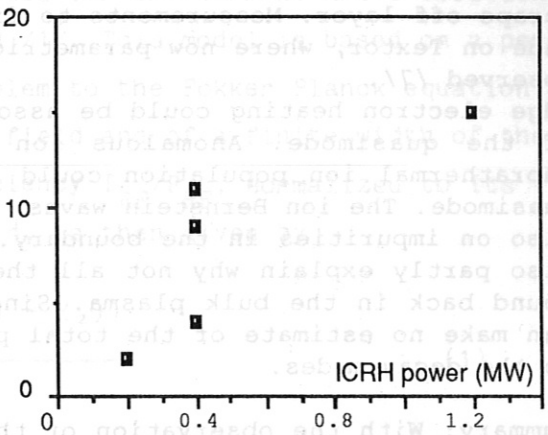

Fig. 5. Dependence of the 2H peak on ICRH power, no NI power

An additional H gas pulse made the instabilities appear, for a near central position of the resonance layer (r=0.03m), under all conditions (any antenna, down to 200 kW ICRH, any NI power). A clear anticorrelation, however, was then found between the amplitude of the 2H peak and the neutral injection power, as shown in Fig. 4. The amplitude of the 2H peak, measured under steady state conditions, increases with ICRH power (Fig. 5). This is in contrast to an experiment where, as the power was ramped up, the amplitude remained almost constant. Those effects can be understood in the following way: a better absorption of the fast wave, provided by the preheating with NI, will reduce the electric fields in the edge and thus the growth rate of the instabilities. The instabilities are also reduced by a higher NI power through the increased boundary temperature (theory predicts that the growth rate of the instabilities decreases for increasing boundary temperature). Higher RF powers result in higher RF electrical fields, and thus more instabilities. The heating of the boundary, due the instabities themselves, seems provide a type of feedback mechanism, so that, when the power is ramped up, the amplitude of the instabilities do not increase. We have also observed the instabilities, with a receiving probe located on the *inside* of the tokamak. Although fewer peaks were

present on the spectra, the 1H peak, with the frequency corresponding to the magnetic field at the *outside* egde of the plasma could, under some conditions, be identified.

Importance of those parametric decay instabilities: In many tokamaks direct energy deposition in the scrape off layer, was observed during ICRH. On Alcator, JET, Textor, among others, increases of electron temperatures in the edge were observed. On ASDEX, fast *deuterons* were observed in the edge, with second harmonic *hydrogen* heating /5/. To explain the Fe production at a target plate in Textor/6/, one has to postulate the presence of fast ions, accelerated in the perpendicular direction, in the plasma edge. The parametric decay instabilities, observed on ASDEX in the second harmonic regime, can provide the much sought after mechanism to explain the direct energy deposition in the scrape off layer. Measurements to find them in the minority regime were made on Textor, where now parametric decay instabilities have also been observed /7/.
Edge electron heating could be associated with electron Landau damping of the quasimode. Anomalous ion heating and the production of a suprathermal ion population could result from the damping of the ion quasimode. The ion Bernstein waves, excited in the edge, may be absorbed also on impurities in the boundary. The parametric decay processes may also partly explain why not all the RF power coupled to the plasma is found back in the bulk plasma. Since the probe was not calibrated, we can make no estimate of the total power transferred from the pump wave to the decay modes.

Summary: With the observation of those instabilities an important step was made in the understanding of the direct energy deposition on the ions and electrons of the scrape off layer. This direct energy deposition could be partly responsible for some of the impurity problems encountered with the ICRF heating method. Further investigation of the parametric decay instabilities may provide clues on how to avoid them and can thus contribute to an optimisation of the ICRF antennas and heating scenarios.

Aknowledgements: This work was carried out with the support of the Euratom Mobility of personnel scheme, and the support of the DOE/ASDEX,ASDEX-Upgrade collaboration contract. The authors also thank the ASDEX, ICRH and NI teams for their excellent support.

References:
/1/K.Steinmetz et al., Plasma Phys. and Contr. Nucl. Fus. Res., (Proc. 11th Int. Conf., Kyoto, 1986) Vol. 1, IAEA.Vienna(1987)461
/2/R.VanNieuwenhove,G.VanOost,J.-M.Noterdaeme,M.Brambilla,J.Gernhardt, M.Porkolab,subm.to Nucl.Fusion, and IPP Rep. III/129,Garching,Jan 88
/3/M.Porkolab, to be published
/4/F.N. Skiff, M.Ono, K.L.Wong, Phys. Fluids 27 (1984) 1051
/5/J.-M.Noterdaeme,F.Ryter et al.,Europhys.Conf.Abs,Vol11D,II(1987)678
/6/B.Schweer et al., Europhys.Conf. Abstracts, Vol 10C, I (1986) 399
/7/R.Van Nieuwenhove, G.Van Oost et al., this conference.

LOWER HYBRID CURRENT DRIVE EFFICIENCY IN ASDEX

F. Leuterer, F. Söldner
Max-Planck-Institut für Plasmaphysik, Garching, Germany
K. Yoshioka, T. Okazaki
Energy Research Laboratory, Hitachi Ltd., Hitachi, Japan
N. Fujisawa
Japan Atomic Energy Research Institute, Naka-gun, Ibaraki-ken, Japan

The ASDEX lower hybrid current drive experiments at 1.3 GHz have been re-evaluated in view of a new analytic model for the current drive efficiency in the presence of a dc electric field /1/. This model is based on a perturbation solution of the adjoint problem to the Fokker Planck equation and includes the effects of a dc electric field and of a finite width of the wave spectrum. The current drive efficiency I_{RF}/P_{RF}, normalized to its value $(I_{RF}/P_{RF})_o$ at zero electric field, is then given by

$$\eta/\eta_o = \frac{I_{RF}/P_{RF}}{(I_{RF}/P_{RF})_o} = \frac{\ln((1 - X_1)/(1 - X_2))}{X_2 - X_1} \qquad (1)$$

where $X_{1,2} = \alpha E_N u_{1,2}^2$ with $\alpha = 12/(Z+7)$, $E_N = E/E_{Dr}$, $u = v_{ph}/v_{th}$, $E_{Dr} = m_e v_{th} \nu_o/e$ and $\nu_o = n_e e^4 \ln\Lambda/2\pi \varepsilon_o^2 m^2 v_{th}^3$. The indices correspond to the limits v_{ph1} and v_{ph2} of the wave phase velocity spectrum. The normalized efficiency, equ. (1), is shown in Fig. 1 for various values of $(X_2/X_1)^{1/2}$, i.e. the width of the spectrum. The efficiency is seen to depend mainly on X_2, corresponding to the high phase velocity boundary of the spectrum. Its dependence on X_1 is rather weak.

For the limiting situation of a very broad spectrum, $X_2/X_1 \to \infty$, equ. (1) becomes nearly independent of X_1 and can be approximated as

$$\eta/\eta_o = - \ln |1-X_2|/X_2 \ . \qquad (2)$$

In the opposite situation of a narrow spectrum with $X_1 = X_2 = X$ we get

$$\eta/\eta_o = 1/(1-X). \qquad (3)$$

In the ASDEX-experiments the plasma current I_p was feedback controlled. The measured quantities are the net RF power P_{RF}, the line averaged electron density n_e, and the rate of change of the primary current I_{OH} in the

OH-transformer which is necessary to maintain a constant plasma current. $I'_{OH,OH}$ is its value just before the application of the RF-power, $I'_{OH,RF}$ its value during applied RF-power. Their ratio is shown in Fig. 2 as a function of RF-power for different densities. From Thomson scattering we obtained the variation of the central electron temperature T_{eo} as a function of P_{RF} and n_e, shown in Fig. 3. Using a measured electron density profile we determined the accessibility condition, $N_{\parallel acc}$, to the central region of the plasma by means of a raytracing code.

The plasma current can be written as the sum of an inductively driven current, for which we assume Spitzer conductivity, and an RF-driven current,

$$I_p = I_{Ind} + I_{RF} \quad . \tag{4}$$

From our measurements the RF-driven current can be determined as

$$I_{RF} = I_p \left[1-(I'_{OH,RF}/I'_{OH,OH})\cdot(T_{e,RF}/T_{e,OH})^{1.5}\right] \quad . \tag{5}$$

The temperature correction in this equation takes care of the variation of the Spitzer conductivity due to additional bulk electron heating by the RF-power, which is obtained from Fig. 3. The quantity X_2 is calculated from

$$X_2 = \alpha\, E_N\, u_{acc}^2 = 580 \cdot \alpha\, E/(N_{\parallel acc}^2\, n_e) \tag{6}$$

in the units V/m, 10^{12} cm^{-3}, with $E = -M\, I'_{OH,RF}/2\pi R$ and $M = 80$ µH for ASDEX. For the current drive efficiency at zero electric field we use our old experimental results of reference /2/

$$(I_{RF}/P_{RF})_o = a\cdot\mu\cdot g/n_e \quad , \tag{7}$$

where µ describes the fraction of accessible power, g is the theoretical dependence of the efficiency changing with $N_{\parallel acc}$, and a is a numerical fit parameter good up to densities of $n_e \approx 1\cdot10^{13}$ cm^{-3}.

In Fig. 4 we show the resulting experimental current drive efficiencies. For the determination of X_2 we took $Z = 3$. Comparing Figs. 1 and 4 we find a reasonable agreement. We should, however, not forget that the above model assumes homogeneous profiles for both current density and power absorption, complete power absorption by the fast electrons and that the central value calculated for v_{phacc} is the right value to substitute for $v_{ph\,2}$.

We may also compare our results in the form of the conversion efficiency P_{el}/P_{RF} as defined by N. Fisch and C. Karney, /3/, where for our situation

$P_{el} = - M I'_{OH,RF} I_{RF}$. Taking the theoretical zero electric field efficiency

$$\eta_o = \beta(u_2^2-u_1^2)/\ln(u_2/u_1) \quad , \tag{8}$$

where $\beta = 4/(Z+5)$, the conversion efficiency becomes

$$\frac{P_{el}}{P_{RF}} = -E \frac{I_{RF}}{P_{RF}} = -E_N \frac{\eta}{\eta_o} \eta_o = \frac{2\beta}{\alpha} \cdot \frac{\ln|(1-X_2)/(1-X_1)|}{\ln(X_2/X_1)} \quad . \tag{9}$$

This is shown as the solid lines in Fig. 5 as a function $X_2^{1/2} = (\alpha/2)^{1/2} \cdot u_{R2}$ with $u_R = v_{ph}/v_R$ and $v_R = v_{th}/(2\ E_N)^{1/2}$. We have confirmed that for the case of a localized spectrum, $X_2/X_1 = 1$, and for $Z = 1$, equ. (9) agrees very well with the numerical result of N. Fisch and C. Karney, /3/, except for the factor $2\beta/\alpha$ which is only close to, but not exactly unity. We see from Fig. 5 that the conversion efficiency is significantly degrated with increasing spectrum width X_2/X_1.

In Fig. 5 we have also plotted $P_{el}/P_{RF} = -M I'_{OH,RF} I_{RF}/P_{RF}$ for our experimental points from Fig. 4. Taking $Z = 3$ these points fit to curves in the range $(X_2/X_1)^{1/2} = 16$ to 32. This seems very high. However, we note that the empirical fit factor a in the steady state current drive efficiency is about a factor of two lower than estimated from theory /2/. If we include an absorption coefficient of ≈ 0.5, as was done in the evaluation of the PLT experiments, /4/, the points would fit to curves around $(X_2/X_1)^{1/2} \approx 4$, which seems much more realistic.

References:

/1/ K. Yoshioka, T. Okazaki, F. Leuterer, N. Fujisawa,
Physics of Fluids, to be published (April 1988)

/2/ F. Leuterer, F. Söldner, D. Eckhartt et al.
Plasma Phys. and Contr. Fus. 27, 1399 (1985)

/3/ C. Karney, N. Fisch, Phys. Fluids 29, 180 (1986)

/4/ C. Karney, N. Fisch, F. Jobes, Phys.Rev. A 32, 2554 (1985)

Figures:

1. Normalized current drive efficiency as a function of electric field.
2. Normalized primary current rate of change as function of the RF-power.
3. Central electron temprature with and without RF-current drive.
4. Experimental current drive efficiency.
5. Efficiency for conversion of RF-power into electromagnetic energy.

Fig. 1

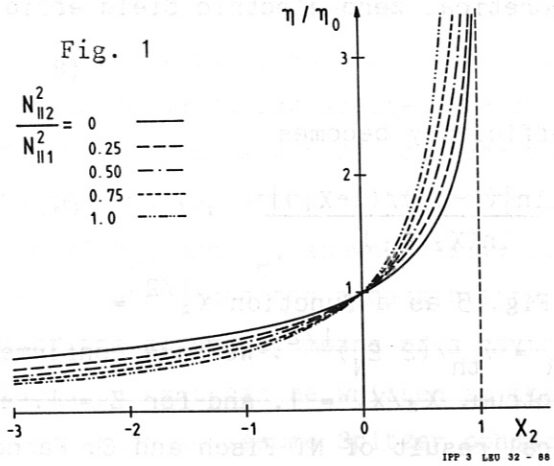

Fig. 3

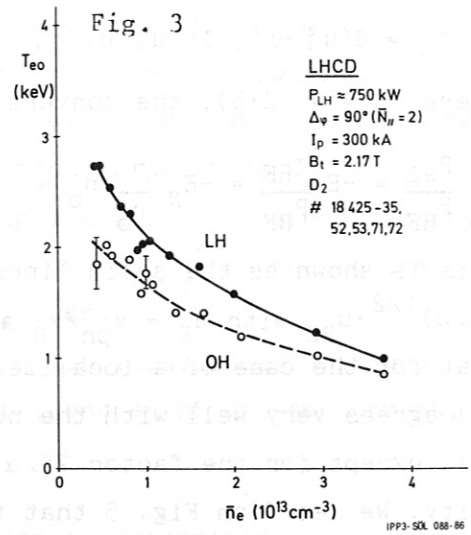

Fig. 4

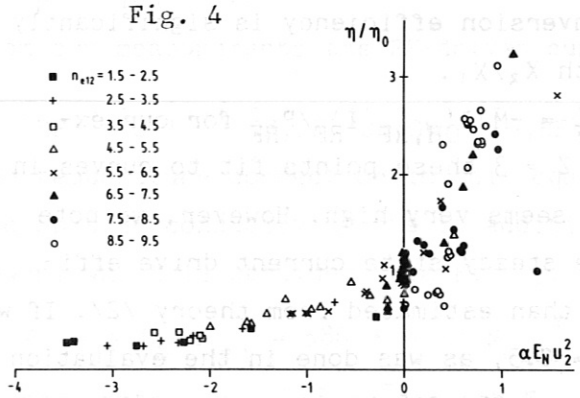

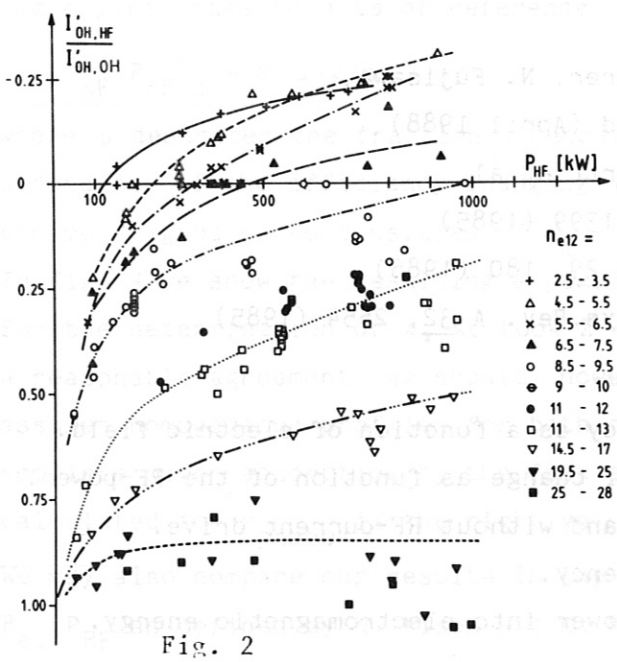

Fig. 2

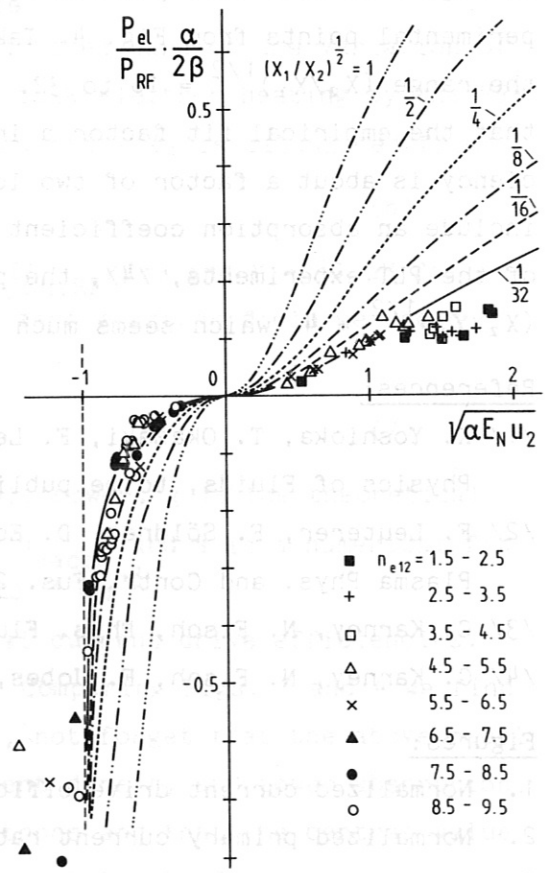

Fig. 5

Z_{eff}-PROFILES IN DIFFERENT CONFINEMENT- AND HEATING REGIMES OF ASDEX

K.-H. Steuer, H. Röhr, D.E. Roberts*, A. Eberhagen, G. Janeschitz, G. Fußmann, O. Gruber, K. McCormick, H. Murmann, J. Roth, F. Wagner
*Atomic Energy Corp., Pretoria, RSA

Max-Planck-Institut für Plasmaphysik
EURATOM Association, Garching, FRG

Introduction

Z_{eff} is an important quantity in fusion research. It should ideally be as small as possible to minimize both fuel dilution and radiation losses. Further, radial profiles of Z_{eff}, together with $T_e(r)$, are needed to derive $j(r)$ used in stability analysis. We report measurements of Z_{eff} profiles for a variety of ASDEX plasmas: ohmic (H and D; gas and pellet fuelling), and co and counter neutral beam heated plasmas.

Z_{eff} measurements

Z_{eff} profiles are measured from the intensity of plasma radiation in the near infrared. In this wavelength region recombination and line radiation are generally unimportant and the radiation is mainly bremsstrahlung. The intensity profiles are measured with the ASDEX 16 channel YAG laser Thomson scattering system (Fig. 1) /Ref. 1/. Each of the 16 detection boxes contains 3 broadband interference filters set at wavelengths of 850, 950 and 1000 nm. This provides a means of checking the λ^{-2} scaling of bremsstrahlung intensity and gives an approximate measure of the absence of line radiation. Up to the silicon avalanche diodes used as detectors, the system is identical to that used for Thomson scattering. For the Z_{eff} measurements, however, a DC-coupled circuit with a bandwidth of 50 kHz is used. The sample rate is typically 200 Hz. Comparison of the Abel-inverted radiation with hydrogen bremsstrahlung determined from simultaneously measured n_e and T_e profiles results in Z_{eff} profiles from +20 cm to -38.5 cm with a spatial resolution of about 3 cm. Under some conditions comparisons have been made with radially averaged Z_{eff} values from plasma resistivity and from sawtooth analysis. The latter method is based on the electron power balance in ohmic discharges, in the plasma centre, during the period of recovery after the sawtooth crash /ref. 2/. In addition, Z_{eff} has been estimated from impurity densities derived by two methods. Firstly, absolutely measured VUV line intensities of the four dominant impurities (Fe, Cu, O, C) are compared with those calculated by a time dependent impurity transport code using measured n_e and T_e profiles.

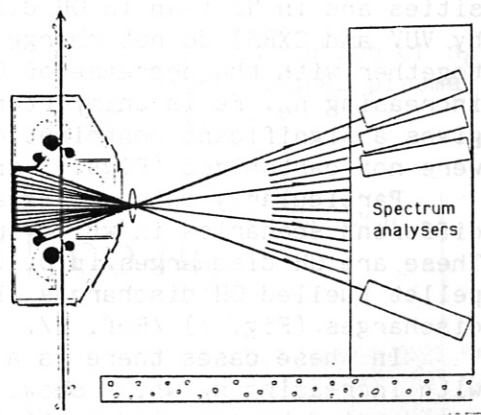

Fig. 1: Bremsstrahlung Z_{eff} setup

From this comparison an independent density profile is obtained for each impurity species, allowing its Z_{eff} contribution to be calculated. Secondly, the densities of the two light impurity species (O, C) can be also derived from charge exchange recombination spectroscopy (CXRS) resulting in an independent measurement of their Z_{eff} contribution. These spectroscopic Z_{eff} are generally less accurate than bremsstrahlung Z_{eff} but the resulting impurity densities yield considerable insight into the Z_{eff} behaviour reported in this paper.

Results and Discussion

Axial values of Z_{eff} as a function of n_e for steady state ohmic and co-NI heated discharges are shown in Figs. 2 and 3. Normally, Z_{eff} is found to decrease with increasing n_e, to be higher in D_+ than in H_+ plasmas, and higher in NI than in ohmic plasmas. The VUV Z_{eff} are in good agreement with the bremsstrahlung Z_{eff}, as are the sawtooth Z_{eff} for OH discharges in H_+. The CXRS Z_{eff} must be normalized to one point from the bremsstrahlung measurements because optical components of the CXRS diagnostic, inside the vacuum chamber, have been inaccessible to direct calibration. The CXRS Z_{eff} then show the same trends with n_e.

The above behaviour can be understood from the spectroscopic results. In ohmically and NI heated discharges O and C are the dominant light impurities with O giving the largest contribution to Z_{eff}. The VUV results for a transition from OH → co-NI heated plasma are shown in Fig. 4 for H_+ and Fig. 5 for D_+. The dominant heavy impurity in the H_+ discharge is Cu. It originates from the divertor plates and is more important at lower densities and in NI than in OH discharges. The densities of C and O (measured by VUV and CXRS) do not change strongly with n_e so it is this fact, together with the decrease of Cu, that explains the decrease in Z_{eff} with increasing n_e. Fe is unimportant in H_+ discharges due to carbonization, but gives a significant contribution to Z_{eff} in D_+ discharges where the walls were not carbonized (Figs. 3 and 5).

Particularly interesting are the Z_{eff} results obtained in three rather different scenarios in which improved energy confinement is found in ASDEX. These are OH discharges in D_+ with reduced gaspuff (Fig. 2) /Ref. 3/, pellet fuelled OH discharges (Fig. 6) /Ref. 4/, and counter-NI heated discharges (Fig. 7) /Ref. 5/.

In these cases there is a reversal of the trend of Z_{eff} decreasing with increasing n_e which shows that the improved energy confinement is accompanied by improved particle confinement. The strong accumulation of light impurities in counter NI discharges can be seen from the O^{8+} (Fig. 7) and C^{6+} densities. The relatively slow initial increase of $n_O{}^{8+}$ and $n_C{}^{6+}$ leads to a decrease of Z_{eff} as in the normal co-NI case. However, the impurity density increase is much steeper later on, so that Z_{eff} increases during the phase when the global energy confinement is also increasing. For counter-NI the neoclassical Z_{eff} is in good agreement with the bremsstrahlung Z_{eff} and this is also true for the OH pellet case (Fig. 6). In the improved confinement OH regime $Z_{eff}(r)$ shows slight peaking at the plasma centre at later times (Fig.8) but this is not seen in the pellet (Fig. 9) or counter-NI discharges.

Summary

The present measurements have shown a wide variety of behaviour of Z_{eff} in ASDEX plasmas and Z_{eff} values ranging from 1.2 to ~5 have been found. In particular, for three different improved energy confinement regimes, the Z_{eff} results indicate correspondingly improved particle confinement.

Ref. 1 H. Röhr, K.-H. Steuer et al., Nucl. Fusion 22 (1982), 1099
Ref. 2 A. Eberhagen, Internal Report IPP III/124, 1987
Ref. 3 E.R. Müller et al., this conference
Ref. 4 O. Gruber et al, this conference
Ref. 5 O. Gehre et al, Phys. Rev. Lett., to be published

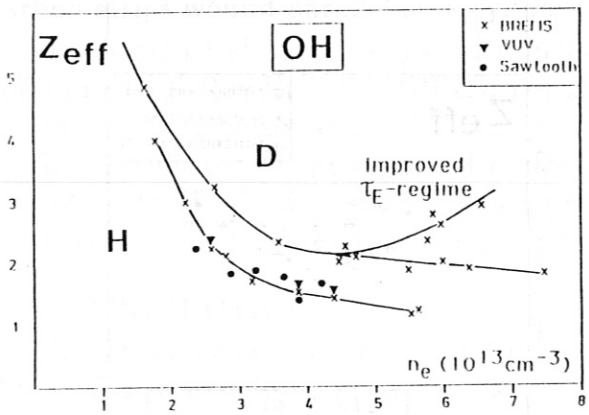

Fig. 2: Z_{eff} as a function of n_e for OH-plasmas in hydrogen (H) and deuterium (D).

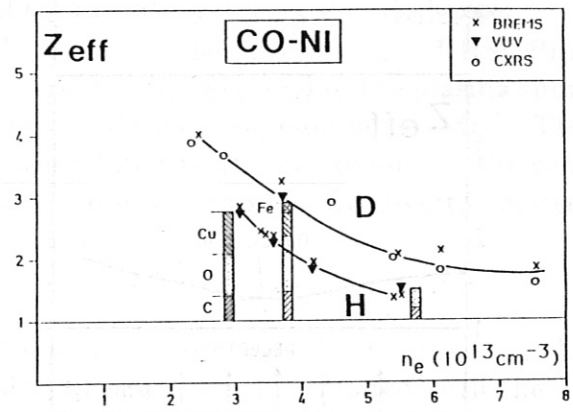

Fig. 3: Z_{eff} as a function of n_e for co-NI heated plasmas in H and D.

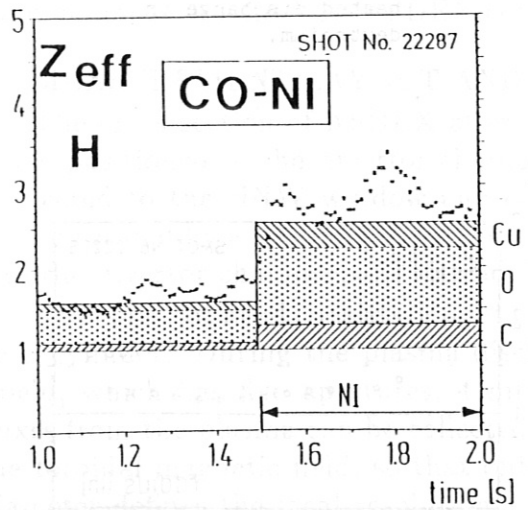

Fig. 4: bremsstrahlung Z_{eff} and the VUV imp. contributions during a transition from OH→co-NI in a hydrogen plasma.

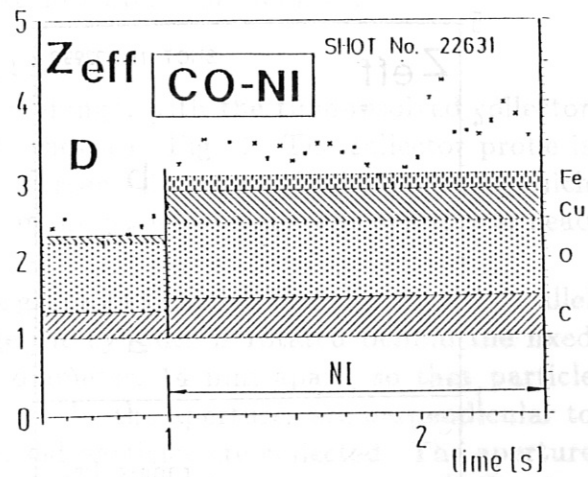

Fig. 5: bremsstrahlung Z_{eff} and the VUV imp. contributions during a transition from OH→co-NI in a deuterium plasma.

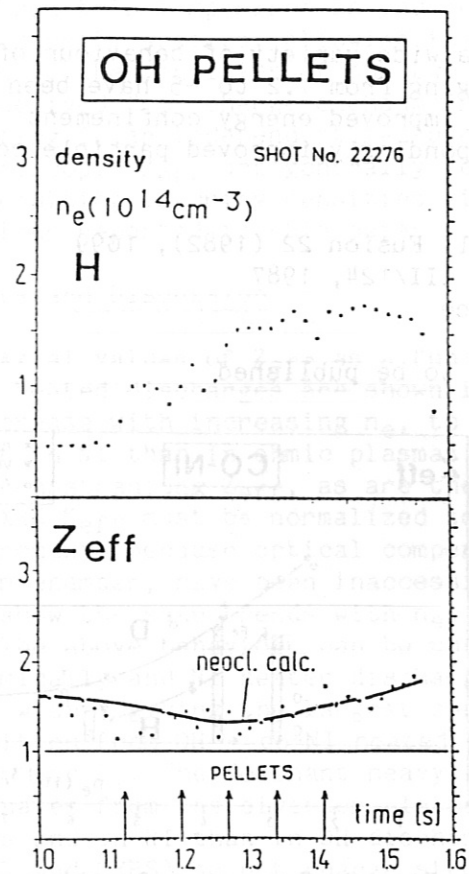

Fig. 6: Time dependence of n_e (above) and Z_{eff} (below) in a OH pellet refuelled discharge in hydrogen.

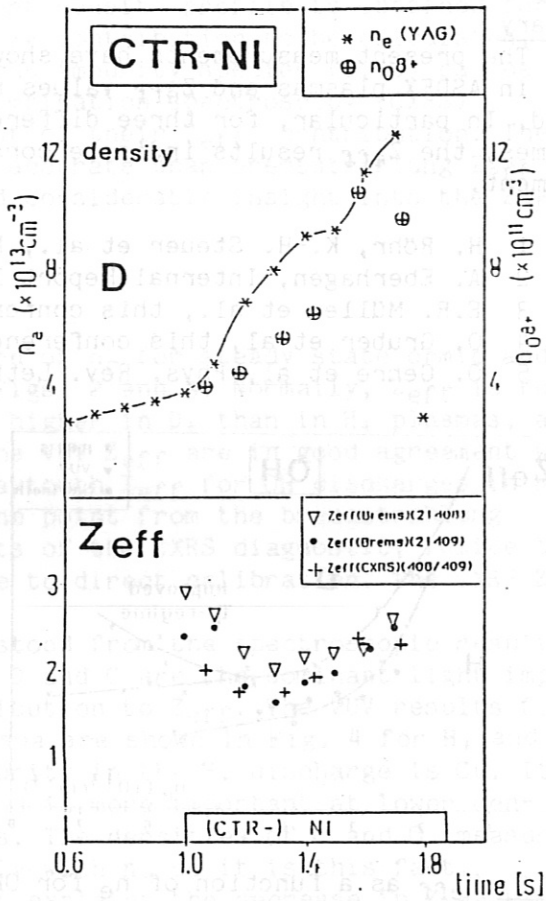

Fig. 7: Time dependence of n_e and n_{O8+} (above) and Z_{eff} (below) in a counter NI heated discharge in deuterium.

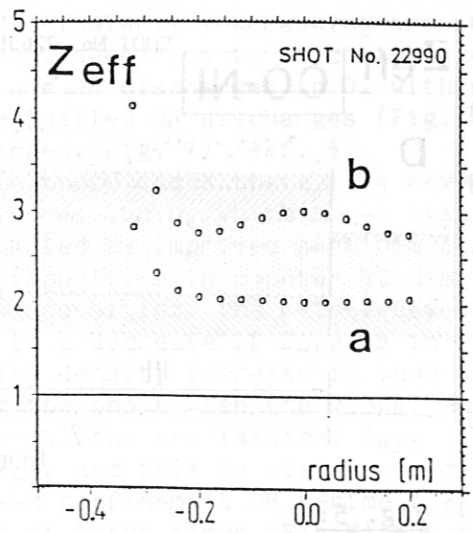

Fig.: 8: Radial profiles of Z_{eff} for OH discharges in deuterium. (a) "normal" regime, (b) improved confinement regime ($n_{eo}=6.6 \times 10^{13}cm^{-3}$, see Fig. 2).

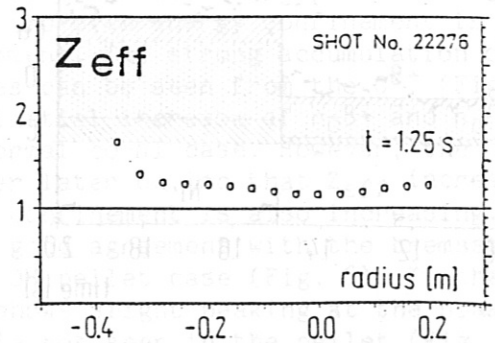

Fig.: 9: Radial profile of Z_{eff} for a pellet fuelled OH discharge in H (see Fig. 6).

IMPURITY FLUX ONTO THE DIVERTOR PLATES OF ASDEX

A. P. Martinelli, E. Taglauer, and ASDEX Team

Max–Planck–Institut für Plasmaphysik, EURATOM Association,
D–8046 Garching, Federal Republic of Germany.

ABSTRACT

Fluxes of metallic impurities onto the divertor plates of ASDEX with different plasma parameters were collected and resolved in space and time by means of five carbon strips wound parallel on a cylindrical core rotating during the discharge.

Ion beam accelerator analysis (Rutheford Backscattering Spectroscopy (RBS), Proton Induced X-Ray Emission (PIXE)) of five carbon strips exposed to the plasma show a different distribution of the Fe and Cu atoms across the scrape-off layer (SOL). The Fe fluxes collected in the centre of the SOL are related to the Fe content in the central plasma; the Cu deposition has a maximum value close to the Cu divertor plates, indicating evaporation or sputtering from the plates.

INTRODUCTION

In earlier measurements prior to the "hardening" process, the Fe fluxes in the ASDEX divertor obtained by means of a collector probe were correlated with the Fe densities measured in the main discharge chamber by using a transport model [**1**]. First measurements with the collector probe differently positioned in the divertor of ASDEX after "hardening"are now reported and discussed, as a basis for establishing again a correlation between probe results in the divertor and plasma parameters in the main chamber, for the new ASDEX configuration after "hardening".

MEASUREMENT LAYOUT AND METHOD

The cross-section of ASDEX after "hardening", with the time-resolved collector probe positioned in the divertor chamber, is shown in Fig. 1. The collector probe is connected to the NNW window and consists essentially of a cylindrical head, which can be rotated by a stepping motor, and of a manipulator to insert the cylindrical head into the divertor chamber, and extract it.

The collector head consists of a set of five graphite (PAPYEX) strips wound parallel on a cylinder. During the plasma discharge the cylinder is rotated behind the fixed shield, which has five apertures, 4 mm in diameter, 14 mm apart, so that particle fluxes from the plasma can be collected. As a rule, the apertures are perpendicular to the toroidal magnetic field, so that only ionised particles are collected. The aperture diameter defines the local resolution and, together with the rotation speed, the time resolution (a few hundred ms).

After plasma exposure, the cylinder is withdrawn from the divertor chamber and the five strips are taken off and analysed for metallic impurities by PIXE and RBS

using a 2.5 MeV van de Graaf accelerator.

The measurement results show coverages (atoms/cm^2) on the strips between 1/10 of a monolayer (roughly the detection limit) and a few monolayers.

EXPERIMENTAL RESULTS

Figure 2 shows the Cu and Fe fluxes calculated from the measured coverages on strip 1 (1 cm from the Cu divertor plate), on strip 2 (2.4 cm from the Cu divertor plate), and so on, as a function of time during discharge no. 21007 (NI discharge).

The Cu flux attains a maximum value of $6 \cdot 10^{16}$ atoms/cm^2 s, a factor of 10 higher than the correspondent maximum Fe flux.

It is seen in Fig. 2 that after about 1.2 s both the Cu and Fe signals strongly drop. At the corresponding spot on the graphite strip one observes a surface-structure change. This change is a consequence of high-energy deposition during neutral beam injection; the deposited metallic impurities cannot be further observed.

Figure 3 shows the Cu and Fe deposits collected on strip 1, strip 2, and strip 3 (3.8 cm from the plate), as a function of the time during discharge no. 21861.

It is again seen that the Cu coverage (flux) is a factor of 10 larger than the Fe coverage (flux) on strip 1.

It is also observed that the coverage (flux) on strip 2 during NI is strongly reduced. Again, surface examination of the strip shows a substantial structure change. This indicates that strip 2 has reached a high temperature during the NI, higher than strip 1, which shows no surface alteration though closer to the divertor plate than strip 2.

This is explained by the position of strip 2 on the separatrix, where the energy deposition is maximal.

DISCUSSION

Further experimental results support the trend shown by the above reported results obtained with the collector probe in the ASDEX divertor after the "hardening" process. By way of discussion and preliminary conclusion the following can be stated:

- collected Cu and Fe fluxes are very different in value and show different radial dependences.
- collected Fe fluxes correlate with the Fe fluxes measured in the main plasma chamber and do not appear to be directly generated in the divertor chamber. The overall Fe outflux from the plasma can be determined by taking the values of the Fe fluxes over the width of the SOL in the divertor and integrating them over the circumference of the divertor and the four divertor sections (upper, lower, inner, outer). Overall Fe fluxes up to $5 \cdot 10^{18}\ s^{-1}$ are obtained.
- measured Cu fluxes close to the Cu divertor plates are a factor of up to 10 higher than the Fe fluxes; this indicates erosion of the divertor plates.

REFERENCES

[1] Taglauer, E., Nucl. Instr. and Meth. in Phys. Research B13 (1986)218-224

FIGURE CAPTIONS

Fig. 1. Schematic cross-section of the ASDEX Tokamak after "hardening" showing the position of the collector probe in the upper divertor chamber.

Fig. 2. Cu and Fe fluxes on strip 1 (1 cm from the divertor plate), strip 2 (2.4 cm), strip 3 (3.8 cm), strip 4 (5.2 cm) as function of the time in discharge no. 21007.

Fig. 3. Cu and Fe deposits (and fluxes) on strips 1, 2, 3 as functions of the time in discharge no. 21861. The upper part shows the discharge parameters I_p (plasma current), n_e (electron density), and NI (neutral beam injection).

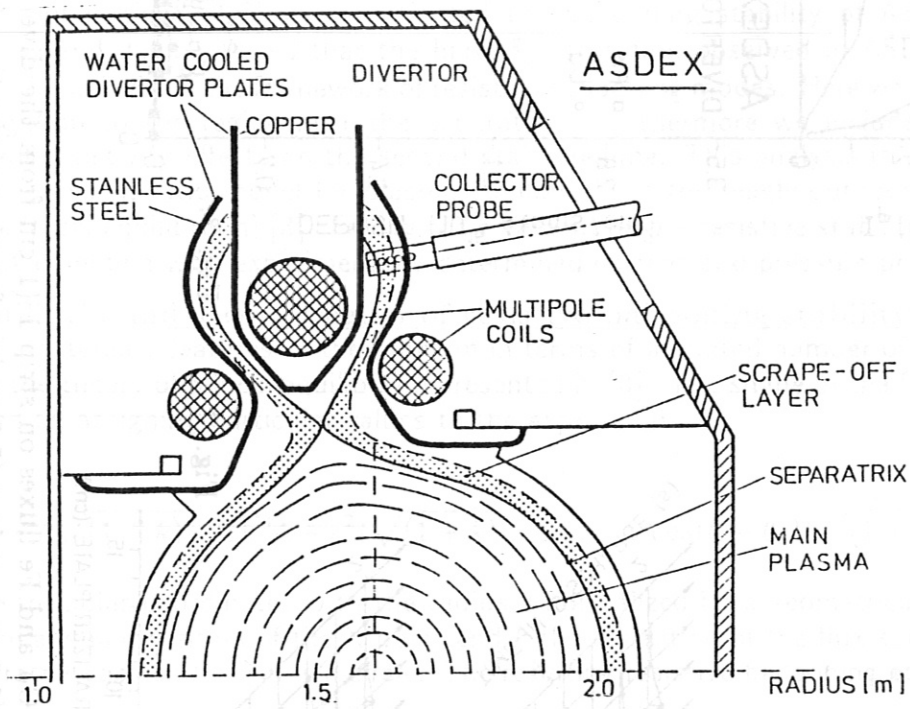

Fig. 1. Schematic cross-section of the ASDEX Tokamak after "hardening" showing the position of the collector probe in the upper divertor chamber.

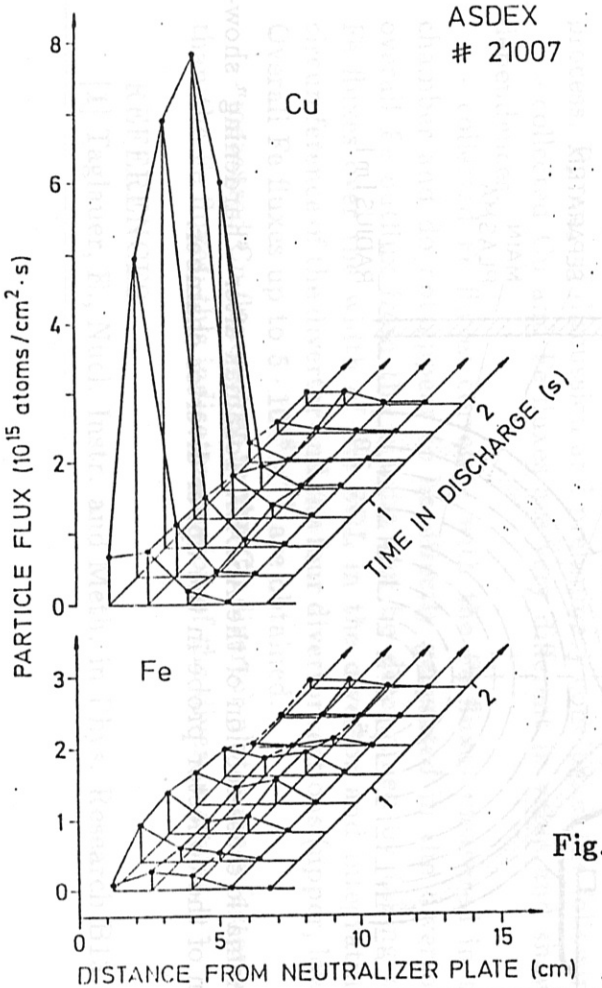

Fig. 2.

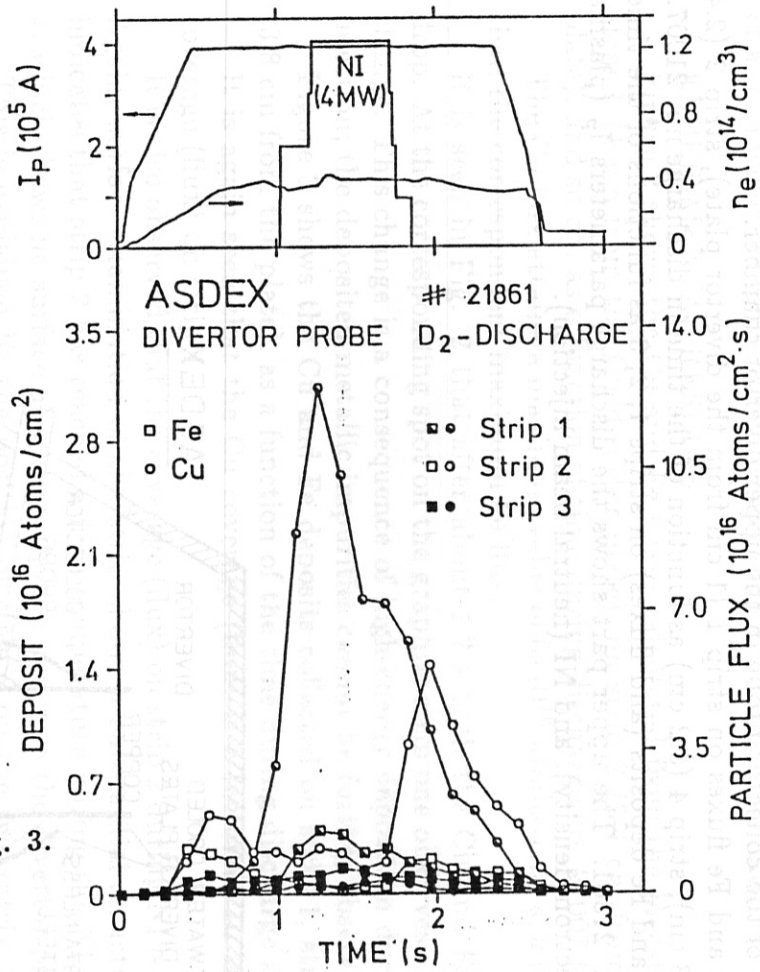

Fig. 3.

Fig. 2. Cu and Fe fluxes on strip 1 (1 cm from the divertor plate), strip 2 (2.4 cm), strip 3 (3.8 cm), strip 4 (5.2 cm) as function of the time in discharge no. 21007.

Fig. 3. Cu and Fe deposits (and fluxes) on strips 1, 2, 3 as functions of the time in discharge no. 21861. The upper part shows the discharge parameters I_p (plasma current), n_e (electron density), and NI (neutral beam injection).

RESISTIVE BALLOONING MODES UNDER PLASMA EDGE CONDITIONS

K. Grassie and H.P. Zehrfeld

Max-Planck-Institut für Plasmaphysik
EURATOM Association, D-8046 Garching, Federal Republic of Germany

C.M. Bishop, R.J. Hastie and T.C. Hender

Culham Laboratory
UKAEA / EURATOM Fusion Association
EURATOM Association, Abingdon, Oxfordshire, OX14 3 DB, U.K.

Introduction: Recently resistive ballooning modes have become the object of intensified theoretical investigation. The reason for this increased interest is that they may be linked to confinement degradation observed in tokamak experiments at high plasma pressure. In previous publications [1,2] we investigated the ballooning stability of ASDEX high-β_p discharges and demonstrated that the hard β_p-saturation observed in ASDEX can be naturally explained within the framework of resistive ballooning modes. Here we concentrate the investigation to the region near the separatrix. Furthermore we include a detailed discussion of resistivity effects on the second stable regime. This analysis is based on an analytic large aspect-ratio model for plasma equilibrium in the neighbourhood of a given flux surface (local equilibrium) [3]. Finally, we comment on the resistive stability of toroidal 2-D ASDEX equilibria with experimentally determined current and pressure profiles.

Local equilibria and second region of resistive ballooning stability: To elucidate the characteristic features of the problem in terms of a limited number of parameters we refer to the theory of a local equilibrium presented in [3]. The shape of the flux surfaces is controlled by assigning particular values to the expression

$$(1)\quad k^2 = r^2(\sqrt{(1+k)}-1)^2[4+r^2(\sqrt{(1+k)}-1)^2 - 4rcos(\theta-\theta_x)(\sqrt{(1+k)}-1)].$$

Here (r,θ) are polar coordinates with the radius r normalized by a geometrical parameter r_0, θ_x is the angular position of the X-point and k the distortion of the flux surface; $k=1$ is the separatrix case and $k=0$ is a circle. The resulting resistive ballooning equations are

$$(2)\quad \frac{b}{h}\frac{d}{d\theta}[\frac{b}{hL}(\frac{1}{b^2}+P^2)\frac{du}{d\theta}] - \alpha K(u+v) - \gamma^2(\frac{1}{b^2}+P^2)u = 0$$

and

$$(3)\quad \frac{b}{q^2h}\frac{d}{d\theta}[\frac{b}{h}\frac{dv}{d\theta}] + \alpha K[4\frac{\gamma^2}{\alpha^2}+\frac{\eta n^2}{S_A\gamma}]u - \{\frac{\eta n^2}{S_A\gamma}[-\alpha K+\gamma^2(\frac{1}{b^2}+P^2)] + \frac{\gamma^2}{q^2}\frac{1+\beta}{\beta}\}v = 0$$

where W, D, b, h and f are defined in [5] and

$$K = -\frac{1}{h}[P(\frac{dr}{d\theta}cos\theta - rsin\theta) + \frac{1}{b}(\frac{dr}{d\theta}sin\theta + rcos\theta)]$$

$$P = -b\int [\alpha\frac{W}{D} - \Lambda + 2\frac{b}{f} - \alpha r cos\theta]\frac{h}{b^3}d\theta$$

$$L = 1 + \frac{\eta n^2}{S_A\gamma}[\frac{1}{b^2} + P^2],$$

with $\alpha = -2\mu_0 r_0 r^2 p'/{B_p}^2$, $\beta = \gamma_T\mu_0 p/B^2$, the magnetic Reynolds number $S_A = \tau_R/\tau_A$ and the ratio of the specific heats $\gamma_T = c_p/c_V$ and the growth rate γ is normalized to the Alfvén frequency $\gamma_A = \sqrt{{r_0}^2{B_p}^2/(r^2\mu_0\rho)}$

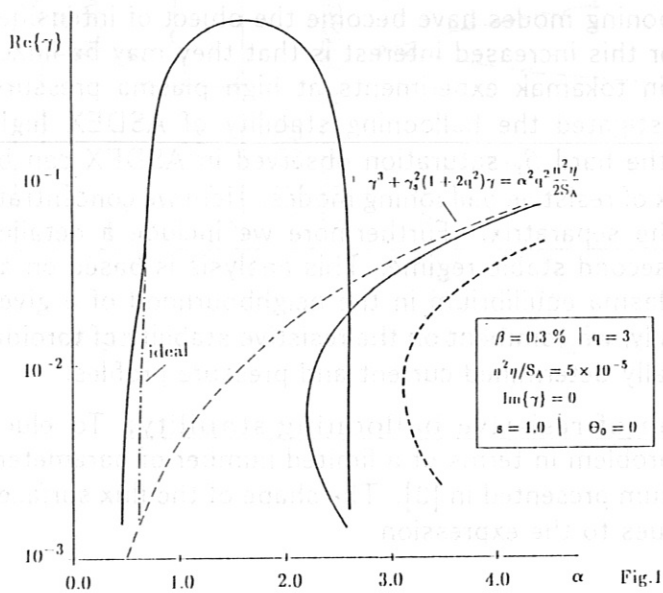

Fig.1

In the limit of circular flux surfaces ($k = 0$) these equations reduce to the $s - \alpha$ model, with the shear s related to the current density parameter Λ by $s = 2 - \Lambda$. We start the investigation of the second regime in this limit. Fig.1 shows the real part of the growth rate versus α for ideal ballooning modes (dot-dashed line) and resistive modes (solid lines). The hat-shaped curve shows second stability behaviour. The slight bulge in this curve at $\alpha \sim 0.6$ indicates the transition to overstability [6]. This resistive curve closely parallels the ideal stability curve and is reproduced by the Δ'-criterion for resistive ballooning modes [6,7] to reasonable accuracy:

$$\Delta' = \frac{2\gamma^{5/4}(1+2q^2)^{1/4}}{S_A(\eta^2 s^2 q^2/S_A)^{3/4}}\left\{\frac{\Gamma(\frac{1}{4})}{\Gamma(\frac{3}{4})} - \frac{\Gamma(\frac{1}{4}+\frac{\hat{\gamma}}{4})}{\Gamma(\frac{3}{4}+\frac{\hat{\gamma}}{4})}\right\}^{-1}. \tag{4}$$

with $\hat{\gamma} = \gamma\gamma_A/\gamma_R$, $(\gamma_R/\gamma_A)^3 = n^2\eta s^2 q^2\beta^2(1+2q^2)/S_A$ and where Δ' is in general to be evaluated numerically [8]. This dispersion relation (4) is derived in the limit $\gamma << \gamma_S = \sqrt{\beta}$, where γ_S denotes the sound frequency. In the other limit ($\gamma >> \gamma_S$) a compressibility mode, not driven by Δ', can occur. Its growth rate is governed by the dispersion relation [9]

$$\gamma^3 + {\gamma_S}^2(1+2q^2)\gamma = \alpha^2\frac{\eta n^2 q^2}{2S_A} \tag{5}$$

This mode can also be seen to occur in our numerical results in Fig.1, where the branch occuring for $\alpha > 2.6$ ($\beta = 3 \times 10^{-3}$) is compared with the solution of (5) (long-dashed line). It should be noted that in general $\gamma << \gamma_S$ for typical tokamak parameters, but in the second stable regime the high α-values make the region where $\gamma \sim \gamma_S$ more accessible. From Fig.1 it can be seen that the dispersion relation (5) continues to apply reasonably well to the regime $\gamma > \gamma_S$ where $\gamma \propto \eta/(S_A \gamma_S{}^2)$. Thus we conclude that the existence of a second stable regime depends on γ_S and S_A – for large enough values of either parameter a second stable region exists below the critical value of α at which compressibility modes (5) are destabilized. This is separately demonstrated by the short dashed curve in Fig.1, representing the compressibility mode for $\beta = 5 \times 10^{-3}$. The corresponding hat-shaped solutions are essentially unchanged with respect to this increase in β, so that effectively a second stable window exists for this case. It should be noted that the picture is in general more complicated, since the region of instability has to be maximized by optimizing the free parameter θ_0 which appears in eqs.3,4. Our conclusions presented above, however, are not affected by the variation of θ_0. Furthermore we find similar results on the basis of a model where the Shafranov shift of circular flux surfaces is taken into account.

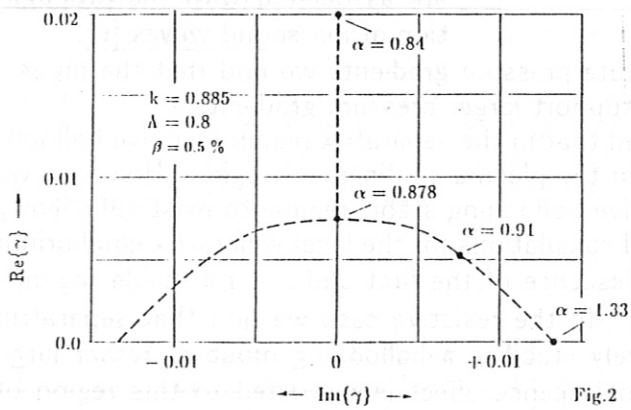

Fig.2

We now move on to study the non-circular case, i.e. $k > 0$. Fig.2 shows for $k = 0.885, \Lambda = 0.8$ the growth rate in the complex γ-plane for a branch entering a second stable resistive ballooning regime. There are, however, branches with $\gamma > \gamma_S$ which do not show second regime stability as α is increased; these branches can be supressed by increasing the sound frequency. For the ideal ballooning mode coalescence of the first and second stable regime occurs as the separatrix is approached ($k \rightarrow 1$) for a sufficiently high current density parameter [5].

It has only proved possible, for the cases examined, to obtain this coalescence for the resistive ballooning mode by increasing the local β_0 to 5%, which is rather larger than the expected values near the separatrix. For $\beta_0 < 5\%$ and large $k > 0.9$ an unstable mode, which may be related to the $\gamma \propto S_A{}^{-1/2}$ (as $S_A \rightarrow \infty$) branches of Ref.10, occurs. The quantitave dependences of these modes on the parameter k and the question whether and how their behaviour is related to the appearence of compressibility modes is still under investigation.

<u>Ballooning stability in the ASDEX separatrix region:</u> We now briefly examine the ballooning stability of a typical ASDEX high-β_p discharge by solving the full resistive ballooning equations on the basis of a separatrix-bounded MHD equilibrium [1,2]. To make parametric studies we alter the value of the pressure gradient from the experimentally observed quantity using a multiplication factor C_p. Results for the real part of the growth rate versus this factor C_p are shown in Fig.3 for various flux surfaces from $r/a \simeq 0.87$ to $r/a \simeq 0.994$.

In line with our previous results [1,2] we find a transition from purely growing to overstable modes, when compressibility effects become important.

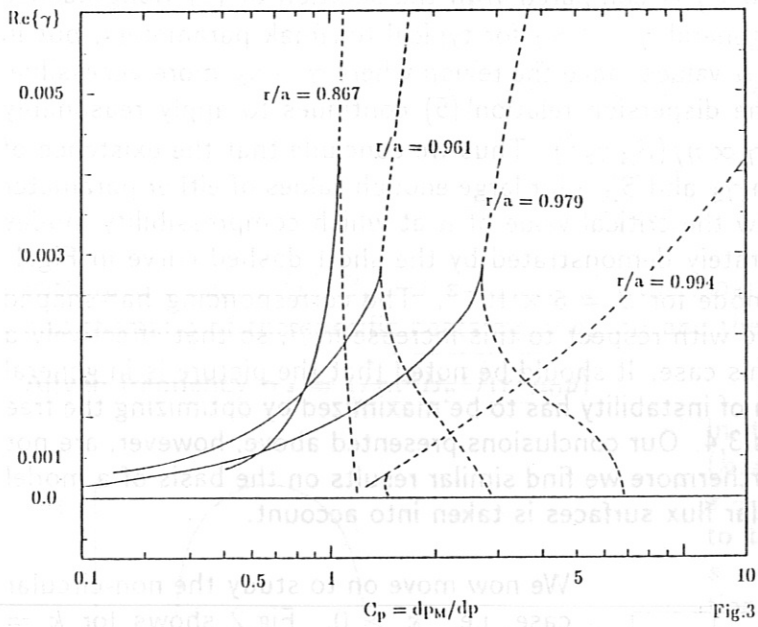

Fig.3

As soon as the bifurcation into the complex γ-plane occurs, the real solutions form separate branches which move to larger multiplication factors with decreasing growth rates (dashed lines), whereas the overstable branches (solid lines) show the opposite behaviour and are therefore the more unstable solutions.
From the observation that the bifurcation to overstability moves to smaller values of $Re\{\gamma\}$ when r/a increases ($\rightarrow \eta$ decreases and the strong compressibility dependence of the bifurcation point we conclude that the overstable branches are associated with the propagation of ion sound waves [6].
Interpreting these results in terms of absolute pressure gradients we find that the higher-shear surfaces close to the separatrix can support larger pressure gradients.

Conclusions: To summarize we have found that in the separatrix region resistive ballooning modes are generally more stable than in the plasma confinement region. However, we have demonstrated that for a second resistive ballooning stable regime to exist sufficiently large values for γ_S or S_A are required. Ideal calculations for the local separatrix equilibrium model show Bishop's results [4,5] for coalescence of the first and second stable regimes as the separatarix is approached ($k \rightarrow 1$). In the resistive case we find that separatrix effects are only strong enough to completely stabilize a ballooning mode at rather large values of $\beta_0 (> 5\%)$. Consequently the coalescence effect is restricted to this region of parameter space. Whether the small growth rates, which in general accompany resistive ballooning modes near $k = 1$, inhibit the L-H transition predicted in Refs. 4,5, requires additional analysis. Finally we found ASDEX high-β_p equilibria to be resistively unstable with small growth rates below the maximum value of β_p. In the separatrix region larger absolute pressure gradients are supported so that growth rates decrease and corresponding effects on the transport do not appear to be significant here.

1. K. Grassie and H.P. Zehrfeld, IPP Report 5/16 (1987) (to be published in Nucl. Fus.).
2. K. Grassie and H.P. Zehrfeld, Signatures of Resistive Ballooning Modes For ASDEX High Beta Discharges (1987) (to be published in Nucl. Fus.).
3. C.M. Bishop, Culham Report CLM-R249.
4. C.M. Bishop, Nucl. Fusion **24**, p. 1579.
5. C.M. Bishop, Nucl. Fusion **26**, p. 1063.
6. J.W. Connor et. al., Baltimore IAEA **III**, p. 403.
7. J.F Drake and T.M. Antonsen, Phys. Fluids **28**, p. 544.
8. A. Sykes et. al., Plasma Physics **29**, p. 719.
9. T.C. Hender et. al., Phys. Fluids **27**, p. 1439.
10. A.H. Glasser et. al., Proc. Oxford EPS, paper A 3.1.

q-PROFILE MEASUREMENTS IN THE CENTRAL PLASMA REGION OF ASDEX

K. McCormick, A. Eberhagen, H. Murmann and the ASDEX Team

MPIPP, EURATOM Association, Garching, FRG

Abstract: Using the Lithium-Beam-Spectroscopy (LBS) technique /1/ q-profile measurements have been carried out in the central region of diverted, ohmic ASDEX plasmas over a range $q(a)=2.9-5.3$ for $\bar{n}_e \sim 1\times10^{13}cm^{-3}$. The experimental results are consistent with a flat q(r) profile having $q(o)\sim1\pm0.06$ and exhibiting a slight tendency towards lower q(o) for decreasing q(a).

Motivation: Previous LBS measurements /2/ of q(o) in ASDEX for $q(a)\sim3.3$ gave $q(o)\sim1$ during ohmic heating. On TEXTOR $q(o)<1$ is measured over the range $q(a)=2.1-6.3$ /3/, whereas on TEXT q(o) is determined to be related to q(a), having $q(o)>1$ for large q(a) and vice versa.

In order to provide a broader data base for comparison with these findings, the LBS technique is used to investigate q(o) for a variety of q(a).

Experiment: The q(a) scan is performed in four discharge series whose parameters are listed in Table 1 along with the deduced q(o) values from neoclassical resistivity (NR) and LBS, as well as the sawtooth (ST) inversion radius r_{ST} from LBS, NR (here $r_{q=1}$ is equated to r_{ST}) and electron-cyclotron-emission (ECE). Three series have two I_p plateaus each, thereby enabling the relative $\Delta q(r)$ to be monitored more precisely since each plateau has a common measurement base line. The fourth series features a radial displacement of the plasma (R~166.5-163 cm) over 0.8 sec to achieve a moderate radial scan within one shot. Except for $q(a)=5.3$, where it is not certain, ST are present in all series with $\Delta Te_0/Te_0\sim5-8\%$. Series #1 is with hydrogen, the others with deuterium. Based on NR, $Z_{eff}\sim4-6$!

The density $\bar{n}_e$ of $\sim1\times10^{13}cm^{-3}$, plasma currents and toroidal fields chosen represent a balance between optimizing the LBS signal (low $\bar{n}_e$, high B_t) and the hindering of runaways (high $\bar{n}_e$, low I_p). Based on the gathered experience a larger q(a) range than covered here is accessible.

Results: The LBS technique measures the local magnetic field pitch angle $\theta_p=\tan^{-1}(B_p/B_t)$. Figure 1 illustrates the noise level and temporal behavior of $\theta_p(t)$ for series #1 at several values of the flux-surface radius r_f. The corresponding pitch angle θ_p^c profiles, adjusted to cylindrical geometry, are plotted in Fig. 4a; the values represent averages over 200 ms around the given time points, hence ST activity is completely averaged out. The representative error bar reflects the base line uncertainty (direction of $\vec{B}_t$) - accounting for ~2/3 of the total - and of θ_p^c itself.

Straight-line fits to the θ_p^c data in the central region, corresponding to a constant $q(=r_f/R\tan\theta_p^c)$, yield $q(o)\sim1.06$ and 0.95 for t=1 and 1.8 sec, respectively. Although neither Thomson scattering nor ECE profiles are available for corroborative evidence, the $r_f(q=1,\ t=1.8)\sim15.2$ cm value matches the $r_f(q=1)\geq1+a/q(a)$ $(1+40.2/2.93=14.7$ cm) scaling of the other series. By the same account, $r_f(q=1)$ for t=1 sec should be ~8.6 cm, meaning that only two measurement points are inside the expected q=1 surface, which is not adequate to characterize q(o).

The 2nd series was plagued with x-rays to the extent that no reasonably reliable θ_p measurement was possible. Nevertheless, the series serves to show that the $r_f(q=1)$ radius derived using neoclassical resistivity, under the assumption of a flat electric field- and Z_{eff}-profile, corresponds well with r_{ST}.

For the 3rd series, x-ray development again disturbed the diagnostic going into the second I_p plateau. Fig. 3 illustrates that up to this point, θ_p changes little in the inner region. The θ_p^c $(r_f,\ t=1.0)$ plot of Fig. 4b yields $q(r_f<9\text{ cm})\sim1.01\pm0.12$. For comparison, θ_p^c and q derived from neoclassical and Spitzer conductivity are also presented.

The typical broadening of the Te profile in response to a decrease in q(a) is demonstrated in Fig. 3a. Figure 3b serves both to convey an impression of the error bars on the Te-based calculation of θ_p^c over the series, as well as to confirm that a perceptible change in θ_p^c vs q(a) is to be expected only for $r_f>10$ cm.

The fourth series produced only a very marginal scan in r_f of ~0.6-1.1 cm due to the fact that θ_p is interrogated along a line inclined about 59° to the midplane. Nevertheless, θ_p^c $(r_f>4$ cm) in Fig. 4c is well documented: $q(r_f<11.2\text{ cm})\sim1.0^{+0.05}_{-0.04}$; $r_{ST}\sim12.1$ cm and $r_f(q=1)=12.9$ cm for neoclassical resistivity.

Discussion: Within this limited data base, varying q_a over 5.3-2.9 has ostensibly altered q(o) from ~1.06 to o.95. However, not enough radial points were present within the potential q=1 surface to convincingly describe q(o) for q(a)=5.3, and at q(a)=2.9 the uncertainty in θ_p^c encloses q(o)=1. One might fault the linear θ_p^c data fit within q=1; notwithstanding, a close examination of such furnishes no compelling motivation to introduce any other algorithm in the central region. Within any one series, local excursions of q(r) from the indicated value cannot be precluded, but may be regarded as unlikely when considering the overall direction of the results.

The experimental data are not consistent with the neoclassical prediction that q continues to monotonically decrease within $r_{q=1}$. On the other hand, the better agreement with the Spitzer profile is probably specious: Quite systematically - over a wider parameter range than presented here - Spitzer resistivity fails to correctly give r_{ST} and for low-q(a), sawtoothing discharges it often yields q(o)>1. In short, it is necessary to invoke neoclassical effects to approximately describe the experimental situation. The discrepancies within $r_{q=1}$ may be at least partially attributed to two effects: a) Due to the absence of points near the plasma center and the fit function chosen, the T_e profile is taken to be more peaked than in fact. (See Fig. 3a), b) The calculations assume a uniform E-field over the plasma cross section, which is known to be invalid in the presence of ST /5/.

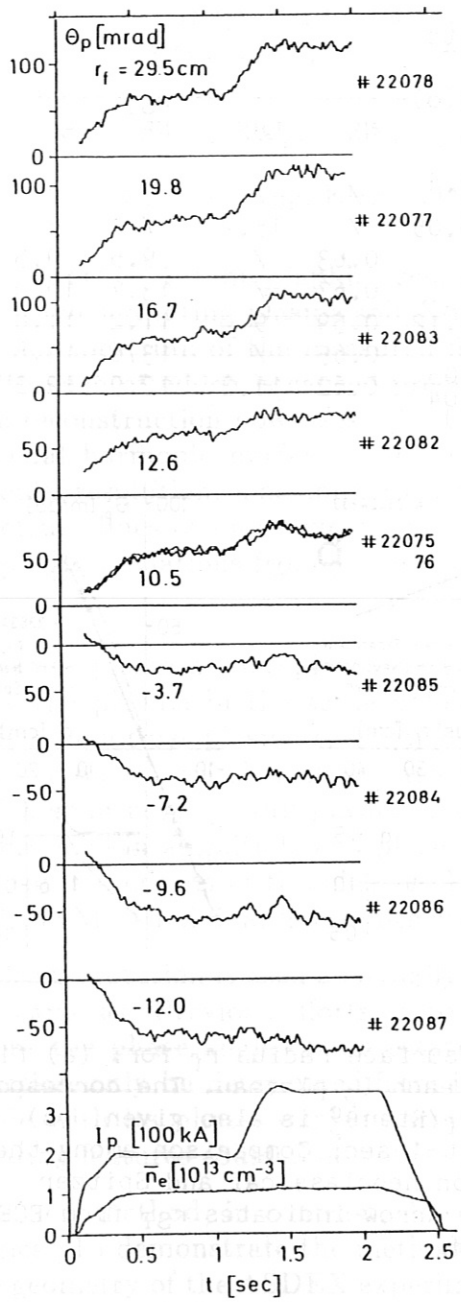

Fig. 1: Temporal behavior of the measured pitch angle θ_p, $\bar{n}_e$ and I_p for series # 1.

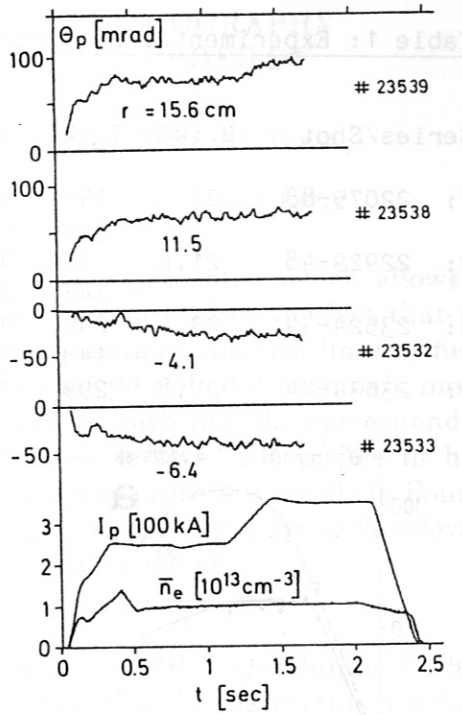

Fig. 2: $\theta_p(t)$, $\bar{n}_e$ and I_p for series # 3.

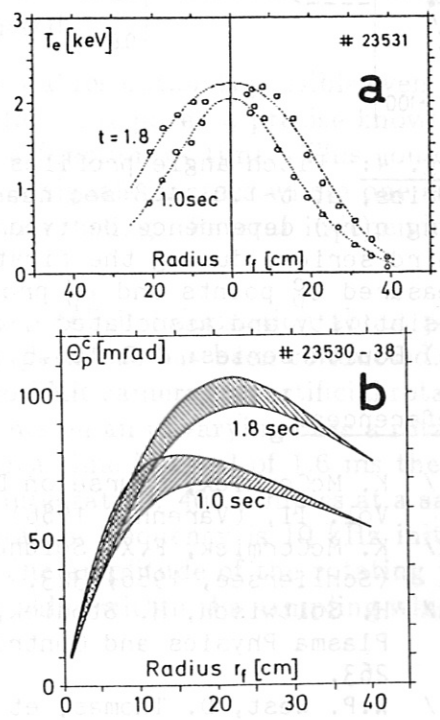

Fig. 3: (a) Te profiles from the YAG Thomson scattering system at t=1.0 and 1.8 sec for series # 3, (b) Pitch angle profiles derived from T_e profiles averaged over the series, assuming neoclassical resistivity.

Table 1: Experimental Parameters and Results

Series/Shot	B_t(kG)	I_p(kA)	q(a)	-----q(o)------ LBS	NR	-------r_{ST}------- LBS	NR	ECE
1: 22075-88	21	194	5.3	$1.06^{+0.8}_{-?}$	/	/	/	/
		348	2.93	0.95 ± 0.05	/	15.2	/	/
2: 22929-48	21.6	228	4.72	/	0.63	/	9.5	9.5
		348	3.06	/	0.67	/	13.7	14.0
3: 23524-39	23	249	4.55	1.01 ± 0.12	0.59	9	11.2	11.0
		348	3.22	/	0.65	/	13.6	13.8
4: 23634-44	22.8	299	3.77	$1.0^{+0.05}_{-0.04}$	0.62	11.2	12.9	12.2

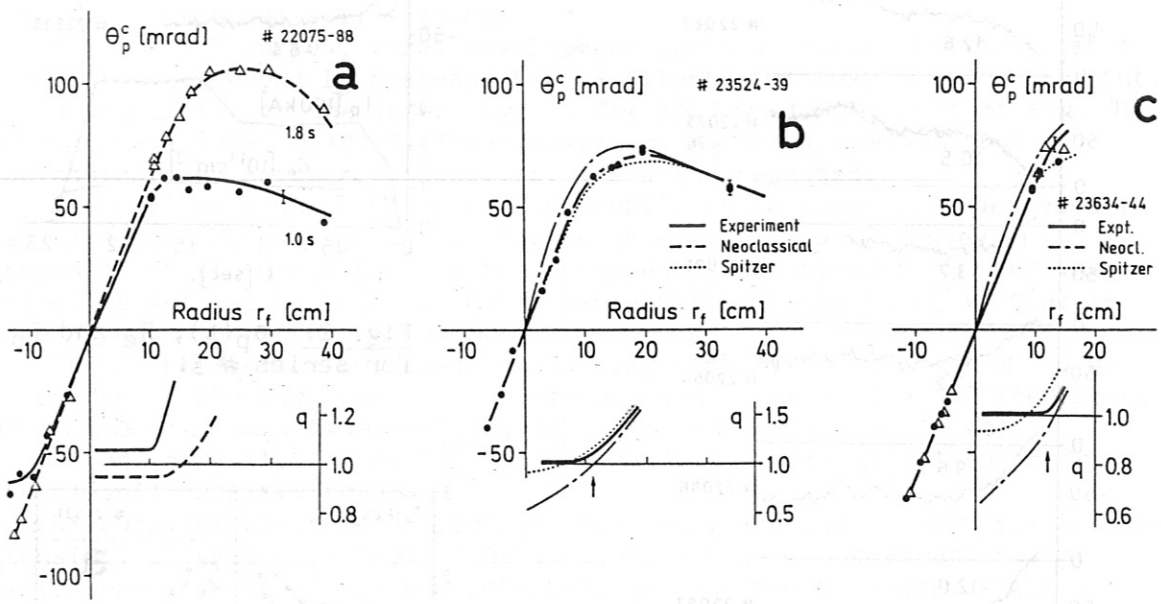

Fig. 4: Pitch angle profiles vs the flux surface radius r_f for: (a) first series, at t~1.0, 1.8 sec near the end of each I_p plateau. The corresponding $q(r_f)$ dependence derived from $q(r_f)=r_f/R\tan\theta_p^c$ is also given. (b) Third series, during the first plateau at t~1 sec; Comparison among the measured θ_p^c points and θ_p^c profiles based on neoclassical and Spitzer resistivity and associated q-profiles. The arrow indicates r_{ST} from ECE. (c) Fourth series: • R~166.5, △ R~163.9 cm.

References:

/1/ K. McCormick, Course on Diagnostic Techniques for Fusion Plasmas, Vol. II, (Varenna, 1986) 635.
/2/ K. McCormick, F.X. Söldner, et al., Proc. 13th EPS Conf., Vol. 2, (Schliersee, 1986) 323.
/3/ H. Soltwisch, H. Stodiek, et al., Proc. of the 11th IAEA Conf. on Plasma Physics and Controlled Fusion Research, Vol. 2, (Kyoto,1986) 263.
/4/ W.P. West, D. Thomas, et al., Phys. Rev. Lett. 58 (1987) 2758.
/5/ F. Alladio, et al., Proc 12th EPS Conf., Vol. 1, (Budapest, 1985) 138.

HIGH RESOLUTION SPARSE CHANNEL TOMOGRAPHY FOR SLOWLY VARYING ROTATING SXR PROFILES

Hermann Krause, Manfred Kornherr, ASDEX Team, NI Team

IPP Garching, EURATOM Association, Fed. Rep. of Germany

Abstract: A tomographic reconstruction algorithm is presented which allows to reconstruct rotating plasma soft X-ray profiles. The method utilises the fact that the Fourier spectrum of the measured line integrals shows distinct spectral lines of finite width each of which is caused predominantly by one single poloidal harmonic mode. The reconstruction now uses a best-fit method to get for each line the corresponding poloidal harmonic modes. The sum of all modes then is the SXR profile in high poloidal resolution. The nonperfect periodicity of the plasma rotation results in Fourier spectrum lines of finite width. Since the best-fit can be performed for each relevant frequency deviations from periodicity are fully taken into account.

Tokamak plasmas are typically observed by SXR pin-hole cameras the chords of which view the plasma in the same poloidal plane. Tomographic reconstruction methods which do not use plasma rotation [1] then permit a poloidal resolution which depends directly on the number of pin-hole cameras available. For each camera with chords which span across a full plasma diameter one single poloidal harmonic mode can be determined in amplitude and phase. The radial resolution depends on the distance of the camera chords in the plasma. For the typical case of two cameras thus the M=0 and the M=1 poloidal harmonics can be reconstructed.

If plasma rotation is used a virtually unlimited poloidal resolution is possible even with few cameras. Previous efforts [2] to use plasma rotation required a precise knowledge about the phase angle of the rotating feature as a function of time. This could, in practice, only be determined from inspection of the signals in cases where one single mode with its phase-coupled harmonics was found rotating. Several independently rotating features could thus not be treated.

The new method, in contrast, does not require an explicit information about phase angles. To demonstrate the method a numerical experiment has been conducted. For the geometry of the ASDEX experiment and its two SXR cameras an artificial rotating SXR profile (cf. fig. 1) is assumed. This profile shows on an unvarying base a rotating feature which is predominantly a M=1 mode. For a time interval of 1.6 ms the line integrals of 58 chords are calculated by numerical integration. 400 samples at a sampling frequency of 250 kHz are simulated. The rotation frequency is 10 kHz initially and speeds up by 5 percent during the interval. The amplitude of the rotating peak on the base profile grows from zero to a maximum value within the sampling window.

Thus the simulated plasma rotation is nonperiodic due to an unstable rotation speed and an unstable mode amplitude.

Figure 2 shows for a typical chord the calculated line integral (top) and the Fourier spectrum of the signal (bottom). The signal clearly shows the growing mode amplitude. The spectrum is calculated using a standard FFT program the result of which is a discrete spectrum i.e. amplitude and phase are determined for discrete frequencies which span the range from 0 to half the sampling frequency in steps of f_0 given by the inverse of the time window width.

As expected the approximately periodic signal results in distinct lines of finite width. E.g. the line near 10 kHz is caused by the M=1 poloidal harmonic, the other lines by the poloidal harmonics M=2,3,4,..., M=0 is centered at small frequencies. Fourier analysis has thus isolated the individual poloidal harmonics from each other.

For tomographic inversion now the plasma profile is represented in polar coordinates as a sum of poloidal harmonics which rotate in both directions at all discrete frequencies (cf. (1)). The radial dependence of the individual cos- and sin-terms is given by a sum over suitable functions. Chosen are modified Zernicke polynomials (cf. (2)). The profile represented is thus determined by the coefficients A^c_{ilm} and A^s_{ilm} which have to be found by a best-fit to the measurements.

$$\epsilon(r,\Theta,t) = \sum_{i=-I}^{I} \sum_{\ell=0}^{L} \sum_{m=0}^{M} \left(A^c_{i\ell m} \cdot \rho_{\ell m}(r) \cdot \cos(m\Theta - 2\pi i f_0 t) + A^s_{i\ell m} \cdot \rho_{\ell m}(r) \cdot \sin(m\Theta - 2\pi i f_0 t) \right) \tag{1}$$

$$\rho_{\ell m}(r) = (1-r^2)^2 \cdot \sum_{s=0}^{\ell} \frac{(-1)^s \cdot (m+2\ell-s)! \cdot r^{m+2\ell-2s}}{s! \cdot (m+\ell-s)! \cdot (\ell-s)!} \tag{2}$$

The determination of the coefficients splits naturally into separate best-fit problems, one for each discrete frequency since an observed Fourier amplitude at the discrete frequency $i \cdot f_0$ can only be caused by poloidal harmonics which rotate at $i \cdot f_0$ and $-i \cdot f_0$ (cf. (1)). The best-fit is performed to the cos- and sin-amplitudes of the observed Fourier spectrum rather than the observed line integrals directly. The best-fit is a standard linear least-square fit. The fit problem is defined by a matrix whose elements describe the response of one measured channel, i.e. the cos- and sin-amplitudes of the Fourier spectrum at a single discrete frequency due to each of the poloidal harmonic modes with one single radial function at unit intensity. The matrix elements are calculated by numerical integration. Considerable savings are possible since matrix elements are independent of the discrete frequency. Again, the number of cameras determines how many poloidal harmonics with both directions of rotation can be fitted to the measured cos- and sin-amplitude at a discrete frequency.

It is thus necessary to define frequency windows around the observed lines in the Fourier spectra and to assign one poloidal harmonic to each window. In case of window overlap there are discrete frequencies for which two ore more modes are assigned. These cases

can still be treated if the number of cameras is larger or equal to the number of modes assigned to a discrete frequency. The process of window setting and mode assignment is a manual input to the process. Obviously window setting is uncritical for narrow lines and difficult for lines which are wider than the line separation. Since line width is determined by deviations from a perfect rigid rotation and line width tends to increase with the higher harmonics there is a practical trade-off between achievable poloidal resolution and how fast the profile of the rotating plasma evolves or how fast the rotation frequency changes.

Figure 3 shows a reconstructed profile to be compared with fig. 1 for the simulated example based on windows 0 to 5 kHz for M=0 and 7 kHz to 15kHz for M=1. The poloidal resolution is thus chosen to be the same as can be achieved with codes that do not utilise plasma rotation. Obviously poloidal structures are considerably smoothed out. Fig. 4 then gives a reconstruction based on M=0 to M=8 with suitable windows defined. Here poloidal resolution is drastically improved.

Figure 5 shows a measured signal of an ASDEX discharge and its Fourier spectrum. The signal is sampled at 250 kHz and shows obvious changes in the signal form during the selected time window. Only 29 channels in two cameras were used for the measurement. The spectrum line near 10 kHz is caused by the M=1 poloidal harmonic and smaller contributions of M=2 to M=5 are visible. A reconstruction with suitable windows defined based on M=0 to M=5 is given in fig. 6.

[1] R. S. Granetz et al., Nucl. Fusion, **25**, p.727, (1985)
[2] P. Smeulders, IPP-Report 2/252 1983 and Nucl. Fusion **23**, p. 529 (1983).

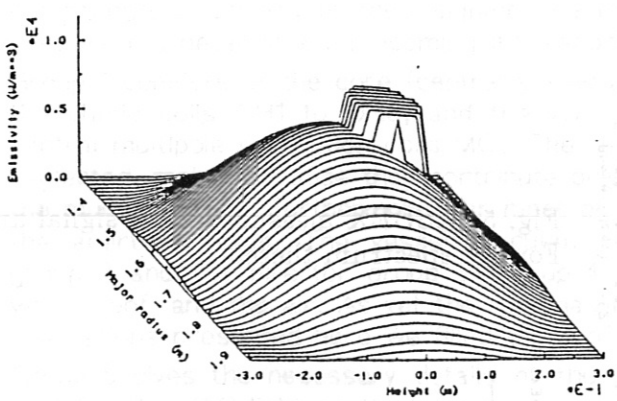

Fig. 1: Simulated SXR profile with rotating peak for t=1.4 ms.

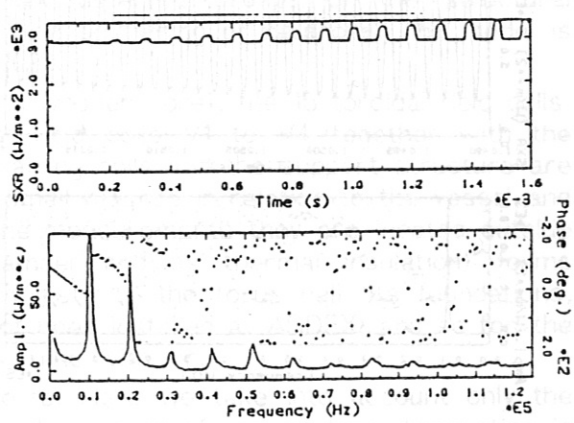

Fig. 2: Calculated SXR line intensity (top) for the rotating profile of fig. 1. Fourier spectrum (bottom) and phases (dotted) of the signal.

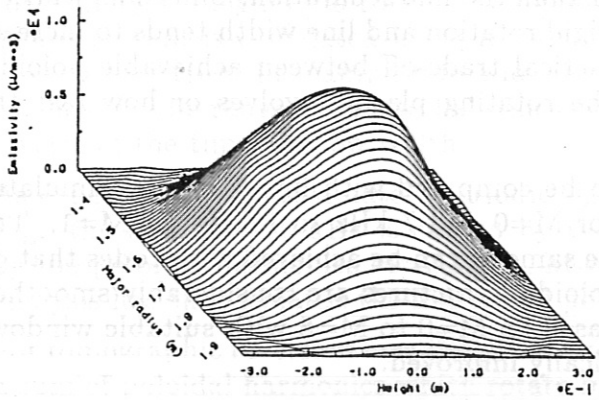

Fig. 3: Reconstruction of the rotating profile of fig. 1 based on M=0 and M=1 for t=1.4 ms.

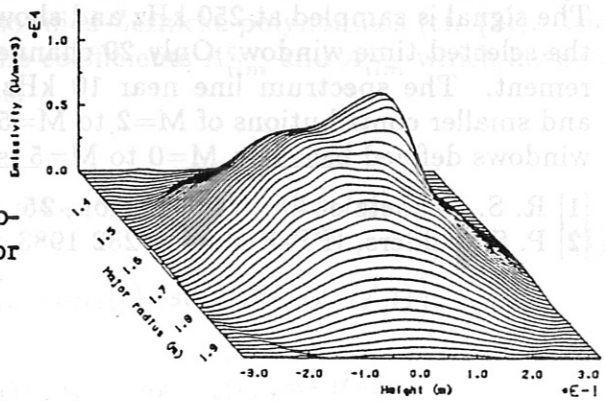

Fig. 4: Reconstruction of the rotating profile of fig. 1 based on M=0 to M=8 for t=1.4 ms.

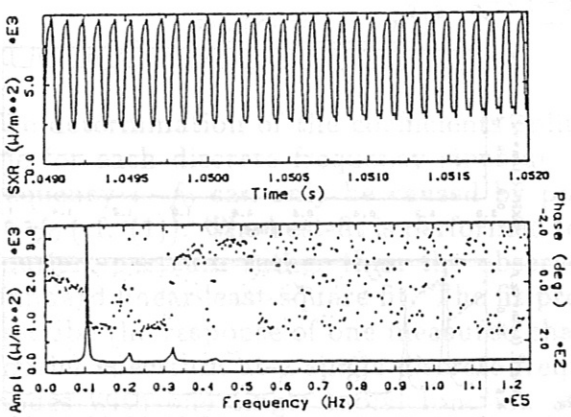

Fig. 5: ASDEX measured SXR signal and Fourier spectrum thereof.

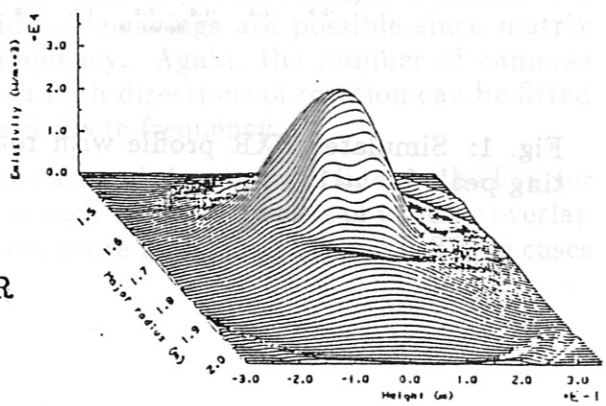

Fig. 6: Reconstruction of an ASDEX SXR profile based on M=0 to M=5.

NUMERICAL AND EXPERIMENTAL INVESTIGATION OF NEUTRON SCATTERING ON ASDEX

K. Hübner, R. Bätzner, H. Hinsch, L. Ingrosso, R. Klein, M. Roos, B. Wolle
Institut für Angewandte Physik II, Universität Heidelberg, D-6900 Heidelberg
B. V. Robouch
Associazione EURATOM-ENEA sulla Fusione,
Centro Ricerche Energie Frascati, I-00044 Frascati
B. Bomba, H. Rapp, W. Herrmann, H. Murmann, A. Eberhagen, H.-U. Fahrbach,
O. Gehre, R. Preis, H. Röhr, K.-H. Steuer, O. Vollmer
Max-Planck-Institut für Plasmaphysik, EURATOM Association, D-8046 Garching

In the past we used the VINIA-3DAMC and NEPMC software [1] to treat the birth, migration and detection of neutrons for the ASDEX facility and compared the results with nuclear emulsion measurements. The agreement between numerical and experimental results was very good, in particular for neutron energies above 2 MeV, despite the fact that we have used a rather simplified ASDEX structure and some approximations in the description of the plasma neutron source.

The VINIA-3DAMC software was improved in order to treat more complex geometric structures, so that a more realistic ASDEX model is now being used. The plasma neutron source was improved, too. Furthermore, the NEPMC software was extended in order to allow arbitrary positions for the nuclear emulsion. Collimators viewing tangentially or in arbitrary directions to the plasma can thus also be interpreted now.

ASDEX model

In our new ASDEX model we distinguish six different groups of the structural components according to their significance for the scattering of neutrons. The model is described in detail in a forthcoming IPP report [2].

Group 1 consists of the core (central screw and wooden core), the 16 toroidal field coils, the ohmic coils OH1 to OH8, and the vertical field coils V1 to V4 together with the central multipole correction coils MC1. The remaining coils and the support structure are neglected, mainly because they contribute only small masses in relation to the vessel and the multipole coils. Furthermore, for most of the measurements they are located outside the aperture fields. The vessel (vacuum chamber and its thermal insulation) forms group 2 and the divertor group 3. Group 4 consists of the torus hall, its foundations, walls, roof, and the air. As yet the roof has not been installed at ASDEX, and so for the calculations presented here we filled the roof volume with air.

Group 5 gives the necessary details of the ports. Here we take into account only the port for the YAG light scattering system, near which most of our neutron diagnostics is at present located. Finally, group 6 contains all the details of the nuclear emulsion equipment, i.e. their supports and collimators.

Plasma neutron source

In the VINIA software, the neutron birth points are determined stochastically by reproducing the measured plasma data. To do so, the NR software [3] is used to calculate the neutron emission profile from the measured density and temperature profiles, the Shafranov shift, and the neutron rate. Only discharges with H^0-injection into

deuterium plasmas are considered here. It is thus assumed that the ion and electron temperatures have the same radial profiles and time dependences. The ion temperature and the rotation velocity were determined by nuclear emulsion measurements [4]. Owing to the integration over different neutron emission angles the emulsion measurement delivers a mean value for the rotation velocity and there is no simple way to determine the velocity on axis. Therefore we used this mean value in the VINIA calculations as input for the central velocity. The rotation velocity profile is assumed to be parabolic.

The angle of emission and the energy of the neutrons are determined with the rotation velocity at the place of birth being taken into account. For H^0-injection we have purely thermonuclear production [4] and in the frame of the rotating plasma the neutron energy distribution is a Gaussian with a half-width determined by the local ion temperature.

The calculations presented here were done for two different shot series, no. 16744-16748 for collimators 3 and 4 (tangential, and antiparallel and parallel to the direction of injection, respectively) and no. 18949-18959 for position 5 (uncollimated, radially directed nuclear emulsion). The corresponding results of the nuclear emulsion measurements are discussed in [4].

The nuclear emulsions were exposed for the whole duration of the discharges. They thus integrate over the time history of the neutron production. In the VINIA calculation this could be simulated by using appropriate time intervals during which the plasma parameters and therefore the neutron production properties do not change considerably and by creating a number of neutrons, for each interval, proportional to the different total neutron yields. An example of this procedure is given in Figure 1 for the shot series no. 16744-16748. Figure 1 shows the time evolution of the neutron rate (mean value for the five discharges). We considered four time intervals, indicated by the vertical lines, using the plasma parameters corresponding to the times indicated by the dots.

Results of VINIA calculations

We present here the results of VINIA test runs for the two collimators 3 and 4 (2830 neutrons each) and the unshielded position 5 (4000 neutrons). So far we looked for qualitative tendencies only and limited our calculations to small numbers of neutrons.

Figure 2 shows the VINIA calculation of the spectral neutron fluences per emitted neutron arriving at the emulsions from the full solid angle. The essentially higher contribution of collided fluence at the unshielded emulsion is obvious. The relative shift of the main line from the emitted neutrons in collimators 3 and 4 is caused by the plasma rotation.

Table 1 compares the emitted and collided contributions normalized to the number of emitted neutrons for the full energy interval considered (1 to 3 MeV) at each of the three positions. For positions 3 and 4 the values without collimator in place are also given.

Table 1 Neutron fluences per emitted neutron in 10^{-7} cm^{-2}

	Coll. 3	Coll. 4	Pos. 3	Pos. 4	Pos. 5
emitted	0.56± 6%	0.68± 6%	2.28± 5%	2.30± 5%	3.78± 3%
collided	0.49±52%	0.10±22%	4.22±21%	2.83±12%	6.82±11%
ratio c/e	0.88	0.15	1.85	1.23	1.80

Position 5 is near the quartz window and positions 3 and 4 are near the toriodal field coils, and the reduction of the fluences at the unshielded positions 3 and 4 compared with position 5 is mainly an effect of shielding by the field coils. The big scatter of the results for the collided fluence inside the collimators is caused by collisions in the collimator material. Because these collisions are rare, their treatment needs an essentially higher number of neutron histories. This is evident also from Table 2, where

where we give the contributions of the different groups of constituents of the ASDEX facility to the collided fluence.

Table 2 Collided neutron fluences per emitted neutron in 10^{-7} cm^{-2}

Group	Regions	Coll. 4		Coll. 3		Pos. 5		
		1 to 2	2 to 3	1 to 2	2 to 3	1 to 2	2 to 3	[MeV]
1	core, coils	0.0030	0.0053	0.0054	0.0113	1.33	0.44	
2	vessel	0.0075	0.0111	0.0087	0.0162	0.55	0.53	
3	divertor	0.0021	0.0013	0.0004	0.0006	0.16	0.21	
4	hall	0.0048	0.0018	0.0061	0.0037	0.032	0.022	
5	quartz window	0.0014	0.0121	0.0007	0.0145	0.39	1.26	
5	rest of port 1	0.0009	0.0107	0.0041	0.0403	0.73	1.08	
6	coll. 3, 4	0.0108	0.0307	0.2079	0.1790	0.067	0.001	
	total	0.0305	0.0730	0.2333	0.2656	3.26	3.56	

Results of NEPMC calculations and measurements

The NEPMC software is used to simulate the response of the nuclear emulsion [1], taking the VINIA results and the measured neutron yield as input. Figure 3 gives the NEPMC results for collimators 3 and 4 compared with the experimental results. In the calculated spectra the line shift caused by plasma rotation is smaller than in the measured spectra by a factor of about 1.9. Hence the true central rotation velocity was about 4×10^7 cm/sec. A more accurate determination would be possible by detailed VINIA calculations.

The collided fluence is reduced by the NEPMC response calculations. This needs further investigation; it may be caused by the directional response of emulsions.

Table 3 compares the normalized calculated and measured neutron fluences for the two energy intervals 1 to 2 and 2 to 3 MeV separately. Good agreement is obtained for the high-energy range, but for the low-energy range the statistical error in the calculation is too large for a comparision.

Table 3: Calculated and measured normalized neutron fluences [10^{-7} cm^3] for collimators 3 and 4

	VINIA calculation		Emulsion measurement		
	1 to 2	2 to 3	1 to 2	2,to 3	[MeV]
Coll. 3	0.24	0.81	0.22	0.68	
Coll. 4	0.03	0.74	0.23	0.72	
mean value	0.14	0.77	0.23	0.70	

Figure 4 gives the results of NEPMC calculations for the proton and neutron energy spectra compared with the experimental results. For an uncollimated nuclear emulsion measurement, the neutron energy spectrum is determined by differentiating the proton energy spectrum. The agreement between numerical and experimental spectra is good; unfortunately owing to limitations during scanning of this plate the measured proton energy spectrum is meaningless for energies below 2.2 MeV and therefore a determination of the absolute values is not possible.

The low-energy wing of the measured neutron energy spectrum is broader than the numerical spectrum. This is probably caused by an underestimation of the measuring errors for the track length in the NEPMC software.

References

[1] K. Hübner, e.a., 14th Europ. Conf. on Controlled Fusion and Plasma Physics, Madrid 1987, part 3, pp 1298-1301, and Report IPP III/122, August 1987
[2] B. V. Robouch, e.a., Report IPP III/132, in preparation
[3] K. Hübner, e.a., this conference
[4] K. Hübner, e.a., 14th Europ. Conf. on Controlled Fusion and Plasma Physics, Madrid 1987, part 3, pp 1294-1297

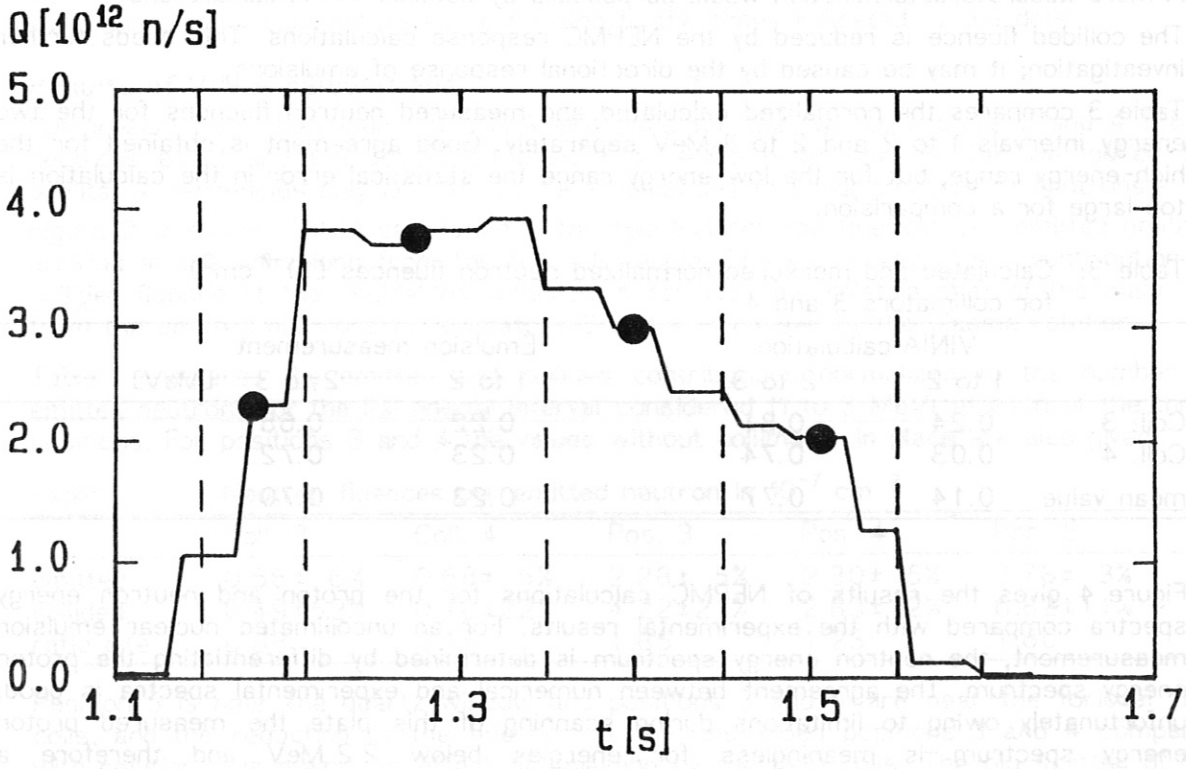

Fig.1: Time dependence of neutron rate and intervals for VINIA calculations

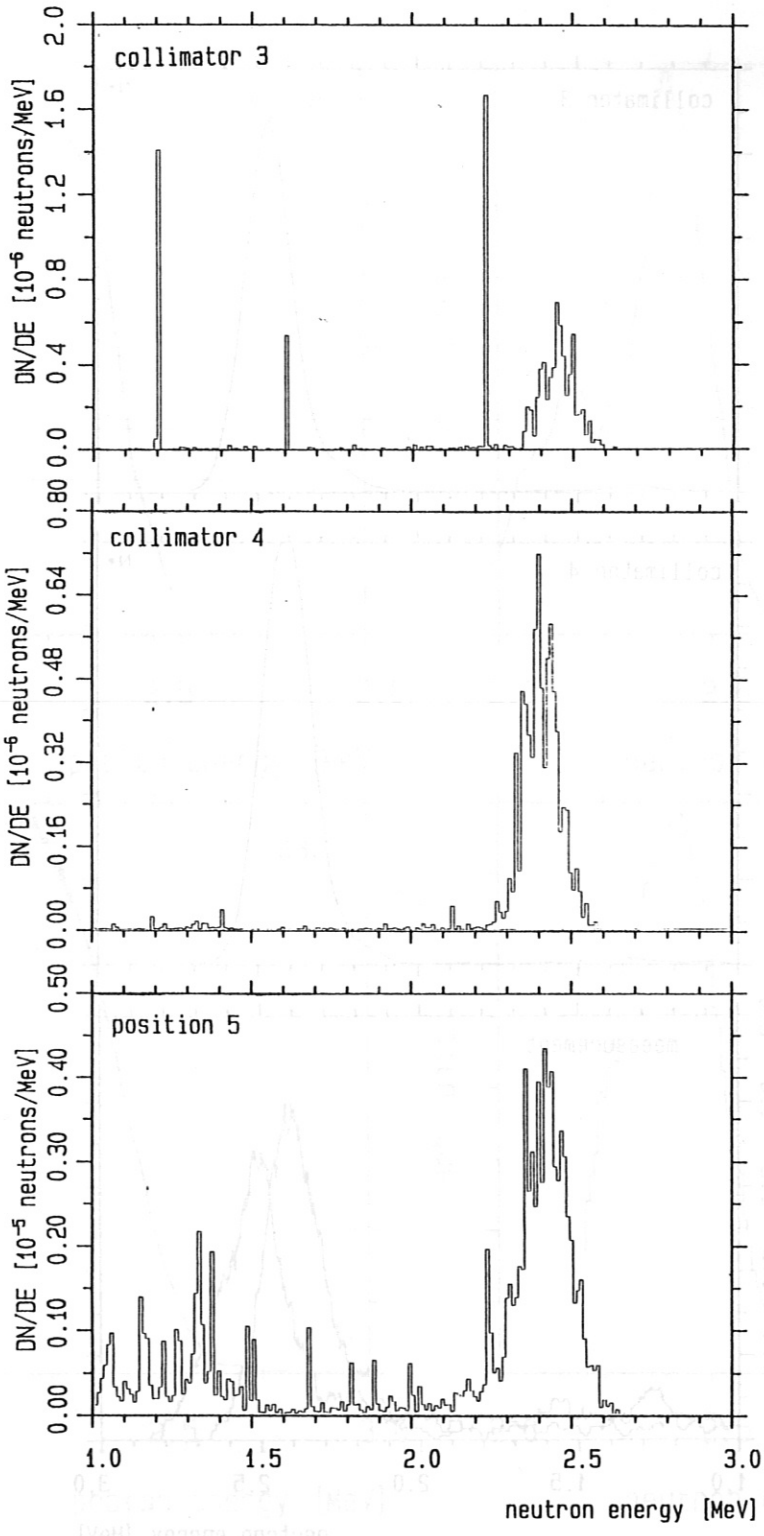

Fig.2: VINIA calculations of the spectral neutron fluence arriving at the emulsion

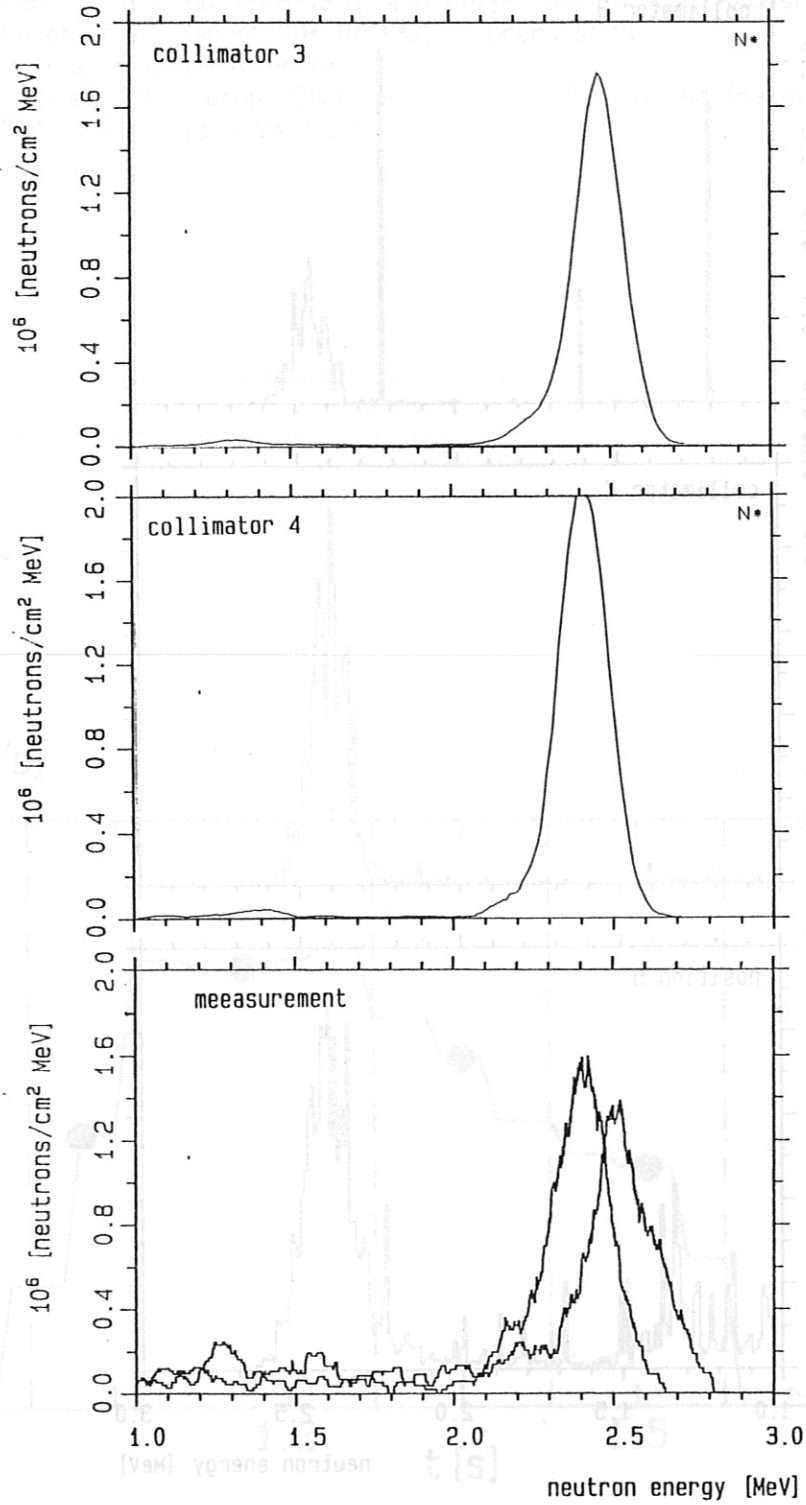

Fig.3: NEPMC results for collimators 3 and 4 and experimental results

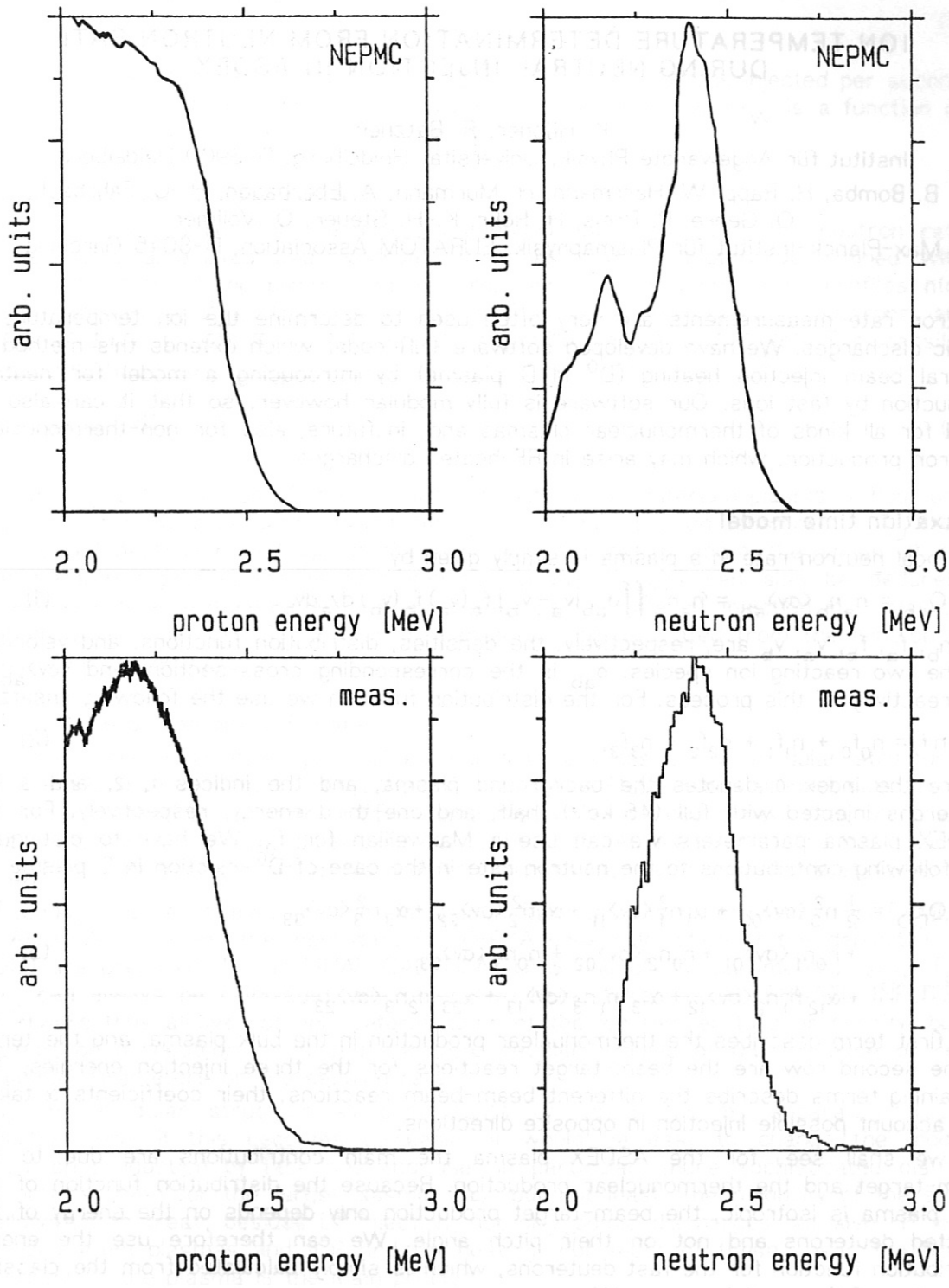

Fig.4: NEPMC results for position 5 compared with experimental results

ION TEMPERATURE DETERMINATION FROM NEUTRON RATE DURING NEUTRAL INJECTION IN ASDEX

K. Hübner, R. Bätzner
Institut für Angewandte Physik, Universität Heidelberg, D-6900 Heidelberg
B. Bomba, H. Rapp, W. Herrmann, H. Murmann, A. Eberhagen, H.-U. Fahrbach, O. Gehre, R. Preis, H. Röhr, K.-H. Steuer, O. Vollmer
Max-Planck-Institut für Plasmaphysik, EURATOM Association, D-8046 Garching

Neutron rate measurements are very often used to determine the ion temperature in ohmic discharges. We have developed software (NR code) which extends this method to neutral beam injection heating (D^0 in D plasma) by introducing a model for neutron production by fast ions. Our software is fully modular however, so that it can also be used for all kinds of thermonuclear plasmas and, in future, also for non-thermonuclear neutron production, which may arise in RF-heated discharges.

Relaxation time model

The local neutron rate in a plasma is simply given by

$$Q_{ab} = n_a n_b \langle\sigma v\rangle_{ab} = n_a n_b \iint \sigma_{ab} |v_a - v_b| \, f_a(v_a) \, f_b(v_b) \, dv_a dv_b . \qquad (1)$$

n_a, n_b, f_a, f_b, v_a, v_b are, respectively, the densities, distribution functions, and velocities of the two reacting ion species, σ_{ab} is the corresponding cross-section, and $\langle\sigma v\rangle_{ab}$ is the reactivity of this process. For the distribution function we use the following ansatz:

$$n f = n_0 f_0 + n_1 f_1 + n_2 f_2 + n_3 f_3, \qquad (2)$$

where the index 0 denotes the background plasma, and the indices 1, 2, and 3 the deuterons injected with full (45 keV), half, and one-third energy, respectively. For the ASDEX plasma parameters we can use a Maxwellian for f_0. We have to distinguish the following contributions to the neutron rate in the case of D^0 injection in D plasma

$$\begin{aligned} Q_{DD} = {} & \tfrac{1}{2} n_0^2 \langle\sigma v\rangle_{00} + \alpha_1 n_1^2 \langle\sigma v\rangle_{11} + \alpha_2 n_2^2 \langle\sigma v\rangle_{22} + \alpha_3 n_3^2 \langle\sigma v\rangle_{33} \\ & + n_0 n_1 \langle\sigma v\rangle_{01} + n_0 n_2 \langle\sigma v\rangle_{02} + n_0 n_3 \langle\sigma v\rangle_{03} \\ & + \alpha_{12} n_1 n_2 \langle\sigma v\rangle_{12} + \alpha_{13} n_1 n_3 \langle\sigma v\rangle_{13} + \alpha_{23} n_2 n_3 \langle\sigma v\rangle_{23} . \end{aligned} \qquad (3)$$

The first term describes the thermonuclear production in the bulk plasma, and the terms in the second row are the beam-target reactions for the three injection energies. The remaining terms describe the different beam-beam reactions, their coefficients α taking into account possible injection in opposite directions.

As we shall see, for the ASDEX plasma the main contributions are due to the beam-target and the thermonuclear production. Because the distribution function of the bulk plasma is isotropic, the beam-target production only depends on the energy of the injected deuterons and not on their pitch angle. We can therefore use the energy distribution function for the fast deuterons, which is simply calculated from the classical relaxation of the particle energy W:

$$dW/dt = - W/\tau_W, \qquad (4)$$

where τ_W is the energy relaxation time. The resulting distribution functions are

$$n_i f_i(W) = \frac{\dot{N}_i D_i(r)}{n} \frac{n\tau_{W_i}}{W_i}, \quad i = 1, 2, 3. \tag{5}$$

Here n is the electron density, $\dot{N}_i$ are the numbers of deuterons injected per second, and $D_i(r)$ their deposition profile. The energy relaxation parameter $n\tau_W$ is a function of only the electron temperature and the energy itself.

Interpretation of neutron rate

The emission profiles for the different contributions in eq. 3 to the neutron rate and thus the volume-integrated neutron rate itself are completely determined with the geometric data of the plasma, the electron density and temperature profiles n(r) and $T_e(r)$, the profile $Z_{eff}(r)$, the deposition profile D(r) of the injected deuterons, and the plasma deuteron density and temperature profiles $n_D(r)$ and $T_D(r)$. The densities of electrons n, deuterons n_D, and protons n_H are related by

$$\frac{Z_x - Z_{eff}}{Z_x - 1} = \frac{n_D}{n}\left(1 + \frac{n_H}{n_D}\right), \tag{6}$$

where Z_x is the charge of the dominant impurity. In a deuterium plasma without protons, n_D could therefore be determined from Z_{eff}, and thus the ion temperature T_D from the measured neutron rate Q_{DD}. If there is any information about the shape of the ion temperauture profile, the neutron emission profile $D_{DD}(r)$ can also be deduced. For plasmas with a mixture of protons and deuterons, as with H^0 injection in D plasma, one of the two parameters T_D and n_D/n_H can always be calculated from the neutron rate if the other is known.

Structure of the NR software

To take care of all these possibilities, our software has a fully modular structure. The scheme is shown in Fig. 1; firstly, the software DATA FILES reads all input data. It is thus easy to adapt changes in the ASDEX data files or to introduce new data which become accessible with the development of new diagnostics. An example of the last is the new $Z_{eff}(r)$ measurement from visible bremsstrahlung which is now availiable at ASDEX.

Secondly, the reactivities and the distribution functions are determined in INTERMEDIATE CALCULATIONS and the input data for FREYA code calculation of the deposition profile D(r) are prepared. In the FINAL CALCULATIONS one of the parameters Q_{DD}, T_D, and n_D can always be calculated, the other two being taken as ALTERNATE INPUTS. The software thus allows not only determination of the ion temperature or density, but also prediction of neutron rates and therefore detailed studies of the influence of relevant plasma parameters on the neutron rate.

By this modular structure all components of eq. 3 can be separately discussed. Furthermore, if this becomes advisable, it would be easy to change the model for neutron production by fast ions and use, in particular, more sophisticated distribution functions, even for the target plasma. Last but not least, the flexibility of the software allows us to treat, besides D^0 injection, not only ohmic discharges but also H^0 injection in deuterium plasmas and ICR and LH heating. For most of these cases the hydrogen content of the plasma is the main problem.

D^0 injection in deuterium plasma

As an example of the treatment of D^0 injection in deuterium plasma, we consider two discharges, one with a high ion temperature of about 3.5 keV (#17061, injection: 4.15 MW,

1.1 - 1.4 sec) and another with a relatively low ion temperature of about 2.0 keV (#16910, injection: 3.1 MW, 1.1 - 1.5 sec). Figure 2 shows for both discharges the time development of the neutron rate Q and the central electron temperature, as well as the time-dependent central deuteron temperature calculated from Q. Table 1 gives for discharge #17061 for some times the components Q_{00}, Q_{01}, Q_{02} (the indices correspond to those in equation 3) and the ratio T_D/T_e, calculated for a content of 10% protons.

The dominant neutron production is due to the full energy beam reactions with the target plasma Q_{01}. The half-energy beam (Q_{02}) contributes about 10% of Q_{01}. At the beginning of the injection this is appreciably higher than the thermonuclear production Q_{00}. But during injection the temperatures increase, causing an increase in the beam-target reactions (owing to T_e and T_D) as well as in Q_{00}. At the maximum of the neutron rate Q_{00} is about twice Q_{02}. The scatter in the results for T_D/T_e reflects the uncertainty of the temperature determination.

TABLE 1

time [sec]	Q_{00}	Q_{01}	Q_{02}	T_D/T_e
	[10^{13}neutrons/sec]			
1.15	0.036	4.41	0.35	1.30
1.20	0.72	10.5	1.03	1.20
1.25	2.07	12.9	1.29	1.10
1.30	2.32	8.31	0.91	1.20
1.35	1.14	7.36	0.83	1.35
1.40	0.39	6.60	0.68	1.20

Table 2 gives the different particle densities $n_i = \int n_i f_i dW$ on the plasma axis. They are of the same order for all components of the beam, but about one order of magnitude smaller for the beams than for the target plasma.

Table 2 Deuteron densities on axis at maximum neutron production

	n_0	n_1	n_2	n_3	
#17061	4.16	0.64	0.45	0.16	10^{13} deuterons/cm^3
#16910	3.37	0.45	0.17	0.12	10^{13} deuterons/cm^3

Table 3 gives for discharge #16910 at 1.3 sec all components of eq. 3, for injection of the total power in one direction and for the hypothetical case of balanced injection with half the power in each beam. Here, owing to the low ion temperature the thermonuclear production is of the same order as the production by the one-third energy beam component, which itself amounts to only 1.5% of the beam production. The production by reactions between the beam particles clearly shows a dependence on the relative velocity, as is to be expected. But owing to the small densities in the beams compared with the target plasma the beam-beam productions are smaller than the one-third energy beam-target production, even in the hypothetical case of balanced injection, and so it is always negligible.

Table 3

	neutron rate [neutrons/sec]	
	unidirectional inj.	balanced inj.
Q_{00}	7.99×10^{11}	7.99×10^{11}
Q_{01}	4.39×10^{13}	4.39×10^{13}
Q_{02}	3.71×10^{12}	3.71×10^{12}
Q_{03}	7.39×10^{11}	7.39×10^{11}
Q_{11}	7.35×10^{7}	1.44×10^{11}
Q_{12}	1.47×10^{8}	8.20×10^{10}
Q_{13}	1.86×10^{8}	2.94×10^{10}
Q_{22}	7.18×10^{5}	3.19×10^{10}
Q_{23}	6.42×10^{5}	8.54×10^{9}
Q_{33}	7.39×10^{3}	2.12×10^{9}

H^0 injection in deuterium plasma

As an example of the treatment of H^0 injection in deuterium plasma we consider the discharge #21502 (1.35 MW, 1.0 - 3.0 sec). In this case we have only the thermonuclear production Q_{00}. Figure 3 shows the measured neutron rate and the ratio n_D/n_H from CX measurements. Figure 4 gives the deuteron temperature calculated with our software and, for comparision, the electron temperature from ECE measurements. Here again we find $T_D/T_e \approx 1.2$. The decrease in the neutron rate is caused by the small decrease in the ion temperature.

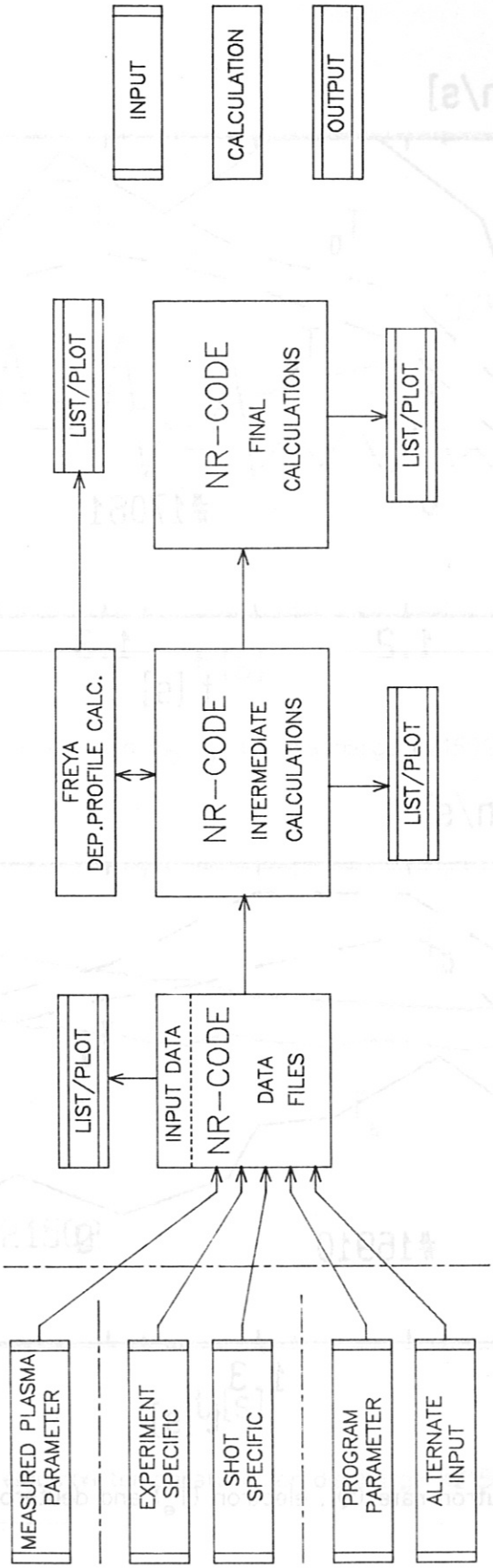

Fig.1: Software scheme

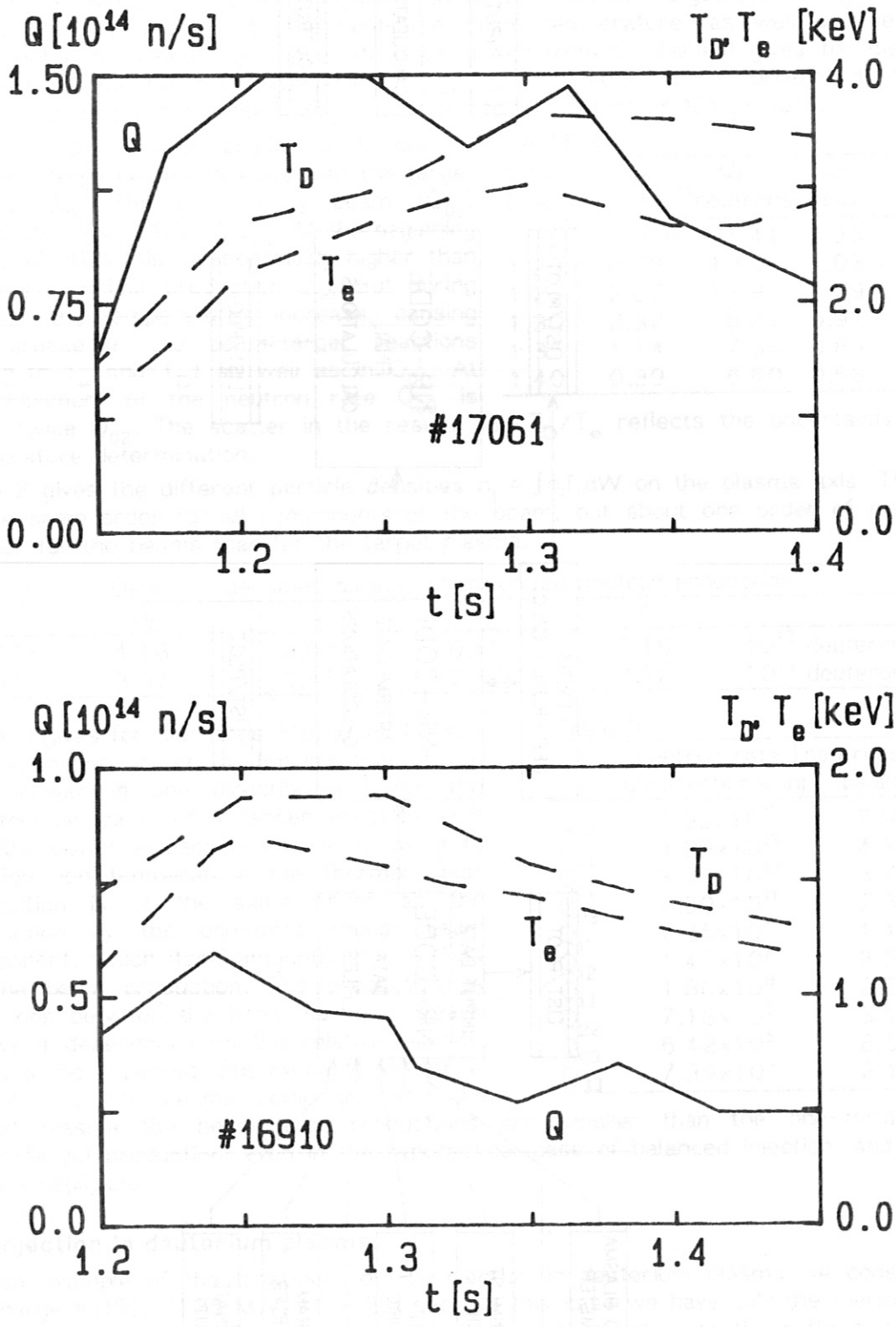

Fig. 2: Neutron rate (Q), electron (T_e) and deuteron (T_D) temperatures

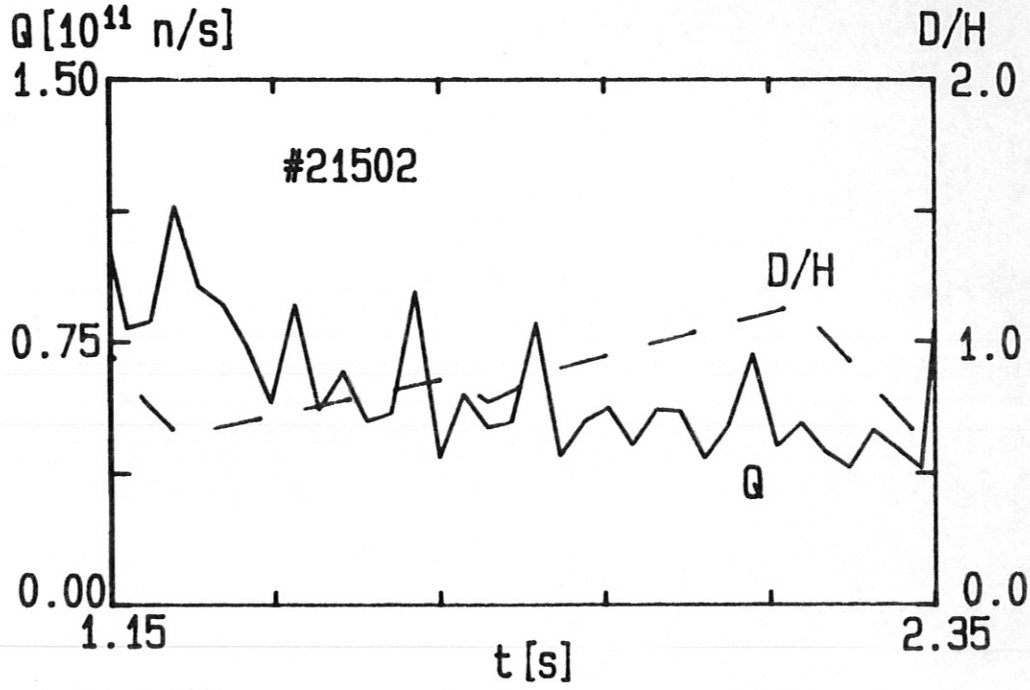

Fig. 3. Neutron rate and n_D/n_H for discharge #21502

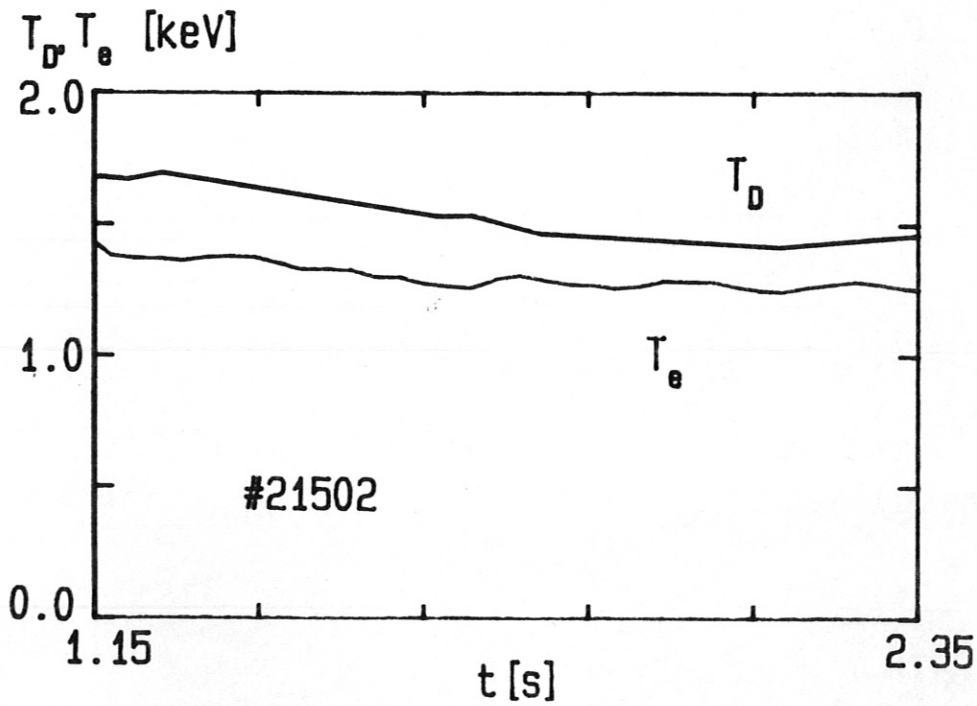

Fig. 4: Ion and electron temperature for discharge #21502